SYNTHESIS AND OPTICAL PROPERTIES OF HYBRID GOLD NANOPARTICLES COUPLED WITH QUANTUM DOTS AND PORPHYRINS

by

Andrew Kevin Tobias Jr.

A dissertation submitted to the faculty of
The University of North Carolina at Charlotte
in partial fulfillment of the requirements
for the degree of Doctor of Philosophy in
Nanoscale Science

Charlotte

2016

Approved by:

_____
Dr. Marcus Jones

_____
Dr. Michael Walter

_____
Dr. Edward Stokes

_____
Dr. Thomas A. Schmedake

_____
Dr. Terry Xu

ABSTRACT

ANDREW KEVIN TOBIAS JR. Synthesis and optical properties of hybrid gold nanoparticles, coated with quantum dots and porphyrins. (Under the direction of DR. MARCUS JONES)

Coupling of optically active materials, or chromphores, to plasmonic nanoparticles represents a new research area which has the ability to produce higher efficiency lighting and photovoltaic materials. The main goal of this project was to create novel systems for plasmonic coupling of different chromophores to gold nanoparticles. The plasmonic platforms utilized were gold nanoparticles coated in semiconductor shells of cadmium sulfide or zinc sulfide. The crystalline, semiconductor shell acts as a dielectric spacer to separate the chromophore from the metal surface. Intimate contact to the metal surface may result in increased energy transfer and nonradiative relaxation mechanisms, resulting in shorts for photovoltaic devices and quenching in applications using light emission. Plasmonically enhanced photo-absorbers can be used to boost the collected photocurrent in photovoltaic applications while enhanced fluorescent materials can be used in imaging or display technologies in which bright and stable, solution-state materials are needed. Quantum dots were linked to the nanoparticle surface, via a carbodiimide linking process. The thickness of the shell was then altered to optimize the spacing distance needed to maximize the quantum dot radiative rate. Porphyrins were linked to the surface of the semiconductor shell via deprotonated phenyl acid groups, located on the 5,10,15 or 20 positions of tetraphenyl porphyrin. Enhancements in the porphyrin extinction coefficient when bound to the nanoparticles were estimated through analysis of the absorbance spectral changes.

DEDICATION

I dedicate this dissertation to my loving parents Andrew Tobias Sr. and Jackie Tobias. Their support and guidance throughout my life has given me the tools and the drive to complete this dissertation. My siblings, Kristie, Joshua and Gabbi, who's encouragement has always kept me grounded and focused. Finally, I want to give a special dedication to my 4 month old daughter Sophia Tobias, who I hope will one day read this and know how much she is loved and cherished.

ACKNOWLEDGEMENTS

I would like to start by acknowledging the help and support from my advisor Dr Jones. The realization of this degree would not have been possible without his support and guidance. Whether through discussion of a difficult problem during group meeting, figuring out how to acquire funding or talking about various life issues, his knowledge has helped to further my own growth and development as a scientist. He has trained myself and everyone in our group to produce quality work and to ensure that we have full expertise over any topic we discuss with the community. I am truly greatful for his mentorship, and advising. He trusted me with the responsibility of leading our wet laboratory and without that experience I would not be the scientist I am today. I would also like to thank my committee, Dr. Walter, Dr. Schmedake, Dr. Stokes and Dr. Xu, for their efforts and willingness to devote their time to being apart of my project. Dr Walter and his group taught me everything I know about the porphyrin aspect of the project and I am very greatful for their assistance and willingness to teach a physical chemist about porphyrin chemistry.

The members of the Jones group have also helped fuel my scientific development and provided close friendships. I must first start by thanking my close friend and someone I consider a mentor, Kevin Major. He was the senior graduate student when I began working in the Jones lab. He was one of my first examples of what a real scientist should be. He not only showed me the technical aspects, from using various instrumentation or loading data, but also showed me the proper mentality a scientist should have. He was always confident in his work but skeptical of his and other results. Although stress and doubt are a normal part of any scientific endeavour, he showed me

how to use those to my advangtage. His frienship and leadership inspired me and my success would not have been possible without his presence. I would also like to thank past members, Danielle and Gaurav, and Mike for their friendship, and support as well. They both offered valuable feedback, advice and friendship. I would also like to thank Kathleen for her friendship and research feedback. I hope the path toward her degree is as rewarding as mine was. I am extremely greatfeul to have been apart of such a wonderful group.

Although not technically part of our research group, Dr. Patrick Moyer played a vital role in my devlepment as a scientist. Discussion between him and his research group helped to fuel my passion, during my master's degree and played a pivitol role in my decion to pursue my PhD in the nanoscale program at UNC-Charlotte. His group members, Ryan Hefti and Sharonda LeBlanc were also great friends and helped with a variety of research issues.

I would like to thank the support from the UNCC chemistry department. Dr Merkert and Dr. Carlin were always willing to help me learn how to use any instrumentation in the department or fix something that was broken.. I want to thank everyone that has worked in the front office, specifically, Caroline Kennedy, Robin Burns, Nancy Queen and Rebeccan Hawes. They have all worked very hard to ensure everything that I needed was taken care of, from forms, to financial issues to ensuring all my academic needs were met. I also would like to think the UNCC Chemistry department for allowing me to use all the various instrumentation needed for my project and the engineering department for the countless hours of TEM time that I logged.

I would also like to thank all the friends I have acquired at UNCC throughout my graduate studies, Graham Collier, Jessica Hanely, Shawn Ridlen, Tiffany Meyers, Nathan Behm, Samantha Dodbele, Zach Lyles, Eric Fink, Keri Dowling ,Reynolds Ivins, John Patterson, Ashley Milton, John Maner, and Matthew Huff and Jarret Rodgers. I thank everyone for helping me to take my mind off research every once and while or listening whenever I needed someone to talk to about my research. I also wish good luck to those listed above who are also completing or currently enrolled in doctoral programs or other graduate degrees.

I also want to give a special thank you to the UNCC Men's lacrosse team for letting me coach them for four years and be apart of their family. I have grown close to many of the coaches, players and families that have been apart of this organization and being apart of the team was a very special experience. Thank you guys for listening to me and letting me see and play some lacrosse.

I would like to thank my friends at home. I often feel distant from them in my time doing research but whenver I visit home or make a phone call they always remain fully supportive and their long term friendship has been something I will always treasure. Caroline Eggars, Matt and Lauren Roach, Chris and Thomas Davis, Chris Long, and Brie Bestrom, I thank you all for our friendship and this would not have been possible without you guys.

I finally want to thank my family. Since they were mentioned in my dedication I will make this portion brief, but without their love, guidance and support I would not be able to finish this degree.

TABLE OF CONTENTS

LIST OF TABLES

LIST OF FIGURES

LIST OF ABBREVIATIONS

FRET	Förester Resonance Energy Transfer
QD	Quantum Dot
NP	Nanoparticle
NSOM	Near-field Scanning Optical Microscopy
MEF	Metal-enhanced Fluorescence
NSET	Nanometal Surface Energy Transfer
TiO_2	titanium dioxide
PMMA	Poly(methyl methacrylate)
CdSe	Cadmium selenide
CdS	Cadmium sulfide
ZnS	Zinc sulfide
QY	Quantum yield
TTP	Tetraphenyl porhyrin
TTPa	Tritolyphenylacid porphyrin
DTDPa	Ditolyldiphenylacid porphyrin
TCO4PP	Tetra (4-carboxooctylphenyl)porphyrin

CHAPTER 1: INTRODUCTION

Nanoparticles are attractive materials due to their physical properties, which are intermediate to that of individual atoms and bulk material. Semiconductors have long been utilized for their optical properties in materials such as LEDs[1 2 3 4 5], lasers[5 6 7 8] , or catalysis[9 10 11]. Recently, preparation of nanostructured semiconductors have become increasingly more efficient and well-understood, leading to their incorporation into similar devices as their bulk counterparts.[12 13 14 15 16 17] When synthesized on the nanoscale size-regime, semiconductor absorption and emission are strongly dependent on the size and shape of the nanoparticle itself.

Metal nanoparticles also have a rich library of utility, dating back to their incorporation into stained glass windows[18 19 20] or their use in medicinal treatments.[21 22 23] The majority of applications involving metal nanoparticle applications, specifically using gold nanoparticles, take advantage of their bright absorption. The strong absorption exhibited by colloidal solutions of gold nanoparticles, is the consequence of a localized surface plasmon resonance, which is an oscillation of surface electrons induced by light excitation. This resonance makes them useful as active materials in a variety of applications which require strong absorption of incident radiation.[17 24 25] The resonance frequency is also dependent on the surface environment of the gold nanoparticles, which

makes them excellent candidates for sensing.[26] [27] [28] Metal nanoparticles have, more recently, been utilized for their ability to boost the efficiency of the optical absorption or emission rates of various chromophores.[29] [30] [31]

The goal of this project was to create a novel system for coupling plasmonic, gold nanoparticles to chromophores. The spacing of the chromphore from the nanoparticle surface was carefully controlled in order to optimize coupling effects. Hybrid nanoparticles or gold nanoparticles coated in cadmium sulfide or zinc sulfide, were utilized as the plasmonic platform for coupling**.** The shell was controlled from 2-20 nm in order to provide different coupling distances for the chromophores.

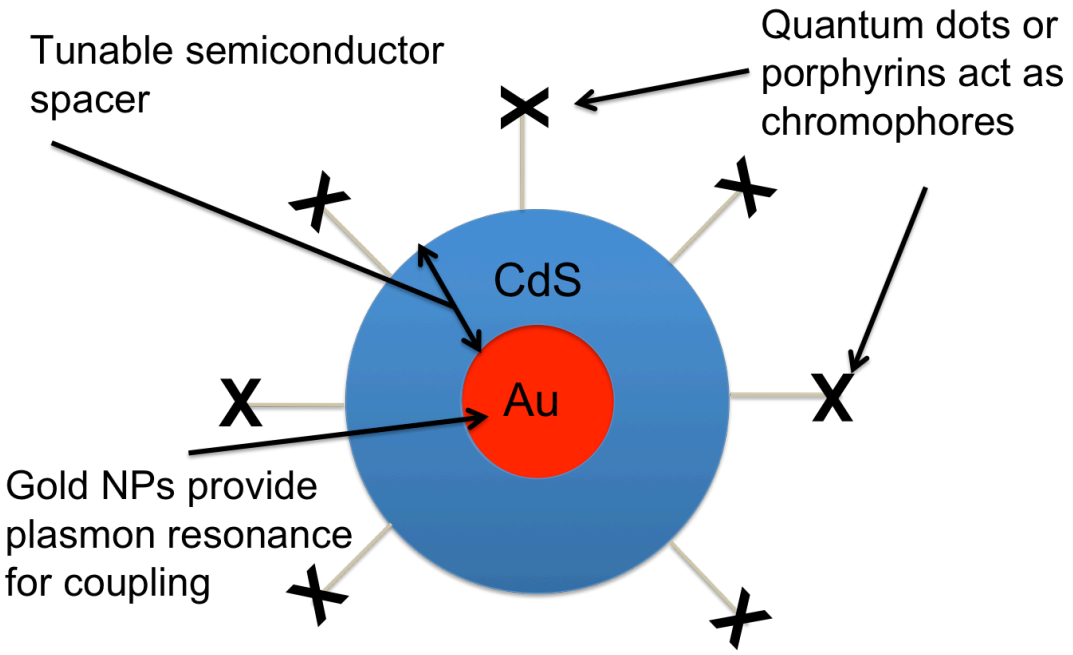

Figure 1.0: Illustration of the coupling system proposed.

Quantum dots were bound via a molecular linker, while porphyrins were bound via phenyl acid groups located on their periphery or amine groups on the center porphyrin ring. The two materials represent common fluorophores and a common absorber in a photovoltaic device, respectively. The improvement of device performance is possible through incorporation of plasmonically enhanced materials such as these. This study aimed to provide a synthetic route for producing these plasmonically-enhanced composites in colloidal solution

CHAPTER 2: LOCALIZED SURFACE PLASMONS AND COUPLING

2.1 Introduction

Noble metal nanoparticles are a branch of heavily studied nanomaterials. Various synthetic techniques have been utilized to synthesize spherical particles out of gold, silver, or platinum to produce nanoparticles in the size range of 10-100 nm in diameter, with various shapes and aspect ratios.[32 33 34 35] Interesting optical properties arise due to the delocalization of the conduction band electrons on the surface of the metal. This phenomenon becomes particularly important, when the metals are synthesized to have features on the nanometer length scale.

The surface electrons can be excited with visible light to cause a phenomenon known as the localized surface plasmon resonance, resulting in strong optical absorption bands at specific frequencies.[36] For noble metals, such as gold , silver or copper, this resonance lies in the visible region and can be very strong. The frequency of the resonance is also extremely sensitive to the size and shape of the particles as well as the surface environment of the nanoparticle. The extinction coefficient of the nanoparticles can then be calculated using a dipole approximation of Mie theory. The theory assumes the particles are much smaller than the wavelength of the incident light , so that only the electron oscillation contributes.

$$\sigma_{ext} = \frac{9 * V * \varepsilon_m^{3/2}}{c} * \frac{\omega * \varepsilon_2(\omega)}{[\varepsilon_1(\omega) + 2 * \varepsilon_m]^2 + \varepsilon_2(\omega)^2} \quad (1)$$

The extinction cross-section, σ_{ext}, of the metal nanoparticle, can be calculated using the equation (1), where V is the volume, ω is the angular frequency of the incident light, c is the speed of light in a vacuum and ε represents the dielectric constant. Two different dielectric constants are taken into account, that of the surrounding material ε_m, and that of the metal.

$$\varepsilon(\omega) = \varepsilon_1(\omega) + i\varepsilon_2(\omega) \quad (2)$$

$$\varepsilon_1(\omega) = -2 * \varepsilon_m \quad (3)$$

The metal dielectric is complex containing a real ε_1 , and imaginary portion ε_2,as seen in equation (2). The real component is negative and takes into account scattering or reflection of the incident radiation. The imaginary component takes into account the absorption of the incident radiation by the nanoparticle. The resonance frequency is then described using equation (3).

According to these equations, the extinction coefficient is then independent of the particle size, in disagreement with experimental data. The Drude free electron theory, can account for this discrepancy by factoring in the electron-surface scattering, which is inversely dependent on the particle radius. This means the resonance is now strongly dependent on particle size and its surrounding environment. In the case of gold or silver nanoparticles, this resonance can be tuned across the visible spectrum, allowing for utility as active materials in devices used for sensing[37 38 38], or imaging[38 39]

2.2 The Localized Surface Plasmon and FRET

Noble metal nanoparticles are useful in many optical application due to their large extinction coefficients, which tend to be many orders of magnitude higher than most chromphores. This results in the strong absorption observed in colloidal solutions or films

made with gold or silver nanoparticles. The absorption of light induces an oscillation of surface electrons, whose electric field can also cause a perturbation of chromophore excitation or fluorescence.[40]

At small separation distances, the effects can manifest as Förester resonance energy transfer (FRET), in which all the excitation energy is dissipated into the metal nanoparticle.[41] In FRET, an excited-state chromophore, is created through optical absorption. The energy can then be transferred to an acceptor species through dipole coupling. The fluorescence quenching of the donor species can be utilized to monitor the efficiency of the FRET process. This process is inversely proportional to R^6 , where R is the distance between the donor and acceptor.

$$E_{FRET} = \frac{N}{N + (R/R_0)^6} \tag{4}$$

The FRET rate is given as a function of the number of acceptors, N, and the distance between the donor and acceptor, R, as shown in equation (1). FRET has been utilized in numerous detection and sensing based applications.[42] [43] [44] [45] Molecules which bind to the nanoparticle surface can also cause an aggregation of the colloidal nanoparticles resulting in a shift of their plasmon resonance which can be detected spectroscopically. [46]

The advantage of using gold nanoparticles to detect the presence of other molecules, lies in their high extinction coefficients, up to 10^8 in some cases, allowing for higher sensitivity and lower detection limits.[38] [44] Gold nanoparticles in close proximity to fluorescent molecules can quench fluorescence intensity and shorten fluorescent lifetimes. This process is due to the introduction of nonradiative relaxation mechanisms such as energy transfer to the metal, with the distance between two adjacent nanoparticles

being correlated to the extent of energy transfer between the two nanoparticles. [45] This distance-dependence can be used to measure molecular distances by collecting spectra before and after these binding events, allowing for production of sensitive molecular rulers.[47] [48]

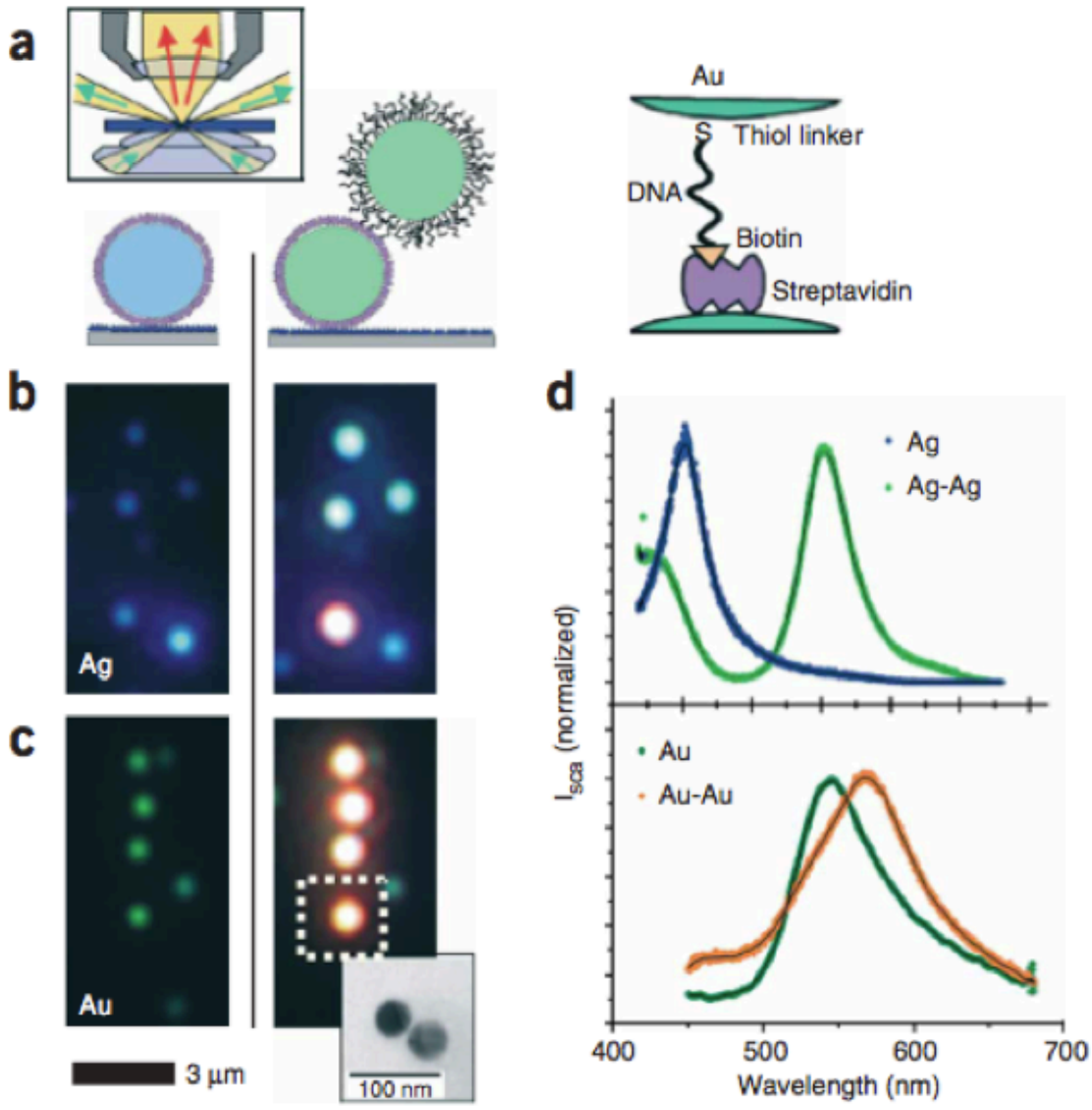

Figure 2.20 Schematic (a), dark-field microscopy and absorption spectra of gold and silver nanoparticles functionalized with DNA and biotin for self-assembly[47]

Functionalization of metal nanoparticles for self-assembly can be accomplished with nucleophillic molecules such as thiols. In Figure 2.20, Alivistatos et al. shows the creation of a two nanoparticle system, where a thiol is utilized to bind to the gold surface. One nanoparticle was then coated with a streptavidin layer and the other nanoparticle was functionalized with DNA to produce a system which can self-assemble by changing the ionic strength of the solution.[47] This binding was observed through a color change caused by coupling of the nanoparticles and a subsequent a change in the scattering and a spectral shift of the plasmon resonance. These studies can be very precisely controlled and the spectral shifts can be correlated to physical distances between the two nanoparticles.[48] FRET between gold nanoparticles and quantum dots can be controlled by binding molecules on the surface that will interact and form strong chemical bonds or interaction.

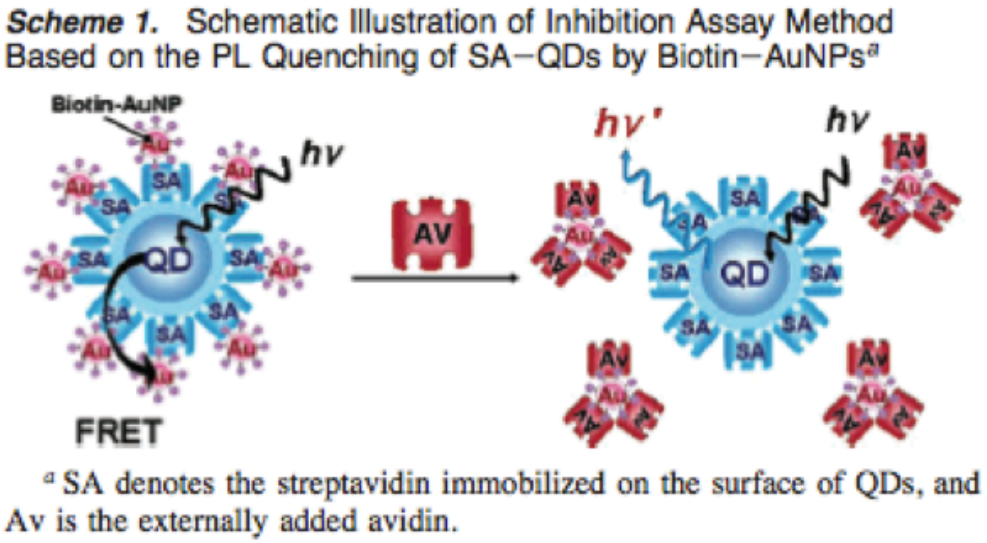

Figure 2.21 Schematic of Inhibition assay based on quantum dot quenching due to proximal gold nanoparticles[42]

If this molecular interaction is inhibited due to the presence of a competing molecule, than the level of fluorescence quenching can be correlated to the amount of the competing molecule in a sample assay. Kim et al. showed that detection of avidin molecules in solution was possible by monitoring the amount of fluorescence quenching of quantum dots caused by coupling to biotin coated gold nanoparticle. Figure 2.21 shows a schematic of the biotin avidin system, where the biotin-coated gold nanoparticles can spontaneously bind to the quantum dot surface causing a quenching of the fluorescence due to FRET. If free avidin is present in solution, the avidin will first bind to the biotin coated gold nanoparticles causing a recovery of the fluorescence.

The extent of coupling can also be controlled via interaction with bi-functional molecules such as DNA. Wu et al, showed that the distance between gold nanoparticles and quantum dots, coated with complimentary DNA strands, can be controlled via addition of Hg^{+} ions. [49] An $1/R^{6}$ dependence of the FRET rate indicates FRET only dominates at close distances and small spatial separation could efficiently eliminate the nonradiative process.[49] A complimentary experiment, utilizing DNA to link CdSe quantum dots to 3 nm, 15 and 80 nm gold nanoparticles, showed that small gold nanoaparticles could provide increased sensitivity for FRET detection.

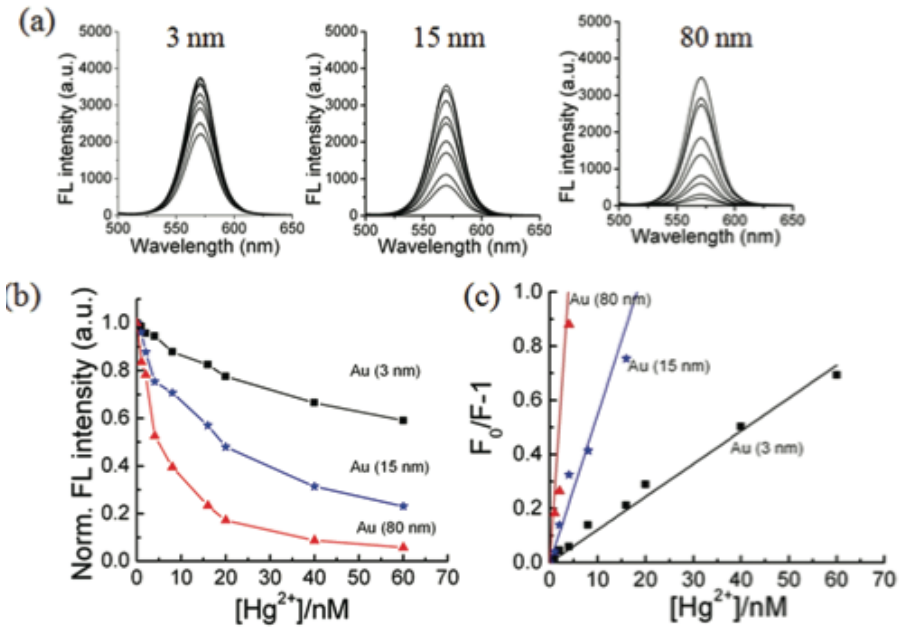

Figure 2.22 Fluorescence quenching of CdSe quantum dots linked to 3 nm, 15 nm and 80 nm gold nanoparticles. The plots on the bottom show the relative quenching as a function of mercury concentration, which causes the DNA to aggregate and bring the particles closer.[50]

The quenching plots in Figure 2.22, show, a much different quenching trend for the small gold nanoparticles, than the bigger 15 and 80 nm gold nanoparticles, Although the small gold nanoparticles do not produce a localized surface plasmon resonance, they still effectively quench the quantum dots at closer distances. The small gold nanoparticles show a R^{-4} dependence on quenching, differing from the usual R^{-6} dependence seen from FRET, pointing to a different quenching mechanism. Nanometal surface energy transfer (NSET) has been theorized as an alternate mechanism for energy transfer between small gold nanoparticles. The advantage to the NSET mechanism, is much larger detection limits are possible leading to highly efficient sensing or detection devices.[50]

These experiments show the practical utility for FRET-based applications utilizing gold nanoparticles. The efficiency of FRET can be used to measure distances

directly, or the amount of fluorescence quenching can be indirectly correlated to distance. The use of FRET requires that the excited chromophore transfer its energy to the acceptor gold nanoparticles, which negates any use of the chromophore itself. FRET is not the only outcome of coupling with gold nanoparticles. Next, the consequence of coupling aimed at utilizing the absorption of the nanoparticle to boost the overall optical performance of the chromophore will be discussed.

2.3: Excitation Field Enhancement

The high demand for energy consumption and the finite fossil fuel stores available, predicate the need for research into alternative and renewable energy sources. One of the most abundant and attractive alternatives to fossil fuels is solar radiation, which can be harvested with the use of photovoltaic cells.[51] [52] Silicon solar cells are common and cheap but suffer from intrinsic losses due to the indirect band gap and low absorption coefficients[53], necessitating the need for materials which can surpass and fix these losses.

Solar cell research has deviated from bulk-heterojunction solar cells to dye-sensitized solar cells, which utilize strongly absorbing molecules as the active material.[51] In general, these solar cells operate by binding of a strongly absorbing dye to a TiO_2 substrate. The TiO_2 acts as a electron transport layer, to separate the excited electron from the hole. The lost electron is then regenerated by an electrolyte layer, usually a triiodide solution. The circuit is completed through transfer of the hole from triiodide to a cathode which are generally made from precious metals such as platinum. Common dyes are typically metal-ligand complexes such as ruthenium-based dyes or conjugated organic molecules such an anthracene-based dyes.

The FRET process is useful and well understood for a variety of systems but utilizing this phenomenon requires that the energy used to excite the fluorophore be transferred to the gold nanoparticle. This can be counterproductive for materials which have utility in lighting or energy harvesting because the nanoparticles will essentially act as energy sinks. Metal nanoparticles possess high extinction coefficients and can effectively concentrate incident electromagnetic radiation into an oscillating electric field in the form of the localized surface plasmon resonance. This process can be utilized to create an antenna effect to boost the excitation of nearby fluorophores[30 54] or semiconductors.[55] Sandoghdar et al. show that the optical properties of fluorophores can be enhanced due to the near-field interaction of nearby metal nanoparticles. Single gold nanoparticles were attached to heat-pulled fiber tips, and the tips were scanned across a thin ,crystalline film of para-terphenyl, doped with terrylene molecules.[30]

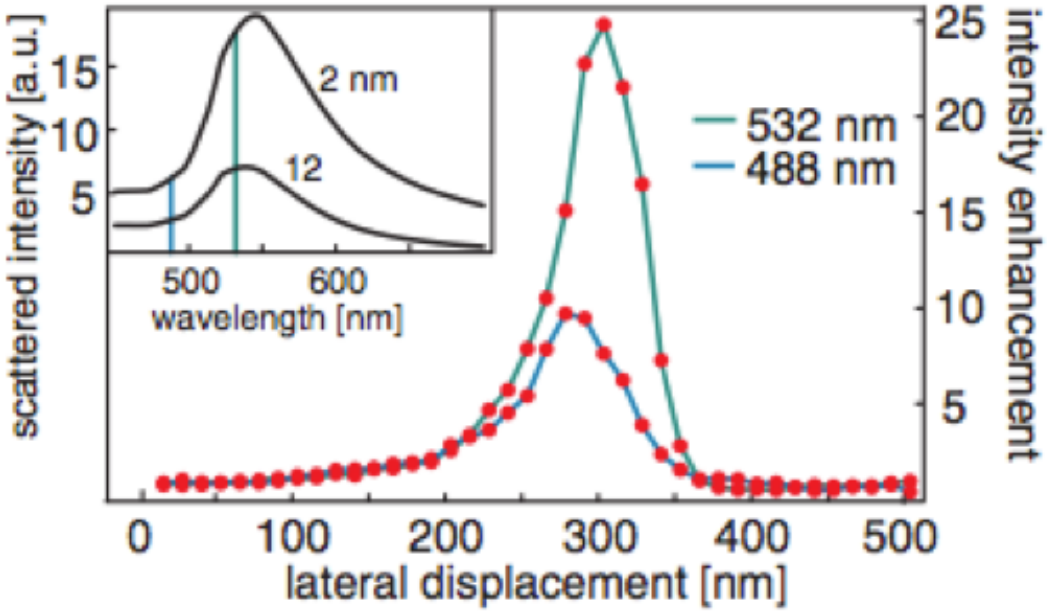

Figure 2.30 Fluorescence enhancement of terrylene molecules doped onto a crystalline, para-terphenyl film as a function of lateral displacement. The fluorescence was monitored via an inverted optical microscope, with a mounted shear-force stage. The molecules were monitored at 2 and 12 nm away from the gold decorated fibers.[30]

In Figure 2.30, the effects of proximal plasmonic fields on the excitation and emission rates can be observed. Fluorescence of terrylene molecules doped into thin films was collected as a function of spacing from gold nanoparticles coated onto fibers. The films were scanned using a stage mounted onto an optical microscope in order to probe the effects of gold nanoparticles on the fluorescence at different separation distances from the molecules. The inset of Figure 2.30 shows how the excitation rate can be greatly improved by controlling the distance from the nanoparticle as shown by 15-fold increase in the scattering intensity at a 2 nm separation distance and a 5-fold increase with a 12 nm separation.

Excitation enhancement can also lead to improvement of photocurrent in detectors[56] or photovoltaic devices.[57] [58] Yu et al. showed that by depositing gold nanoparticles onto Silicon p-n junctions, the photocurrent production could be enhanced and optimized to specific wavelengths, depending on the size of the gold nanoparticles and surface plasmon resonance wavelength.[55] Similar photoconductivity enhancements were shown by Hong et al. in the production of photoconductive films of CdS nanowires decorated with gold nanohemispheres.[59]

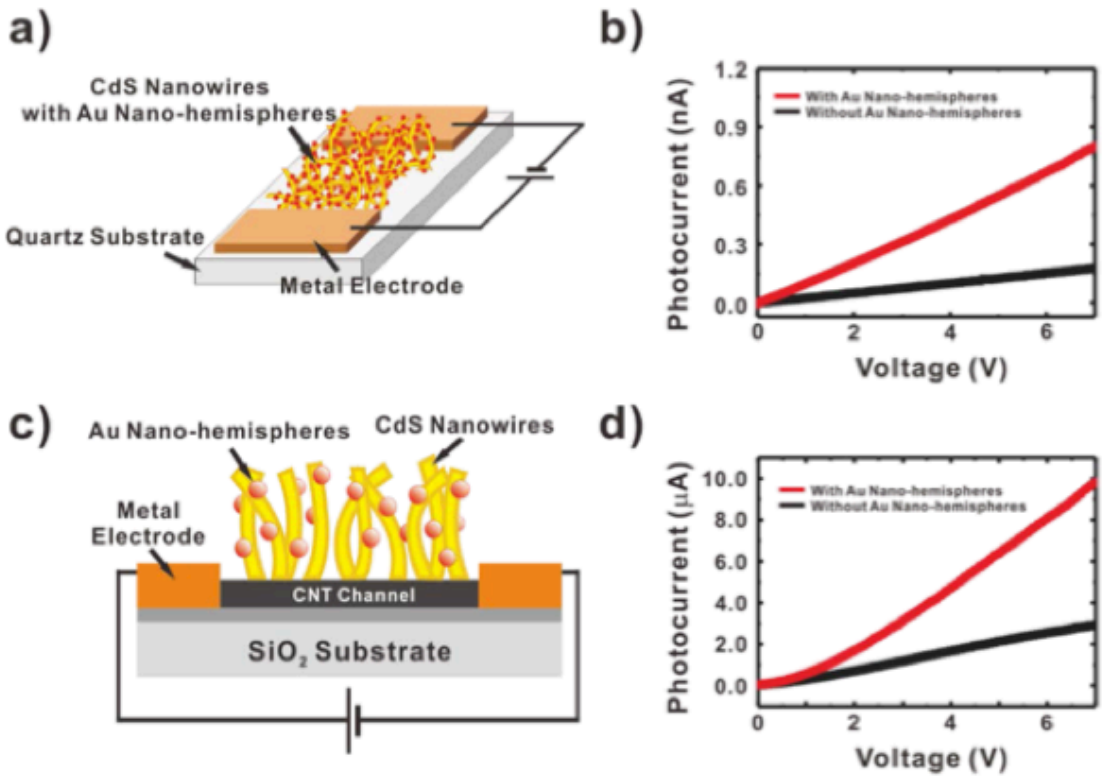

Figure 2.31. Schematic of Au nanosphere and CdS nanowire photoconductive device (left) and photocurrent Vs. applied voltage curves for devices.[59]

Interaction between the excitons formed in the CdS nanowires and the plasmons in the gold hemispheres lead to increased absorption and therefore increase in the photocurrent produced from the device, as shown in Figure 2.31.[59] Ginger et al also showed that local field enhancements could be separated into three separate regimes, excitation enhancements, radiative rate enhancements and nonradiative rate enhancements.

Utilizing silver nanoprisms allowed for mainly enhancement in the excitation rate.[60] These experiments show the ability to couple materials to gold nanoparticles to boost and alter their intrinsic properties. Increasing the rate of excitation or amount of material absorption would result in an increase in the output of the device, whether it be electricity or chemical production, resulting in more efficient, and decreasing the amount of material needed.

2.4: Coupling with Fluorescence

2.4.1: Introduction to Plasmonically Coupled Fluorescence

The development of highly efficient luminescent materials for use in display, lighting and imaging technologies can be made possible through coupling with gold nanoparticles or surfaces. It was previously discussed how gold nanoparticles are important materials in current nanotechnology and optical science due to their strong interaction with electromagnetic radiation which can produce a controlled oscillation of surface electrons known as a surface plasmon resonance[61 62 63]. This electron oscillation produces a local electric field, which can concentrate incident light for collection[64 65], chemical reactions[66] or for electronic interaction with nearby chromophores[67].

The ability to alter absorption of nearby chromophores has already been investigated in the previous section but emission dipoles can be also be altered when

strongly coupled to the electric field produced from the plasmon oscillation. This is similar to Förester resonance energy transfer, which can efficiently quench fluorescence when the chromophore is in intimate contact with the metal surface.[68 47 69] This quenching also increases, exponential, with decreasing separation distance.[70 71 72] Using the dyes in conjugation with gold nanoparticles, functionalized with specific targeting moieties, allows for the production of molecular sensors[44 73] and biological analysis devices, which respond to contact with the target chemical or biological binding site respectively.[74 75]

2.4.2: Enhanced Fluorescence

Enhancement in chromophore fluorescence can be observed when the coupling is carefully controlled, as is the case for molecular enhancement using lithographically fabricated nanobowties. [30 76] The bowties provided a local enhancement which can increase spontaneous emission rates in fluorophores within the field, a phenomenon known as the Purcell effect.[77 78 79 80] Colloidal quantum dots are particular useful as chromophores, [81 82 83 84 12 85] with utility as absorbers or emitters in applications from lighting [83 12] , solar concentration[86 87] and photocatalysis. [88 89 90 91] Coupling of quantum dots to metal nanoparticles represents a new genre of nanoparticle research, which can produce hybrid materials with highly efficient and tunable optical properties. These materials are dependent on both the nature and strength of the interaction between the two species.

The electric field produced from the plasmon oscillation can alter the fluorescence of molecules or quantum dots by perturbing the radiative transition.[41 92 93 94] The plasmon lifetime can be orders of magnitude shorter than that of fluorescent decays, causing a

shortening of the time between excitation and re-emission of a photon or the radiative average lifetime. The coupling of the plasmon electric field can also increase the strength of the radiative transition leading to increase in quantum yield. This effect on the radiative rate can be beneficial for any application which requires a substantial amount of emission. Decoration of lithographic gold arrays with quantum dots was shown to enhance the fluorescence of quantum dots with careful control of the spacing.[93] Emission of quantum dots next to gold nanoparticles of various sizes can produce brighter emission sources for nanophotonic application as well.[94] Fluorescence of individual CdSe ZnS quantum dots in close proximity to silver nanoparticles has been shown produce multi exciton generation, femtosecond nonradiative decays times, and fluorescence enhancements up to 16-fold [95]. The spatial environment of the quantum dots was controlled by deposition of the quantum dots onto gold-coated glass slide coated with an additional layer of PMMA.[96]

2.4.3: Modeling Fluorescence Coupling

Coupling plasmonic metals with quantum dots represents a unique and attractive challenge due to the heightened possibility to introduce nonradiative mechanisms, which can be deleterious to fluorescence efficiency.[49] Lacowicz et al. showed the surface plasmon coupled emission of quantum dots bound onto a 50 nm silver film coated with 5 nm of SiO_2, which acts as a spacer. The fluorescence was shown to be polarization dependent when coupled to the silver film, in contrast to the free quantum dots.[97] Gao et al, showed that it is possible to couple lipid-functionalized quantum dots with gold and although the fluorescence is not enhanced, an increase in photo stability of the quantum dot fluorescence can be produced.[98] Artemyev et al showed that a 10-fold enhancement

of quantum dot fluorescence could be possible by controlling the spacing between the metal surface and the quantum dot with a polyelectrolyte layer.[99]

To understand radiative rate perturbations, the simplest case of a single molecule interacting with a metal interface, such as is the case in near-field scanning optical microscopy (NSOM) , can be considered. Xie et al. showed that single sulforhodamine 101 molecules next to an aluminum tip show markedly different fluorescent lifetimes depending on the spacing of the tip away from the molecule.

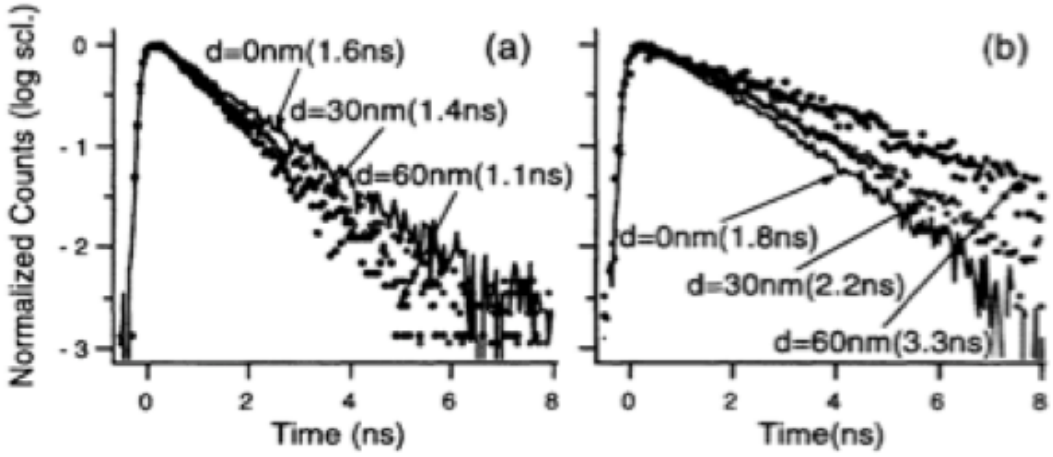

Figure 2.430. Fluorescence lifetimes from and NSOM experiment of single sulforhodamine 101 molecules at three different lateral displacements and two different vertical displacements from a an aluminum tip[100]

From Figure 2.430, when the metal tip was at height of about 5 nm from the molecule, the lifetimes were longer when centered at the tip and shorter at the tip edge but at a spacing of about 20 nm this phenomenon is reversed. Finite difference time-domain calculations were used to model and elucidate the physical nature of the lifetime change.

The simulations showed that at close distances the nonradiative energy transfer dominates the fluorescence dynamics, which are maximized around the tip edges leading to the shortest lifetimes. When the separation was increased, the radiative rate was shortened more at the edges but the nonradiative mechanisms do not play as significant a role ,therefore modification of the radiative rate is responsible for the shortening of lifetimes at the tip center.[100]

These results are crucial evidence showing that radiate rate effects can be separated from nonradiative rate effects by varying the distance between a metal surface and the fluorophore. Similar results were shown for single molecular fluorescence next to a gold nanoparticle immobilized onto a optical fiber conducted by Novotny et al.[30] Mathematical simulations point out that at small separation distances, the near-field, excitation field enhancement is outweighed by an increase in the nonradiative decay rate due to the gold nanoparticle. Optimized separation distances however can result in a minimization of these nonradiative decay rates and an increase in purely radiative rates of the molecules.[101]

2.4.4: A Radiating Plasmon

Plasmonically-coupled fluorescence can be described, considering a fluorophore coupling with a metal surface. Lacowicz describes the fluorophore metal interaction in terms of a radiating plasmon.[41] Quenching and enhanced fluorescence can be described using the same phenomenon for each, which depends on the wave vector k_1, of the surrounding medium, where c is the speed of light and ω is the frequency. The fluorophore will induce a change in the surface charge distribution when close to the

metal surface. The plasmon induced through this interaction has two orthogonal wave vectors, parallel to the surface, x, and normal to the surface, z.

$$k_{1x}^2 + k_{1z}^2 = (\frac{\omega}{c})n_1 \tag{5}$$

$$k_{1x} > \frac{\omega}{c} n_1 \tag{6}$$

Analysis of equations (5) and (7) show that in the case where the real component of the wave lies in the direction parallel to the metal surface, the energy propagates into the far-field as an evanescent wave. The term far-field refers to any distance longer than the wavelength of the incident radiation. The condition where the far-field wave vector is much smaller than that of the in-plane wave vector is shown in the inequality above The in-plane wave-vector dominates and the fluorescence is quenched. If the wave vector in the z-direction fits the inequality, then the far-field component is real and can now radiate, producing a fluorescent plasmon. The decay rate of the fluorophore will appear to increase as this far-field propagating plasmon is produced. We consider the fluorophore as an oscillating dipole near the metal surface in equations (8)-(10) below.

$$\frac{b}{b_0} = \frac{\tau_0}{\tau} = 1 + \frac{3qn_1^2}{2\mu_0 k_1^3} \mathrm{Im}(\tilde{E}_R) \tag{8}$$

$$\frac{b_{\|}}{b_0} = 1 + \frac{3}{4} q \,\mathrm{Im} \int_0^\infty [(1-\mu^2)R^{\|} + R^{\perp}] \exp[-2l_1 k_1 d] \frac{\mu}{l_1} d\mu \tag{9}$$

$$\frac{b_{\perp}}{b_0} = 1 - \frac{3}{2} q \,\mathrm{Im} \int_0^\infty R^{\|} \exp[-2l_1 k_1 d] \frac{\mu^3}{l_1} d\mu \tag{10}$$

The ratio of the decay rate of the original oscillation (b_0) and after coupling with the metal (b) can be described as a function of the quantum yield, q, the refractive index of the medium n_1, the wave vector at the specific frequency, k_1, the dipole, μ, and $Im(E_R)$, the reflective field at the dipole.[41] These decay rates are also dependent on the orientation to the metal surface, perpendicular or parallel, which are shown, respectively in equations (11) and (12).

$$R^{\parallel} = \frac{\varepsilon_1 l_2 - \varepsilon_2 l_1}{\varepsilon_1 l_2 + \varepsilon_2 l_1} \tag{11}$$

$$R^{\perp} = \frac{l_1 - l_2}{l_1 + l_2} \tag{12}$$

A new term needs to be defined, which is the reflection coefficient R. The reflection coefficient can be written in terms of the extinction coefficient ε.

$$l_j = -i(\varepsilon_j / \varepsilon_1 - \mu^2)^{\frac{1}{2}} \tag{13}$$

The term l is defined in terms of the dielectric constants of the fluorophore and the medium. ε_j and ε_l in equation (13).The effect a plasmon has on the decay rate can now be estimated. To further simply the problem, only the far-field case is considered. The dipole, μ, can now be simplified into a ratio of the wave vector k.

$$\mu = \frac{k_x}{k_1} = \sin\theta \tag{14}$$

When $\sin\theta < 1$ in equation (14), the dipole portion of the integral is real and describes a wave which can propagate into the far-field or a detectable fluorescence signal is

produced from the plasmon. When the portion of the integral containing μ is imaginary or when sinθ is greater than 1, the term describes the decaying evanescent field.[41] [40]

2.4.5: Modification of the Decay Rate

Plasmon-coupled fluorescence can now be understood as a fluorophore, interacting with a plasmonic surface to induce a fluorescent plasmon. To quantify this phenomenom, effects on the decay rate of the fluorophore must be considered. The plasmon resonance decays on the order of femtoseconds, orders of magnitude shorter than normal fluorescence lifetimes, usually on the order of nanoseconds. [40] The speed of this decay indicates that energy transfer to the metal, from the fluorophore must be the dominate mechanism in fluorophore metal interactions, and subsequent fluorescence must come from the radiating plasmon.

An extra decay term must now be introduced, the modified decay rate in the presence of the plasmon, $\Gamma_{m,}$ which describes the decay of the radiating plasmon,. The new average lifetime in the presence of the metal plasmon, τ_m , and the quantum yield ,QY, are now mathematically described with the metal modified decay rates.

$$\tau_m = (\Gamma + \Gamma_m + k_{nr})^{-1} \quad (16)$$

The modified fluorescence lifetime due to the metal presence, τ_m, is described as a sum of the original fluorophore decay rate, Γ, the modified decay rate, $\Gamma_{m,,}$ and the nonradiative decay rates, k_{nr} in equation (16). The decay rate of the metal-coupled term must be significantly larger than the original decay rate since the lifetime is so much shorter. An increase in the radiative decay rate, by incorporating the metal coupled term, will then correspond to a decrease in the overall fluorescence lifetime.

It must be noted, that if these increases are simply due to energy transfer then this same decrease in lifetime would be observed. If simply fluorescence quenching occurs, then this decrease in lifetime will also accompany a decrease in the quantum yield. Due to the fast decay of the plasmon resonance, the modified decay rate is much larger than the original decay rate of the fluorophore.

$$QY = \frac{\Gamma + \Gamma_m}{\Gamma + \Gamma_m + k_{nr}} \tag{17}$$

Quantum yield is defined as the ratio of the radiative rates over the sum of all the radiative and nonradiative rates, as shown in equation (17). If the modified radiative rate due to the metal interaction, $\Gamma_{m,}$ is added into the quantum yield calculation an increase in quantum yield is possible if there are no changes to the nonradiative rates as well. This provides impetus to not only couple the plasmon with the fluorescence transition dipole, but to have control over the nonradiative rates as well.

Plasmonic coupling with the emission of fluorophores can result in decreased fluorescence lifetimes and increased quantum yields, but these increases can often be dominated by energy transfer or nonradiative mechanisms induced by the metal surface. Careful control of separation distances may result in purely radiative rate increases and thus an increase in the quantum efficiency of the fluorophore. This increase in emission rate represents and intriguing opportunity to boost the efficiency of fluorescent materials but there is still a vast amount of optimization required in order to utilize plasmonic coupling effectively with minimal nonradiative losses.

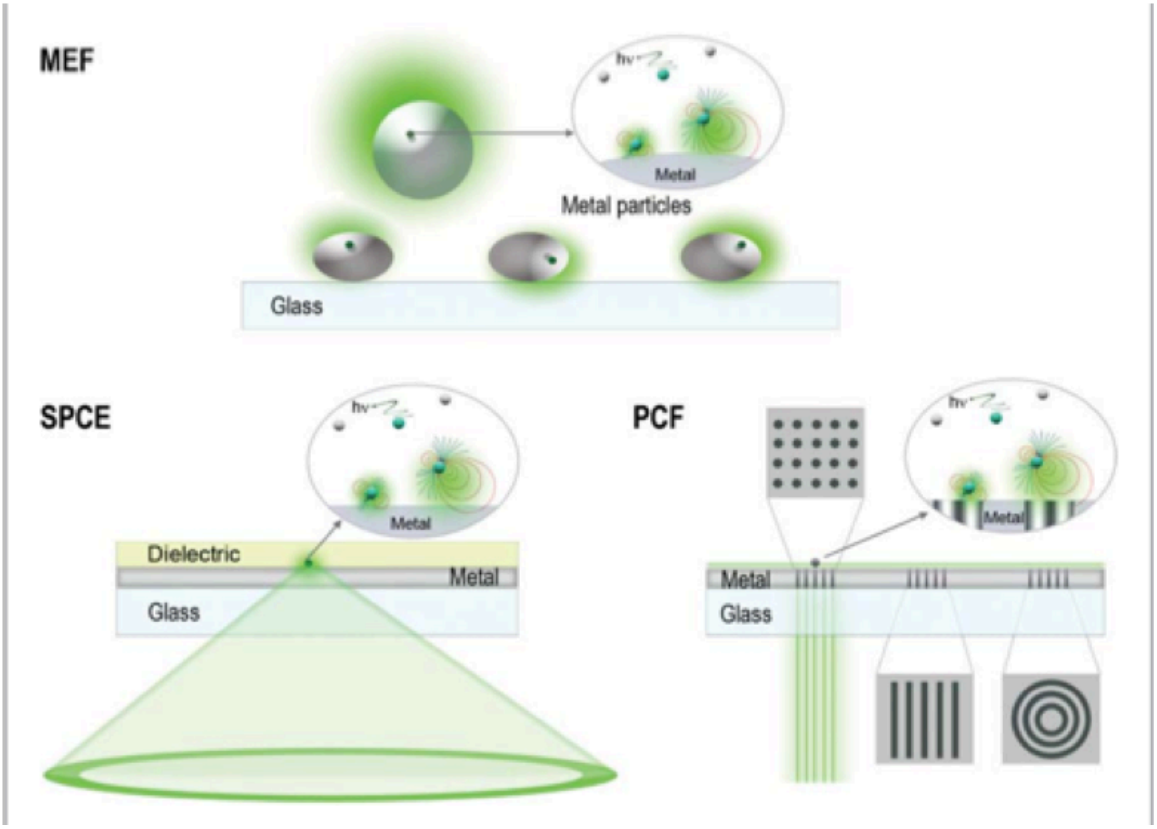

Figure 2.450 Illustration of three different regimes of emission coupling due to plasmonic interaction

Lacowicz summarized three different regimes for a fluorophore coupling to a metal surface shown in Figure 2.450. Metal enhanced fluorescence, MEF, is characterized by an increase in quantum yield with a correlated decrease in fluorescence lifetime of the fluorophore. The lower left and right hand illustrations refer to surface plasmon-coupled emission and plasmon-controlled fluorescence. These two phenomenons occur when the fluorophore is located next to a thick metal surface and do not result in an enhancement of the optical properties but rather a mixing of the plasmon emission. For plasmon-coupled fluorescence, the metal surface merely induces a polarization dependence on the resulting emission but the quantum yield and lifetime

remain unchanged. Plasmon-controlled fluorescence occurs when the metal surface is decorated in concentric rings. The fluorescence is now wavelength dependent but no changes in the quantum yield or lifetime occur.

2.5 Concluding Remarks about Plasmons and Coupling

In this chapter, enhancements in chromophore excitation and emission have been discussed. The main issue in producing these enhancements lies in negating the nonradiative mechanisms, such as energy transfer, which may be introduced upon coupling to a metal surface. The most prominent optical property possessed by the metal nanoparticles or surfaces, is the ability to focus incident radiation to a relatively small area, due to the high metal extinction coefficient. If coupled to the chromophore this can result in an antenna effect which will increase the amount of radiation that can be used to excite the chromophore. This phenomenon is referred to as excitation field enhancement and can be useful for applications which require the conversion of large amounts of incident radiation to chemical or electrical energy. The excitation field enhancement can result in increased photo absorption or photocurrent production in these devices when the increase is coupled with increased excitonic dissociation.

Fluorescence coupling and enhancement is a more complicated phenomenon, which derives from perturbation of the fluorescence dipole with that of the plasmon dipole. In general the plasmon relaxation rate, which is orders of magnitude faster than most fluorescence relaxation rates can cause a decrease in the fluorescence lifetime. The presence of the plasmon electric field can also result in an increases in the spontaneous relaxation rate. When these two phenomena occur simultaneous, an increase in the

radiative rate is observed. This can be useful for lighting and imaging techonoligies which require bright and stable emission sources.

Our aim was to study the nature of the coupling and production of enhancements in colloidal species due to nearby metal nanoparticles in colloidal solutions. This requires intimate control over the metal plasmonic behavior, the chromophore optical properties and the spatial coupling between the two.[36 40 41] The original chromophore properties are important to understand the type of coupling which would maximize the utility of the specific chromophore after coupling. Optimization of the plasmonic coupling with different types of materials will allow for the production of technologies with higher efficiency, lower cost and more stable output.

CHAPTER 3: DIELECTRIC SPACING LAYER

3.1 Introduction

Coupling chromophores to metal surfaces can produce composites with optical and electronic properties intermediate to that of each individual species. Earlier experiments focused on coupling quantum dots[102 97, 99] or dyes[103 104 105] to metal surfaces or films of metal nanoparticles. The local electric field produced from an excited plasmon resonance, can couple with the transition dipoles of the chromophores resulting in a mixing of the plasmon and the fluorescence or excitation of the chromophore. It was shown in Chapter 2, how this mixing of the optical transitions with the plasmon can result in an increase in excitation, through concentration of the local excitation field, and increases in the fluorescence through both a lowering in the lifetime and increase in the quantum yield.

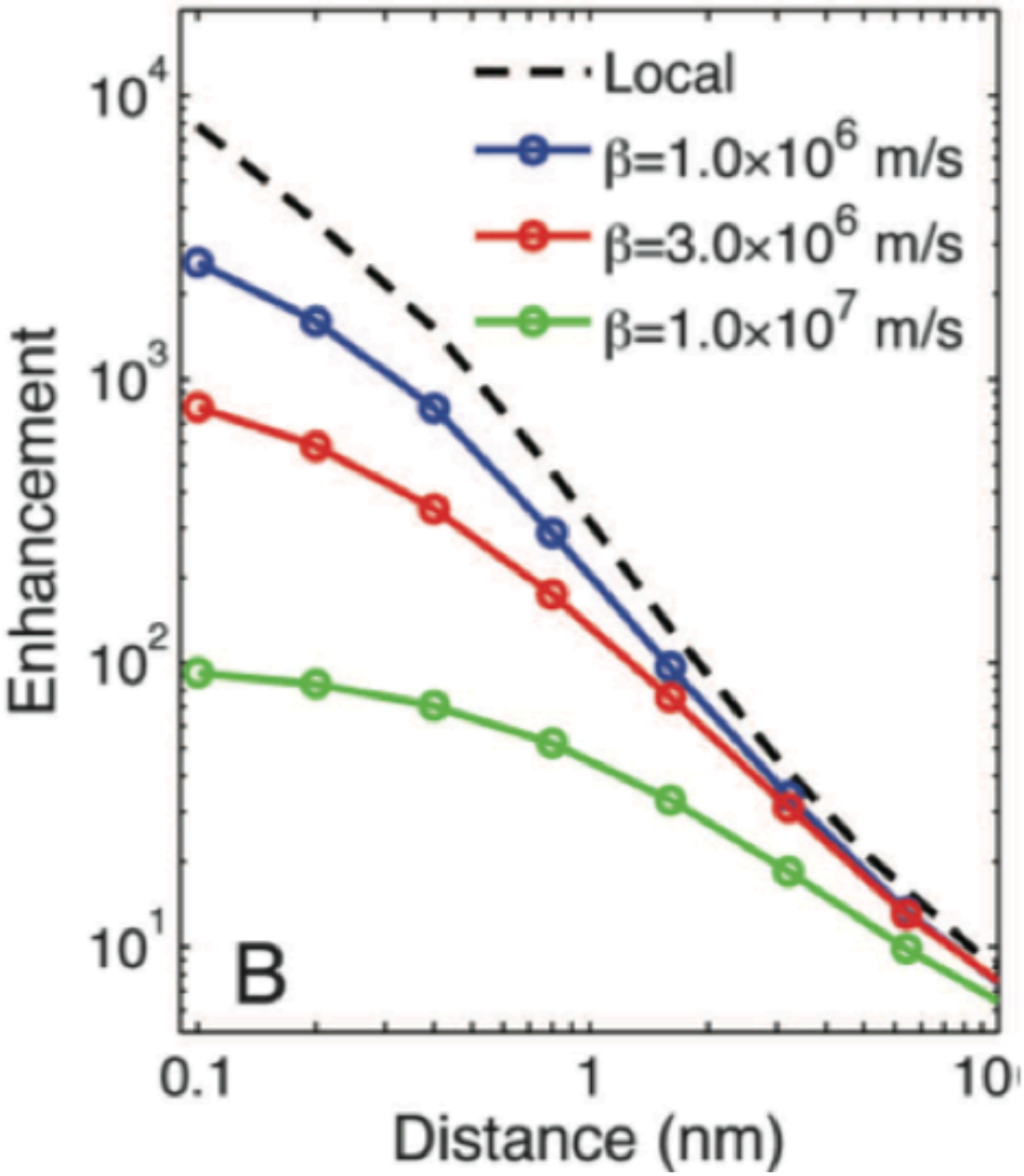

Figure 3.10. Plot of the local field enhancement vs. spacing distance of a gold nanoparticle placed on a gold film with a dielectric spacer.[31]

Ciraci et al, theorized the limit of such enhancement on the plasmon resonance of a gold particle, placed on a thick gold film. The gold nanoparticle is spaced from the gold using a molecular dielectric spacer. While this system differs from the chromophore-plasmon

coupling, it still gives insight into the extent of enhancement which can be experienced. Large enhancements, up to 10^4 were calculated when the gold nanoparticle is placed less than a nanometer from the film. Utilizing this method can produce large enhancements of fluorescence or absorption but smooth and homogeneous films can be difficult to reproduce and may not be the best to mimic real world device applications, as large films of gold or silver would not be cost effective. Large arrays of gold may also introduce nonradiative relaxation mechanisms when directly coupled. In order to negate these processes, the chromophores must be physically separated from the metal surface.

3.2 Distance-Dependence of Enhancement

Large, local-field enhancements are possible through coupling with a metal surface, but in the case of a coupled chromophore, significant losses may also be introduced upon coupling. Energy transfer is the dominant interaction between the chromophore and metal at separations on the nanoscale regime. If the chromophore makes direct contact with the metal, a large increase in the energy transfer rate may occur, negating even large enhancements in excitation or fluorescence. In order to take advantage of these enhancements, the spacing at which energy transfer is negated and local-field enhancements dominate must be utilized.

Thin films of gold nanoparticles can be utilized to monitor the optical effects of fluorophores in close proximity. Artemyev et al[99] show a robust method for coating glass slides with citrate-coated gold nanoparticles, and subsequently with quantum dots, to monitor the effect on the fluorescence intensity. Gold nanoparticles were linked to glass using polydiallyldimethylammonium chloride. The film spacing is conducted by depositing layers polystyrene sulfonate on top of the gold nanoparticles followed by

another layer polydiallyldimethylammonium chloride. The two polymers are added sequentially until the approprate thickness is achieved. Quantum dots are then added dropwise on top of a polydiallyldimethylammonum chloride layer.[99]

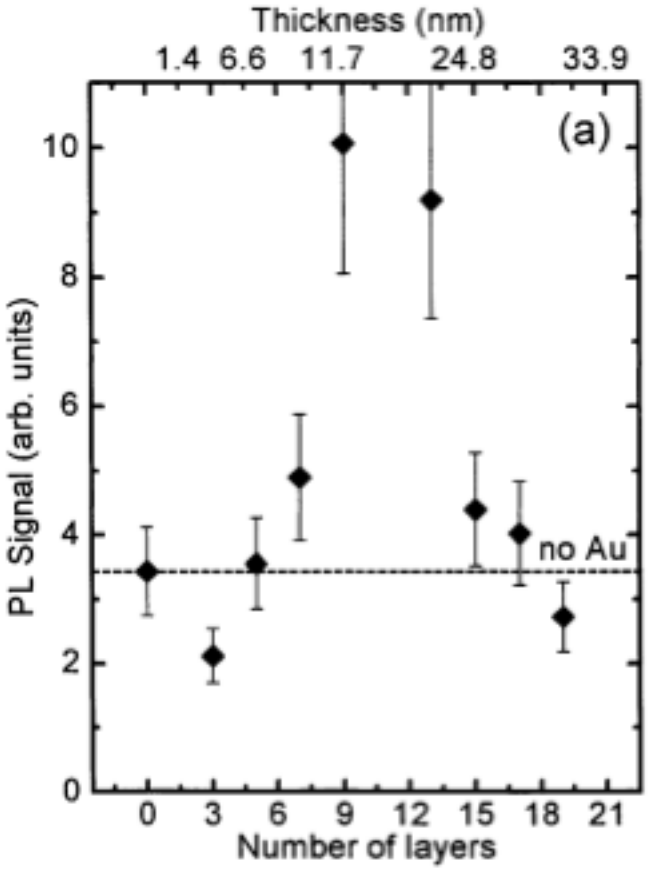

Figure 3.20. Plot of the Fluorescence signal vs. layers of polymer coated onto the gold film. The Quantum dots utilized were CdSe with a ZnS shell.[99]

The thin films utilized in Figure 3.20, show a distinct dependence of the PL intensity on the number of polymer layers, or the separation distance. When the number of layers deposited is both below 6 and above 15 the fluorescence intensity matches the original quantum dot intensity or in some cases, is lowered. This increase in fluorescence is

attributed to local enhancements from the gold nanoparticles while the decreases are attributed to energy transfer.[99]

Klimov et al show the possibility for this enhancement in colloidal systems containing gold nanoparticles as the plasmon source instead of gold films. The gold nanoparticles were coated with silica which acts as the tunable dielectric spacer. This method allows for plasmonic coupling to be utilized with solution-state colloidal samples, without the need for film deposition. The silica shells were formed by treating gold nanoparticles with (3-mercaptopropyl)trimethoxysilane to form the silica shell. The quantum dots were then bound after coating the silica shell with (3-aminopropyl)trimethoxysilane.[106] Fluorescence spectra of the quantum dot solutions before and after binding were taken in order to compare enhancements at different shell thicknesses. The shell thickness represents the spacing of the quantum dot fluorophores from the metal surface.[106]

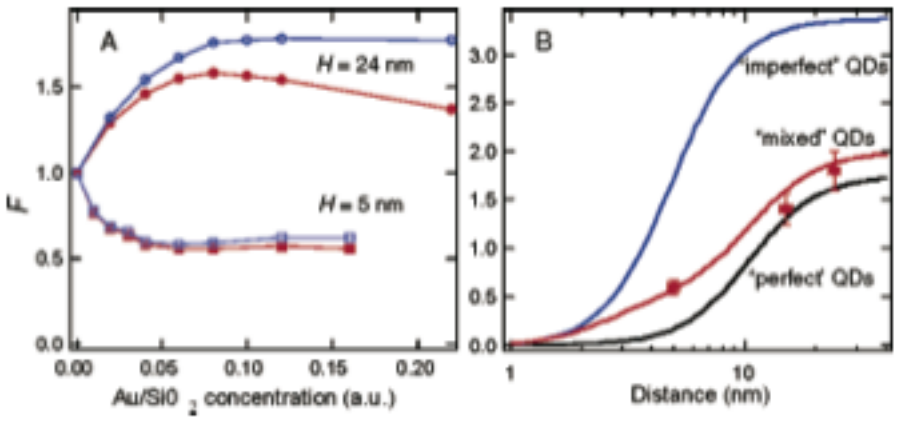

Figure 3.21. Plots of the enhancement factor (F) of quantum dots bound to silica-shelled gold nanoparticles vs. nanoparticle concentration (left) and vs. distance. The distance is determined by the distance is measured by the shell thickness.[106]

The plots in Figure 3.21 show the effects of both nanoparticle concentration and spacing distance. The plot on the left shows that as the silica-coated gold nanoparticles are added into the quantum dot solution, the fluorescence of the quantum dots bound to the thicker shelled nanoparticles (H=24) increases and then saturates to a constant value. The thinner shells trend in the opposite manner, showing fluorescence quenching upon binding. The figure on the right also confirms this enhancement with the thicker-shelled nanoparticles, as the fluorescence increases as the thickness of the silica shell increases as well.[106]

3.3 Concluding Remarks on Dielectric Spacing

These studies show that plasmonic coupling with fluorescence transitions is possible with precise control over the binding conditions and environment. In order to utilize enhancements, the energy transfer efficiency must be decreased through careful spacing from the metal surface. Too large a spacing will result in minimal plasmonic interaction and no enhancement, while at small separation distances, energy transfer dominates and enhancements will not be observed. For excitation enhancement, close proximity to the metal surface is preferential to take advantage of the maximum extent of the plasmonic field. Intimate contact may, however, result in low diffusion lengths of excitons due to the introduction of recombination sites at the metal interface, so thin spacers are still necessary. These literature studies help to elucidate the proper environment to maximize plasmonic coupling and minimize losses due to introduction of energy transfer or other nonradiative mechanisms.

CHAPTER 4: CHROMOPHORES

4.1 Introduction to Quantum Dots

Quantum dots are semiconductor nanocrystals utilized for the broad absorption and tunable fluorescence. They offer a viable alternative to modern day bulk semiconductors due to their size tunable properties and increased surface to volume ratio. In comparison to their bulk counterparts, quantum dots are quantum confined materials which means, upon reduction of size, the electron wave functions are confined to a smaller spatial area than in bulk material. The allowed electron and hole states are now described by discrete states instead of energy bands. This occurs when the separation between excited electron and hole pair is larger than the allowed distance in the bulk material known as the Bohr radius.

$$a_B = \frac{\varepsilon \hbar^2}{\mu e^2} \tag{18}$$

The Bohr radius (a_B) is defined in terms of ε is the material dielectric constant, and μ is the reduced electron mass in equation (18). The optical and electronic properties can now be defined by the extent of the quantum confinement. When the nanoparticle radius is on the same regime as the Bohr radius, the material is said to be weakly confined. Under weak confinement, the electron and hole wave functions can move freely and bulk properties can be used to describe electronic transitions in the material. We define the electron dynamics in terms of energy bands. The bands consist of a number of allowed energy states defining the electron wave function. Intermediate confinement exists when

the radius of the nanoparticle is approximately equal to the Bohr radius. In this intermediate regime, some spatial confinement of the electron exists and the bulk properties no longer apply, due to the emergence of discrete energy states instead of the continuum of states observed in the bulk regime. The excited electron and hole become a coulombically paired exciton and their separation energy is now shifted to higher energies than the bulk material. In the strong confinement regime, the exciton energy is now strongly dependent on the spatial dimensions of the nanoparticle, giving rise to size dependent and tunable optical transitions. Increasing the spatial confinement of the material, or decreasing size, shifts the band gap or the required energy to move an electron from the valence band to the conduction band, to higher wavelengths. Larger particles possess lower excitation energies with a minimum energy equal to that of the bulk band gap.

Quantum dots offer a more robust alternative and potentially cheaper alternative to modern dyes in dye-sensitized solar cells or as the absorber in bulk heterojunction solar cells. Quantum dot sensitization of solar cells can result in moderate efficiencies approaching and sometimes surpassing around 5%.[107, 108] Upon light absorption, an electron would be transferred into the LUMO of a TiO_2 layer and the hole to the redox electrolyte. Higher efficiency devices would be possible if the amount of current and voltage produced could be enhanced. For the former, a lower band gap or more absorption at higher wavelengths would cause an increase in the maximum photocurrent produced from solar radiation.[53, 109] Quantum dot band gaps can be tuned by simply changing the size of the nanoparticle, so creating larger particles may result in an increase in device photocurrent, though these particles may suffer losses due to surface-mediated

exciton recombination processes. Quantum dots also offer utility for applications based on their fluorescence properties such as imaging, or LEDs.

4.2: Quantum Dot Electronic Properties

Quantum dots can be synthesized through a variety of wet chemical techniques allowing for easily tunable size and shape which will also alter their optical properties.[110] When subjected to some electronic excitation an exciton is created in the nanocrystal.

$$\mu = \frac{m_e^* m_h^*}{m_e^* + m_h^*} \tag{19}$$

The reduced effective exciton mass using m^*_e and m^*_h as the effective masses of the electron and hole respectively in equation (19). This reduced effective mass can be used to calculate the Columbic attraction between the electron and hole or the exciton binding energy.

$$E_{ex} = -\frac{13.6 \, {}^{\mu}/_{m_e}}{({}^{\varepsilon}/_{\varepsilon_0})^2 n^2} eV \tag{20}$$

The exciton binding energy ,E_{ex}, can be defined, in equation (20), with μ being the reduced exciton effective mass, m_e is the free electron effective mass, ε is the material dielectric constant, ε_0, is the permittivity of free space and n is the principle quantum number. An excitonic binding energy of zero will result in an unbound electron hole pair. Most exciton binding energies, for semiconductors, are on the range of a few tens of meV. The exciton binding energy for GaAs is about 4.6 meV while the exciton binding energy for CdS is 28 meV.[110] The optical properties in semiconductors significantly depend on their size, once the particle radius approaches the Bohr radius in the exciton, or when quantum confinement increases.

$$E_{g,eff}(R) = E_g(\infty) + \frac{\hbar^2\pi^2}{2R^2}\left(\frac{1}{m_e^*} + \frac{1}{m_h^*}\right) - \frac{1.8e^2}{\varepsilon R} \quad (21)$$

The quantum-confined, effective band gap ($E_{g,eff}$) in a spherical nanocrystal with radius R and the bulk band, $E_g(\infty)$ can be calculated for a given material,a s shown in equation (20). In semiconductor materials, photon emission will only be seen between states with electronically allowed transition. An electronically allowed band edge transition occurs when the conduction band minimum matches with valence band maxima at k=0, or the gamma point, in direct band gap semiconductors. [110] The absorption of QDs remains broad throughout the visible spectrum but the emission band is usually narrow. The fluorescence is much more dependent on the band gap energy of the specific quantum dot material. The ability to tune this energy simply by changing the size of the nanoparticle is what gives QDs their unique, size-dependent fluorescence.

4.3: Quantum Dot Synthesis

Colloidal QD synthesis is driven through precipitation of reactive nuclei from a supersaturated solution of molecular precursors. Gibbs free energy of the precipitated nuclei formed from the supersaturated solution is the driving force for nucleation of particles due to the solution's thermodynamic instability.

$$\Delta G = -\frac{4}{V}\pi r^3 k_B T \ln(S) + 4\pi r^2 \gamma \quad (21)$$

The change in Gibbs free energy is described as a function of the nuclei volume, V, the temperatureT, the radius of the nuclei r, boltzmanns constant k_B, the supersaturation ratio S, and the surface free energy per surface area of the nuclei, γ as seen in equation (21). At a supersaturation greater than 1, a critical radius ,r^*, can be calculated in which ΔG is

maximum positive value. At this critical radius, any particles larger will dissolve and any smaller particles will continue to grow.

$$r^* = \frac{2V\gamma}{3k_B T \ln(S)} \tag{22}$$

The derivative of the previous equation is shown in equation (220 and used to solve for the Gibbs free energy of the nanoparticle growth, shows that this critical size can be calculated for a given temperature and nuclei concentration. This provides a self-sharpening of the precipitated nanoparticles if the supersaturation is kept constant, meaning the nanoparticle nuclei will approach a common radius.[111]

The synthesis of Group II-IV quantum dots has been optimized in the past decade due to their robust nature and tunable absorption and emission maximums which can be pushed through though the visible spectrum.[112] The quantum dots are capped with an organic layer of tri-octyl phosphine oxide (TOPO) or long chain aliphatic amines. For a typical synthesis of CdSe quantum dots, a solution of TOPO and hexadecylamine (HDA) is degassed at 120 ^{0}C for an hour. This solution is then heated to around 300 ^{0}C under nitrogen atmosphere. The high temperature creates a fast nucleation event in order to provide a more controlled and monodisperse template for growth. The reactive cadmium precursor is created by heating a mixture of cadmium acetyl acetonate, 1,2 hexadecane diol (reducing agent) in tri-octyl phosphine(TOP). The selenium precursors must be a 1.0 M selenium:TOP complex, which is made by dissolution of elemental Se into TOP in an inert atmosphere overnight. The reactive solutions are then injected into the hot TOPO/HDA solution for nucleation and growth. The longer the solution is allowed to stir after injection the larger the resulting nanoparticles. The nanoparticle maximum size

approaches the Bohr radius of CdSe in order to avoid the formation of bulk CdSe.[113] The nanoparticles are washed of excess reagent via centrifugation and redispersion and can be coated with larger band gap semiconductors such as CdS or ZnS to aid in surface passivation and improve optical properties such as quantum yield.[114,115]

4.4: Plasmonic Coupling with Quantum Dots

Coupling plasmonic materials with quantum dots represents a unique and attractive challenge. Quantum dot are useful for their broad absorption bands but their main utility lies in their size tunable and sharp fluorescence bands. This poses a problem to plasmonic coupling due to the possibility for introduction of nonradiative, energy transfer mechanisms which can be deleterious to fluorescence efficiency. In order to negate these nonradiative mechanisms, it is imperative to provide some dielectric spacing layer which allows for propagation of the plasmonic field to reach the quantum dot but also provide sufficient spacing to negate energy transfer mechanisms.

An interesting procedure published by Gao, shows that it is possible to coat lipid-functionalized quantum dots with gold. Once coated with a lipid layer, poly-l-histidine is then added to the surface to bind gold ions. To adjust the spacing from the inner quantum dot, alternating layers of charged polymers were added. Finally a reducing agent is added to the solution and a gold shell of 2-3 nm can be formed.[98] The resulting nanoparticles, although not enhanced, show an increase in photostability as well as optical signals from both florescence and plasmon resonance in the gold shell.[98]

Artemyev et al showed that an enhancement of quantum dot fluorescence could be possible by controlling the spacing between the metal surface and the quantum dot using a tunable polyelectrolyte layer. In order to deposit the polyelectrolyte layer, the

layer by layer deposition technique was used to coat negatively charged gold particles with alternating layers of polydiallydimethylammonium chloride and polystyrene sulfonate. Quantum dots are then deposited on top of the polyelectrolyte layer. A polyelectrolyte layer around 12 nm in thickness resulted in almost a 10-fold enhancement in the fluorescence and PLE measurements confirm that the excitation of the quantum dots is due to the gold nanoparticles.[99]

4.5: Introduction to Porphyrins

Porphyrins are highly conjugated, cyclic macromolecules consisting of four pyrrole units ,each interconnected via a methine bridge.

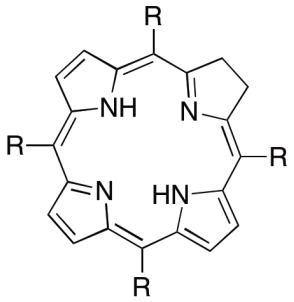

Figure 4.50. Illustration of the porphyrin backbone. The R groups are generally functionalized with phenyl groups.

In nature, plants utilize molecules with porphyrin backbones, such as chlorophyll in order to convert sunlight into chemical energy.[116] The ability to synthesize new derivatives and modify the chemical makeup of these molecules relatively easily makes them ideal candidates for light absorbers in solar cells.[117] Long exciton lifetimes, lower LUMO level than TiO_2 , and the ability to add nucleophilic binding groups to the exterior of the structure are other properties making porphyrins an exciting group of materials for solar

harvesting technology.[109] Porphyrins can be synthesized with addition of pyrrole ,acetic anhydride and an aldehyde in an propionic acid, allowing for versatile surface chemistry and electron withdrawing or donating substiuents to be explored.[118] Porphyrin-sensitized solar cells represent a growing field due to their electronic properties, but research into improving their photoabsorption properties needs to be conducted in order to maximize their photocurrent production.

4.6 Porphyrin Electronic Structure

Porphyrins are highly absorbing molecules which are utilized in photodynamic[119] [120] [121] therapy and photovoltaics[52] [122] [81] due to their ability, to transform incident radiation into chemical or electrical energy. Their strong absorption stems from the large pi conjugation present in the backbone of the porphyrin molecule.

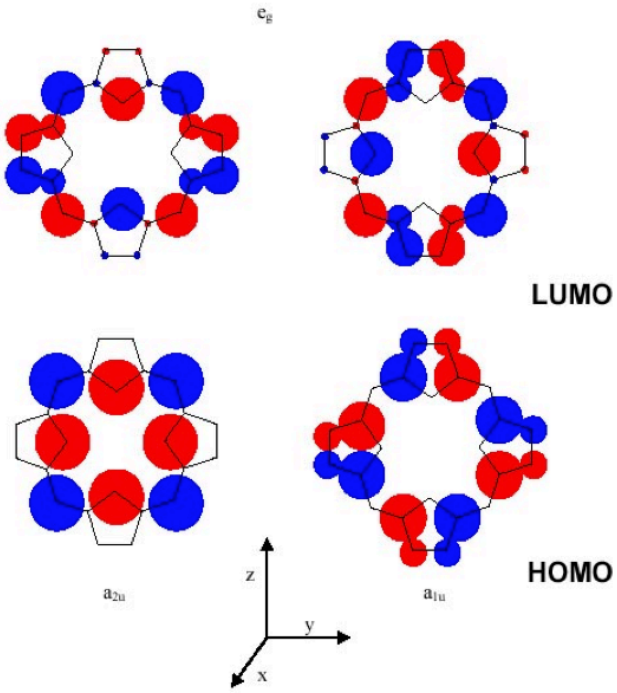

Figure 4.60. Model of the Highest occupied molecular orbitals and Lowest energy molecular orbitals of porphyrin, known as the Goutermann four orbital model.[123]

The conjugation consists of 18 pi electrons delocalized around the backbone, which gives the porphyrin molecules aromaticity. This aromaticity allows them to strongly interact with light via π to π* transitions. In Figure 4.60 the four-frontier orbital model first proposed by Gouterman shows that the electronic transitions are dominated by transitions between two degenerate HOMO and LUMO levels. [123] The HOMO and LUMO levels are degenerate but can be altered by binding a transition metal to the center pyrrole units, altering the *meso* position located on the methine bridge or the β-pyrrole position. The most common modifications are addition of substituted phenyl groups at the *meso* position or metallation of the de-protonated pyrrole nitrogen atoms.

The ground state π orbitals have slightly different energies depending on the type of substituent present on the porphyrin. Transitions from either the $a1_u$ or $a2_u$ into two degenerate $e2_g$ orbitals produce two transitions which are slightly offset energetically. Excitation from these ground state π orbitals into two degenerate π^* orbitals, give rise to the absorption transitions in free base porphyrins. The Soret absorption band has a higher oscillator strength and therefore much larger extinction coefficient, up to 50,000 cm^{-1} M^{-1}. The weaker transitions, known as the q-bands, give rise to 4 absorption energies from around 500 nm to 700 nm. Donating or accepting electron density from the center pyrrole units can be modified via substitution of the *meso* or β-pyrrole unit on the porphyrin macrocycle and influence the transition energies of the porphyrin molecule.[123]

A more substantial shift from the free-base porphyrin spectrum occurs when the center two pyrrole units are occupied by a metal ion or the porphyrin becomes metallated. There are two different types of metallated porphyrins depending on whether the metal has an empty or full d-shell. In the former case, the metal orbtials have little affect on the π to π^* transition of the macrocycle and changes in the spectrum are due to symmetry changes. When the metal has a full d-orbital, the d orbitals can now backbond into the porphyrin π orbitals of the ring causing a blue-shift of the π to π^* transition energy.[124]

4.7: Plasmonic Coupling with Porphyrins and Dyes

Utilization of plasmonic enhancement in solar cells is a relatively newer field with sparse reviews in literature. Typically, the utilization of metals in solar cells would introduce recombination centers for electrons and holes, diminishing photocurrent. These dye-nanoparticle composites need to be carefully structured in order to produce enhanced photo excitation, while minimizing changes into the charge carrier transport throughout

the device. Hupp et al. showed that silver nanoparticles can aid in extinction enhancement of commonly used ruthenium based dyes. Cells were created with FTO glass and silver nanoparticles coated with varying thicknesses of TiO_2 were used as the anodic layer of the device. This loading method helps to decrease the surface area of the TiO_2 layer , which can be responsible for high dark current with increased surface area. This method may help to increase the maximum photovoltage produced but can also decrease the maximum photocurrent available by lowering the dye loading. The silver nanoparticles can boost the dye extinction coefficient and make up for the loss of loading.[125]

Hupp found that a 2.0 nm coating of amorphous TiO_2 could increase the dye extinction coefficient by about 9%. Yamada and et al.[126] showed that thin films immersed in 40 nm silver nanoparticles and coated with various molecular dyes such as tetra phenyl porphyrin or phthalocyanine derivatives show an increase in photocurrent, and fluorescence. They deduced that the origin of these affects is due to the excitation of plasmonic fields on the nanoparticles which can in turn excite the dye molecules. [126] An alternate study conducted by Hupp, shows a plasmonic enhancement of dye photocurrent through the use silver nanoparticles coated with TiO_2. [125] The nanoparticles are coated with varying thicknesses of TiO_2 using atomic layer deposition followed by loading with (cis-bis-(4,4'-dicarboxy-2-2'-bipyridine) dithiocyanato ruthenium(II)) dye.

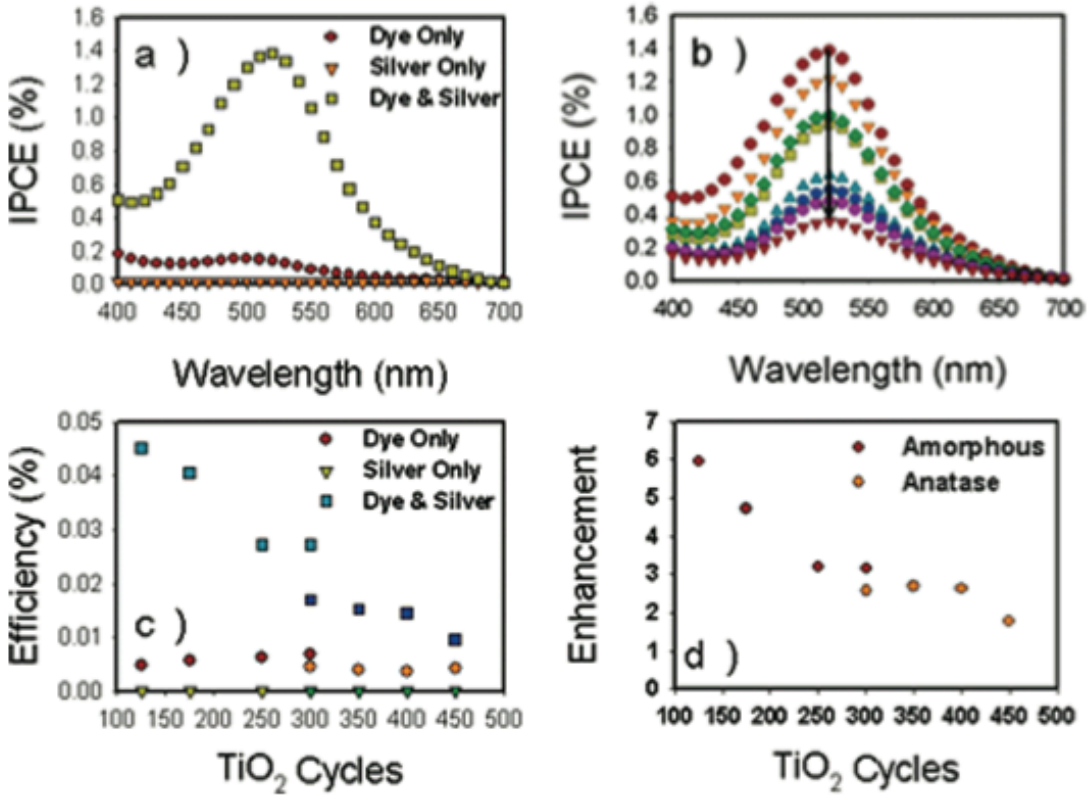

Figure 4.70. Internal Photon Conversion Effciecny (IPCE) for films of nanoparticles and dye (top). Efficiency of cells made as a function of TiO_2 thickness (bottom). Cycles refer to the number of atomic layer depostion cycles. The more cycles, the thicker the TiO_2 thickness.[125]

There is a distinct dependence of the IPCE on the plasmon resonance of the silver nanoparticles, as shown in Figure 4.70. The shape of the IPCE vs. wavelength mirrors that of the plasmon resonance, proving that increases in photocurrent stems from plasmonic coupling with the silver nanoparticles. As the thickness of the TiO_2 coated on the nanoparticles increases, the enhancement observed decreases, showing that only at close distances can the plasmon produce significantly enhanced absorption. These studies are paramount into elucidating the optimal environment, necessary to produce plasmonically-enhanced dye absorption which can be used in a photovolataic cell with minimal losses.

4.8 Concluding Remarks for Coupling with Quantum Dots and Porphyrins

Quantum dots and porphyrins represent chromophores with utility in myriad of different fields. Quantum dots are best utilized for the tunable and bright fluorescence while porphyrins are utilized for the absorption in the visible region, ability to functionalize and high exciton diffusion lengths. Plasmonic coupling of these two materials can produce materials which improve efficiency for their respective devices and applications while retaining and improving their original optical properties

For quantum dots plasmonically coupled fluorescence, can be realized using techniques outlined in this chapter. The common paradigm for these techniques is that the spacing between the metal and quantum dot must be precisely controlled in order to control and maximize the enhancement. Coupling with quantum dots represents plasmonic coupling with fluorescence in this work. The composites will be optimized in order to maximize local-field enhancements from the gold nanoparticles while negating energy transfer or any nonradiative relaxation mechanisms.

Porphryin and porphyrin derivatives can be specifically useful in plasmon-mediated photocurrent enhancement due to the presence of longer wavelength absorption bands which can be coupled with plasmon resonances. Porphyrins, in particular, are useful due to the wide range of functional groups which can be added at the meso position of the inner ring. Photocurrent enhancements of thin film-based devices of thiol-substituted porphyrin and phthalocyanine molecules attached to monolayers of gold nanoparticles have been shown in literature.[127] [128] These experiments show that addition of gold nanoparticles may aid in the production of photocurrent, but more insight needs to be gained before full utilization in an optimized solar cell configuration.

CHAPTER 5: SYNTHESIS OF GOLD NANOPARTICLES AND NANORODS

5.1 Introduction

Metallic nanoparticles have become widely used in applications ranging from photovoltaics,[59 64 125] catalysis,[17 129] to biological imaging and sensing.[130 38 26 44] The main reason for their wide utility, is their ability to absorb light, through activation of a surface plasmon resonance which is strongly dependent on size, shape and the general surface environment. Though this light absorption is tunable, it is also very sensitive to change, therefore, in order to effectively utilize this absorption in a specific region of the spectrum, the physical parameters must be both well-controlled and well-understood. Simple, solution based synthetic methods for these particles are preferable to any mechanical or lithographic method due to the lower cost input and larger sample output. The synthesis of gold nanoparticles with both aqueous and organic solubility is well documented and the extinction coefficient of their plasmon resonance changes in peak frequency, and amplitude when the surfactant composition and solvent are altered. This shift in peak resonance can also be utilized to characterize the nanoparticles.

Solubility is determined by the nature of the surfactant molecules present on the nanoparticle. Alkyl thiols, such as dodecanethiol have can be utilized to cap gold nanoparticles to impart solubility into organic solutions.[131 132] Primary amines, can also be used to replace the thiol, allowing for stable coverage with more versatility in post synthetic surface modifications.[133] Gold precursors such as gold triphenylphosphine[134 135]

can be dissolved into organic solvents and mixed with the appropriate surfactant, followed by addition of a reducing agent.[134] Aqueous gold nanoparticles are much more common, and can made through a synthesis known as the Turchevich method,[136 137 138] requires heating of an aqueous solution of chloroauric acid to boiling and addition of an aqueous solution of citrate, which acts as both the reducing agent and surfactant. Tertiary amines such as tetraoctylammonium bromide can also be useful surfactants for aqueous nanoparticles, while allowing for better control of post-synthetic ligand exchanges on the surface of the gold. These synthetic methods also lend themselves to the production of rather large nanoparticles, (>50 nm) or small (<10 nm). For the latter, a method known as seed-mediated growth can be utilized to further increase the diameter of the nanoparticles.[139 140]

A fast and robust reduction of the particles can be conducted utilizing strong reducing agents such as sodium borohydride to produce highly monodisperse nanoparticles whose size is dependent on growth time, temperature and surfactant concentration. These “seed” nanoparticles can be mixed with more gold precursor and a weaker reducing agent such as ascorbic acid to reduce more gold onto the surface of the existing gold nanoparticles. This control over the diameter of the nanoparticle allows the plasmon resonance to be altered from around 500- 600 nm. This shift includes sizes from a few nanometers to 100s of nm and can be modeled using Mie theory. In order to push the absorption range more into the infrared, a longitudinal plasmon mode must be introduced by creation of nanoparticles with different aspect ratios or gold nanorods.

Nanorods represent a step towards shifting the plasmon absorption into the infrared. The plasmon resonance of spherical particles usually lies around 500-520 nm

for monodisperse samples. This plasmon resonance is still present in a gold nanorod and is known as the transverse plasmon mode. The electron oscillation due to the long axis of the nanorod, or the longitudinal plasmon mode, is resonant at much longer wavelengths, and can range from 600 nm to around 2000 nm. These nanorods can be useful for their ability to further tune the plasmon resonance through the visible to the infrared. Their synthesis can be relatively simple as well. The most common method for nanorod synthesis, is very similar to seed-mediatd nanoparticle growth. The synthesis relies on the use of tertiary amines which bind specifically to the ends of the nanoparticles allowing for lateral growth of the rods. First, spherical seeds, capped with cetyltrimetylammonium bromide (CTAB) are synthesized utilizing a sodium borohydride reduction of aurorachloric acid. A small volume of the seeds are then injected into a growth solution containing more gold ions , silver ions, ascorbic acid and CTAB. The rods are grown overnight with the length dependent on the gold and silver concentration.

The understanding of the synthesis and optical properties of different gold nanoparticles is crucial for maximum control over the plasmon resonance. The resonance is very sensitive to the nature of the nanoparticle surface environment, including surfactant and solvent. The ability to alter the surfactant identity allows for carful tuning of the plasmon resonance during initial synthesis of the nanoparticles. The coating of the nanoparticles will require careful surfactant choice to one that will promote growth of even and spherical shells without being to bulky or too strongly binding to impede diffusion of the shell material to the nanoparticle surface. Nanoparticle coated with CTAB would be ideal since they are used to create uniform seeds for nanorod growth. Xie et al show that chloride salt can be useful for well-controlled silver nanocages around

gold nanoparticles. This surfactant provides much more uniform shells by eliminating the formation of insoluble AgBr in solution when adding silver ions for shell formation. Careful control over the formation of CTAC-coated gold nanoparticles will be crucial in order to limit polydispersity in sample size. These nanoparticles will then provide the template for the further production of hybrid nanoparticles.

5.2 Synthesis of Dodecanthiol-capped Nanoparticles

In a typical synthesis, 0.31 g chloro (triphenylphosphine) gold (I) [$AuPPH_3Cl$] was dissolved into 100 mL Benzene inside a round-bottom flask. To this solution, 0.866 g tert-butyl amine borane was added at once and the solution was heated to 55^0 C for 1 hour. The solution was then cooled and purified via ethanol addition and centrifugation. To measure concentration of gold particles, the dried particles were placed on a scale and monitored until no change is seen. The weight of the centrifuge tube was then subtracted to calculate the mass of the dried particles. The gold nanoparticles were then redispersed in a measured amount of anhydrous hexanes.

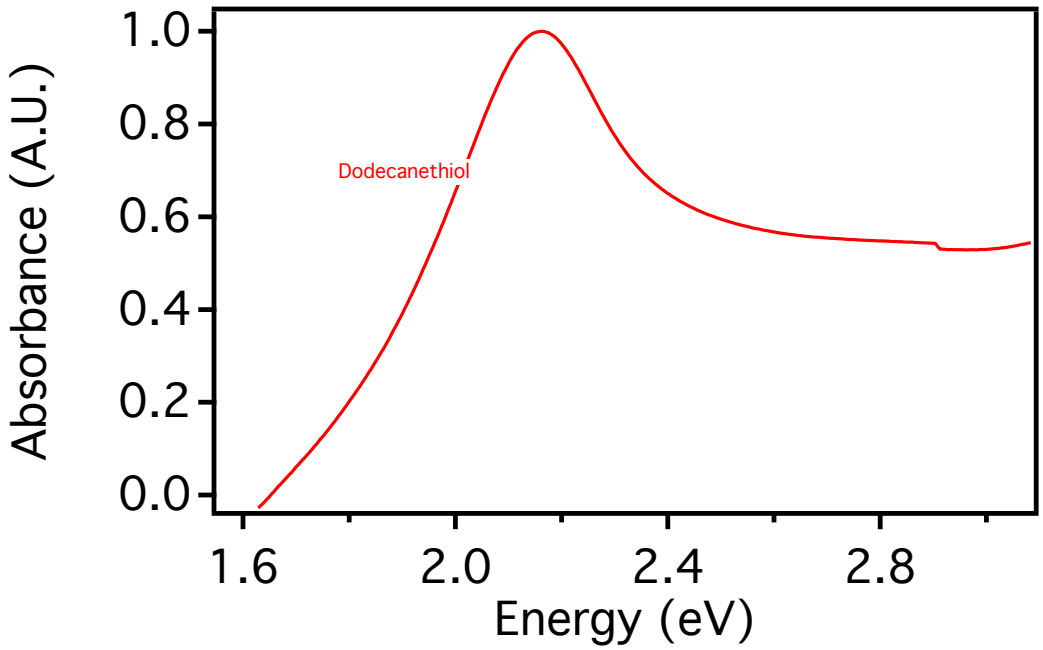

Figure 5.20. UV-vis absorption spectrum of dodecanethiol-capped gold nanoparticles in hexanes.

In Figure 5.20 the plasmon resonance of the gold nanoparticles was shown to lie at 2.2 eV. The nanoparticles were dispersed into hexanes and are stable for months at a time. The nanoparticles are physically characterized via TEM microscopy to investigate the size distribution of the sample.

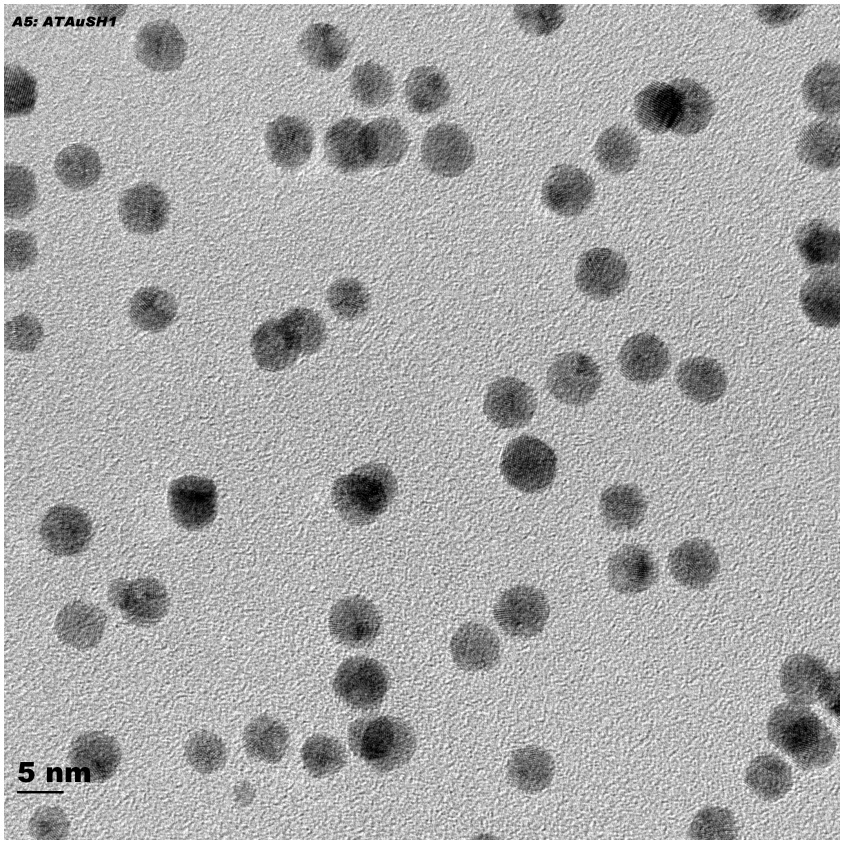

Figure 5.21. TEM image of dodecanethiol-capped gold nanoparticles in hexanes.

The TEM image in Figure 5.21 shows gold nanoparticles with an average diameter of 5.3 nm and a standard deviation of 1.1 nm. The nanoparticles produced from this method contained some size discrepancies but were fairly uniform. This synthesis proved to be successful for uniform gold nanoparticles, that were spherical and around 5 nm in diameter. The nanoparticles were very stable in solution, which proved difficult for purification. The thiol surface attachment was very strongly binding, which could interfere with subsequent surface modifications. The reducing agent, borane tert-butyl amine, showed to be useful in reduction of the gold for the formation of uniform particles and would be utilized for syntheses using other surfactants.

5.3. Synthesis of Gold Nanorods

Prior to nanorod synthesis, a variety of stock solutions were created. First, a 1 mM $HAuCl_4$ was created by first drying a 20 mL glass vial in the oven for at least 1 hour after thoroughly cleaning with aqua regia and rinsing with MilliQ water. The vial was then placed into the glove box, where, 0.339 g $HAuCl_4$ was weighed and placed into the flask before being sealed and taken out of the glove box. The $HAuCl_4$ was dissolved with MilliQ water and transferred into a 1000 mL volumetric flask is rinsed with copious MilliQ water and the wash was placed into the volumetric flask. Once all the $HAuCl_4$ had been transferred ,the flask was then diluted to the mark with MilliQ water.

A 0.5 mM $HAuCl_4$ solution was created by first drying a 20 mL glass vial in the oven for at least one hour after thoroughly washing with aqua regia and rinsing with MilliQ water. To this vial, 5 mL of 1 mM $HAuCl_4$ solution was added and diluted to 10 mL by addition of MilliQ water by filling to the mark in a 10 mL volumetric flask.

A 4 mM $AgNO_3$ solution was created by dissolving 0.068 g $AgNO_3$ with MilliQ water into a 100 mL volumetric flask and diluting to the mark. The solution was stored in an amber bottle due to photosensitivity

A 0.2 M Cetyl trimethylammonium bromide (CTAB) solution was created by dissolving 3.66 g CTAB into a 50 mL volumetric flask and diluting to the mark with MilliQ water.

A 0.064 M ascorbic acid solution was freshly prepared before use in any synthesis. The ascorbic acid solution was created by dissolving 0.564 g into a 50 mL volumetric flask with MilliQ water and diluting to the mark.

A 0.01 M sodium borohydride ($NaBH_4$) solution was freshly prepared used immediately after preparation. The $NaBH_4$ solution was created by dissolving 3.8 mg $NaBH_4$ in a clean and dry 20 mL vial and diluting to 10 mL with MilliQ water.

The first step in the nanorod synthesis was to prepare a growth solution for the nanorod seeds. 9.1 g CTAB, 1.1 g 5- bromosalicylic acid, and 250 mL MilliQ water were mixed together inside a 1000 mL Erlenmeyer flask equipped with a stir bar and covered with a strip of parafilm. The flask was heated to 50-70 ^{0}C by setting the hotplate to 55 ^{0}C. The solution was stirred vigorously until the solution was colorless and clear (not cloudy and no solid at the bottom). Once dissolve, the flask was cooled to 30 ^{0}C without any stirring. Once colorless, 8-24 mL 4 mM $AgNO_3$ solution was rapidly injected to the flask and allowed to sit undisturbed at least 15 minutes. 250 mL 1 mM $HAuCl_4$ solution was then added to the flask under 400 RPM stirring (along with 2.1 mL concentrated HCl if necessary) and allowed to stir for 15 minutes. Once aged for 15 minutes, 2 mL of freshly prepared 0.064 M ascorbic acid solution was then added and stirred vigorously until the solution was colorless. Once colorless, 0.4- 0.8 mL gold seed solution was added and stirred vigorously for 30 seconds. The solution was then allowed to sit at least 12 hours (overnight) to achieve nanorod growth.

The gold seed solution was prepared in a clean 20 mL glass vial equipped with a small stir bar (cleaned with aqua regia and dried in the oven for > 1 hour). First, 5 mL of 0.2 M CTAB solution was mixed thoroughly with 5 mL 0.5 mM $HAuCl_4$ solution (at this time the 0.01 M $NaBH_4$ was prepared). 0.6 mL of the $NaBH_4$ solution was transferred to a small clean and dried vial and diluted to 1 mL with MilliQ water. The diluted $NaBH_4$ solution was then rapidly injected into the seed solution vial under 1200 RPM stirring for

2 minutes. The seed solution was then allowed to sit for 30 minutes undisturbed before use.

Purification was conducted via centrifugation at 9000-10000 RPM. The reaction solution was transferred directly to centrifuge tubes and centrifuged for 30 minutes at 20 ^{0}C. Once centrifugation was completed the supernatant was then decanted and discarded. The precipitated particles are then washed one times by filling the tubes with MilliQ water and centrifuging in the same manner. The aspect ratio of the nanorods was controlled through variation of the gold seed added, the silver nitrate added and the amount hydrochloric acid solution added during the synthesis.

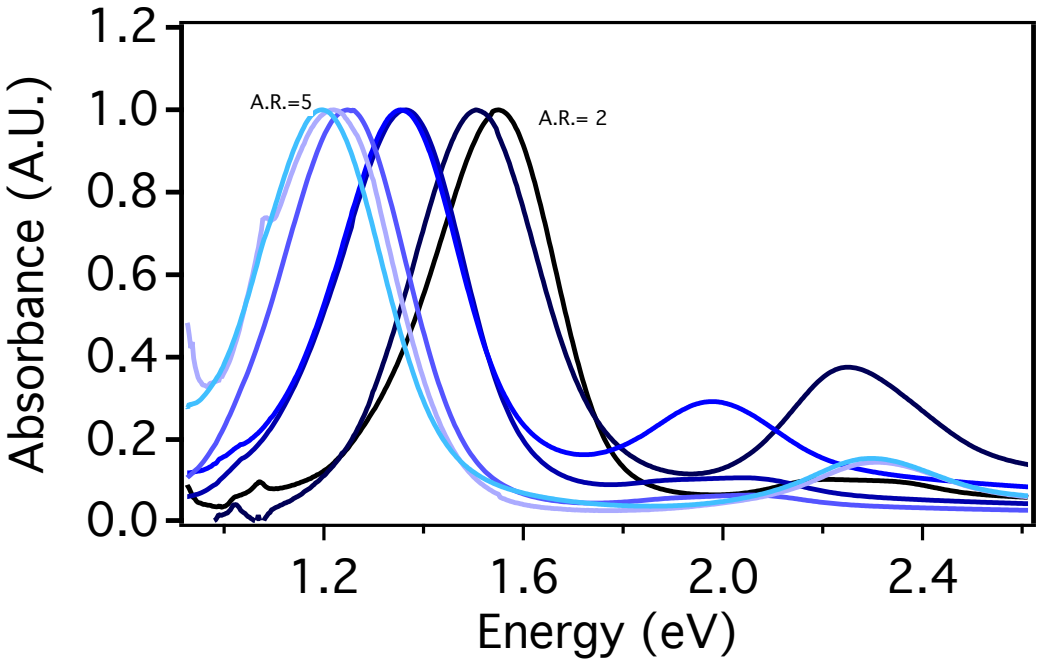

Figure 5.30. UV-vis absorption of gold nanorods with aspect ratio ranging from 2 to 5

The UV-vis absorption spectra can then be correlated to the aspect ratio of the gold nanorods, which can be varied from around 5 to 2. The aspect ratio is defined as the length divided by the width of the nanorod. The maxima of the plasmon resonance should shift when the dimension of the nanorods are changed. The transvere plasmon mode, corresponding to the nanorod diameter is higher energy from 2.0 to 2.4 eV, while the longer, longitudinal plasmon mode shifts from 1.6 to 1 eV. TEM images were not taken on the samples utilized in Figure 5.30, but the aspect ratio calculations were taken from literature. In order to further confirm these assignments, another sample was synthesized and TEM images were taken.

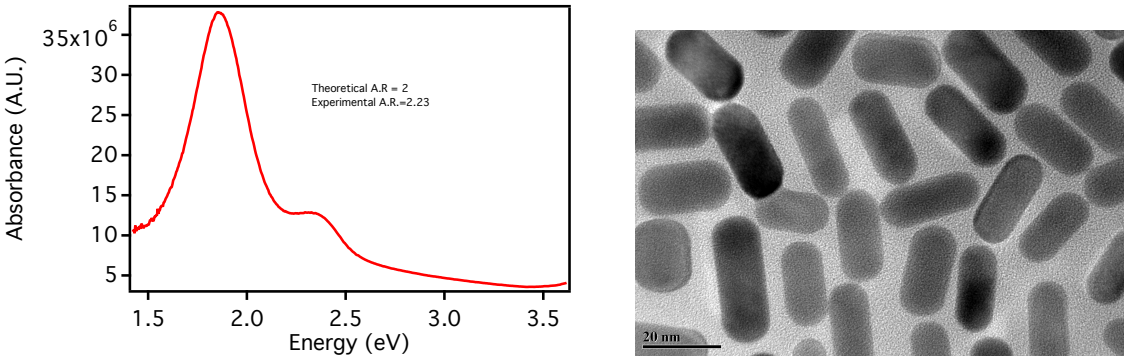

Figure 5.31 UV-vis absprtion of gold nanorods with aspect ratio of 2 (left) and TEM image of the same gold nanorods with measured aspect ratio of 2.23

The gold nanrods had a relatively low, theoretical aspect ratio of 2 when the literature values were utilized. The TEM images were then analyzed using the image J software to find an actual aspect ratio of 2.23 which is very close to the literature value. The synthesis of gold nanorods provides some insight into the nature of how the gold plasmon resonance relates to the shape and structure of the gold surface. The plasmon

resonance can be pushed into the near-infrared range with longer nanorods. The synthesis also gives insight into the synthesis of uniform gold nanoparticles. The reduction of gold to produce well-defined gold templates before gold can be grown into longer rod shapes. This knowledge will be used for the production of highly monodisperse gold nanoparticles.

5.4: Chloroauric Acid as the Gold Precursor

An in depth study into the nature of nanoparticles produced via different synthetic methods is vital to the understanding of plasmonic coupling. Very monodisperse samples which can still be susceptible to subsequent surface chemical modifications are necessary for the production of plasmonic coupling with low sample heterogeneity. The synthesis of the gold nanorod seeds can be used as a template for monodisperse gold nanoparticles. The nanorod seeds need to be uniform in order to grow a monodisperse nanorod sample and the gold and ascorbic acid must slowly diffuse to the seed surface, therefore the surface must still be accessible for chemical modification. The use of bromide salts, represents solubility issues for Pb and Ag which could impede reactions involving them, therefore the hexadecyltriemtylammonium chloride (CTAC) were utilized to replace the bromide salt. Tetraadecyltriemtylammonium chloride (TTAC) was also utilized in these studies. An aqueous synthesis of bigger gold nanoparticles was conducted based on the gold nanorod seed production.

Nanoparticles were synthesized by addition of borane-tert butyl amine in a 1:1 ratio with a Au^{+3} solution. For a typical synthesis, 20 mL of 1 mM chloroauric acid in water is heated to 70 degrees Celsius with 20 mL of either 0.2 M aqueous CTAC or 0.2 M oleylamine in toluene. The mixture is stirred vigorously for 10 minutes until borane

tert-butyl amine was added. The mixture turned deep red and was stirred for 30 minutes. The solution was cooled and stored without further purification. Long chain, primary amine-capped nanoparticles were also be synthesized from this method by replacing the aqueous CTAC or TTAC solution with oleylamine in toluene.

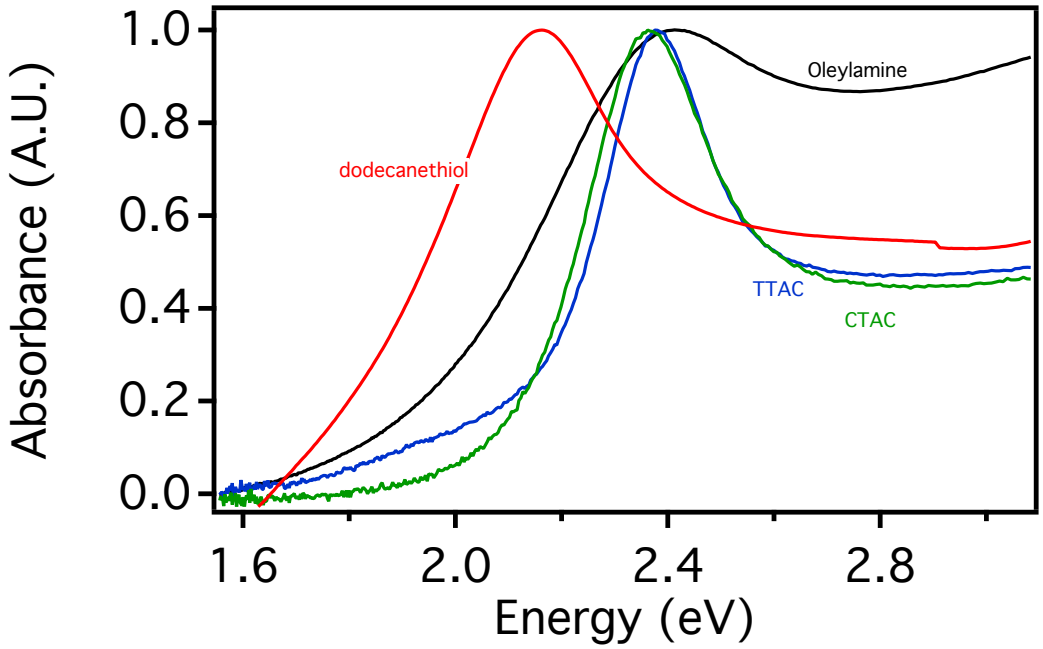

Figure 5.40. Normalized absorption spectra of three different capping agents, oleylamine, dodecane thiol, tetradecyltrimethylammonium chloride (TTAC) ,cetyltrimethylammonium chloride (CTAC).

In Figure 5.40 the absorbance spectra of nanoparticles produced from this synthetic method ,with different capping ligands is shown in comparison with the goldtriphenylphosphine reduction method. The oleylamine and dodecane thiol-capped nanoparticles show a much broader plasmon resonance, produced from the larger size distribution in the samples. The dodecanethiol-capped nanoparticles are also slightly red-

shifted in comparison to the tertiary amine-capped nanoparticles, while the oleylamine-capped nanoparticles are slightly blue-shifted.

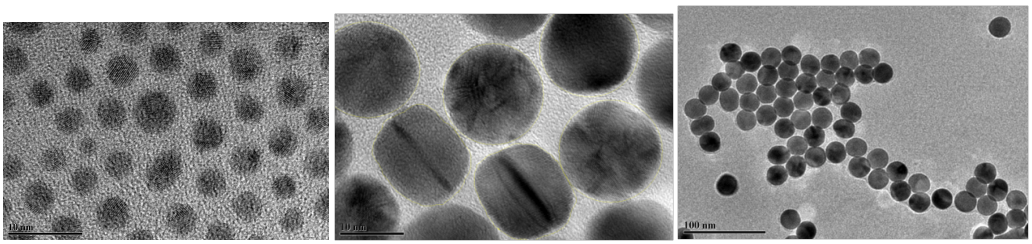

Figure 5.41 TEM images taken a 200 kV accelerating voltage. The nanoparticles are oleylamine-capped (left), CTAC-capped (middle) and TTAC-capped right. The scale bars are 10 nm (left),10 nm (middle) and 100 nm (right)

The TEM images support this hypothesis that the width of the absorption spectrum is directly correlated to the sample polydispersity. The oleylamine-capped nanoparticles shown are slightly smaller around 5 nm in diameter but show a much larger size variation of 0.96 nm than the TTAC with a 0.02 nm standard deviation or CTAC coated nanoparticles with a a 0.4 nm standard deviation. In comparison, the dodecane-capped nanoparticles had a standard deviation of over 1 nm. TTAC-coated nanoparticles have an average diameter of 26 nm while the CTAC-coated nanoparticles have 16 nm diameter on average. In order to optimize conditions for the gold synthesis, an investigation on the affect of the reducing agent to gold ratio was conducted.

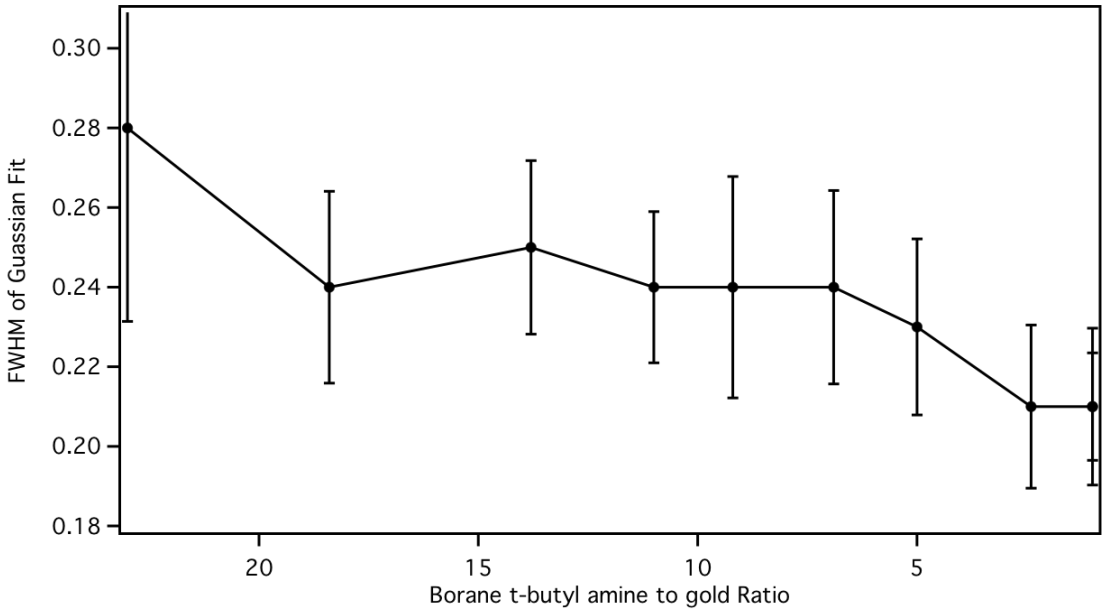

Figure 5.42 Plot of the FWHM of Guassian fits to the absorption spectrum of CTAC-coated gold particles as a function of different rations of borane t-butyl amine. The error bars represent error in the Guassian fitting of the absorption spectra.

In Figure 5.42 the FWHM of a Gaussian fit of the each absorption spectrum is plotted vs. reducing agent to gold ion ratio, with samples ranging from 23:1 to 1:1 in reducing agent to gold a 1:1 reducing agent. The narrowest FWHM is seen at the 1:1 ratio. Ensuring there are stoichiometric equivalents of borane tert-butyl amine and $HAuCl_4$ may provide a more steady reduction rate and produce nucleates with a narrow size distribution. The images were analyzed using ImageJ software to find the particles to be single crystalline with lattice spacing of a approximately 2.3 angstroms (literature value = 2.04 angstroms).

5.5 Concluding Remarks for Gold Nanoparticle Synthesis

The data shown in these experiments aid in the production of uniform gold nanoparticles with controllable plasmon resonances. The comparison of aqueous vs. organic soluble nanoparticles show that the former can be synthesized with higher

uniformity and control over the surfactant system. The synthesis of gold nanorods aided in development of a novel synthesis of tertiary amine-capped gold nanoparticles. These nanoparticles are highly uniform and stable in solution. These nanoparticles possess a narrow plasmon resonance band which will aid in controlling the resonance of the plasmon once the surface of the nanoparticle is altered with ligand exchanges and shell deposition.

CHAPTER 6: SYNTHESIS OF SEMICONDUCTOR SHELLS

6.1 Introduction

Silica-coated nanoparticles, as shown by Klimov et al,[106] and polymer coated gold surfaces[31 99] have been utilized to space chromophores from gold surfaces to take advantage of plasmonic, local field enhancements. Recently, noble metal nanoparticles have been combined with semiconductor or magnetic nanoparticles to produce hybrid nanoparticles with enhanced and tunable functionality.[129 84] Recent literature, such as the study conducted by Zhang *et al*., has shown the possibility for the synthesis of these particles, but only limited control in the uniformity of the hybrid species is possible due to a distribution of gold nanoparticle sizes and compounded by the lack of optical characterization coupled with physical characterization at each stage of growth.[141] Zamkov *et al.* showed similar uniformity in shell formation but only one shell thickness was utilized with different core sizes, with some shells not being fully formed around the nanoparticles.[142]

In order to effectively utilize these nanoparticles for plasmonic coupling, the precise optical response must be known and characterized for a variety of shell thicknesses. Applying a dielectric spacing layer between the plasmonic metal surface and a fluorophore can be an efficient method for diminishing losses due to nonradiative mechanisms of relaxation from the excited state of the fluorophore and also prevent donation of energy to the metal species, as previously noted.[45, 125] This spacing layer can

also aid in the study of dependence of the fluorophore optical properties on the spatial separation from the metal surface.[40 41 127] Colloidal solutions allow for improved scalability and can be spin cast onto thin films for lighting or photovoltaic devices. The aim of this study was to control plasmonic coupling between gold nanoparticle and an external fluorophore. Studies on the effects of different separation distances, strength of the surface bond, and chemical composition of the shell material are needed in order to optimize parameters for maximum enhancement.

The hybrid nanoparticles were synthesize using a method adapted from that utilized by Zhang *et al* ,in which gold nanoparticles are coated with a semiconductor shell via a 3 step procedure.[141] The previous method produced uniform shells, but the inner gold nanoparticles were not monodisperse, which would lead to differences in the resulting plasmon resonance. The first modification was the use of aqueous, CTAC-coated gold nanoparticles as the gold template, shown previously in Chapter 5. The gold nanoparticles produced in the original method, were oleylamine-capped and dissolved in organic solvents such as toluene. The second modification was the system for silver deposition. The unpurified gold nanoparticles were then coated with silver with the use of silver nitrate as the silver source and ascorbic acid as the reducing agent. The previous method utilized, silver acetate as the silver source which produces solubility issues in aqueous solutions. The nanoparticles, were purified and redispersed into clean water. The silver-shelled gold nanoparticles were characterized via TEM and UV-vis absorption spectroscopy. The next modification was the use of a phase-change to produce the silver sulfide shell. The aqueous nanoparticles were added to a sulfur solution in toluene. The nanoparticles were then transferred to the organic phase upon sulfide formation, with the

aid of oleic acid and oleylamine. Finally, the cation exchange to produce the semiconductor shell was conducted similar to the orginal procedure.

The hybrid nanoparticles were synthesized with a semiconductor shell thickness in three regimes, small (1-5 nm), medium (5-10 nm) and large (10-20 nm). The dielectric constant can also be altered by changing the composition of the semiconductor shell from ZnS to CdS with the latter having a slightly larger dielectric constant. These materials are in sharp contrast to studies conducted utilizing SiO_2 as the spacing layer due to the much higher dielectric constant, almost 3x that of SiO_2. The overlap of the plasmon with the fluorophore absorption or emission band can also be controlled by changing the local electric field around the gold nanoparticle. CdS or ZnS shells of the same thickness will cause slightly different electronic interactions with the metal surface, resulting in different resonance frequencies. Porphyrins and quantum dots will be the chromphorpes utilized in the coupling study to monitor plasmonic coupling with both excitation and fluorescence, respectively.

6.2: Deposition of Silver on Gold Nanoparticles

A silver shell will next be deposited around the gold nanoparticle based on the molar equivalents of gold in the nanoparticles. Since the silver shells must also be transformed to an amorphous silver sulfide shell in the subsequent step, the synthesis method must be both robust and repeatable. It has been shown that particles coated with CTAC can provide a template for uniform growth of a silver nanocubes due to the formation of gold particles with both 100 and 111 crystal plane orientation and preferential growth on the 111 facets.[143] If the gold particles possess a majority of 111 facets, accelerated growth rates for the silver deposition will be possible.

This method was utilized to produce tunable, spherical shells of silver onto gold nanoparticle cores. First, a series of shells with increasing thickness were produced in order to monitor the shift of the surface plasmon resonance. To control the shell growth, 4 mM silver nitrate was added to a solution of CTAC-coated gold nanoparticles. Ascorbic acid was also added in a 25 times excess to the molar ratio of silver to control reduction onto the silver surface. The silver nitrate was added according to the ratio of gold in solution, increasing from 0.1 to 1 silver to gold, to 5 to 1.

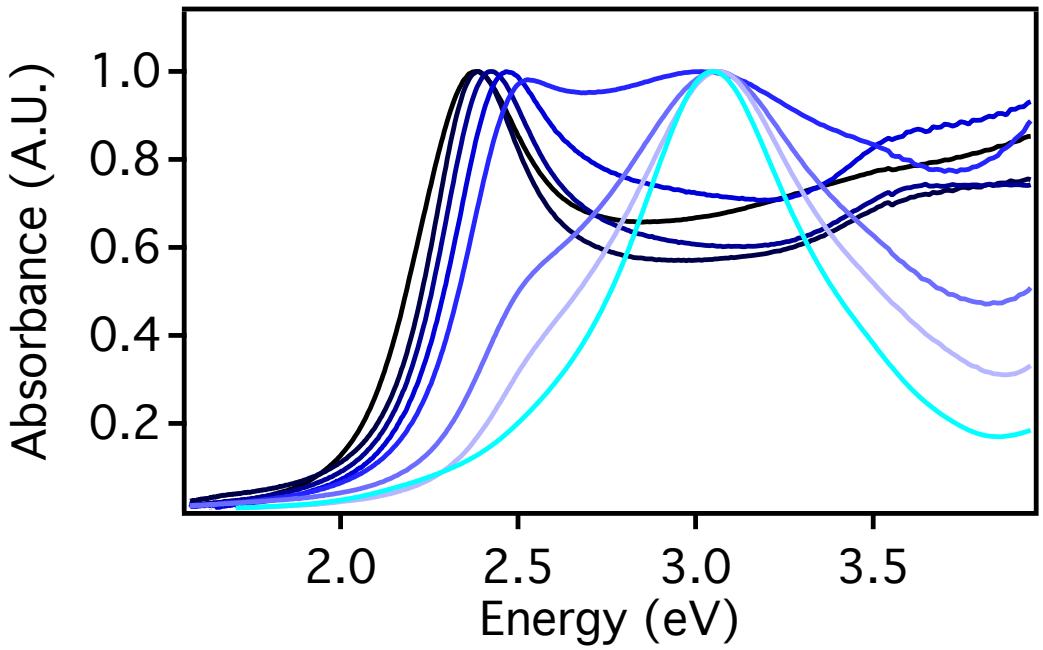

Figure 6.20 Normalized absorbance spectra of gold nanoparticles coated with silver in increasing in shell thickness (darker blue to lighter blue)

A blue shift in the spectrum of about 0.6 eV was observed for the surface plasmon resonance, from the characteristic gold peak at 2.38 eV to around 3.0 eV with the thickest silver shell. Two distinct plasmon resonance peaks were also observed at higher silver concentrations, starting from 2.4 eV. To ensure that this shift is not due to the formation of small silver nanoparticles, solutions with varying ratios of gold and silver nanoparticles are created and monitored using UV-Vis spectra.

The CTAC-coated silver nanoparticles were synthesized utilizing the same method as for gold nanoparticles with the same surfactant. For a typical synthesis, 25 mL of a 1 millimolar solution of silver nitrate was added to 25 mL of 0.2 M CTAC. The solution was heated to 70^0C in an oil bath for 10 minutes before 2 mg of borane tert butyl

amine was added to the solution. The solution is allowed to stire 30 minutes before being collected without purification.

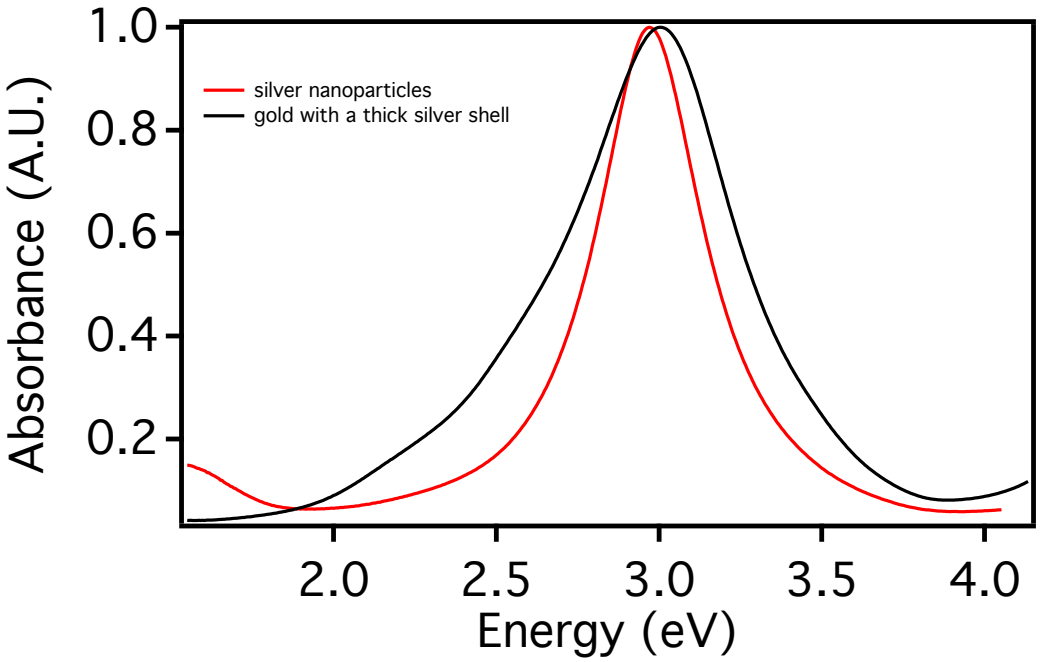

Figure 6.21 UV-vis absorption spectra of CTAC-capped silver nanoparticles (red) and gold nanoparticles with a thick silver shell (black).

The spectra in Figure 6.21 shows the absorbance spectra of silver nanoparticles compared to that of gold nanoparticles with a silver shell. The plasmon of silver is located at 3.0 eV, substantially blue-shifted to that of gold. The spectra of the silver-shelled nanoparticles looks similar but some distinct differences are observed. First, the silver nanoparticles plasmon spectra is much more narrow to that of the gold nanoparticles with silver shells. The plasmon peak of the silver-shelled nanoparticles is slightly blue-shifted when compared to pure silver nanoparticles also.

In order to further ensure that the silver nanoparticles can be differentiated from deposited silver on gold, with UV-vis spectroscopy, silver nanoparticles are then mixed with gold nanoparticles to observed the spectral difference.

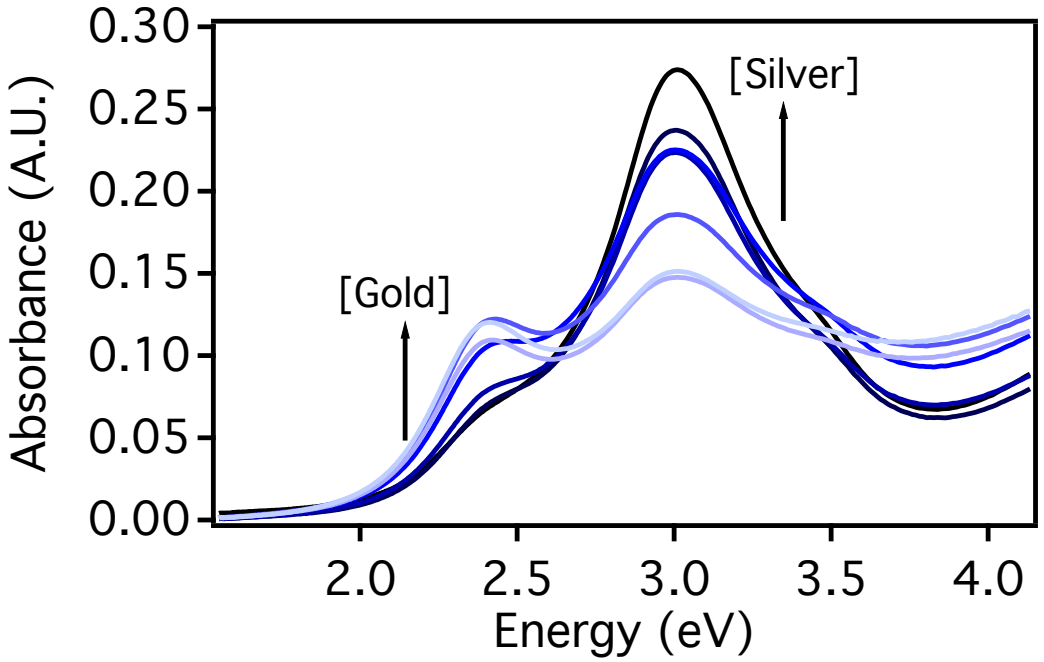

Figure 6.22 Absorbance spectra gold nanoparticle and silver nanoparticles in varying ratios. The ratios range from 4:1 to 1:4 gold to silver with the darkest curve representing a 1:4 silver to gold nanoparticle ratio.

Observation of the plasmon shift in Figure 6.22 shows that, with a mixture of gold and silver nanoparticles, the plasmon resonance does not gradually shift to higher energies, but rather decreased or increased in intensity when the ratio of either nanoparticle was altered. If majority silver nanoparticles were present in the mixture, than the peak at 3.06 eV was more prominent, but no change in the position of the gold

plasmon occurred. When deposition of silver on the gold surface occurred, the gold plasmon red shifted and broadened, until a second silver plasmon was observed at 3.06 eV. Finally with thick silver coverage, the gold plasmon was eliminated and only a plasmon peak at 3.06 eV was observed. While microscopy could easily be utilized to determine if silver nanoparticles had been produced, UV-vis is useful in compare the resulting shift in the plasmon produced by silver nanoparticles or deposited silver onto gold. The latter shifts the plasmon gradually with increasing shell thickness, while the formation of silver nanoparticles causes an increase in the plasmon intensity only.

In order to more carefully control the shell thickness, the amount of silver needed to form a specific thickness was calculated. The calculations began by assuming a spherical gold nanoparticle and then calculating the volume of the original gold particle and the subsequent shelled nanoparticle. The difference of the two volumes was found and used as the volume of the shell. The shell volume was then converted to the mass of silver using the density of silver and finally to moles of silver using the molar mass of silver. The volume of a 4 milimolar silver nitrate solution, in water, needed for a specific shell thickness was then calculated and added dropwise to the gold nanoparticle solutions at 70^0C. Ascorbic acid was added, in 25 x molar excess, prior to silver addition to ensure reduction of the silver on the gold surface.

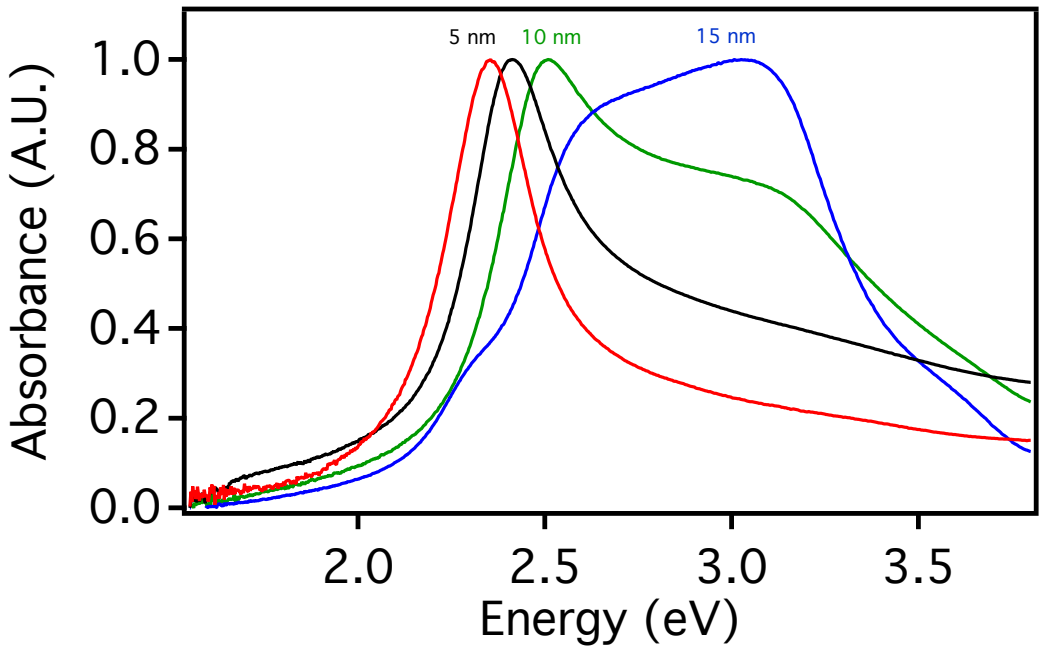

Figure 6.23 UV-vis absorption spectra of gold nanoparticles (red) and gold nanoparticles coated in silver shells of radius 5 nm (black), 10 nm (green) and 15 nm (blue).

Figure 6.23 shows the spectra from coating of 3 different silver thicknesses. The shells mirror the results seen in Figure 6.20 but can now be related to calculated radius. The shells show a shift to higher energy plasmon resonance, indicative of a formation of a silver surface. The thinnest shells, show simply a red-shift of the plasmon resonance, and upon thicker shell formation, a second plasmon peak is formed which blends into one broad peak centered around 3.0 eV. These data provide correlation between size and surface plasmon resonance. Transmission electron microscopy images were also taken in order to monitor physical dimensions of the nanoparticles..

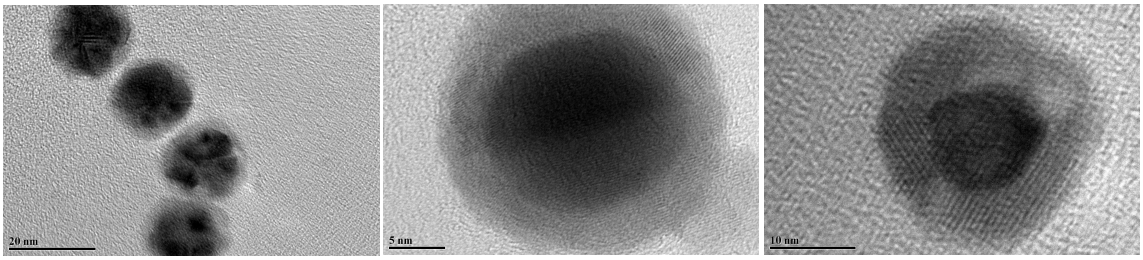

Figure 6.24 TEM images taken at 200 kV accelerating voltage. The top TEM images have silver shells with a 3 nm radius (top), 5 nm radius (middle) and 7 nm radius (bottom).

TEM images were analyzed using ImageJ software to find the particles to be single crystalline with lattice spacing of a approximately 4.13-4.3 angstroms similar to that of fcc silver as well as an absence of isolated silver particles. The inner gold nanoparticles were also analyzed to find that the spacing was slightly smaller than the bare gold nanoparticles with values from 3.6-4 angstroms. This could be due to a small amount of stress place on the nanoparticles when the shell is deposited. Overall the shell thickness seems uniform and mostly spherical with a few samples having a slightly asymmetric shell with one elongated end. This elongation is more pronounced in the smaller shell sizes, as the larger shell thicknesses seem to be more uniform. Analysis of the shell radius shows the 2.8 nm for the 3 nm sample, 4.6 nm for the 5 nm sample, and 7.4 for the 7 nm shell.

The analysis of the TEM samples show a fairly uniform size distribution and deviation from theoretical calculations of less than half a nanometer. This shows that we can precisely tune the thickness of the silver shell which will provide the template for the remaining steps of the semiconductor shell formation. This shows a successful first step in the production of a tunable and uniform semiconductor shell. The nanoparticles were

mxed with ethanol and centrifuged at 14,000 RPM to remove and formed silver nanoparticles and un-reacted silver ions. The nanoparticles were then stored in clean water. The next step will be to transform the shell into a silver sulfide shell.

6.3: Chemical Transformation of the Shell to Silver Sulfide

Once colloidal solutions of Au/Ag core shell nanoparticles were synthesized, the nanoparticle shell was then converted to silver sulfide. Three separate routes to convert the silver, to silver sulfide were studied and characterized via UV-Vis absorption spectroscopy, in order to ensure a reproducible and robust conversion to an amorphous silver sulfide shell. The plasmon resonance of the nanoparticles has been reported to red shift with increasing shell thickness due to the change in the refractive index from Ag to Ag_2S.[144]

The first method utilized was drop wise addition of a 10 mM solution of aqueous sodium sulfide to the colloidal mixture of Au/Ag colloids. The reaction was conducted at room temperature and open to air. Sodium sulfide is a cheap sulfur source that would allow for the reaction to be conducted without a phase change. The plasmon peak red shifts with increasing coverage of silver sulfide. The amount of silver sulfide used was calculated based on the moles of silver present in the shell. An interesting phenomenon occurred when a large volume of sulfur ions, which would be necessary for thicker shells. The plasmon resonance disappeared and a broad, featureless absorption was observed.

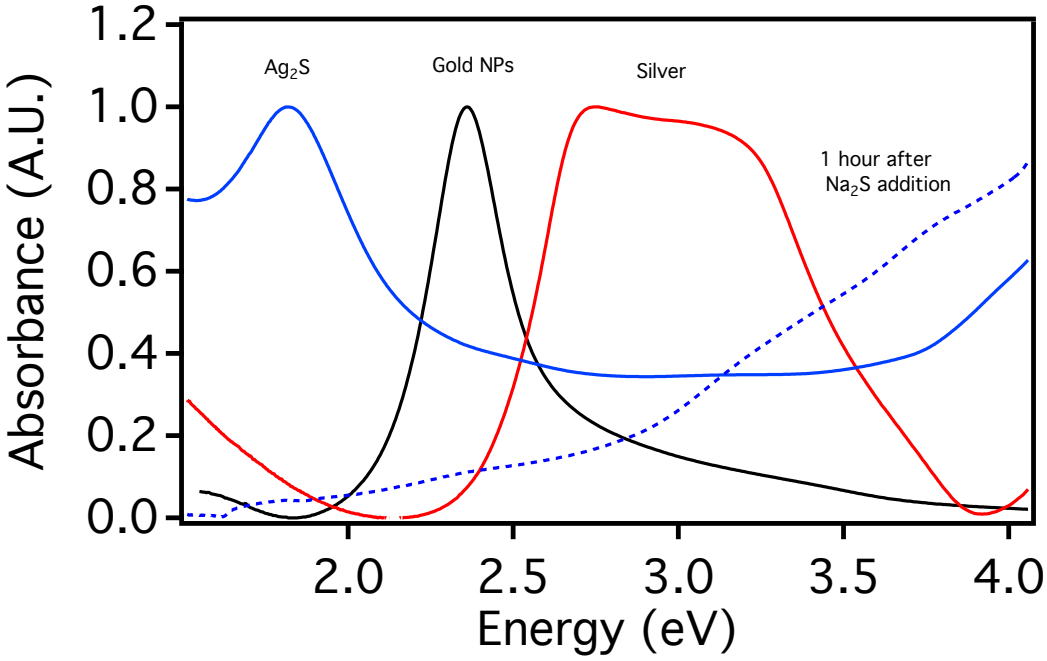

Figure 6.30 Absorption spectra of gold nanoparticles (black), gold nanoparticles with a silver shell before (red), Au /Ag nanoparticles after initial addition of Sodium sulfide (blue) and 1 hour after after addition of sodium sulfide (blue dashed line).

The nanoparticles seem to dissolve, observed as an elimination of any plasmon absorption. Once the sulfur solution is added to the colloids, a broad featureless spectrum is observed as seen in Figure 6.30 This is a very interesting phenomenon in the fact that not only does it seem the silver shell has been dissolved but the entire nanoparticle itself has either been aggregated or re-dissolved into solution. This requires that a strong oxidizing agent such as H_2S or sulfuric acid be formed in solution with excess sulfur. A less reactive sulfur precursor was then investigated for the reaction.

6.3.1 Thioacetamide as the Sulfur Source

An alternate sulfur precursor thioacetamide, has been utilized as a sulfur ion source in various organic reactions, through.[141] This may provide a less reactive sulfur

source providing more accurate shell control and eliminate the dissolution of the nanoparticles in solution.

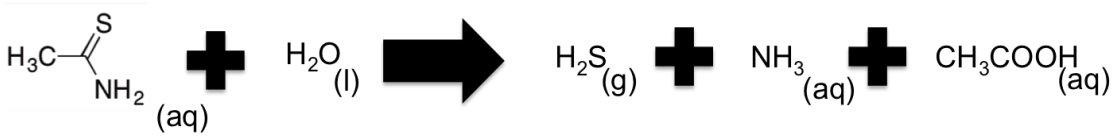

The reaction scheme above shows the dissolution of thioacetamide in water. The formation of hydrogen sulfide in solution provides a slower and more controlled route to production of sulfide ions in aqueous solutions. Solid thioacetamide was added to the aqueous nanoparticles, at room temperature, in 5 mg increments until no color change was observed. The total amount of thioacetamide varied from 30 to 100 mg for the thickest shells.

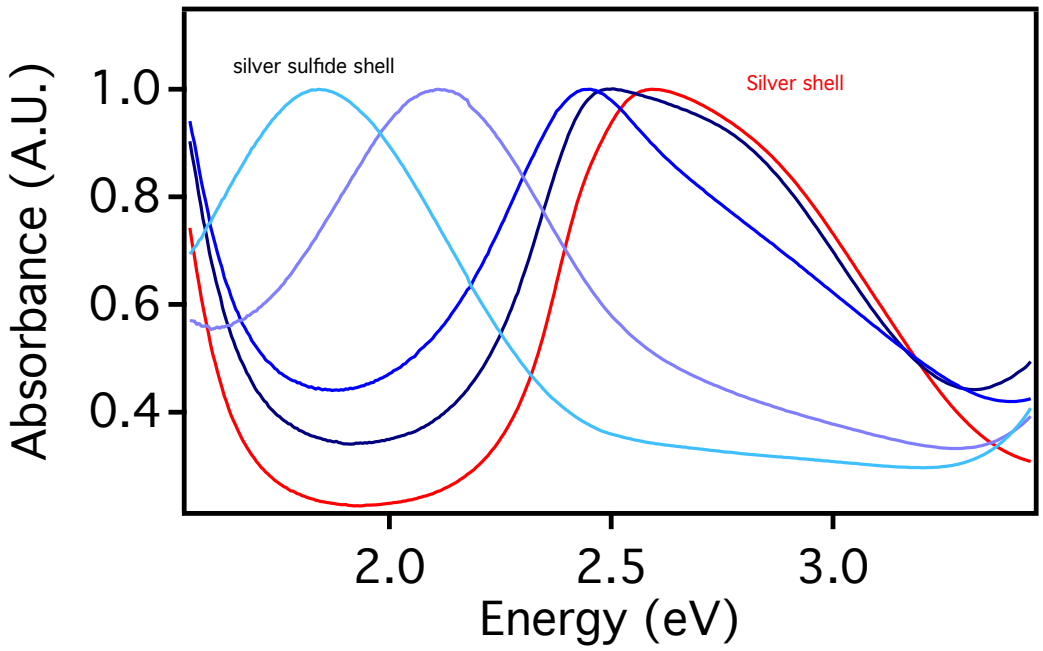

Figure 6.310 Absorption spectra of silver nanoparticles with a silver shell before (red) and after addition of thioacetamide (blue spectra). Addition was done in 5 mg increments until all the silver had been converted (light blue).

Conversion of Au/Ag colloids to Au/Ag_2S proved successful as shown in Figure 3.310, through observation of a sharp red shift from the original silver shelled nanoparticles to about 1.85 eV. The shell composition could be slowly controlled through careful addition of solid Thioacetamide to the aqueous solution as shown through the gradual redshift with increasing additions. This method proved to be a more controllable sulfur source but the same phenomenon was observed as the sulfur precursor in larger shelled samples. In order to investigate this phenomenon further, experiments were conducted on silver nanoparticles synthesized with CTAC as the surfactant. The synthesis was conducted the same as for CTAC-capped gold nanoparticles with 1 mM silver nitrate substituted for the chloroauric acid solution.

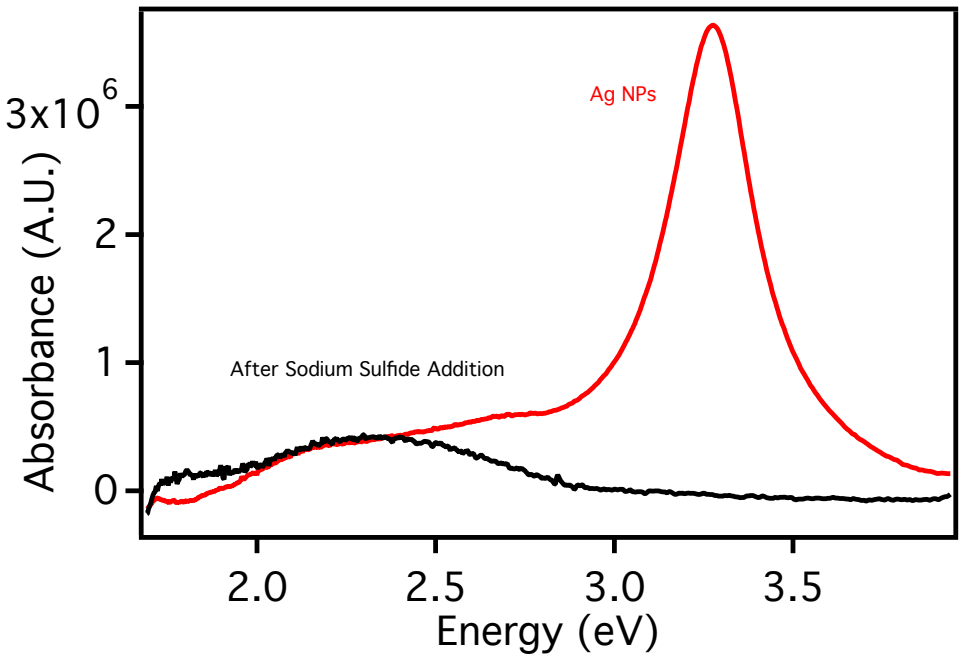

Figure 6.311. Absorption spectra of silver nanoparticles with a silver shell before (red) and after addition of sodium sulfide (red).

In Figure 6.311 we see this trend preserved for silver nanoparticles in a solution of sodium sulfide. The silver Plasmon at 3.06 eV is completely eliminated leaving a broad spectrum with a peak around 2.2 eV, which seems to indicate aggregation of the nanoparticles. These data prompted a move from the aqueous sulfur precursors to a source which would be soluble in the organic phase. This could be helpful for the cation exchange in the last step of the reaction which needs to be performed in toluene.

6.3.2 Elemental Sulfur as the Sulfur Source

Elemental sulfur was dissolved into a toluene to be used as the sulfur source. Prior to addition to the toluene solution, the silver nanoparticles are concentrated into 1 to 3 mL of water to ensure an easier phase change into the toluene. This also helps to remove any unreacted silver ions and prevent formation of isolated silver sulfide nanoparticles.

The silver shells were added to a sulfur solution with oleylamine and oleic acid, in order to convert the silver shell to silver sulfide. A large excess of sulfur can be utilized with no effect on the nanoparticle stability, ensuring complete conversion of the silver to silver sulfide. The resulting nanoparticles can then be isolated via centrifugation and redispersed into hexanes or toluene.

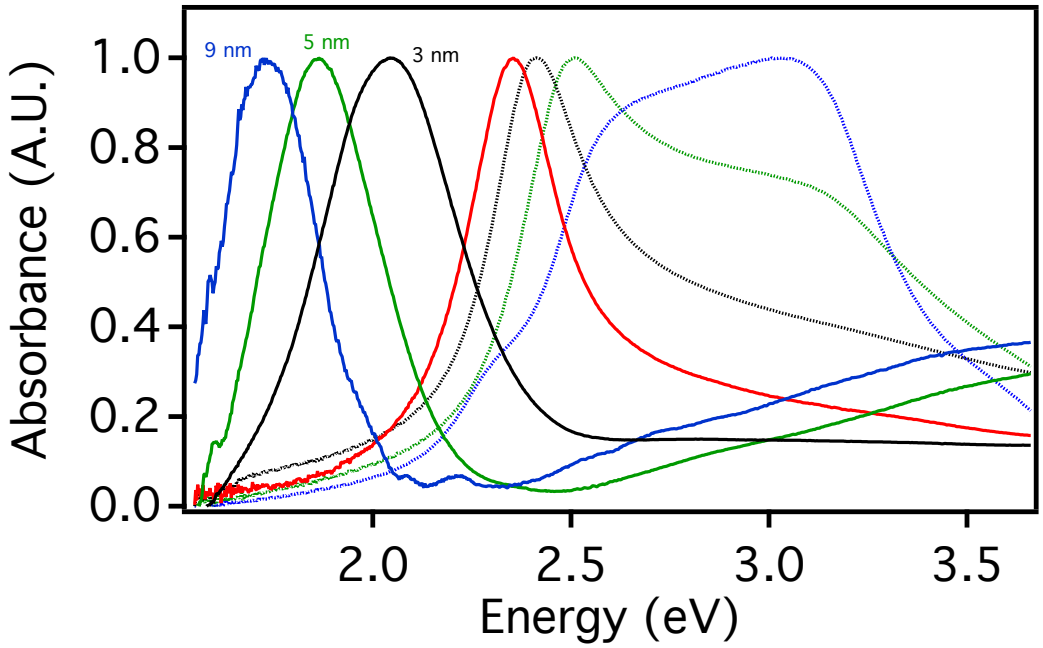

Figure 6.320. Absorption spectra of silver nanoparticles with a silver shell before (red) and after transformation into silver sulfide. The shells are varied from 5 nm (black), 10 nm (green) and 15 nm (blue). The dotted spectra are the respective silver shelled nanoparticles

The spectra in Figure 6.320 show a range of silver sulfide shells from 5 -15 nm. The plasmon resonance drastically red-shifts upon formation of the silver sulfide shell and elimination of the two plasmon peaks associated with the silver shell was also

observed. The plasmon peak red shifted due to the larger refractive index of silver sulfide and contribution from the semiconductor band gap of silver sulfide which lies around 1 eV. The amount of silver sulfide used was calculated based on the number of moles of silver present in the shell. An excess of 5 times the molar amount of silver is used to ensure complete conversion of all the silver. According to literature, the silver sulfide shell should be amorphous to promote the cation exchange for the final stage in the semiconductor shell formation. TEM is utilized to analyze the resultant physical and crystalline structure of the gold silver sulfide nanoparticles.

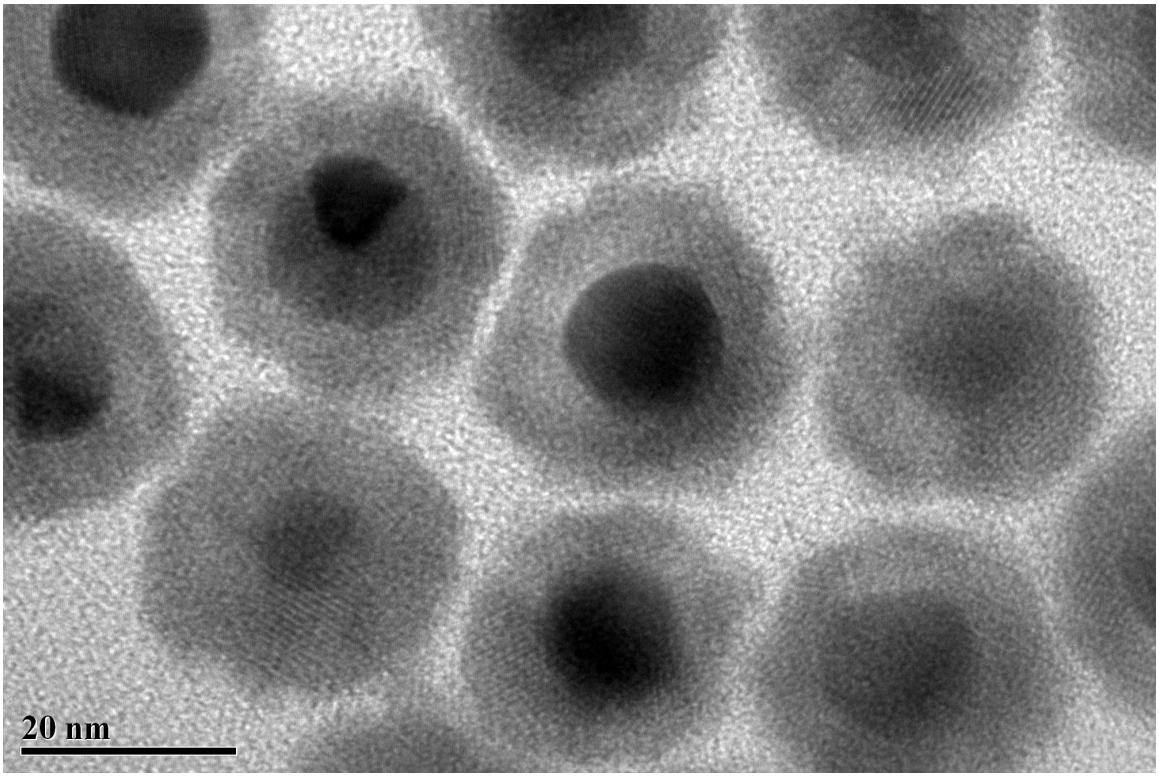

Figure 6.321. TEM images taken a 200 kV accelerating voltage. The theoretical shell radius is 5 nm and the experimentally measured radius is 6.3 nm.

The TEM images shown in Figure 6.321 were analyzed using ImageJ software to find the particles to be amorphous or polycrystalline, unlike the gold particles or the silver shell which were single crystalline In the majority of the nanoparticles, no crystal lattice fringes appeared, however, a few small regions of crystallinity were seen with spacing of 2.38 angstroms, which is consistent to the literature values for monoclinic silver sulfide.[145] In general the silver sulfide shell tends to be a little bit larger than the previous silver shells but very uniform and spherical with a standard deviation of 1.8 nm. The inner gold nanoparticles also retained their single crystallinity with spacing of 3.51 angstroms. This continued compression of the gold lattice supports the theory that increased stress from the shell is causing a compression of the gold particle.

These data showed success in the second step of the shell formation and the first half of the semiconductor shell. The silver sulfide shells tended to be slightly larger than the initial silver shells but very uniform. The nanoparticles were capped with oleylamine and oleic acid and remained stable in toluene for long periods of time. To ensure no excess sulfur remained in the solution, the nanoparticles were mixed with ethanol and centrifuged. The nanoparticle solution volume was kept at 10 mL or 20 mL for larger batches in order to ensure the nanoparticle concentration remained the same as the starting gold nanoparticles.

6.4: Cation Exchange for Production of CdS or ZnS Shells

The silver sulfide was subsequently converted to cadmium sulfide or zinc sulfide via the literature method.[141] The colloidal solutions in toluene were first heated to 50 or 65 degrees Celsius under nitrogen atmosphere, with the higher temperature being used for the zinc sulfide shells. Cadmium or zinc nitrate, in a 0.8 molar concentration in

methanol was added to the mixture in a molar amount equivalent to the moles of silver present in the shell. Once the colloidal solutions were mixed for 10 minutes, 0.2 to 1 mL of tributylphosphine was added to help the diffusion of metal ions to and from the shell. The shells were allowed to stir for 120 minutes for the cadmium shells and 20 hours for the zinc shells. The resulting nanoparticles were then washed with ethanol and centrifuged to isolate the nanoparticles. The nanoparticles were then dispersed into clean toluene, in the same volume as the previous silver sulfide shells.

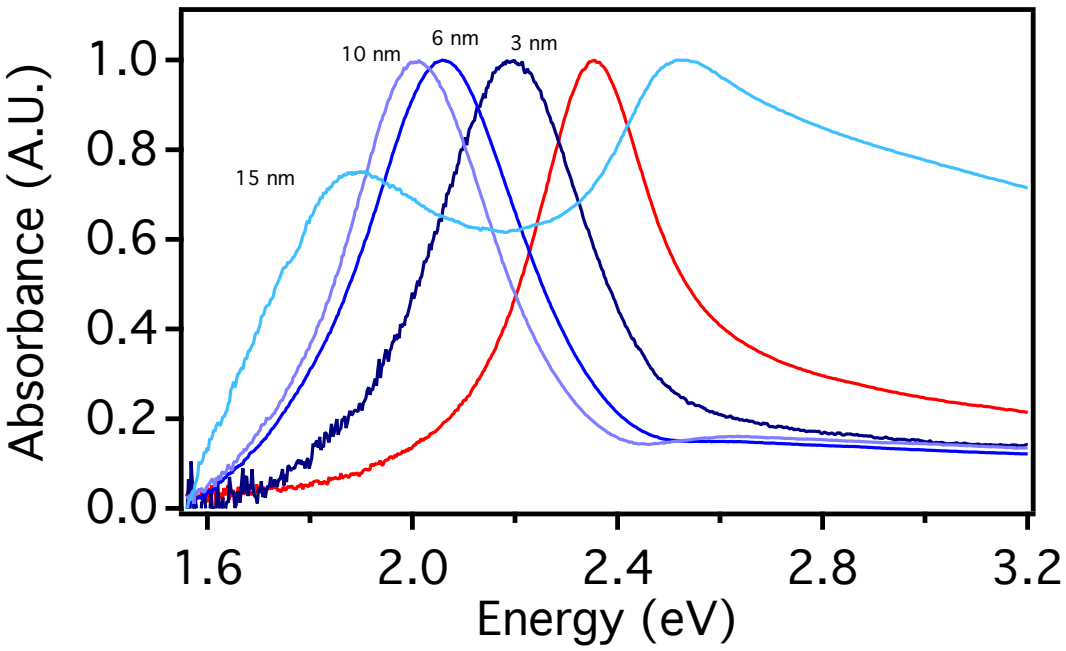

Figure 6.40. Normalized absorbance spectra of gold nanoparticles (red) and nanoparticles coated with varying thicknesses of CdS from 3 nm (dark blue) to 15 nm (light blue).

The absorbance spectra in Figure 6.40 show a distinct dependence of the plasmon resonance on the size of the CdS shell. Compared to the silver sulfide shell, the plasmon

was slightly blue-shifted for each nanoparticle samples. The plasmon resonance remained fairly narrow for all samples with only the 30 nm shell showing a slight broadening.

The 30 nm shell also showed a high energy absorption, indicative of CdS excitonic excitation. This feature was only present in the largest shells, most likely due to the much higher extinction coefficient of gold in comparison to the cadmium sulfide. The plasmon shift is due to the change in dielectric environment when the CdS is present on the surface. In general the spectra remained red-shifted to that of the original gold nanoparticles, with the larger shells having a lower plasmon resonance energy.

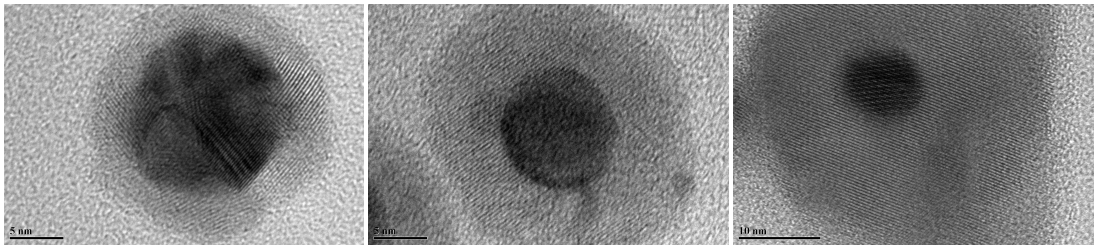

Figure 6.41. TEM images taken at 200 kV accelerating voltage. The nanoparticles have three different shell thicknesses, 4 nm radius (top), 7 nm radius (middle) and 15 nm radius (bottom).

The TEM images above show the tunability of the CdS shell deposition, with radii ranging from 4 to 15 nm. Analysis of the crystallinity shows a spacing of 6.00 angstroms on average, consistent with Zinc-Blende crystal structure.[146] The shells showed high monodispersity at each thickness and no aggregation of the nanoparticle was observed. A few nanoparticles showed a small spot where there seems to be a lack of shell coverage. This could be caused by an inability for the cation exchange to occur at that region due to the silver sulfide being crystalline in some regions as opposed to amorphous. The

nanoparticles were overall spherical in nature and no isolated regions of CdS quantum dots were observed. ZnS shells were also synthesized in a similar manner and analyzed to monitor both the shift in plasmon resonance and size.

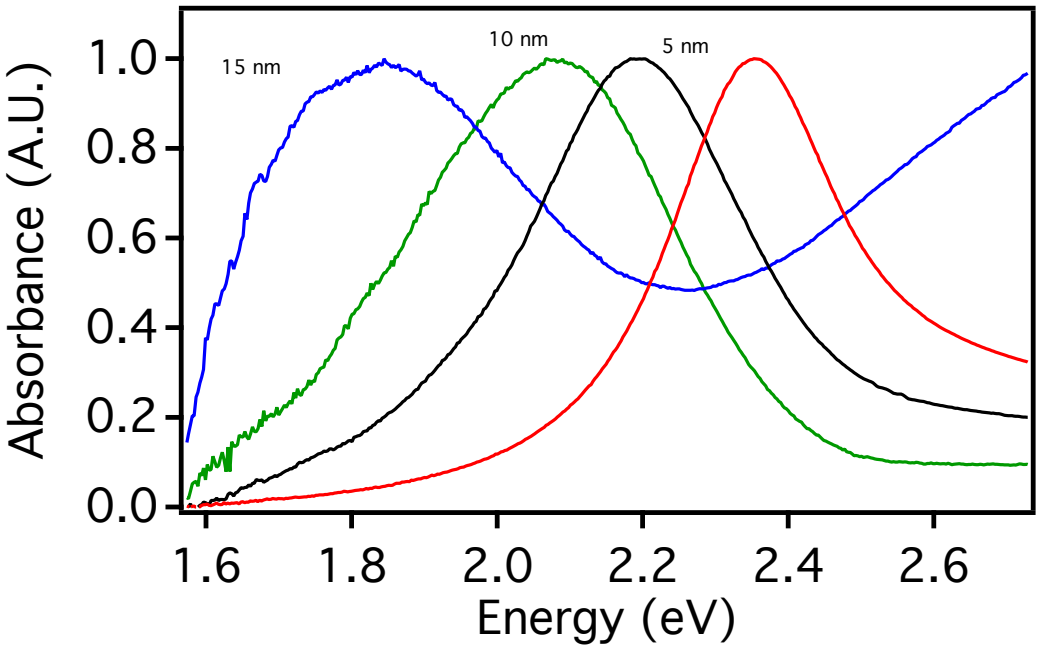

Figure 6.42. Normalized absorbance spectra of gold nanoparticles (red) and nanoparticles coated with varying thicknesses of ZnS from 5 nm (black) to 15 nm (blue).

The spectra in figure 25 show the ZnS shelled nanoparticles. Overall, the plasmon resonance was slightly blue-shifted for similar shell sizes, in comparison to the CdS samples. The spectra was also broadened slightly for each sample, with the thicker samples showing the more broadened spectra. The synthesis for the ZnS shells proved to produce less monodisperse samples, and the samples tend to form incomplete shells with more voids.

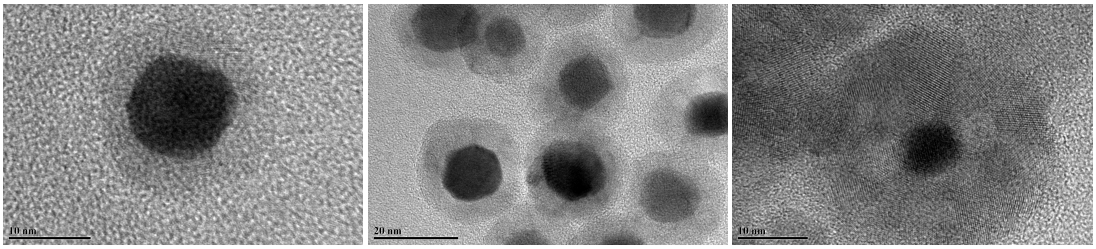

Figure 6.43. TEM images taken at 200 kV accerlating voltage. The nanoparticles have a 4.5 nm (left), 6.8 nm, and 13 nm shell thickness.

The ZnS shell analysis showed spacing of 5.31 angstroms on average, which is consistent with Zinc-Blende crystal structure.[146] The shells are uniform with an average radius of around 5 nm. The shells are much thinner than the CdS shells which is due to the lower amount of electrons in the lighter zinc when compared to cadmium and were more difficult to image. Inhomogenieties still occurred on a few particles which could be due to either pre-existing defects in the silver sulfide shell or the longer reaction time and higher temperatures required for the ZnS cation exchange reaction.

6.5: TEM analysis of CdS and ZnS Shells

TEM was utilized to physically characterize the hybrid semiconductor shells. The shells were measure by measuring the distance from the outer edge of the gold nanoparticle to the outside of the semiconductor shell. The shells were not perfectly symmetrical, therefore the average of ten different measurements was used as the effective shell size for each sample. The measurements were conducted using the ImageJ software program. The scale bar taken from the TEM images was used as to calibrate the measurements. The samples were separated into cadmium sulfide and zinc sulfide shells and then arranged into three different regimes, thin, medium and thick. Thin shells were

defined as one to four nm in shell radius, medium was defined as four-eight nm in radius and thick was defined as being greater than eight nm in radius.

6.5.1: Thin CdS Shells

The thin CdS shells were synthesized using slightly lower concentration for all the precurors. The silver stock solution utilized for these shells was 4 millimolar and the cadmium nitrate solution utilized was 0.4 molar. The samples were highly soluble in organic solvents, therefore purification was more difficult and sometimes required larger volumes of ethanol. This large volume of ethanol, at time, produced irreversible sample aggregation. The samples were estimated to have the same stock concentration of 5 micromolar as the stock CTAC-coated gold nanoparticles.

No isolated CdS nanoparticles were observed in the TEM images. The nanoparticles also didn't appear to be significantly aggregated in this size regime. The shells were slightly red-shifted compared to that of the original gold nanoparticles as shown in section 6.4. The samples shown in this section demonstrate the lowest size limit of this hybrid nanoparticle synthesis.

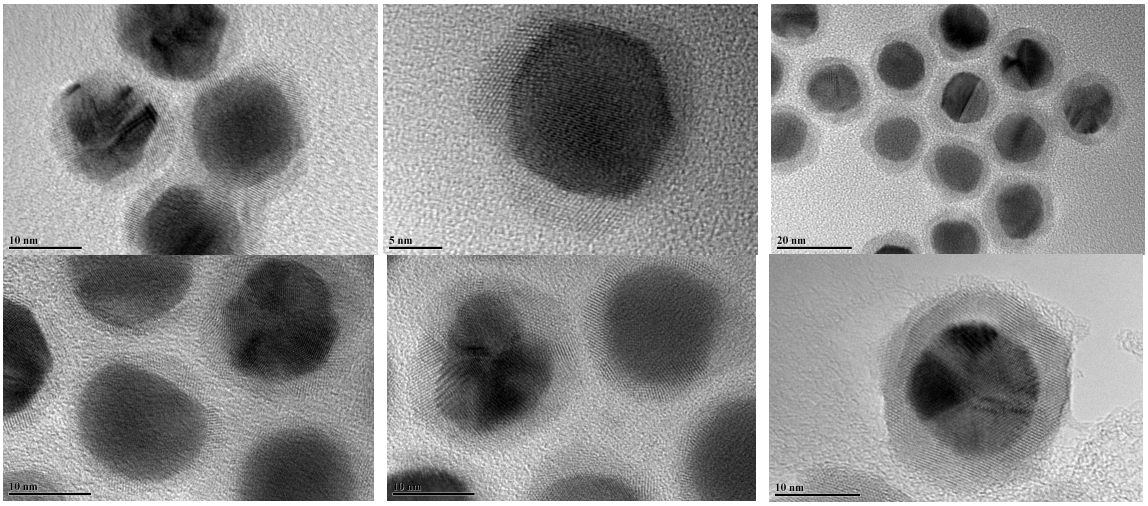

Figure 6.5.1: TEM images of six different, thin cadmium sulfide-shelled gold nanoparticles. The samples are numbered 1-3 from left to right on the top and 4-6 from left to right on the bottom. The images were taken at various magnifications under 200 kV accelerating voltage.

Sample #	Shell Thickness (nm)	Standard Deviation (nm)
1	2.55	0.57
2	2.55	0.57
3	3.8	0.63
4	1.9	0.60
5	2.8	0.63
6	3.6	1.3

Table 6.5.1: Summary of thin cadmium sulfide shell radii and standard deviations.

Six different CdS shells were measured and displayed in this section and summarized in a series of TEM images in Figure 6.5.1 and Table 6.5.1. The shells were fairly uniform with standard deviations between 0.5 and 0.7 nm. The thin shells measured in radius from the smallest sample at 1.9 nm on average to the largest being 3.8 nm on average. Within the limits of the standard deviation, the thin CdS shells could be

synthesized with diameters ranging from around 1 nm in radius to almost 5 nm in radius. The nominal size for these samples was usually 3-5 nm. It should be noted that the resultant samples sizes tend to be slightly smaller upon TEM analysis.

6.5.2: Medium CdS Shells

The medium CdS shells were synthesized using an 8 millimolar silver nitrate solution during the silver deposition and an 0.8 molar cadmium nitrate solution for the cadmium cationic exchange reaction. The samples were highly soluble in organic solvents, and purification was much easier than for the smaller shell sizes. The samples readily pelleted out of solution with addition of 1.5 times the solvent ration of ethanol, most likely due to the larger size and weight of the nanoparticles. The samples were estimated to have the same stock concentration of 5 micromolar as the stock CTAC-coated gold nanoparticles.

No isolated CdS nanoparticles were observed in the TEM images. The nanoparticles also didn't appear to be significantly aggregated in this size regime. The shells were much more significantly red-shifted compared to that of the original gold nanoparticles as shown in section 6.4. The samples shown in this section demonstrate the median and most common size limit of this hybrid nanoparticle synthesis.

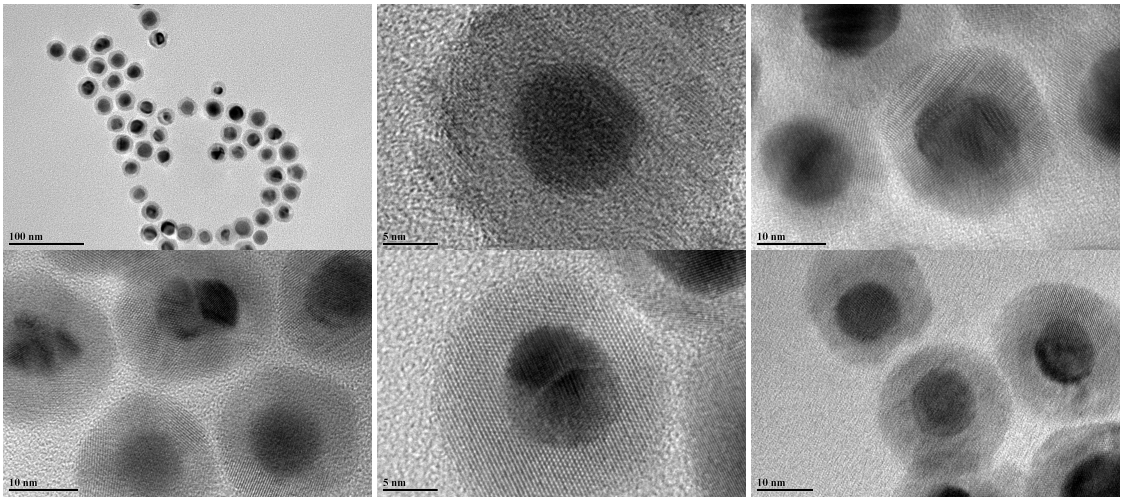

Figure 6.5.2: TEM images of different, medium cadmium sulfide-shelled gold nanoparticles. The samples are numbered 1-3 from left to right on the top and 4-5 from left to right on the bottom. The images were taken at various magnifications under 200 kV accelerating voltage.

Sample number	Shell Thickness (nm)	Standard Deviation (nm)
1	7.4	1.3
2	6.7	1.3
3	5.6	0.75
4	5.1	0.60
5	5.1	0.86
6	6.5	1.1

Table 6.5.2: Summary of medium cadmium sulfide shell radii and standard deviations.

Six different CdS shells were measured and displayed in this section and summarized in a series of TEM images in Figure 6.5.2 and Table 6.5.2. The shells were uniform with standard deviations between 0.60 and 1.3 nm, slightly larger than were observed for the thin shells. The medium shells measured in radius from the smallest sample at 5.1 nm on average to the largest being 7.4 nm on average. Within the limits of

the standard deviation, the medium CdS shells could be synthesized with diameters ranging from around 4.5 nm in radius to almost 9 nm in radius. The nominal size for these samples was usually 5-10 nm. It should be noted that the resultant samples sizes tend to be slightly smaller upon TEM analysis.

6.5.3: Thick CdS Shells

The thick CdS shells were synthesized using an 16 millimolar silver nitrate solution for the silver deposition and an 0.8 molar cadmium nitrate solution for the cadmium cation exchange reaction. The samples readily pelleted out of solution with addition of 1.5 times the solvent ration of ethanol, most likely due to the larger size and weight of the nanoparticles. The samples were estimated to have the same stock concentration of 5 micromolar as the stock CTAC-coated gold nanoparticles. The thicker shells were much more soluble and remained soluble for longer periods of time than the smaller shells. This could be due to the larger amounts of oleylamine needed to synthesize these shells.

No isolated CdS nanoparticles were observed in the TEM images. The nanoparticles also didn't appear to be significantly aggregated in this size regime. The shells were much more significantly red-shifted compared to that of the original gold nanoparticles as shown in section 6.4, and in some cases should a higher energy absorption band, indicative excitonic absorption of cadmium sulfide. The samples shown in this section demonstrate the highest size limit of this hybrid nanoparticle synthesis.

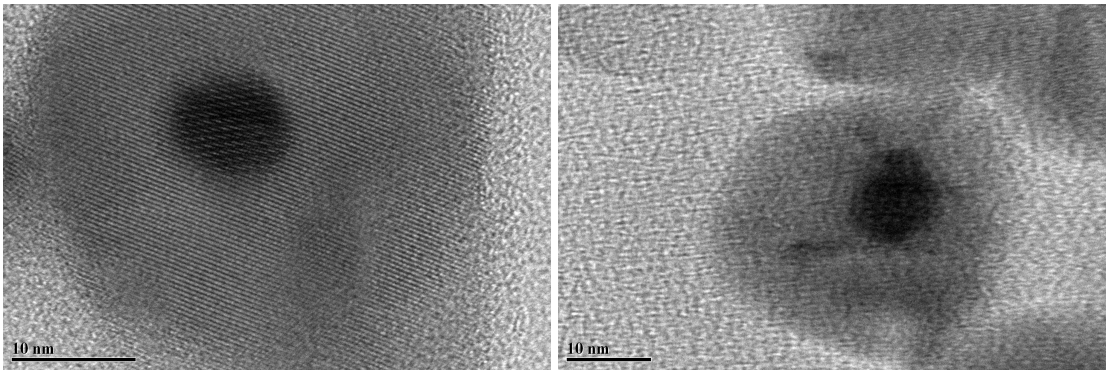

Figure 6.5.3: TEM images of two different, thick cadmium sulfide-shelled gold nanoparticles. The samples are numbered 1-2 from left to right. The images were taken at various magnifications under 200 kV accelerating voltage.

Sample Number	Shell Thickness (nm)	Standard Deviation (nm)
1	14.8	2.0
2	11.1	2.8

Table 6.5.3: Summary of thick cadmium sulfide shell radii and standard deviations.

Two different CdS shells were measured and displayed in this section and summarized in a series of TEM images in Figure 6.5.3 and Table 6.5.3. The shell deviation was observed to correlate directly with shell size. The thick shells showed significantly higher deviations of around 2.0 nm. The thick shells measured in radius from the smallest sample at 11.1 nm on average to the largest being 14.8 nm on average. Within the limits of the standard deviation, the medium CdS shells could be synthesized with diameters ranging from around 9 nm in radius to almost 15 nm in radius. The nominal size for these samples was anywhere between 15-30 nm. The measured TEM sizes varied much more dramatically from the nominal shell size than for the smaller shells.

6.5.4: Thin ZnS Shells

The thin ZnS shells were synthesized using the lower concentration for all the precursors. The silver stock solution utilized for the silver deposition was 4 millimolar and an 0.4 molar zinc nitrate solution was used for the zinc cation exchange. The samples were highly soluble in organic solvents, therefore purification was more difficult and sometimes required larger volumes of ethanol. This large volume of ethanol, at time, produced irreversible sample aggregation. The samples were estimated to have the same stock concentration of 5 micromolar as the stock CTAC-coated gold nanoparticles.

The ZnS shells were proved more difficult and often resulted in impurities formed in the samples. No isolated ZnS nanoparticles were observed in the TEM images but in others, some isolated regions of indentified products were formed. The nanoparticles were somewhat aggregated, in some samples but overall remained separated. The shells were slightly red-shifted compared to that of the original gold nanoparticles as shown in section 6.4 bu also blue-shifted and broadened with respect to the thin CdS shells. The samples shown in this section demonstrate the lowest size limit of this hybrid nanoparticle synthesis.

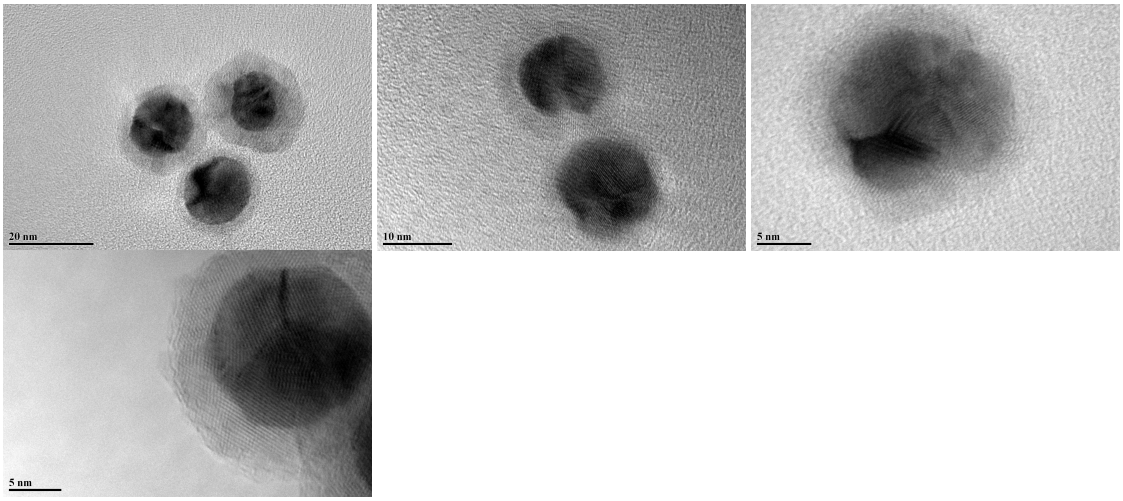

Figure 6.5.4: TEM images of four different, thin zinc sulfide-shelled gold nanoparticles. The samples are numbered 1-3 from left to right on the top and 4 on the bottom. The images were taken at various magnifications under 200 kV accelerating voltage.

Sample Number	Shell Thickness (nm)	Standard Deviation (nm)
1	3.6	1.0
2	2.6	0.66
3	2.3	0.28
4	3.7	0.50

Table 6.5.4: Summary of thin zinc sulfide shell radii and standard deviations.

Four different ZnS shells were measured and displayed in this section and summarized in a series of TEM images in Figure 6.5.4 and Table 6.5.4. The shells showed larger standard deviations than the zinc sulfide shells between 0.28 to 1.0. The thin shells measured in radius from the smallest sample at 2.3 nm on average to the largest being 3.7 nm on average. Within the limits of the standard deviation, the thin CdS shells could be synthesized with diameters ranging from around 1.5 nm in radius to almost 4.5 nm in radius. The nominal size for these samples was usually 3-5 nm. It

should be noted that the resultant samples sizes tend to be slightly smaller upon TEM analysis.

6.5.6: Medium ZnS Shells

The medium ZnS shells were synthesized using an 8 millimolar of silver nitrate for the silver depostion and an 0.8 molar zinc nitrate solution for the zinc cation exchange. The samples were highly soluble in organic solvents, and purification was much easier than for the smaller shell sizes. The samples showed uniformity mirroring that of the medium ZnS- shelled samples and minimal impurities were observed. The samples were estimated to have the same stock concentration of 5 micromolar as the stock CTAC-coated gold nanoparticles.

No isolated CdS nanoparticles were observed in the TEM images. The nanoparticles also didn't appear to be significantly aggregated in this size regime. The shells were much more significantly red-shifted compared to that of the original gold nanoparticles as shown in section 6.4 but still blue-shifted compared to the same ZnS shell size. The samples shown in this section demonstrate the median and most common size limit of this hybrid nanoparticle synthesis.

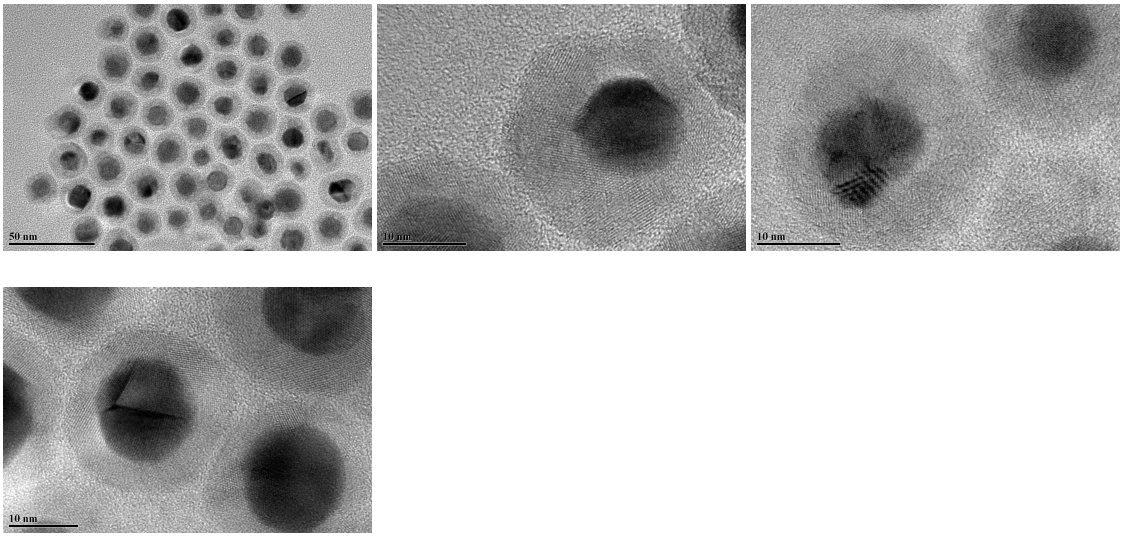

Figure 6.5.5: TEM images of four different, medium zinc sulfide-shelled gold nanoparticles. The samples are numbered 1-3 from left to right on the top and 4 on the bottom. The images were taken at various magnifications under 200 kV accelerating voltage.

Sample Number	Shell Thickness (nm)	Standard Deviation (nm)
1	6.0	1.1
2	6.5	1.6
3	7.0	1.6
4	5.1	0.87

Table 6.5.5: Summary of medium zinc sulfide shell radii and standard deviations.

Four different ZnS shells were measured and displayed in this section and summarized in a series of TEM images in Figure 6.5.5 and Table 6.5.5. The shells showed standard deviations on par with that of the same sized ZnS shells. The medium ZnS shells also measured very similarly to the ZnS shells with radii ranging from 5.1 nm on average to the largest being 7. nm on average. Within the limits of the standard deviation, the medium ZnS shells could be synthesized with diameters ranging from

around 4.3 nm in radius to almost 9 nm in radius. The nominal size for these samples was usually 5-10 nm. It should be noted that the resultant samples sizes tend to be slightly smaller upon TEM analysis.

6.5.6: Thick ZnS Shells

The thick ZnS shells were synthesized using an 16 millimolar silver nitrate solution for the silver deposition and an 0.8 molar zinc nitrate solution for the zinc cation exchange. The samples readily pelleted out of solution with addition of 1.5 times the solvent ration of ethanol, most likely due to the larger size and weight of the nanoparticles. The samples were estimated to have the same stock concentration of 5 micromolar as the stock CTAC-coated gold nanoparticles. The thicker ZnS shells were highly crystalline with roughly spherical shapes.

No isolated ZnS nanoparticles were observed in the TEM images. The nanoparticles also didn't appear to be significantly aggregated in this size regime. The shells were much more significantly red-shifted compared to that of the original gold nanoparticles as shown in section 6.4 and substantially broadened spectrally. The spectra also showed no evidence of zinc sulfide excitonic absorption, most likely due to the much higher band gap energy of zinc sulfide. The samples shown in this section demonstrate the highest size limit of this hybrid nanoparticle synthesis.

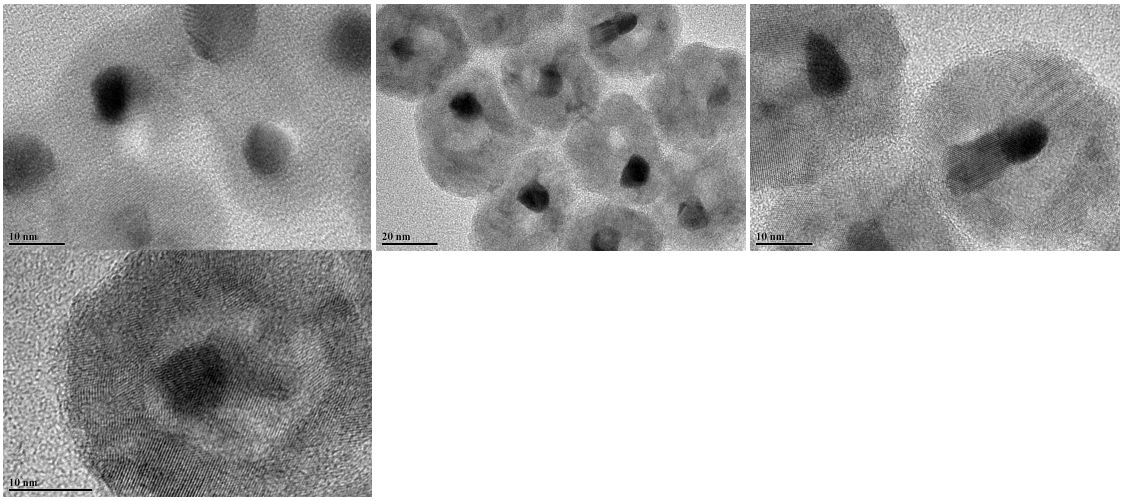

Figure 6.5.6: TEM images of four different, thick zinc sulfide-shelled gold nanoparticles. The samples are numbered 1-3 from left to right on the top and 4 on the bottom. The images were taken at various magnifications under 200 kV accelerating voltage.

Sample Number	Shell Thickness (nm)	Standard Deviation (nm)
1	9.0	2.1
2	14.6	4.4
3	12.2	2.1
4	12.6	3.1

Table 6.5.6: Summary of thick zinc sulfide shell radii and standard deviations.

Four different ZnS shells were measured and displayed in this section and summarized in a series of TEM images in Figure 6.5.6 and Table 6.5.6. The shell deviation was observed to correlate directly with shell size. The large ZnS shells showed the largest deviation of any sample, with the highest being greater than 3 nm. These sample discrepancies stem from the lower reactivity of the ZnS reaction and the higher sample temperature. The thick shells measured in radius from the smallest sample at 9.0 nm on average to the largest being 14.6 nm on average. Within the limits of the standard deviation, the medium ZnS shells could be synthesized with diameters ranging from

around 7 nm in radius to exactly 15 nm in radius. The nominal size for these samples was anywhere between 15-30 nm. The measured TEM sizes varied much more dramatically from the nominal shell size than for the smaller shells.

6.6 Concluding Remarks on Synthesis of CdS and ZnS Shells

Semiconductor shells of CdS or ZnS were possible through a cation exchange with silver sulfide shells. First, gold nanoparticles, coated in CTAC, had silver shells deposited. The silver shells could be deposited with nanometer precision from 2 nanometers to 30 nanometers. The silver shell can be resolved via UV-vis absorption and blue-shift the plasmon resonance of the gold nanoparticles to around 3.0 eV. TEM microscopy, also, reveals a crystalline silver shell.

The shell was then converted to silver sulfide with addition of elemental sulfur, which were then capped with oleic acid and oleylamine. The silver sulfide shells were polycrystalline or amorphous, through analysis with TEM. The silver sulfide shells red-shifted plasmon resonance in comparison to the silver shells, with a maximum around 1.0 eV.

These shells were then be treated with cadmium or zinc ions in the presence of tributyl phosphine to form the final CdS or ZnS shells, capped with oleylamine. These shells were single crystalline and mirrored the thickness of the silver-shelled gold nanoparticles. The UV-vis spectra showed a slight blue-shift from the silver sulfide-shelled nanoparticles after the cation exchange to produce the semiconductor shells. The ZnS shells were also more blue-shifted in comparison to the CdS shells.

The TEM data showed the physical discrepancies between the shells size and composition. The Zinc sulfide shells were overall less homogenous than were the CdS

shells of the same size. The samples remained crystalline with a higher concentration of defects and impurities in the larger CdS shells and thinner ZnS shells. The samples could overall be made with sizes from 1 nm in radius to 15 nm in radius.

These methods show the production of hybrid gold nanoparticles with size and composition- tunable semiconductor shells around gold nanoparticles. The gold nanoparticles were highly uniform which produced a very narrow plasmon resonance upon formation of the semiconductor shell. These shells are the plasmonic platform with a tunable dielectric spacer. The spacer is homogenous throughout the colloidal solution and stable in organic solvents such as toluene or hexanes. The shells will be linked to chromophores to study the coupling effects and distance-dependence of those effects.

CHAPTER 7: QUANTUM DOT COUPLING

7.1 Introduction

The aim of the quantum dot coupling was to monitor the effect of the plasmon coupling on the emission rate of the quantum dots. Quantum dot emission is bright and can be tuned to produce narrow line-widths at specific wavelengths. Inhomogeneities present in synthesized quantum dots can produce nonradiative mechanisms which will result in decreased ensemble fluorescence. Plasmonic coupling would be a viable solution to counteracting this negative effect. Plasmonic enhancement of quantum dot emission rates could eliminate the need for complex architectures aimed at improving the quantum dot fluorescence.

The plasmon electric field extends a finite distance away from the gold nanoparticle, therefore if the quantum dots are too distant, the field cannot be utilized. In order to take advantage of fluorescence coupling, the distance needed to be carefully controlled. To study the optimal distance needed to maximize enhancements, quantum dots were bound to the surface of hybrid gold nanoparticles with varying shell thicknesses. Coupling of the two nanoparticles in colloidal systems needed to be selective and reproducible in order to elucidate effective data on the plasmonic interaction. To bind quantum dots to the core shell nanoparticle surface, both surfaces were first activated.

The 1-ethyl-3- (dimetyhlaminopropyl) carbodiimide, or EDC, coupling mechanism shown in Figure 7.10 was utilized to accomplish this task, with nanoparticle 1 being the core shell particles and nanoparticle 2 being the quantum dots.

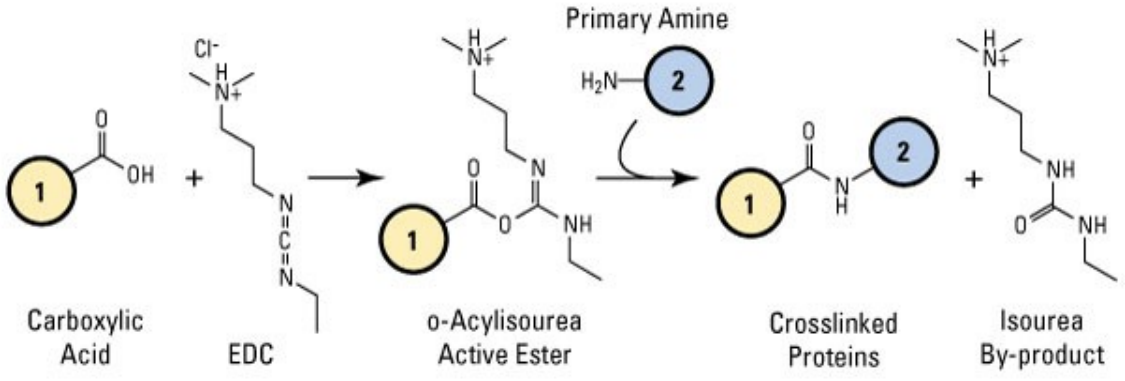

Figure 7.10. Scheme of the EDC coupling technique, used to link quantum dots to the hybrid nanoparticle surface. Particle 1 was the hybrid gold nanoparticles and particle 2 was the quantum dots.[147]

The EDC coupling mechanism is an effective way to cross-couple carboxylic acid and amine functional groups and was used two bind the two nanoparticles together. The core shell nanoparticles were first coated with 11-mercaptoundecanoic acid (MUA) to produce an outer carboxylic acid surface. Treatment with EDC and N-hydroxysuccimide (NHS) produced stable NHS- ester functionalized particles which were then reacted with amine coated quantum dots for binding to produce and amide bond between the two nanoparticles. A ligand exchange of the quantum dots from octadecylamine to hexamethylene diamine resulted in amine-terminated quantum dots for the amidation. FTIR was used to monitor the ligand exchanges as the two nanoparticles were coupled.

TEM was used to both confirm binding and measure the separation distance of the quantum dots from the metal surface.

UV-vis absorption and steady-state fluorescence were used to monitor changes in the spectra and to calculate changes in the fluorescence quantum yield upon binding to the nanoparticles. Fluorescence decays were collected using time-resolved fluorescence, in order to calculate the average lifetime of the fluorescence. These data were combined to calculate and compare the radiative before and after binding.

7.2: Quantum Dot Synthesis and Analysis

In a 250 mL 3-neck round bottom flask, 10 g hexadecylamine, 11 g trioctylphosphine oxide and 5.0 mL trioctylphospine were mixed and heated to 120 ^{0}C, under vacuum for 2 hours to eliminate free oxygen and water from the system. The flask was then heated to 300 ^{0}C under a nitrogen atmosphere, while a separate precursor flask was prepared containing 1.2 g of 1, 2 hexadecane diol, 0.64 g cadmium acetylacetonoate and 10 mL trioctylphosphine. The precursor flask was then heated to 100 ^{0}C under vacuum. The precursor flask was then cooled to 80 ^{0}C under nitrogen atmosphere. Once at 80 ^{0}C, 6.0 mL of 1.0 M solution of trioctylphosphine:Se complex was then added to the flask and stirred vigorously for less than one minute. The entire precursor solution was injected into the flask at 300 ^{0}C and allowed to stir at 280 ^{0}C for 2-3 minutes before being cooled to room temperature with a nitrogen stream. The solution was then washed with copious acetone and centrifuged at 6,500 RPM 10 minutes. The supernatant was decanted from the quantum dots which were stored dry for further use.

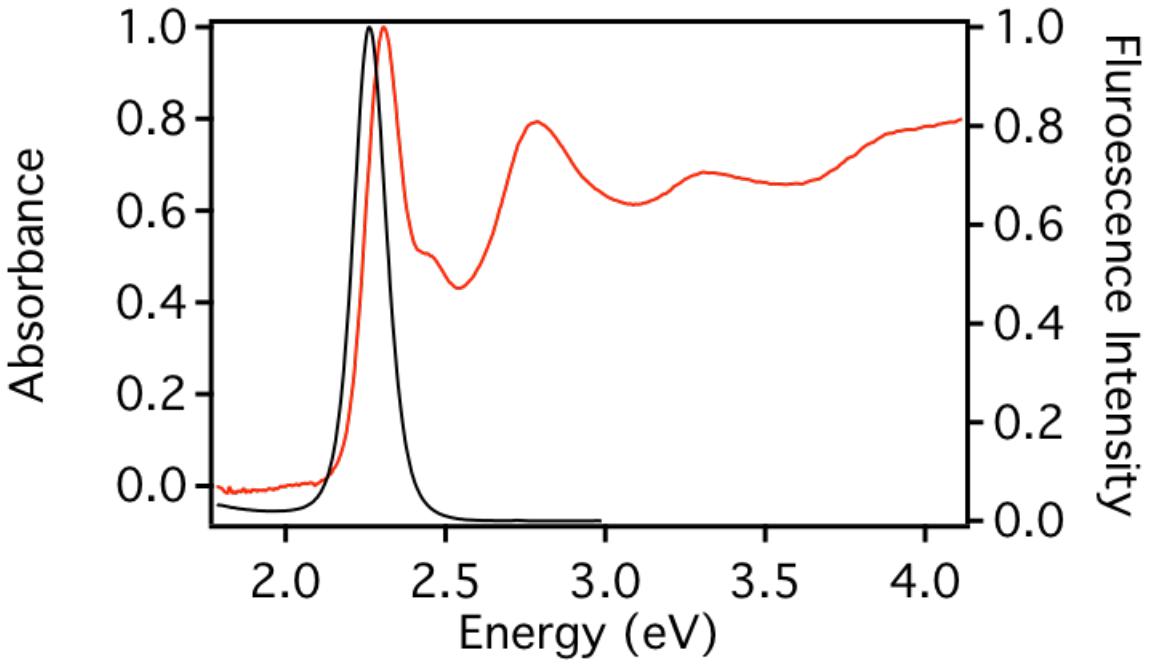

Figure 7.20. UV-vis Absorption Spectra (red) of CdSe quantum dots in hexanes and Fluroescence spectra of the same quantum dots at 400 nm excitation (black).

The absorption spectra in Figure 7.20 shows a sharp absorption maxima, centered around 2.4 eV, indicative of the ground-state excitonic transition. The peaks at higher energy corresponding to higher order transitions of the quantum dots. The spectrum in black is the fluorescence spectra of the same quantum dots at 400 nm excitation. The fluorescence is very sharp, and red-shifted from the absorption maxima, to about 2.2 eV.

In order to quantify intensity changes, the quantum yield was calculated, using equation (23) below, where PL is the fluorescence area of the sample, PL_{dye} is the fluorescence area of rhodamine in methanol, abs is the absorbance calculated at 400 nm, abs_{dye} is the absorbance calculated at 400 nm for rhodamine in methanol and RI is the refractive index of the solvent used for either the dye or sample. The quantum yield calculated from the spectra of core CdSe quantum dots averaged around 10 to 20. These

quantum dots were analyzed next with TEM to physically characterize their size and shape.

$$QY = \frac{PL}{PL_{dye}} * \frac{abs_{dye}}{abs} * \frac{RI^2}{RI_{dye}^2} * 0.95 \quad (23)$$

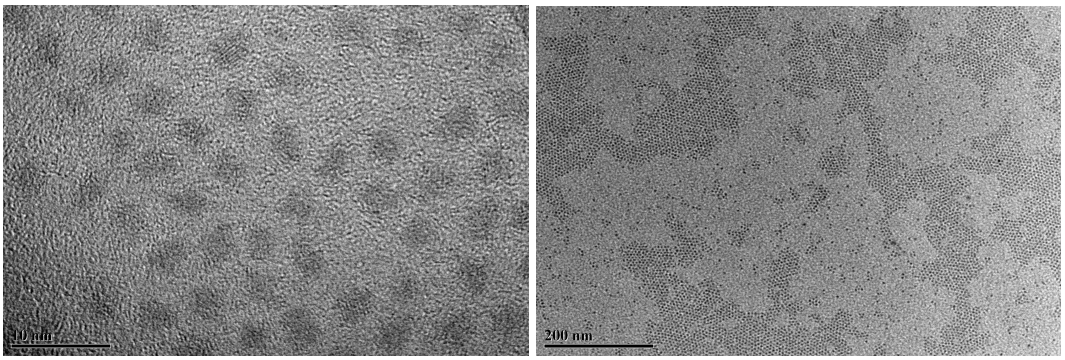

Figure 7.21. TEM images of CdSe quantum dots taken at 200 kV accelerating voltage.

TEM grids were prepared from a dilute solution of quantum dots in hexanes.One drop of the solution was placed onto a TEM grid, which was placed in the vacuum oven for at least 24 hours. The quantum dot TEM images shown in Figure 7.21 were analyzed using the ImageJ software. The quantum dots were found to be, roughly spherical with an average diameter of 3.4 nm and a standard deviation of 0.4 nm. These quantum dots were then coated with a shell of CdS to aid in protection of the nanoparticle surface.

7.2.1: Coating of Cadmium Sulfide Shells onto Cadmium Selenide Quantum Dots

CdS shells were used to protect the core quantum dots and further red shift the fluorescence. CdS was applied 1 monolayer at a time. To coat the CdSe quantum dots with CdS first ,a 0.1 M cadmium oleate solution was made, by dissolving 2.1 g CdO, 15.1 g oleic acid and 140 mL octadecene. The solution was heated to 120 ^{0}C under vacuum for

1 hour. Nitrogen atmosphere was then applied to the flask which is then heated (250 ^{0}C) until the solution turns pale yellow and homogenous. The solution was cooled to 100 ^{0}C and kept under vacuum overnight. To make a 0.1 M Sulfur solution, 32.06 g sulfur powder was added to 100 mL of octadecene. The solution was heated, under vacuum, until a pale yellow or colorless solution was formed (150^{0}C). The solutions were allowed to cool to room temperature and kept under nitrogen atmosphere. The flasks were then placed under vacuum at 100 ^{0}C for 1 hour and switched to nitrogen atmosphere before use.

The amount of precursor solution for each monolayer was first calculated assuming spherical particles and a CdS monomer radius of 0.35 nm. The calculations also assume that one monolayer increases the nanoparticle radius by the same amount. The shell deposition was halted after 8 complete monolayers, which should increase the diameter of the nanoparticles by around 5 nm. This provided significant passivation of the surface while, keeping the quantum dot size less than 10 nm in diameter.

Core CdSe quantum dots were mixed with octadecylamine and oleic acid and heated to 100 ^{0}C under vacuum to remove oxygen and water. The flask was then heated to 230 ^{0}C under nitrogen for shell growth. For the first 3 monolayers, the precursors are added a quarter of the necessary volume at a time with 15 minutes in between each injection with the sulfur injection preceding the cadmium. The heat was then increased to 240 ^{0}C for further shell growth and the injections were increased to one half a monolayer at a time. Once the last addition was complete, the nanoparticles were stirred at 240 ^{0}C 30 minutes before being cooled to 70 ^{0}C under nitrogen. The flask was allowed to stir overnight before purification. For purification, the solution was washed with copious

acetone and centrifuged at 6,500 RPM 10 minutes. The nanoparticles were stored dry for further use.

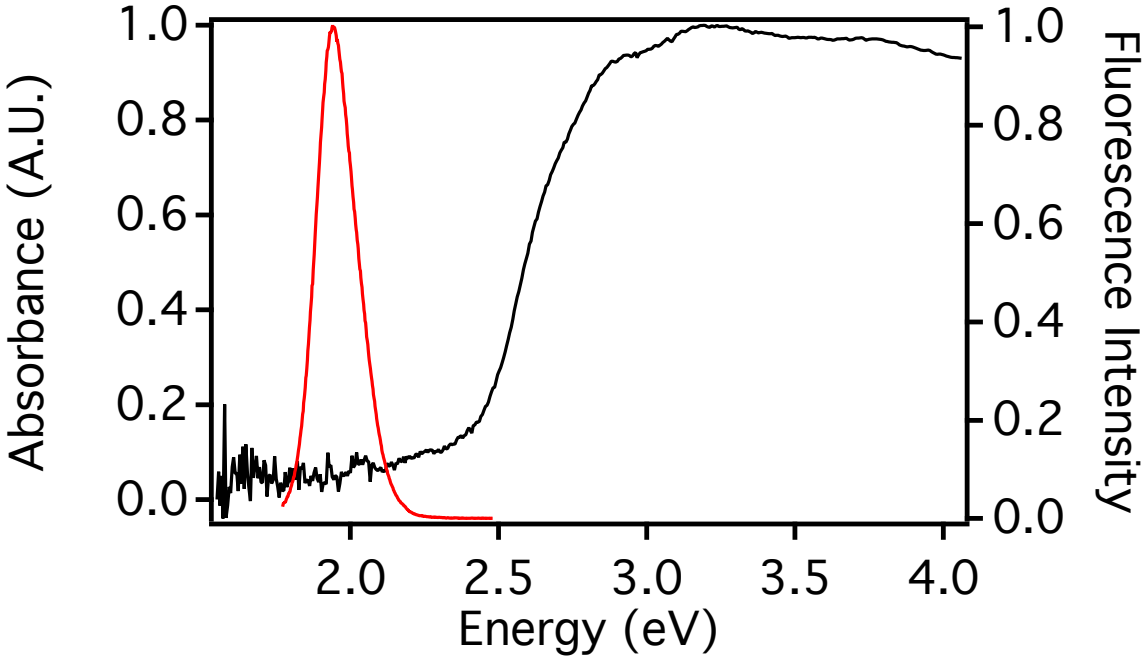

Figure 7.210 UV-vis Absorption Spectra (black) of CdSe quantum dots coated with 8 monolayers of CdS, in hexanes. The fluorescence spectra of the same quantum dots at 400 nm excitation (black).

The spectra in Figure 7.210 is significantly different to that of the core CdSe quantum dots. The UV-vis absorption spectra in black show a change from the sharp absorption features seen with the core CdSe to a much broader absorption with a sharp increase around 2.5 eV. This broadening is due to the delocalization of the exciton into the CdS shell. The CdS band gap, which is around 2.4 eV is much higher energy than the band gap of CdSe around 1.74 eV. This band gap difference is the cause of the blue-shift in the absorption onset of the CdS coated quantum dots. The fluorescence spectrum, in red, is

also red-shifted compared to the CdSe fluorescence by about 200 meV, due to delocalization of the exciton into the CdS shell. The quantum yield of these samples also increases to an average of 30-50%.

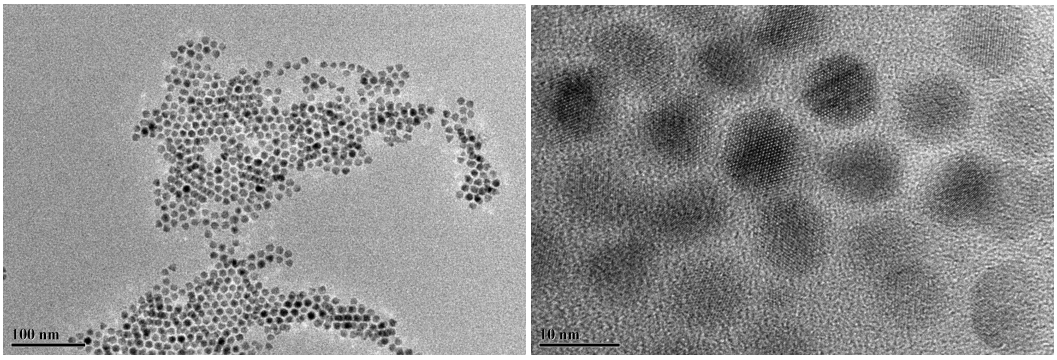

Figure 7.211: TEM images of CdSe quantum dots coated with 8 monolayers of CdS. The images are taken at 200 kV accelerating voltage.

The TEM images in Figure 7.211 show the quantum dots after shell deposition. The quantum dots increase in diameter to 9.3 nm with a much smaller standard deviation of .03 nm. The quantum dots remain spherical in shape and no contrast is observed between the core and shell. The lack of contrast is due to the relatively small lattice mismatch between core and shell and the large size difference between the 3 nm core and 5 nm shell.

7.3 Ligand Exchange to Hexanemethylenediamine and Characterization

Stock core/shell quantum dots dispersed into hexanes were washed with acetone and centrifuged at 6,500 RPM for 10 minutes. The nanoparticles were redispersed into dichloromethane and added to a solution containing hexamethylene diamine in a 10 times molar excess to the quantum dots. The solution was stirred overnight at 40^0C with a

nitrogen atmosphere. The quantum dots were washed with ethanol and centrifuged to pellet the nanoparticles. The nanoparticles were stored dry and redispersed into clean dichloromethane before use.

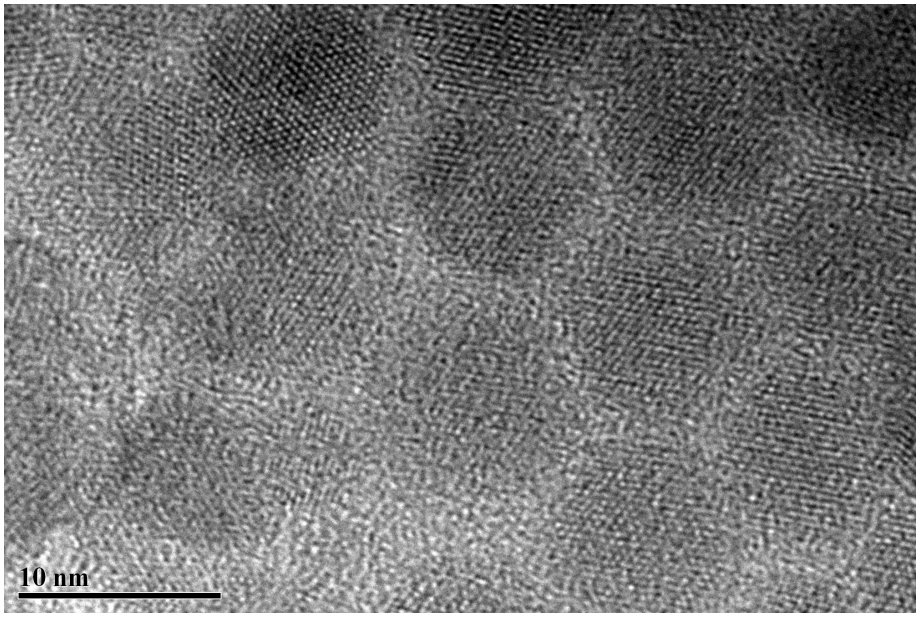

Figure 7.30: TEM taken at 200 kV accelerating voltage. The quantum dots utilized here are purified after the hexamethylene diamine ligand exchange.

The TEM images of the quantum dots, post-diamine ligand exchange are shown in Figure 7.30. The quantum dots, with some slight size variation were 8-10 nm in diameter and roughly spherical in shape. Aggregation was observed in some areas but overall, the nanoparticles were evenly dispersed. The quantum dots were stored dried before being weighed and dissolved into the appropriate solvent.

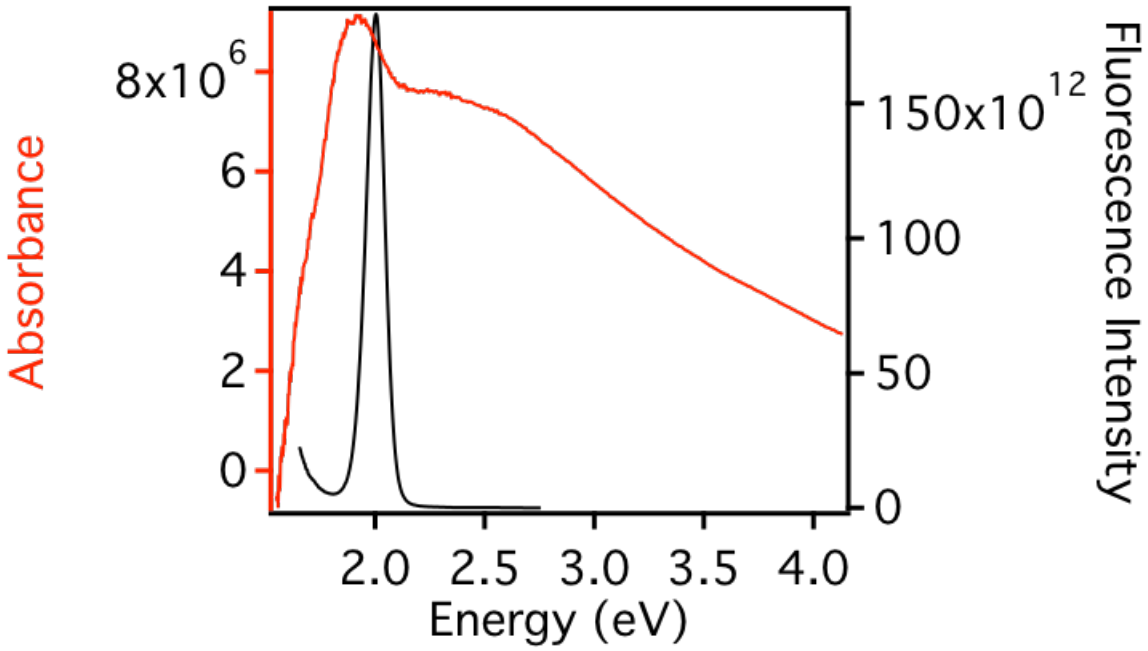

Figure 7.31: UV-vis and fluorescence spectra of quantum dots after hexane diamine ligand exchange.

The UV-vis absorption and fluorescence line shape spectra for the quantum dots in dichloromethane are shown in Figure 7.31. The UV-vis shows a sharp increase around 2.0 eV and an excitonic absorption band centered around 2.5 eV. Otherwise there are no dominant features in the absorption spectra for the quantum dots. The fluorescence was very narrow and centered at 2.0 eV. A rise begins to form around 1.5 eV in the fluorescence spectra due to the second order excitation of the lamp source.

The stock CdSe quantum dots, shelled with 8 monolayers of cadmium sulfide and capped with octadecylamine and oleic acid had an average quantum yield, in hexanes of 60%. Post ligand exchange with hexamethylene diamine, the quantum yield drops to 40-30% on average, which could be due to a higher degree of aggregation and solvent exchange to higher dielectric solvents such as dichloromethane. The average fluorescence

lifetime of the quantum dots were also analyzed by measuring the fluorescence decay and fitting to a sum of exponentials.

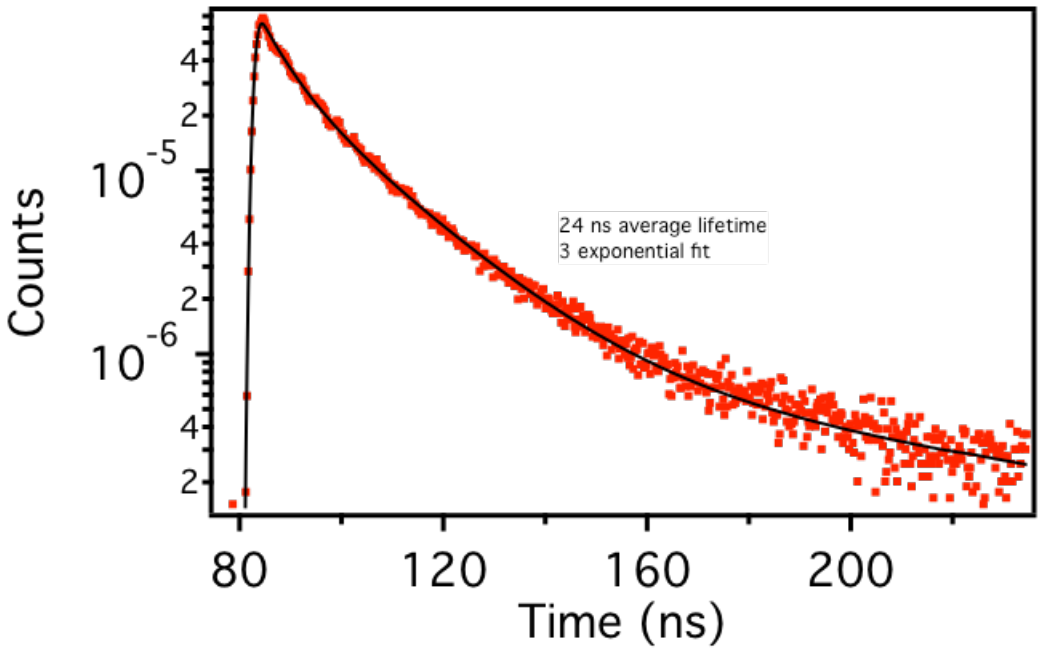

Figure 7.32: Time-resolved fluorescence spectra of diamine-capped quantum dots in dichloromethane. The samples is excited at 398 nm with and 1 nm slit width. The decay is fit to 3 exponentials.

The decay is shown in Figure 7.32 on a log axis versus a time axis in nanoseconds. The decay can be fit to an exponential function, fit to 3 exponentials and the average fluorescence lifetime in the sample above is 24 ns on and represents the average for the quantum dots samples. The lifetime is important due to its sensitivity to parameters such as sample aggregation, change in solvent and interaction between foreign contaminants. Once the quantum yield and average lifetime of the stock quantum dots is calculated, it will be compared to the case when they are bound to the hybrid nanoparticles.

7.4: Ligand Exchange to 11-Mercaptoundecanoic acid, Subsequent NHS- Esterification and Amide Bond Formation between Quantum Dots and Hybrid Nanoparticles

The stock nanoparticles were washed with ethanol and centrifuged to pellet the nanoparticles. The nanoparticles were redispersed into clean toluene and sonicated for 5-10 minutes. The number of available cadmium or zinc surface sites was calculated and 10 times the molar equivalent of MUA was dissolved into toluene. The nanoparticles were then added into the MUA solution and stirred at 50^0C overnight. The nanoparticles were washed with ethanol and centrifuged to pellet the nanoparticles. The supernatant was decanted from the nanoparticles which were stored dry and dispersed into clean dichloromethane before use.

To a solution of MUA coated nanoparticles dispersed into dichloromethane, 4-dimethylaminopropylpyridine was dissolved, in a 1.5 molar ratio to the available Cd surface sites. The reagent 1-ethyl-3-(dimethylaminopropyl)carbodiimide (EDC) was dissolved into 3 mL of anhydrous DMSO and added to the mixture under stirring. N-hydroxysuccinimide (NHS), in a 1:1 mole ratio was then added to the mixture which was stirred at 0 ^{0}C for 4 hours and then allowed to stir at room temperature for 48 hours. The nanoparticles were centrifuged to pellet them out of solution and stored dry and in the freezer until the amidation step.

The amine coated-quantum dots were dispersed into dichloromethane and a molar equivalence of n-ethyldiisopropyl amine was added. The NHS-ester coated nanoparticles, dispersed in dichloromethane were then added and the solution was stirred at 50^0C for 48 hours. The nanoparticles were centrifuged to pellet them out of solution and stored in ethanol.

7.4.1 FTIR Characterization of Quantum Dots and Hybrid Nanoparticle Surfaces

In order to facilitate binding, the quantum dots must be coated with an external, primary amine group. The native surface was coated with olelyamine which needed to be removed and replaced by a diamine, so that one end can bind to the surface of the quantum dot and the other remains exposed to the solution. The CdSe quantum dots with a CdS shell were first washed with acetone and centrifuged to remove oleylamine. The quantum dots were then stirred in a solution of hexamethylene diamine in ethanol and washed to remove excess, unbound diamine.

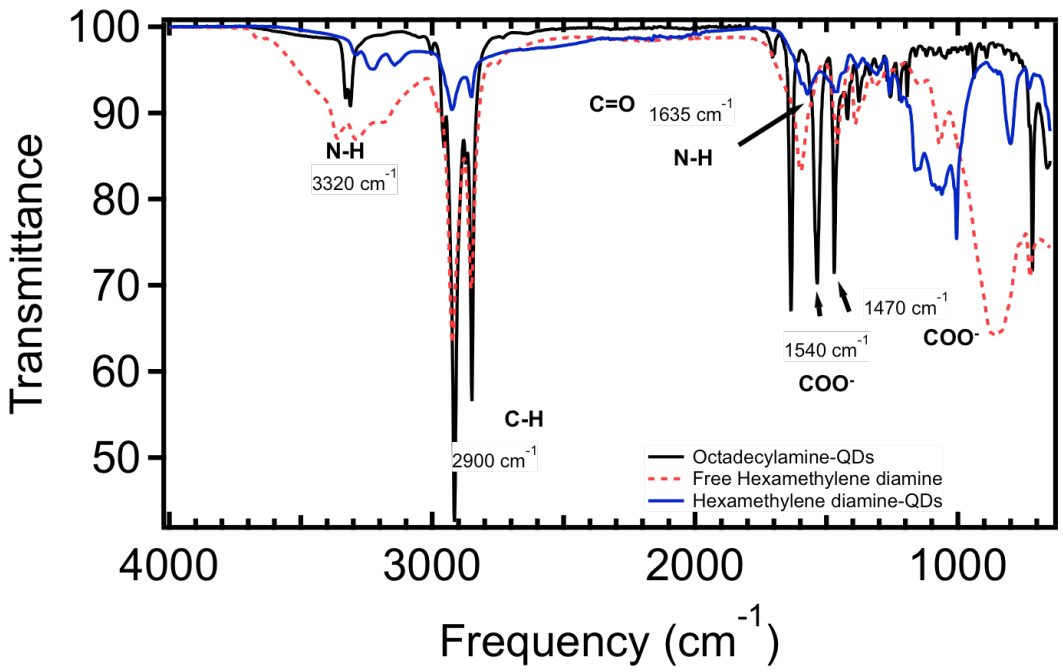

Figure 7.410: FTIR spectra of stock quantum dots (black) and quantum dots after a ligand exchange with 1,6 hexmethylenediamine. The amine stretch at 3300 cm^{-1}, shifts to 3200 cm^{-1} when the diamine is bound to the surface.

The FTIR spectra in Figure 7.410, show the difference in surface chemistry before and after binding of the diamine linker. The native ligand on the quantum dots was octadecylamine, and the spectrum (black) correlates to stock quantum dot samples coated in the native ligand. A very narrow amine stretching doublet around 3300 cm^{-1}, can be seen in the stock quantum dots, in contrast to the much broader stretching modes of the free diamine molecule, in red, located at higher frequency around 3300 and 3100. The shift of the stretching mode to lower frequency was indicative of conjugation to a surface. The amine stretch shifted to even lower frequency,compared to the free diamine molecule, upon binding of hexamethylene diamine to the quantum dots shown by the blue trace. The N-H wag seen around 1600 cm^{-1} was observed in all 3 spectra but was shifted to higher frequency for the octadecylamine-coated quantum dots. The small carbonyl stretch observed in the octadecylamine-coated quantum dots was due to remaining oleic acid from the CdS shelling procedure, as are the two carboxylate stretching vibrations for the asymmetric and symmetric stretching vibrations, located at 1540 cm^{-1} and 1470 cm^{-1} respectively.

The next functionalization step was to coat the core shell nanoparticles with 11-mercaptoundecanoic acid (MUA), allowing the nanoparticles to be functionalized with an external carboxylic acid group. This represents the first step in carbodiimide coupling of reaction, which will be used to link the quantum dots to the nanoparticles. The nanoparticles were mixed with ethanol to wash off the native olelylamine from the surface of the nanoparticles, exposing free cadmium sites on the surface of the shell. The thiol group of MUA will then coordinate to these metal sites more readily than the carboxylic acid, ensuring the acid group will be exposed. The carboxylic acid was then

activated by forming an ester with EDC. The EDC dissolved in DMSO, was mixed with the acid-functionalized nanoparticles dissolved in DCM. N-hydroxysuccinimide was then added to replace the more active EDC producing a more stable ester. Once the reaction had gone for 48 hours the nanoparticles were centrifuged to separate by-products and free or unreacted MUA, NHS or EDC. The dried nanoparticles were then analyzed via FTIR spectroscopy before the final functionalization step.

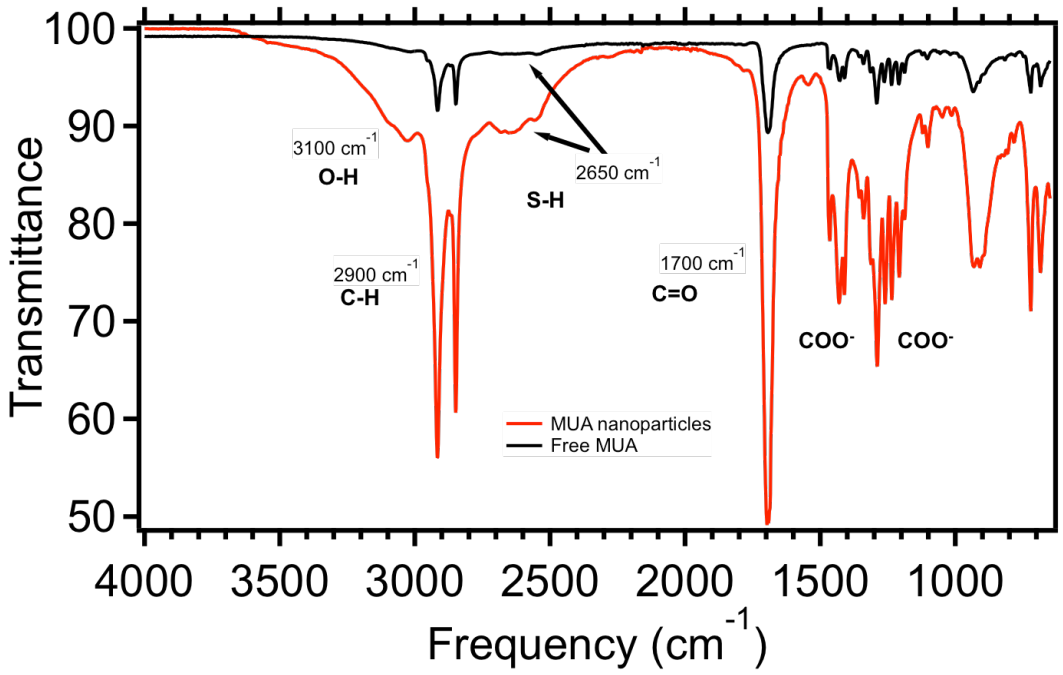

Figure 7.411: FTIR spectra of free 11-mercaptoundecanoic acid (black) and hybrid nanoparticles coated in MUA (red). The only noticeable change upon binding is a slight shift in the S-H stretch of thiol from 2250 cm^{-1} for Free MUA to 2260 cm^{-1} in bound MUA and a noticeable broadening of the stretch.

The FTIR spectrum in Figure 7.411, shows that a strong carbonyl stretch, indicative of a carboxylic acid group was present on the particles after this ligand

exchange with MUA. The binding of S-H was monitored through analysis of the S-H stretch around 2650 cm^{-1}. The S-H stretch broadened and increased in frequency upon binding. A hydroxyide stretch can be seen to form upon binding as observed by the growth of a broad shoulder around 3000 cm^{-1}. The rest of the spectrum was almost identical to that of the free MUA. The MUA-coated nanoparticles were then treated with EDC in DCM and DMSO. EDC will form an ester with the free- acid group on the bound MUA but is unstable and prone to hydrolysis. N-hydroxysuccinimide was added to replace EDC and form a more stable ester.

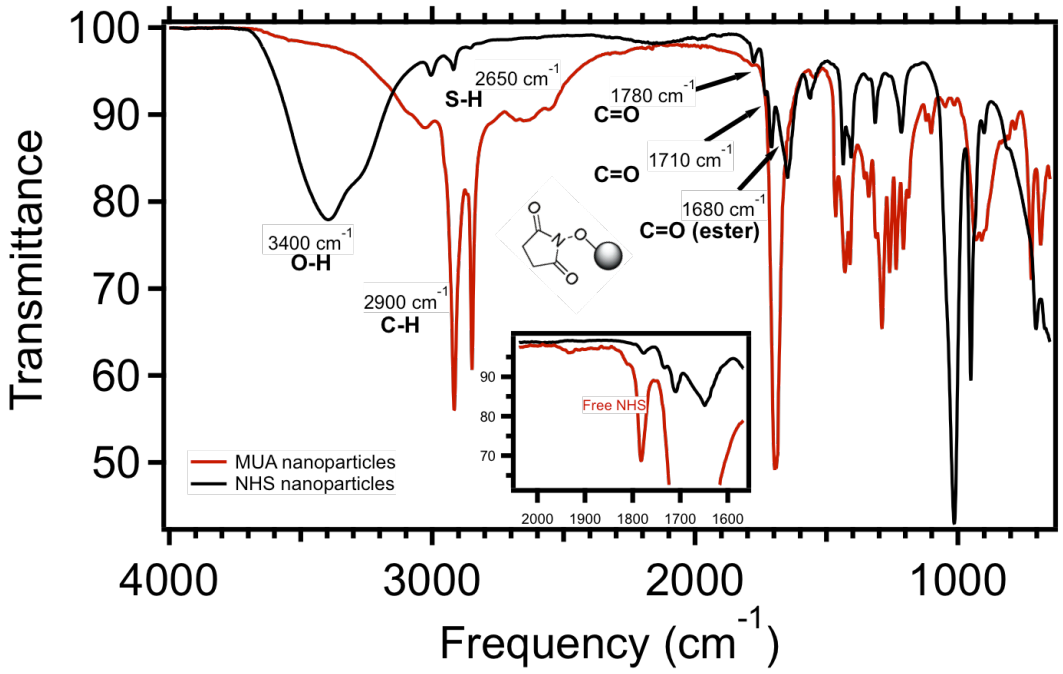

Figure 7.412: FTIR spectra of hybrid nanoparticles coated with 11-mercaptoundecanoic acid (black) and NHS-esterified 11-mercaptoundecanoic acid (red). Carbonyl stretch at 1700 cm^{-1} from the carboxylic acid group shifts to form peaks at 1777 cm^{-1}, 1710 cm^{-1} and 1650 cm^{-1} once the acid group is esterified with NHS. The inset shows the split carbonyl is also present in free NHS

Once activation of the carboxylic acid group was completed to form an ester with N-hydroxysuccinimide, a splitting of the carbonyl stretch into three separate peaks at around 1800, 1710 and 1700 was observed for the NHS ester. These peaks are characteristic of the imidyl group on the succinimide for the higher frequency stretches and an ester carbonyl stretch. This peak was confirmed through comparison with free NHS as seen in the inset in figure 7.412, although the peak at 1710 cm^{-1} is absent . NHS. Another striking future is the emergence of a strong and broad O-H stretch around 3400 cm^{-1}, due to excess, unbound NHS molecules.

Once the NHS activation was completed, the nanoparticles were dispersed into clean DCM and mixed with the diamine-coated quantum dots in dichloromethane. The reaction was conducted for 48 hours and the nanoparticles were washed and stored in ethanol. The dried nanoparticle composite was characterized via FTIR and TEM.

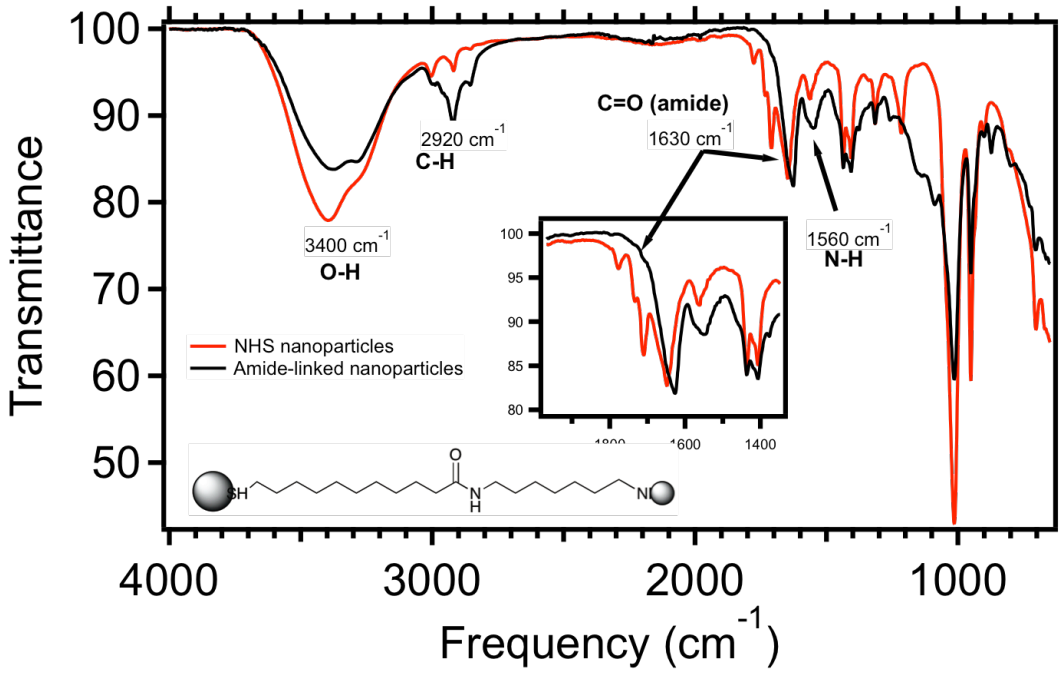

Figure 7.413: FTIR spectra of hybrid nanoparticles coated with NHS-esterified 11-mercaptoundecanoic acid (red) and linked to quantum dots via and amide bond (blue). The splitting of the carbonyl stretch is reduced and the peak is shifted from 1650 cm^{-1} to 1630 cm^{-1}

Upon amidation, the 3 carbonyl stretches disappeared and a single, lower frequency stretch at around 1650 cm^{-1} remained. In Figure 7.413, the lower frequency stretch was indicative of conjugation, via bonding to the surface of the nanoparticles. The N-H stretch around was slightly shifted to lower cm-1 and was much broader due to contribution from both the amide nitrogen hydrogen bond and the diamine bonds located on the quantum dot surface.

FTIR characterization of the different ligand exchange steps, allowed for observation of the chemical changes associated with each surface molecule. In most cases, free ligand was assumed to be minimized after washing and centrifugation. Esterification and subsequent amidation of the carboxylic acid group via the EDC

coupling mechanism, proved successful and resulted in linked quantum dot hybrid nanoparticle composites.

7.5 TEM and Optical Characterization of Quantum Dot: Hybrid Nanoparticle Composites

7.5.1 TEM Characterization

In order to characterize the physical nature of the binding, TEM images of the composites were taken. The TEM samples were prepared by placing a drop of the stock composite solution, in toluene, on a TEM grid. The sample is placed in the vacuum oven at least 24 hours before use. The samples were then characterized with ImageJ to measure the shell thickness and spacing from the gold core.

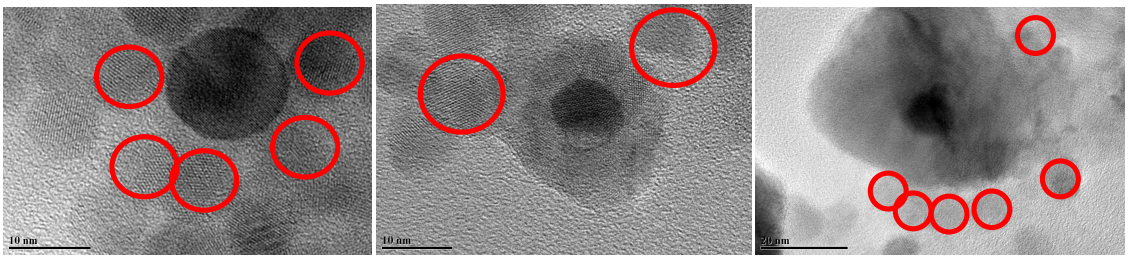

Figure 7.510: TEM images of quantum dots bound to gold nanoparticles with increasing spacer layer thickness

TEM images were taken in order to prove physical binding of the quantum dots to the shell of the nanoparticles and to measure the distance away from the core gold nanoparticle. In Figure 7.510, TEM images of quantum dots bound to semiconductor shells increasing from left to right from a couple nanometers in diameter to 20 nanometers are shown. The distance between quantum dots and core gold nanoparticle was then measured and averaged to determine the dielectric spacing distance. The TEM samples show quantum dots both directly bound and free on the TEM grid. The presence

of unbound quantum dots is due in part to the large excess of quantum dots in comparison to the hybrid nanoparticles. The bound quantum dots were separated by less than 3 nm, in most cases, which would be the theoretical length of the carbon chain linking the two nanoparticles.

The spacing distance was varied in order to determine the optimal distance away from the gold core, necessary to produce the most efficient plasmonic enhancement of the radiative rate. Due to sample inhomogeneities, only cadmium sulfide shells were studied, although binding reactions were performed on zinc sulfide shells also. The radiative rate was calculated through analysis of the solution-state absorption and fluorescence spectra of each sample. Quantum yields were calculated from the absorption and fluorescence data. Fluorescence average lifetimes were calculated through fitting or fluorescence decays.

7.5.2 UV-vis Absorption Characterization

The absorption of the composite was taken post-reaction and after purifcaiton. The dried composties were redispered into 1 mL of ethanol. The comospites remained soluble in polar solvents due to the polarity of the amide group linking the two nanoparticles. The absorption spectra of of free quantum dots and the linked composites were compared to moniter spectral differences upon binding.

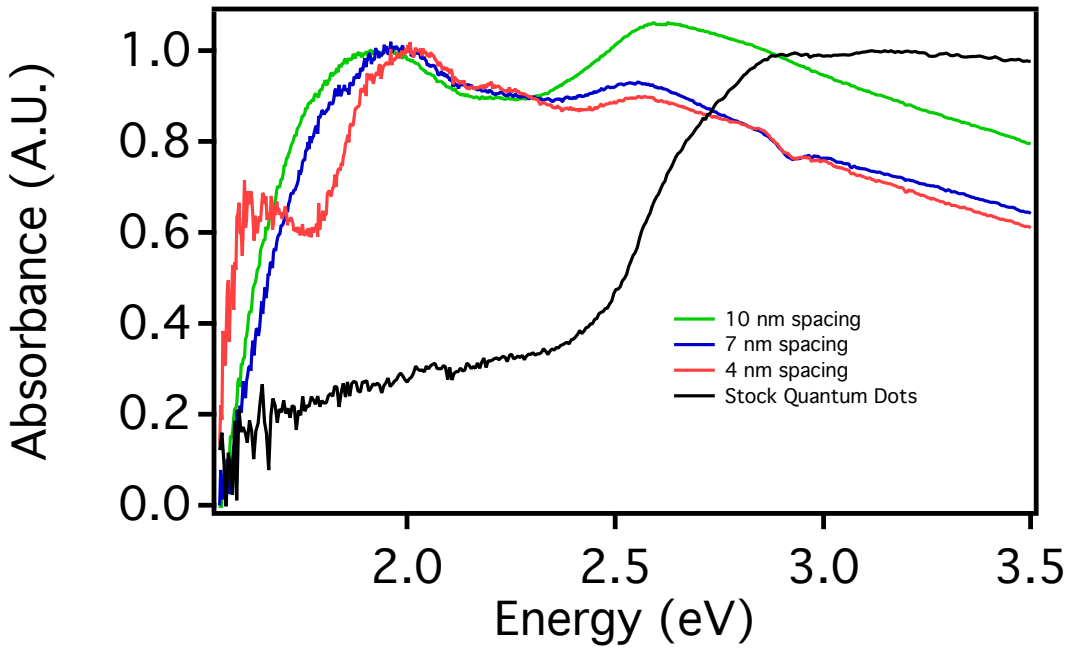

Figure 7.520: Absorbance spectra of quantum dots unbound (black) and bound with a separation distance 4-10 nm.

In Figure 7.520, the absorption spectra of unbound quantum dots and quantum dots bound to a thin, medium and thick-shelled hybrid gold nanoparticles. The spectra of the unbound were mainly featureless, with absorbance increases around 2.5 eV indicating the excitonic absorption transition. In the bound samples, the excitonic absorption onset was substantial red-shifted and broadened compared to the unbound quantum dots. This red-shift is due to electronic coupling of the exciton with the hybrid nanoparticles. The quantum dots separated by 4 nm, showed two distinct absorption maxima at 2.0 eV and 1.6 eV produced from the excitonic transition and the plasmon resonance respectively. The 7 nm spaced sample showed only one broadened absorption band, red-shifted with respect to the exciton and blue-shifted to that of the plasmon resonance. At 10 nm, the

spectrum was broadened to produce a band intermediate in energy compared to the quantum dots and the plasmon resonance of the hybrid nanoparticles.

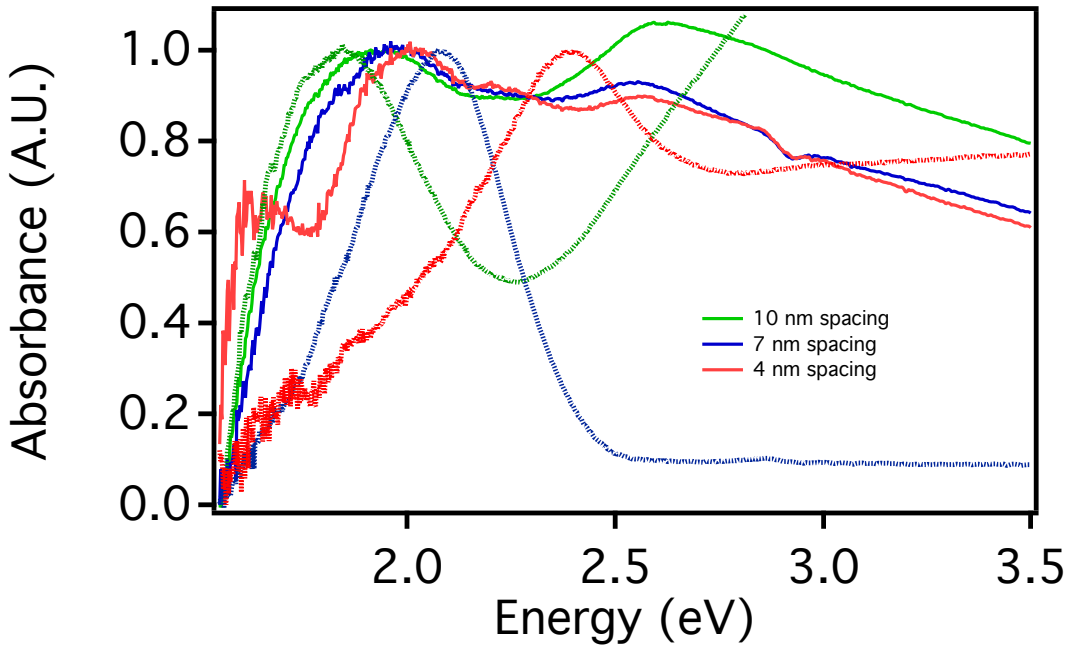

Figure 7.521 Absorbance spectra of quantum dots bound with a separation distances of 4-10 nm and their corresponding hybrid nanoparticles without quantum dots. The hybrid nanoparticle spectra are taken in toluene while the bound quantum dots are dissolved in ethanol.

In Figure 7.521, the hybrid nanoparticles corresponding to each shell thickness are shown. The plasmon resonance red-shifted for all the nanoparticles, except the nanoparticles representing the 10 nm spacing. The hybrid nanoparticles with a 10 nm shell were observed to blue-shift from the original nanoparticle spectrum. Although much broader, the plasmon resonance retains the same shape in the samples with quantum dots bound to the surface. The red-shift is due to both a change in dielectric from the new

surface environment of the amide linker and quantum dots and different refractive indexes of ethanol and toluene.

These spectra indicate that upon binding, there was minimal change in the spectral shape upon binding quantum dots to the nanoparticle surface. The quantum dots did alter the plasmon resonance, indicating a change in the local dielectric environment around the nanoparticle. The minimal changes in the absorption spectra indicate relatively weak plasmonic coupling with the exciton. In this weak coupling regime, losses due to energy transfer into the gold core should be minimized, allowing for possible enhancements in the emission rates.

7.5.3 Fluorescence Characterization

Fluorescence spectroscopy was utilized to probe the effects on the radiative rates of the quantum dots. Quantum yields were calculated from the absorption and the area of the fluorescence peak. An increase in quantum yield was the first goal in enhancement of the radiative rates. Time-resolved fluorescence decays were then taken to calculate fluorescence lifetimes of the quantum dots. A decrease in fluorescence lifetime would indicate coupling of the plasmon resonance with the fluorescence dipole of the quantum dots. Similar to when a radiating plasmon is produced, the resulting transition should occur at much faster time scales when coupled with the plasmonic electric field.

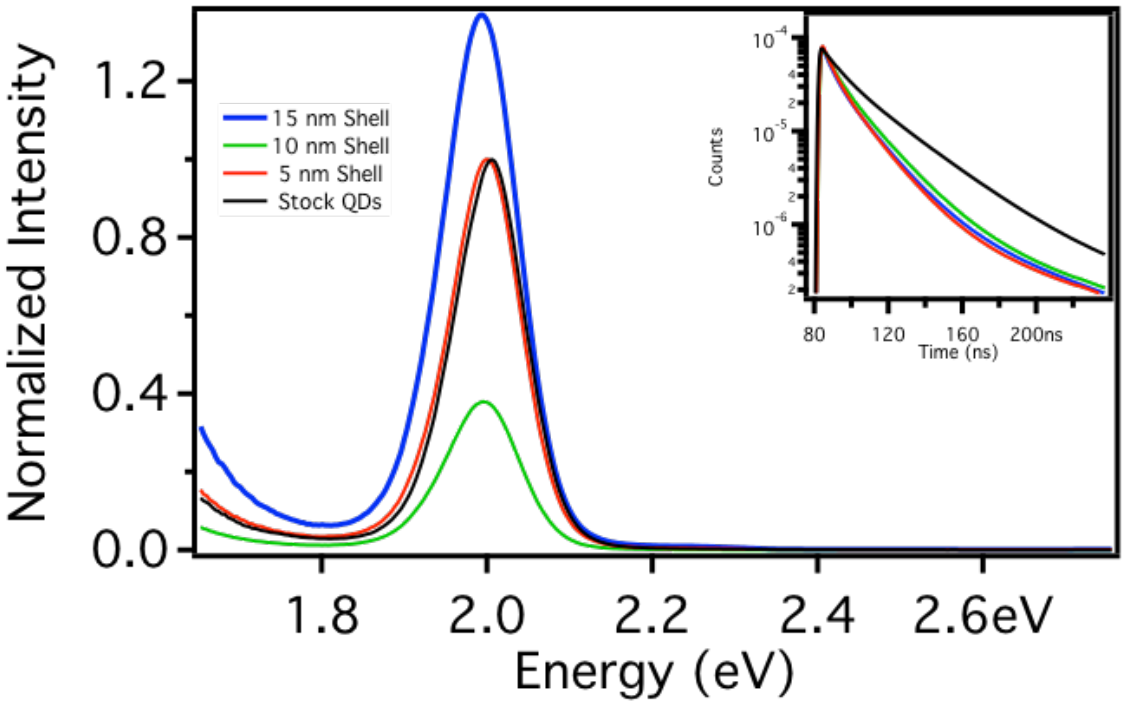

Figure 7.530: Steady State fluorescence of quantum dots unbound (black) and bound to a thin (red) and thick (blue) CdS shell. The fluorescence spectra are all normalized to the peak maxima and then multiplied by the quantum yield change, relative to the unbound quantum dots. Inset: Fits to fluorescence decays for the same quantum dots.

Figure 7.530 shows the normalized steady-state fluorescence spectra taken from 450 nm to 750 nm. The fluorescence spectra were normalized by first dividing the sample spectrum by its maximum intensity value. The spectrum is then multiplied by the relative quantum yield compared to the unbound quantum dot. The quantum dot fluorescence (black) is centered at 617 nm or 2.0 eV. The fluorescence peak doesn't shift or broaden significantly upon binding but intensity shifts were observed. The fluorescence was normalized to the sample absorption at the excitation wavelength of 400 nm. The normalized fluorescence showed a dependence on the sample shell thickness. For these three samples, the quantum yield increases was maximized with the thickest, 15 nm shell

and a quenching was observed for the 10 nm Shell. The 5 nm Shells are slightly increased in comparison to the original quantum dots. The fluorescence decays shown in the inset of Figure 7.530, show a sharp decrease upon binding to the hybrid nanoparticles.

The fluorescence decays, which are shown in the inset of Figure 7.530, are taken using a pulsed-LED source, 1us TAC range and 2 nm slit widths. The decays are fit using a sum of exponentials ranging from 3- 5 exponentials, depending on the sample, and the average lifetimes are calculated from the fit of the decay. The Durbin-Watson and chi-squared parameters are used to ensure the fit is within statistical error. The samples show a much faster decay upon binding to the hybrid nanoparticles, which indicates strong coupling of the fluorescence with the plasmon as noted earlier. For all samples the calculated lifetime decreases between 3- and 40 % of the original quantum dot average lifetime.

7.6 Quantum Yield and Radiative Rate Analysis

In order to quantify the intensity changes, the quantum yields were calculated for each sample. For the CdS samples, the quantum yield was calculated and then plotted versus the shell thickness. Vertical error bars were calculated from the uncertainties in the quantum yield measurements, and each point refers to a separate reaction. The horizontal error bars were calculated from the standard deviation in the shell thickness, calculated from TEM images using the ImageJ software.

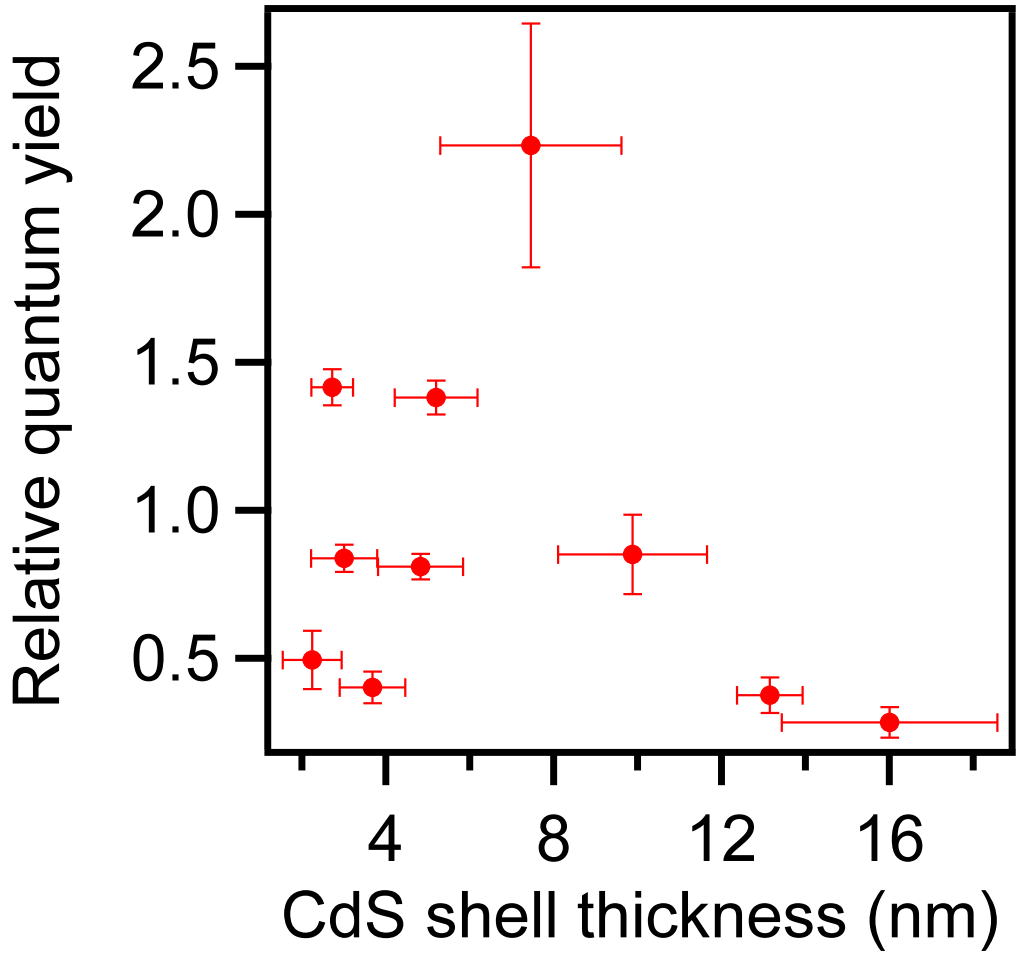

Figure 7.60: Quantum yield of bound quantum dots as a function of shell thickness. Only CdS shells were utilized for this analysis. The samples were dispersed in ethanol and quantum yields were calculated in reference to ethanol. The quantum yields were normalized to the unbound quantum dot value, taken as 1.

In Figure 7.60 the average quantum yield versus separation distance is shown for the hybrid nanoparticle-quantum dot ensembles, with the sample set containing only CdS shells. The quantum yield was normalized to the original, unbound quantum dot quantum yield. The fluorescence was quenched at the smallest and largest shell sizes as seen by the relative quantum yield being less than 1. An increase in quantum yield ,up to 2.5 times that of the original quantum dots, was observed for shells with 8 nm spacing. The

plasmonic coupling with the fluorescence transition was observed to increase the fluorescence intensity the most for quantum bounds to shells of this thickness

Separation by 10 nm or greater results in a decrease in quantum yield due to minimal coupling with the plasmon at the larger separation distance. Nonradiative recombination of the electron or hole into the CdS shell of the nanoparticle is a plausible explanation for this decrease at larger distances, as energy transfer to the gold should be less competitive at these distances. The average lifetimes of all samples decreased with the 8 nm shells showing the largest decrease to around 70% that of the original quantum dots.

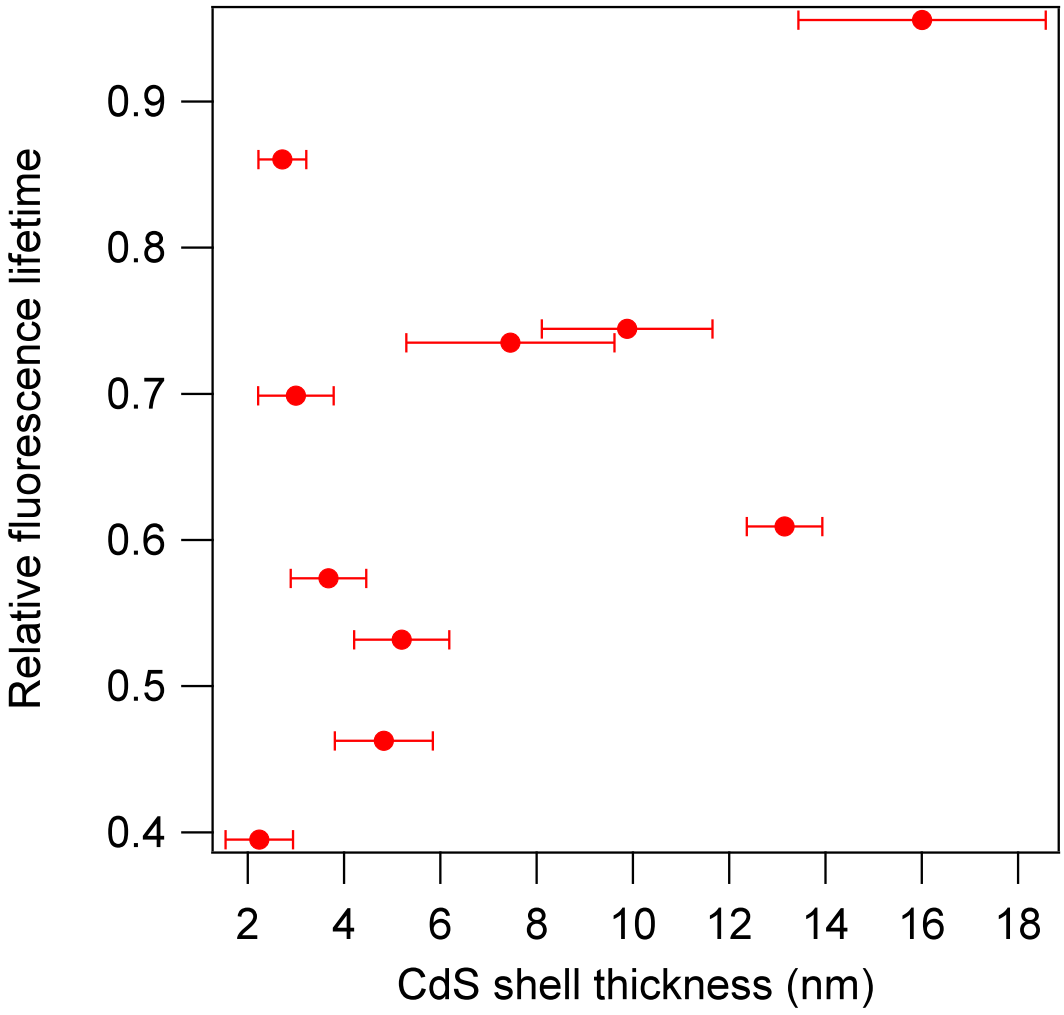

Figure 7.61: Average lifetime of bound quantum dots as a function of shell thickness. Only CdS shells were utilized for this analysis. The samples were dispersed in ethanol and quantum yields were calculated in reference to ethanol

In Figure 7.61, the average lifetime as a function of the shell thickness is shown. The lifetime of all samples decreases with the thinnest samples showing the sharpest decrease in lifetime. This shortening of the lifetime at close distance was indicative of strong coupling with the plasmon resonance. This shortening was also accompanied with a decrease in quantum yield, which indicates quenching via energy transfer to the gold or was the dominate mechanism for the resulting decrease in lifetime. The thickest shelled

samples shows the highest average lifetime, approaching unity, which means its behavior was similar to unbound quantum dots. This points to insufficient coupling at the larger separation distances.

In order to calculate the radiative rate, the quantum yield and average lifetimes must defined in terms of the radiative rate (k_r) and nonradiative rate (k_{nr}). In equation (24) the average lifetime can be represented as the inverse of the sum of the radiative and nonradiative rates and the quantum yield can be defined as the radiative rate of the sum of the radiative and nonradiative rate in equation (25).

$$\tau_{avg} = \frac{1}{k_r + k_{nr}} \tag{24}$$

$$QY = \frac{k_r}{k_r + k_{nr}} \tag{25}$$

$$k_r = \frac{QY}{\tau_{avg}} \tag{26}$$

These equations can then be rearranged to solve for the radiative rate in terms of quantum yield (QY) and average lifetime as shown in equation (26). The radiative rate was then plotted versus the shell thickness

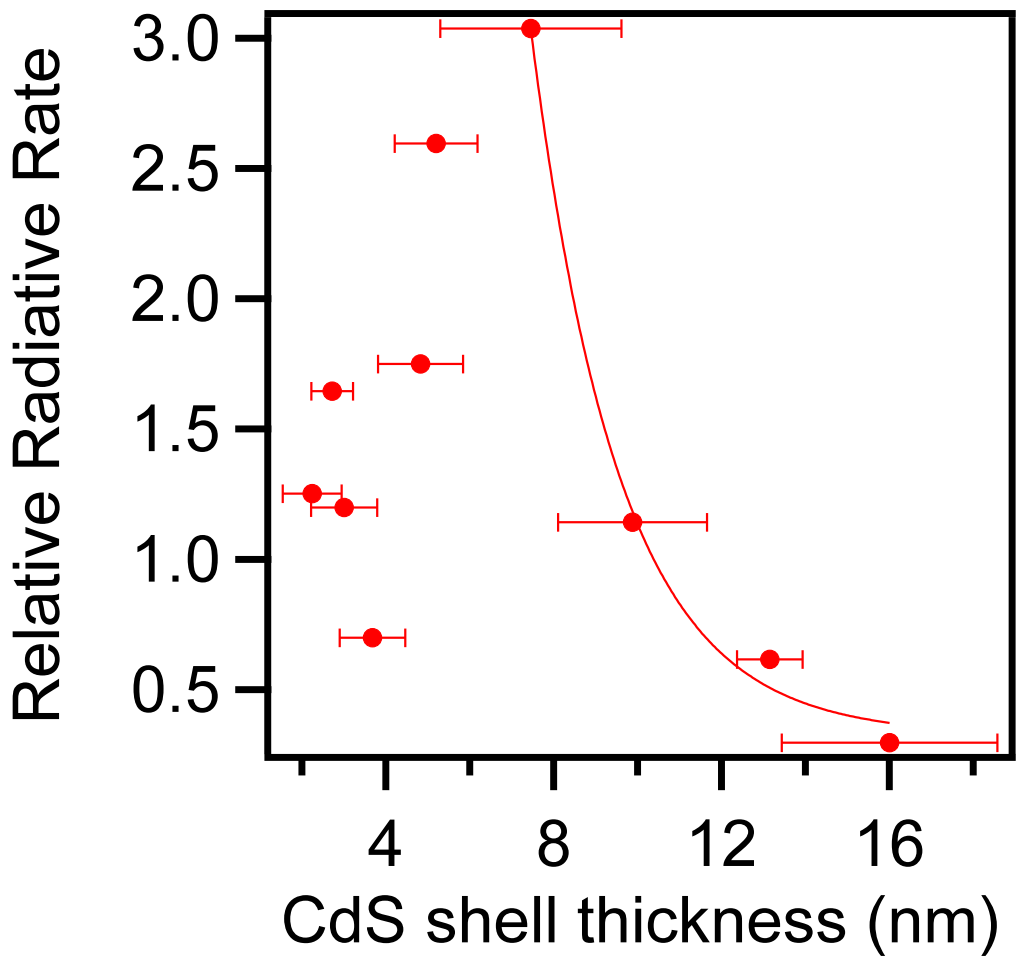

Figure 7.62. Fractional change in the radiative rate plotted as a function of separation distance. The radiative rate is normalized to the unbound quantum dot radiative rate.

The radiative rate as a function of separation distance, plotted in Figure 7.62, shows a maximum in the radiative rate enhancement at around 7-8 nm of CdS. The plot trends very similarly to the quantum yield plot in Figure 7.60, indicating careful control over the sample quantum yield is paramount for increasing the radiative rate. The larger CdS shells showed a decreased radiative rate up to almost 20% lower than the unbound quantum dots. A small decrease in the radiative rate was also observed for the medium shells at about 95% that of the unbound quantum dots. Although not plotted, the ZnS

shell enhancement is much more modest at about 1.5 x that of the unbound quantum dots at thickest size of 13 nm shell thickness. The smaller shell sizes were centered close to 1, indicated majority unbound quantum dots may be in solution due to the decreased loading from the smaller shell size. The trend for the larger shells sizes seems to decay exponentially, which would indicate a strong dependence of the shell thickness on the coupling strength.

7.7: Binding Yield

An issues which needs to be discussed is the full extent of coupling. From TEM images, it is clear that not all the quantum dots in the ensemble are bound to the hybrid gold nanoparticles. A large quantity of unbound quantum dots remain, indicating that there is a significant population in solution as well.

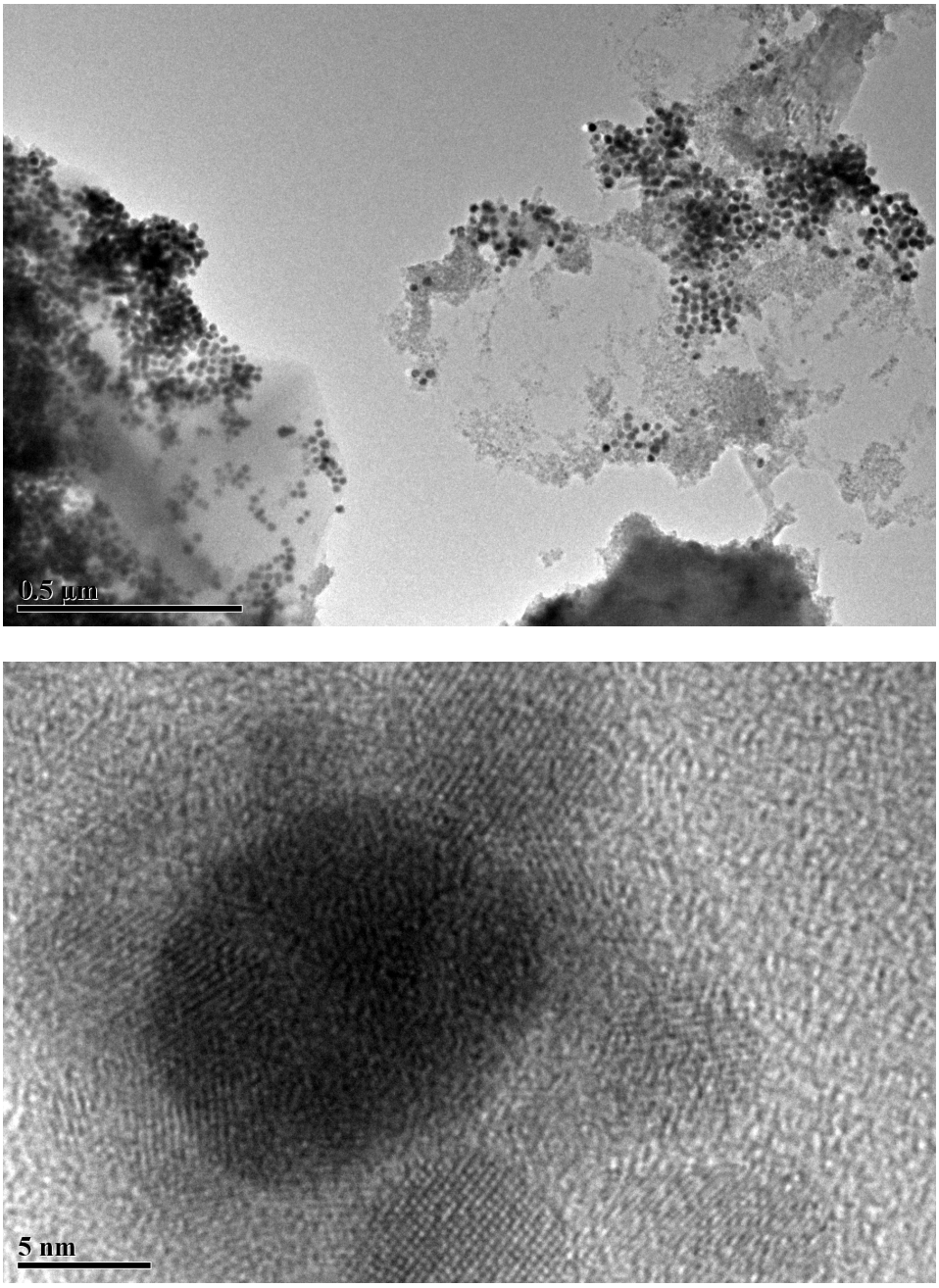

Figure 7.70 TEM images taken at 200 kV accelerating voltage. The Images are of gold nanoparticles with a 7 nm shell thickness after the linking of quantum dots. The scale bar on the top image is 0.5 uM and the scale bar on the bottom image is 5 nm.

Observation of the close up TEM image (bottom) in Figure 7.70 show that the nanoparticles and quantum dots are physically linked but a large cluster of quantum dots can be seen with the gold nanoparticles dispersed throughout. The quantum dots, are somewhat aggregated but maintain some spacing in between individual particles. The bottom image shows that quantum dots are randomly bound to the nanoparticle outer shell and not bound to the face of the nanoparticle.

Although large bunches of unbound quantum dots remain, the spectral data still indicate a distance dependence on the quantum yield, average lifetime and calculated radiative rate. This may reveal the nature of the binding interaction. If only unbound quantum dots were being observed, the samples would not show a distance dependence, indicating a significant interaction with the hybrid nanoparticles. The changes in radiative rate and quantum yield were quite modest but are only indicative of the bound species. Control experiments indicate that when nanoparticles were added, without the linker molecules, only quenching was observed at all shell thicknesses.

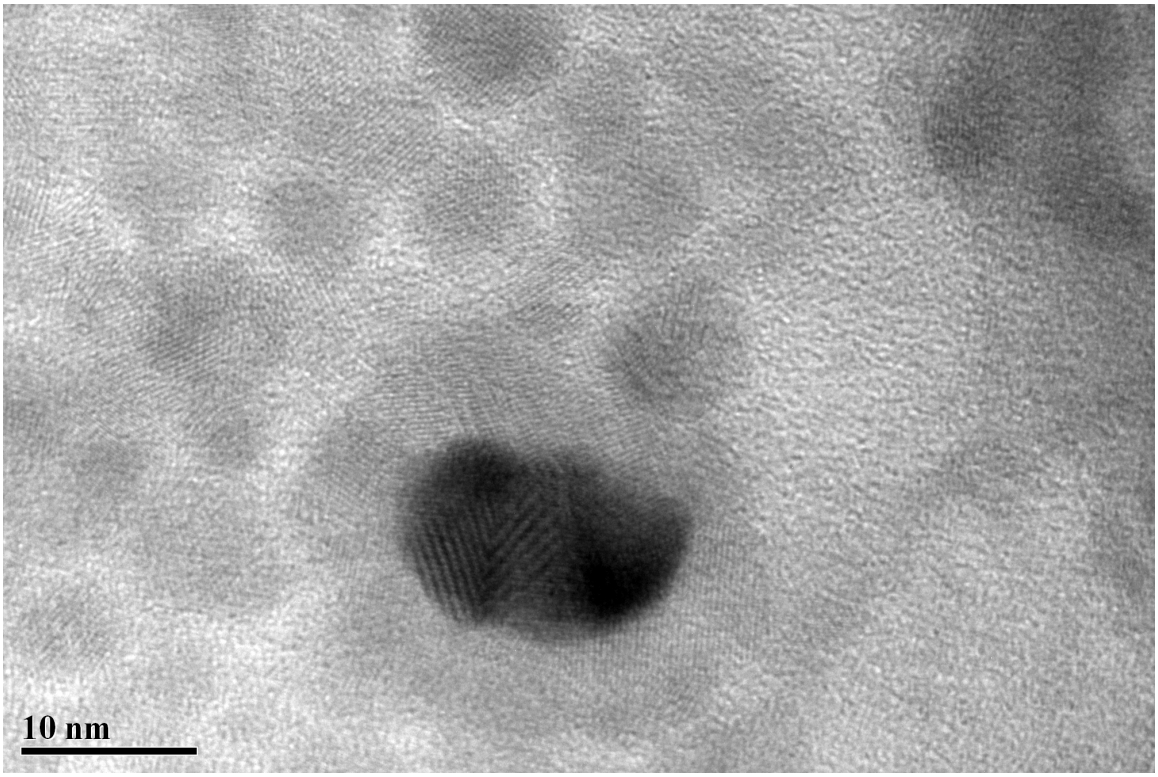

Figure 7.71. TEM image taken at 200 kV accelerating voltage. The image shows the prescence of both bound and unbound quantum dots to the nanoparticle surface.

The image in Figure 7.71, gives a good example of the ensemble system, negating changes due to the TEM conditions, (high vacuum, incident electron beam etc). The amide linker measures roughly 3 nm in length, so quantum dots within that distance were assumed to be bound. A rough estimation of the number QDs within binding distance and unbound gives about a 30% bound to unbound ratio. This image indicates that the majority of quantum dots in the samples remain unbound. If this ratio were increased to 100% the maximum radiative rate enhancements would increase from 3 times to 10 times that of the unbound quantum dot.

The thinnest shells showed a relatively lower radiative rate as compared to the 7-8 nm shells. The plasmonic coupling should be stronger with decreased spacing and

produced larger enhancements in the radiative rate. This trend was attributed to the presence of free quantum dots, dominating the fluorescence signal at these shell sizes. In all samples, we assume there will be some equilibrium concentration of unbound quantum dots as observed in the TEM images seen in Figures 7.70 and 7.71. This population would then be greater for the smaller shells, as they do not contain as many binding sites as the larger shells. Thus, the radiative rate values of the shells smaller than 4 nm, trend more towards the unbound quantum dot radiative rate value of 1.

7.8 Spectral Overlap of the Composites

Plotting the radiative rates versus shell size gave insight into the nature of how far the plasmon field needs to be spaced away from the quantum dots in order to maximize plasmonic coupling. Changing the shell thickness, however, also changes the plasmon resonance energy by changing the local dielectric environment. In order to effectively couple with the quantum dot radiative rate, the plasmon resonance needs overlap with the fluorescence spectrum.

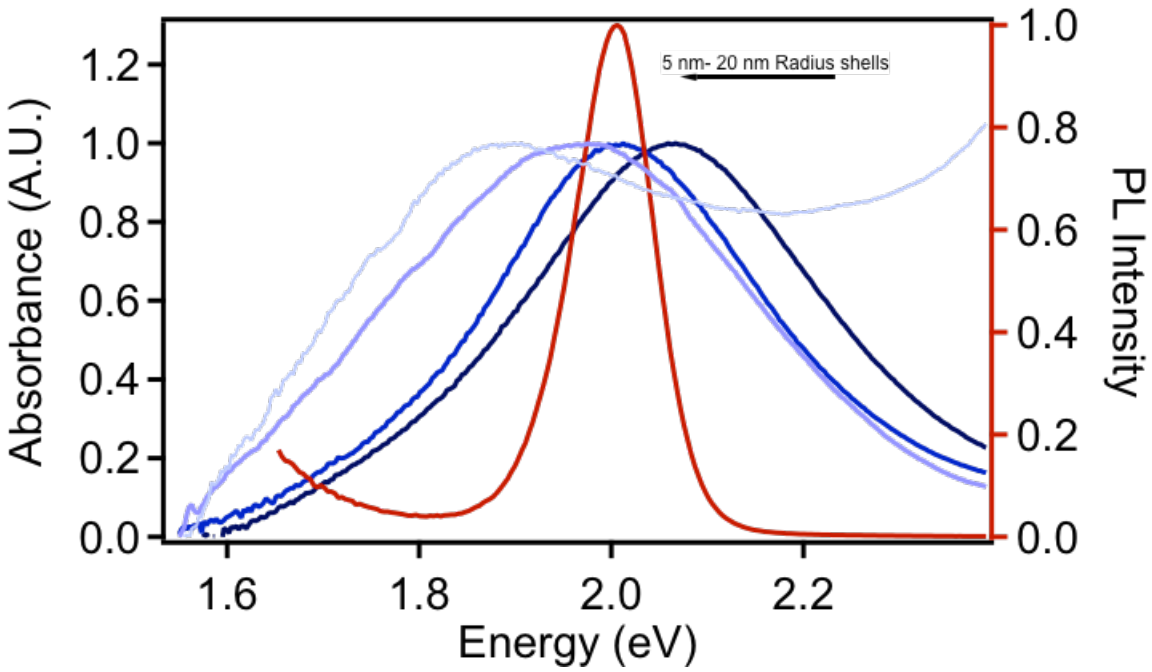

Figure 7.80 Absorbance Spectra of Au coated with CdS shells and increasing shell thickness from right to left. Right axis (red) Fluorescence spectrum of unbound quantum dots.

In Figure 7.80 the fluorescence spectrum of the quantum dots was plotted versus the plasmon resonance of 4 different CdS shell sizes. As the resonance maxium red shifts, the size of the shell increaes. The thickest and thinnest shells represent the lowest overlap while the two middle shell sizes represent maxmium overlap. FTIR, TEM and optical characterization are all conducted the same as the previous experiments in order to calculate the radiative rates after binding. The spectral overlap can be definned as the absolute energy difference between the plasmon resonance maximum and the fluroesecne maximium. The radiative rates are binned into three regimes, a lower fractional radiative rate (less than 1), medium enhancement (1-1.5 x) and large ehancement (greater than 2 x ehanced) and plotted vs. the spectral overlap as defined previously.

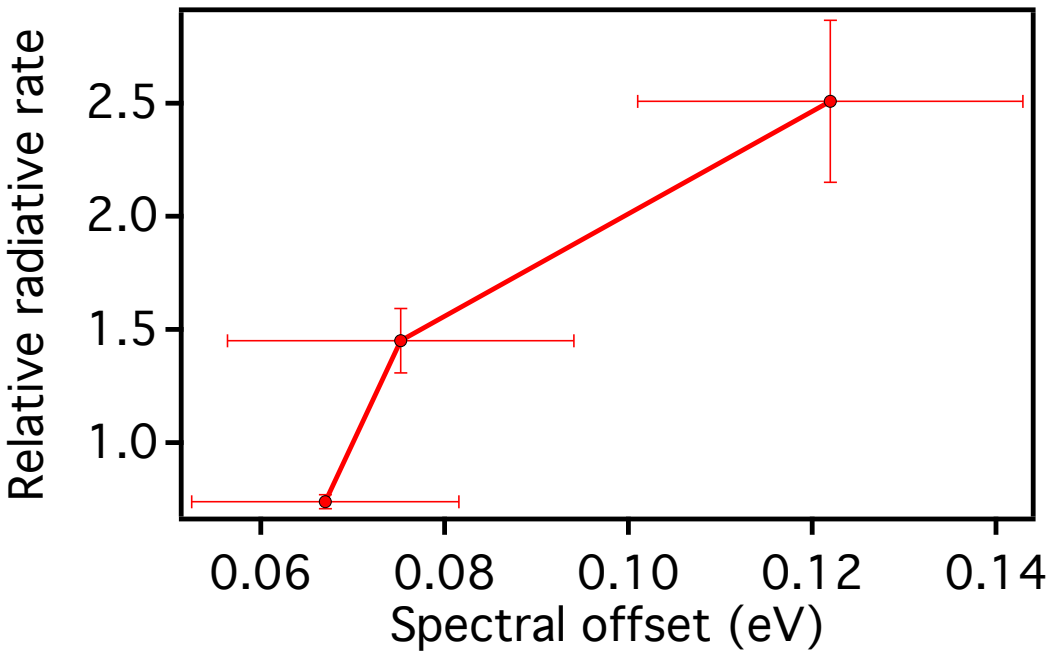

Figure 7.81 Plot of the change in QD radiative rate as a function of plasmon overlap with the fluorescence spectrum.

In Figure 7.81, the radiative rates versus spectral overlap of the plasmon with the fluorescence is shown. The plot shows a direct dependance of the radiative rate on spectral overlap in that a strong overlap with the plasmon resonance produces the lowest radiative rate and a weaker overlap corresponds to a strongly enhanced rate. The shell size does play a role in this phenomenom as this shifts the maximium plasmon resonance due to changes in the dielectric function of the enviorment.

These data indicate that several factors need to be considered when seeking to modify the fluroescent rates of quantum dots. The physical seperation from the gold surface seemed to have the largest effect on the quantum yield of the quantum dots. The fluroescence lifetime was affected very similarly upon binding regardless of the shell

size. This could be due to the prescence of both bound and unbound quantum dots. Full seperation of thebound quantum dots could indicate a much larger decrease in the average lifetime and their prescence outweighs the unbound quantum dots resulting in a net decreased in lifetime. The composition of the shell also effects the resulting optical parameters, as seen by the larger enhancements produced with CdS shells. Finally, the spectral overlap of the fluroescence with the plasmon resonance of the hybrid nanoparticle needs to be slightly offset to maximize the radiative rate increaes.

7.9 Discussion of Binding and Optical Analysis

FTIR was utilized as the main tool to monitor each ligand exchange during the EDC coupling reaction. First, exchange of the native ligands on the QDS for hexamethylene diamine is monitored and confirmed via a shift to lower frequency in the bound amine stretching signal. Oleylamine was exchanged on the hybrid nanoparticle surface with MUA and was confirmed via a small shift in the thiol stretch at around 2250 cm^{-1}.

The esterification of the terminal carboxylic acid on the hybrid nanoparticles with NHS was also confirmed through the unique split in the carbonyl stretch from 1800 – 1650 cm^{-1}. The esterified NHS contains and extra carbonyl stretch at around 1700 cm^{-1}, which is used to differentiate from free NHS. The formation of an amide bond between the quantum dots and nanoparticles was also confirmed from a decrease in the frequency of the carbonyl stretch and a dissapearance of the extra stretching modes. To further confirm binding, TEM was used to show numerous quantum dots in close proximity with the perimeter of the shells and elemental analysis through EDX spectroscopy confirms the presents of both quantum dots and the gold nanoparticles.

According to our data, plasmonic coupling to improve the radiative was most efficient at 6-8 nm away from the metal surface, in aggreement with other distance-dependant studies on plasmonic coupling.[148] [149] [150] Suppression of nonradiative relaxation pathways were accomplished through careful spacing from the gold surface due the dominance of energy transfer with close contact to the metal surface. This suppression can result in increased quantum yields, if the radiative relaxation is be unperturbed or even increased. Quantum dots bound around 3- 4 nm from the gold surface show a 40% decrease in the quantum yield, but when separated 5-8 nm from the gold surface increases in quantum yields of up to twice that of the unbound quantum dots were observed. Separation of the quantum dots by greater than 10 nm resulted in quantum yields decreases of close to 20%.

In order to increase QD radiative rates, a shortening of the QD average lifetime needed to accompany the increased quantum yield. Relaxation of the plasmon dipole happens on the order of picoseconds[151] [152] [153] ,which is at several orders of magnitude faster than radiative relaxation in QDs. If the plasmon relaxation can efficiently couple with the radiative transition dipole, a substantial shortening of the florescent lifetime will be observed.[41] [40] In all samples bound to the hybrid nanoparticles a decrease in the average lifetime was observed, confirming efficient coupling with the plasmon relaxation at all spacing distances. QDs separated by 5-6 nm show a substantial drop of almost 50% in fluorescence lifetime. Increasing the spacing resulted in a recovery of the fluorescent lifetime, approaching 90% that of the unbound quantum dots at 15 nm spacing distances.

Analysis of these data gave insight into the nature and extent of coupling with the plasmon electric field. Quantum dots bound at a close distances (2-4 nm), show decreases

in both quantum yield and average fluroescence lifetime compared to that of the unbound quantum dot. This points to a strong coupling with the plasmon electric field increasing both nonraditive and radiative relaxation rates. Although, the radiative relaxation rate is increased, energy transfer to the gold still dominates at this distance resulting in strongly quenched fluroscence and decreased radiative rates. At larger separation distance, the average lifetime decreases are much less substantial at 20% that of the unbound quantum dots and the quantum yield decreases to the same extent. This indicates that the plasmon electric field cannot couple as effectively with the quantum dot transtion dipole at this distance. The average lifetime approaches that of the unbound quantum dot in this case. Binding through the semiconductor surface can decrease the rate of nonradiative relaxtion with thicker shells, however, this process is still fast enough to compete with the relatively slower radiative relaxtion, as indicated by a longer fluroescence lifetime.

Finally, the spectral overlap also seems to play an important role in effective radiative rate engineering. Maxmium overlap of the plasmon with the fluroscence spectrum produces significant decreases in the radiative rate. This seems counterintutive since strong spectral overlap is necessary for effcient plasmonic coupling but can be explained through absorption of photons by the hybrid nanoparticles. This absorption would result in seemingly quenched fluroscence, which can be accounted for through calculation of inner filter effects.[154] [155] Simply engineering the plasmon resonance, through size or surface modifications, will be necessary for this and future light emission applications in order to take full advantage of plasmonically ehanced fluorescence.

Quantum dot aggregation is also an issue that increases when the nanoparticles are introduced. Quantum dot aggregation being the cause for the observed changes would

result in a red-shifting of the fluroesecne peak, due to the delocalization of the exciton wavefunction across the aggregate. To ensure the ehancements are due to binding as opposed to just mixing of quantum dots with the hybrid nanoparticles, controls are made by mixing nanoparticles with quantum dots without performing the ligand exchanges to produce the amide bond linkage. Regardless of the shell size the control samples always show a large decrease in the radiative rate, indicative of a large amount of quenching via from coupling to the core shell nanoparticles. This obeservation shows that the nanoparticles need to be electronicly linked to support plasmonic ehancement as opposed to simply being proximal in solution.

7.10 Concluding Remarks

A spacing of 6-8 nm was shown to boost the radiative rate of the quantum dots up to 3 times their orginal value in ensemble measurements. These composties could be used in quantum dot devices for applications in display and imaging technolgies. These composites materials can dropcasted or spincoated onto films, as well as dried for storage. This study is unique in that it allows for analysis of the plasmonic coupling in gold nanoparticles which are not anchored onto a surface and can be used to couple a large amount of quantum dots to these hybrid nanoparticles. This ensemble coupling can decrease the amount of material needed for coupling, since more than one quantum dot can couple with each nanoparticle. This novel distance study on plasmonic coupling can also be used to further understand and model the complex nature of plasmonic interaction with transition dipoles of other species.

This study demonstrated a novel techniqe for coupling ensembles of gold nanoaprticles and quantum dots in solution. A semiconductor spacer was first coated

around the gold nanoparticles, which was also used to study distance-dependance of the plasmonic coupling. The coupling proceeded through four different ligand exchange procedures which can monitored via FTIR spectroscopy. The spacing was then calculated from TEM images using the ImageJ software. A spacing of 6-8 nm was shown to boost the radiative rate of the quantum dots up to 3 times their orginal value in ensemble measurements. These composties can dropcasted or spincoated onto films, as well as dried for storage, to be used in devices for displays and imaging. This study was unique in that it allows for analysis of the plasmonic coupling in gold nanoparticles which are not anchored onto a surface and can be used to couple a large amount of quantum dots to these hybrid nanoparticles.

CHAPTER 8: PORPHYRIN COUPLING

8.1 Introduction

The aim of the porphyrin binding was to produce hybrid-porphyrin composites. These composites will have enhanced extinction coefficients in the visible to near-IR range. This could potentially increase the percentage of incident solar absorption, boosting the current output of photovoltaic devices. Shells in the lowest size-regime, about 5 nm in radius, will be utilized to produce coupling with the plasmon resonance while still providing significant spacing from the metal surface. In the overview of excitation field enhancement, close proximity to the metal surface is desirable to maximize the extent of plasmonic contribution to the photo-absorption of the dye molecules.

Optimization of the binding conditions was conducted by comparing the results of porphyrins with varying substituents. The possible binding sites lie on the surface of the hybrid nanoparticles. Unpassivated cationic Cadmium or zinc sites could support binding from nucleophillic functional groups such as amines, or carboxylic acids. Tetraphenyl Porphyrin (TTP) and Tetra (4-carboxooctylphenyl)porphyrin TCO_4PP have no exterior binding groups but when unmetallated, the center pyrrole groups could bind in this manner. These porphyrins represent the face-on binding configuration where the porphyrin should lay flat on the nanoparticle surface. To facilitate axial binding or binding where the porphyrin face sits perpendicular to the nanoparticle surface, 5-(4-

carboxyphenyl)-10,15,20-tritolyl porphyrin or tritolylphenyl acid porphyrin (TTPa) and 5,10-di(4-carboxyphenyl)-15,20-ditolyl porphyrin or ditoyl di phenyl acid porphyrin (DTDPa) were utilized.

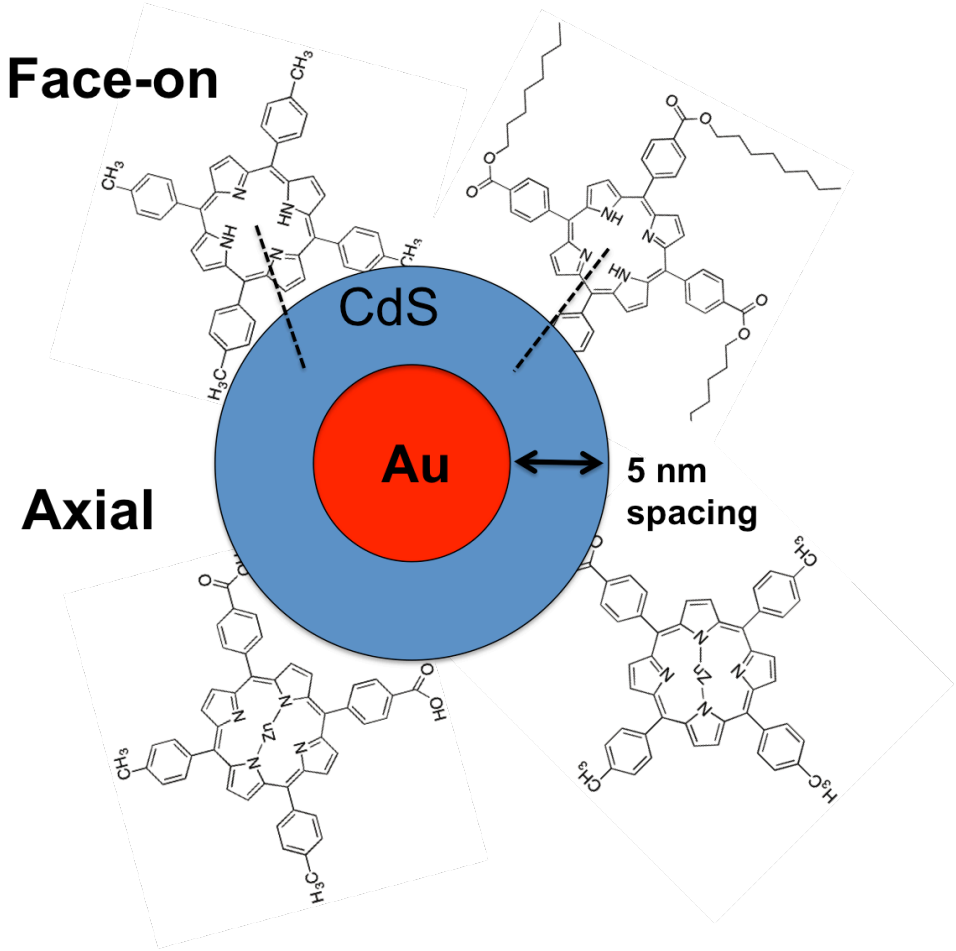

Figure 8.10. Illustration of the porphyrin binding to the hybrid gold nanoparticles. Porphyrins with two different binding modes, axial and face-on will be utilized to study their effect on the optical characteristic of the porphyrin post-binding.

The purpose of the binding to the hybrid nanoparticles, illustrated in Figure 8.10, was to increase the extinction coefficient of the lower energy absorption bands, known as

the q-bands. The Soret absorption band, which derives from the highest energy HOMO to LUMO transition has a large extinction coefficient, greater than 10^5. The q-bands derive from degeneracy lifting of the HOMOs and have extinction coefficients significantly lower than that of the Soret transition. Their extinction coefficients also decrease as the peak wavelength increases approaching 10^2 for the longest wavelength energy band. The q-band absorption bands range from around 500-700 nm, allowing for optimal spectral coupling with the plasmon resonance.

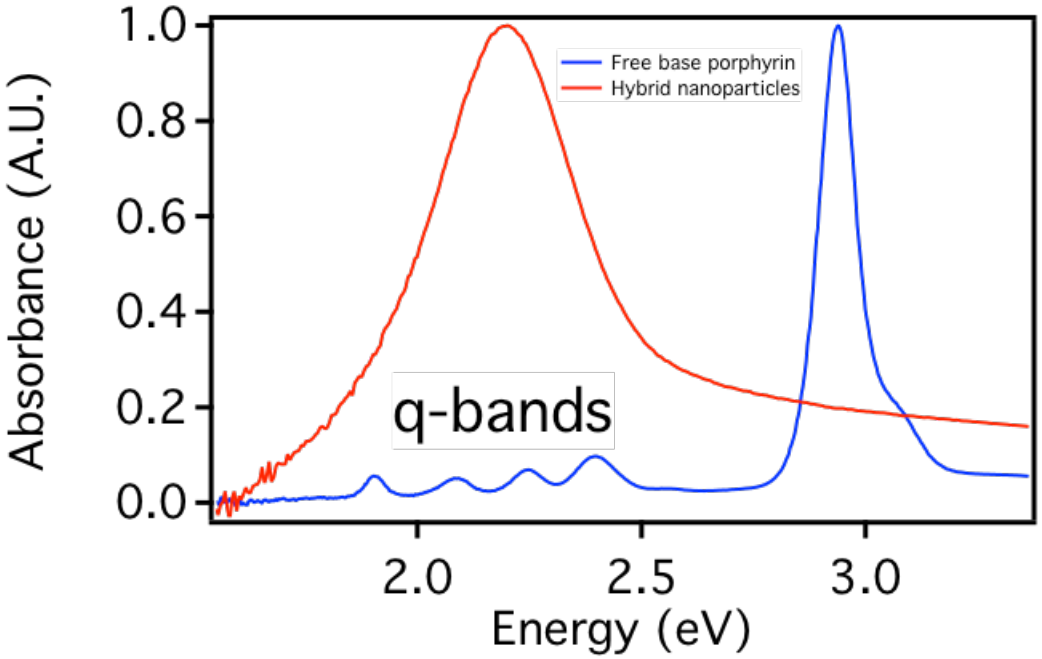

Figure 8.11. UV-vis absorption spectra of free base porphyrin and the plasmon resonance of hybrid gold nanoparticles with a thin CdS shell.

In Figure 8.11, the normalized absorption spectra of hybrid gold nanoparticles with a thin CdS shell and that of free base porphyrin is shown. It is clear that the plasmon band spectrally overlaps with the lower intensity q-band absorption peaks. Utilizing this

overlap can increase the absorption of the bound porphyrin in the lower energy region, resulting in an increase in the potential photocurrent production in a device incorporating them.

8.2: Binding Method

Tetraphenyl porphyrin was the base porphyrin and was modified with carboxylic acid functional groups on the meso positions of the phenyl rings. Studies were conducted to qualitatively identify binding events via changes in UV-vis absorption and fluorescence quenching. FTIR was also utilized to identify the chemical signals associated with the binding groups. UV-vis absorption and fluorescence were then utilized to understand the electronic effects of coupling with hybrid nanoparticles.

In order to maximize loading on the particle shell and align the plasmon dipole with the absorption dipole of the porphyrin, both flat binding to the face of the porphyrin molecule, and axial binding via mono-substituted and bi-substituted porphyrins, were characterized and compared to identify the optimal binding configuration. The different porphyrin species were separated from a mixed pot using column chromatography. Metallated porphyrins were also used to prevent protonation of the porphyrin or binding to the face of the nanoparticles through the center pyrrole units.. The presence of any free protons can effectively displace the center metal ion necessitating the use of a proton scavenger. The proton scavenger also serves a dual purpose. The carboxylic acid need to be deprotonated in order to form a carboxylate anion, which will bind to a free cadmium site.

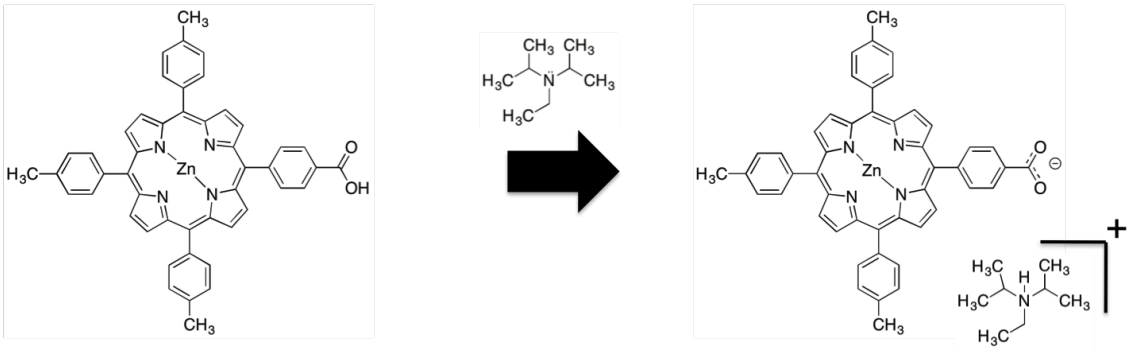

Figure 8.20: Illustration of the deprotonation of Tritolylphenyl acidporphyrin (TTPa) with N-ethyldiisopropyl amine.

N-ethyldiisopropyl amine acts as an efficient proton scavenger because of its two bulky isopropyl groups which help to prevent coordination but are still large enough to facilitate a proton binding to the lone pair on the nitrogen atom. Tetrahydrofuran (THF) was the solvent used for the binding system since it can dissolve both the oleylamine-capped nanoparticles and the porphyrin. Unbound porphyrin was separated from the nanoparticles with bound porphyrin using centrifugation. The washes were repeated until no detectable signal from the porphyrin remained in the absorption spectrum. The nanoparticles were then redispersed into clean THF at the original volume of the nanoparticle solution used.

Absorption spectroscopy was the main tool for study of the extinction coefficient enhancement. First, a comparison of the unbound to the bound porphyrin signal was conducted to show if any electronic interaction between the plasmon was evident. Changes in the height and location of the q-bands were monitored to characterize the degree of plasmonic interaction.

FTIR spectroscopy was then utilized to probe the chemical makeup of the nanoparticle surface. Comparison of the FTIR spectra of oleylamine-capped nanoparticles, unbound porphyrin and the nanoparticle-porphyrin system was conducted to confirm binding to the surface. The electronic interaction of the porphyrin can be estimated by utilizing the ratios of the q-band absorption modes. The four orbital model describes two degenerate HOMOs which can be affected by metal binding and porphyrin functionalization. Binding of the porphrin to the hybrid nanoparticles should also affect this degeneracy and can be monitored by observing changes in the relative intensities of the q-bands. Finally, comparison of the q-band absorption before and after binding was utilized to estimate the extent of the electronic interaction between the porphyrin and nanoparticle.

8.2.1 Enhancement of Extinction Coefficient and Quantification of Binding

In order to gather accurate values for the enhancements in the extinction coefficient, concentrations of surface molecules were extracted and compared to absorption measurements. Calibration curves were first created for each of the stock porphyrin solutions by drying down and weighing a specific amount of each porphyrin .The extinction coefficients were then extrapolated from the calibration curves and used in the concentration analysis. The difference in concentration of the original porphyrin and unbound porphyrin, post-reaction, was the amount of porphyrin available for binding to the nanoparticles.

The concentration of the porphyrin bound to the nanoparticles was calculated based on the absorption of the washed nanoparticles and compared to the amount of porphyrin available for binding. Two factors were used to calculate the amount of

enhancement. First, the ratio of the Soret band height to the q-band height and second the absorption of the porphyrin bound to the particles compared to the maximum available porphyrin for binding.

The goal of this project was to not only optimize plasmonic enhancement but to quantify the amount of porphyrin loading onto the nanoparticles. Plasmonic enhancement of the porphyrin extinction coefficient was calculated based on the ratio of the specific q-band heights to the Soret band peak. A relative increase in the q-band height indicates an enhancement in the extinction coefficient. The amount of porphyrin must then be calculated in order to compare the total absorption of the bound vs. unbound porphyrin. Finally, the number of nanoparticles was calculated in order to investigate the loading efficiency of the porphyrin on the different particle types. These data will allow us to formulate a system with optimal shell thickness and composition for the maximum amount of extinction coefficient enhancement.

8.3: Porphyrin Synthesis and Characterization

TTP,TTPa and DTDPa porphyrins were all synthesized by Dawn Marin in the Walter research group via the method by Litte et al.[156 157] A condensation reaction is conducted through addition of pyrrole, benzaldehyde, 4-carboxybenzaldehyde and acetic anhydride conducted in propionic acid. The reaction produces a mixture of TTP,TTPa and DTDPa. The DTDPa will be produced in both cis and trans forms, where the cis has phenyl acid groups located adjacent to one another and the trans phenyl acid groups are located on opposite sides of the porphyrin.

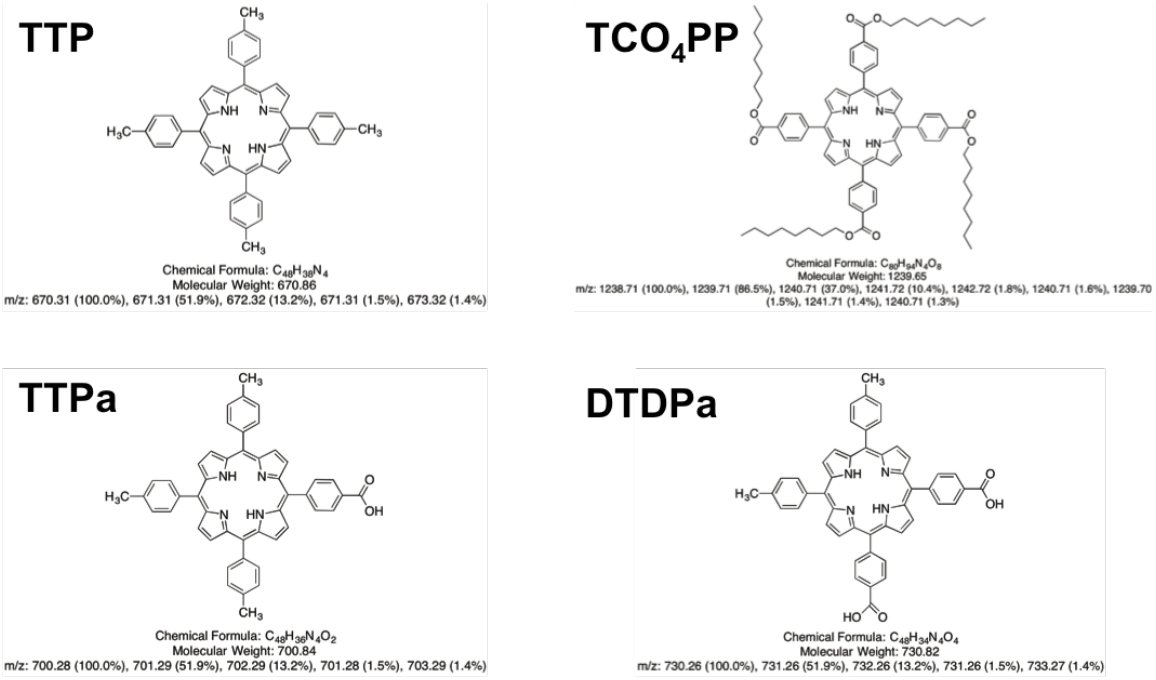

Figure 8.30: Structure of TTP (top left) , TCO_4PP (top right), TTPa (bottom left) and DTDPa (bottom right) with their corresponding mass analysis shown underneath.

The four porphyrins show in Figure 8.30 range in mass from 670.86 grams per mole for TTP to 1239.65 for TCO_4PP. `The theoretical calculations were then compared to the experimental data from the ESI-MS experiments and are summarized in appendix B. Deviations from the theoretical values, stem from isotopic variances of the large macromolecules. The applied cone voltage applied during analysis is 120 V, which improves the sensitivity for the larger molecules. The porphyrin solutions were first separated using column chromatography. The dried porphyrin stock solution contains TTP,TTPa and DTDPa and was dissolved into dichloromethane and added to the a silica gel column. The less polar, TTP eluted off the column first with addition of dicholoromethane. Once the column ran clear, a 1% methanol in dicholormethane was utilized to elute the TTPa from the column. Finally, 10% methanol was utilized to elute

DTDPa from the column. The porphyrin solutions were dried and redispersed into clean THF. Finally, before injection into the spectrometer, the samples were diluted into a 10% anhydrous methanol solution in dichloromethane.

The mass spectrometry data was compared to theoretical calculations from the ChemDraw software. The porphyrins were unmetallated when the ESI-MS experiments were conducted in order to facilitate ionization. The porphyrins utilized were all based on the TTP base structure. The differences lie on the substituents of the meso position of the phenyl ring. The TCO_4PP porphyrin contains a carbooctyl group, while TTPa and DTDPa contain one or two carboxylic acid groups respectively.

TTP, TTPa and TCO4PP were all characterized previously and ESI-MS was utilized to confirm their identity with no further characterization. DTDPa, however had not been previously purified, therefore NMR spectroscopy was also utilized to identify if the cis or trans confirmation was more abundant in solution, based on the similar characterization done by Walter et al.[117]

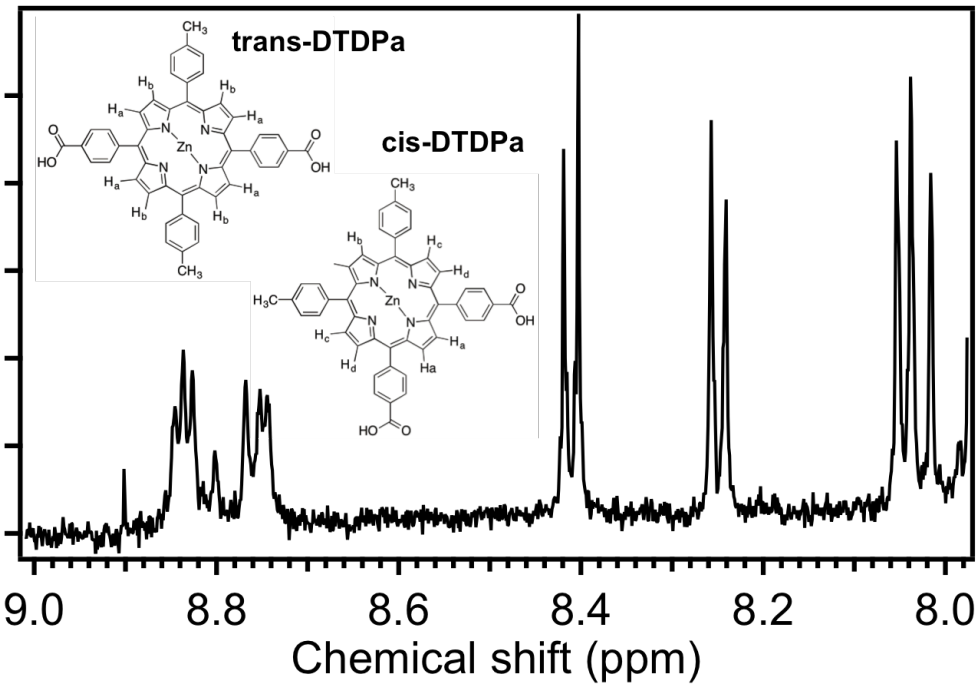

Figure 8.31: ^{1}H NMR (500 MHz. $CDCl_3$) of beta pyrrole hydrogen region of DTDPa purified from a silica gel column.

The NMR spectrum in Figure 8.31 shows two sets of triplets at 8.7 and 8.9 ppm, indicative of the beta pyrrole hydrogens of a doubly substituted carboxyphenyl porphyrin. The splitting pattern of two doublets with overlaid singlets matches more closely to that of the cis ocnfirmation from the work done by Walter et al. The doublets at 8.4 and 8.3 are from the hydrogens on the phenyl rings of the porphyrin. The peaks at 8.0 are also from phenyl hydrogens but the unique splitting and presence of extra peaks indicates that the solution contains impurities.[117]

8.4: FTIR Characterization of Porphyrin Binding

For the porphyrin binding studies, TTPA and DTDPa were utilized. These porphyrins possess one or two carboxylic acid groups which can bind to un-passivated metal sites on the semiconductor surface of the nanoparticle. As a control, TTP was

added to the nanoparticles in the same manner to monitor changes when there is no binding group present. The porphyrin species with carboxylic acid groups should preferentially bind axially to the nanoparticle surface with the outer edge of the porphyrin extending out into the solution. In order to bind the porphyrins to the nanoparticle surface they were mixed with a solution of washed hybrid nanoparticles for at least one hour. The nanoparticles were pelleted down with centrifugation and washed to remove any unbound porphyrin molecules.

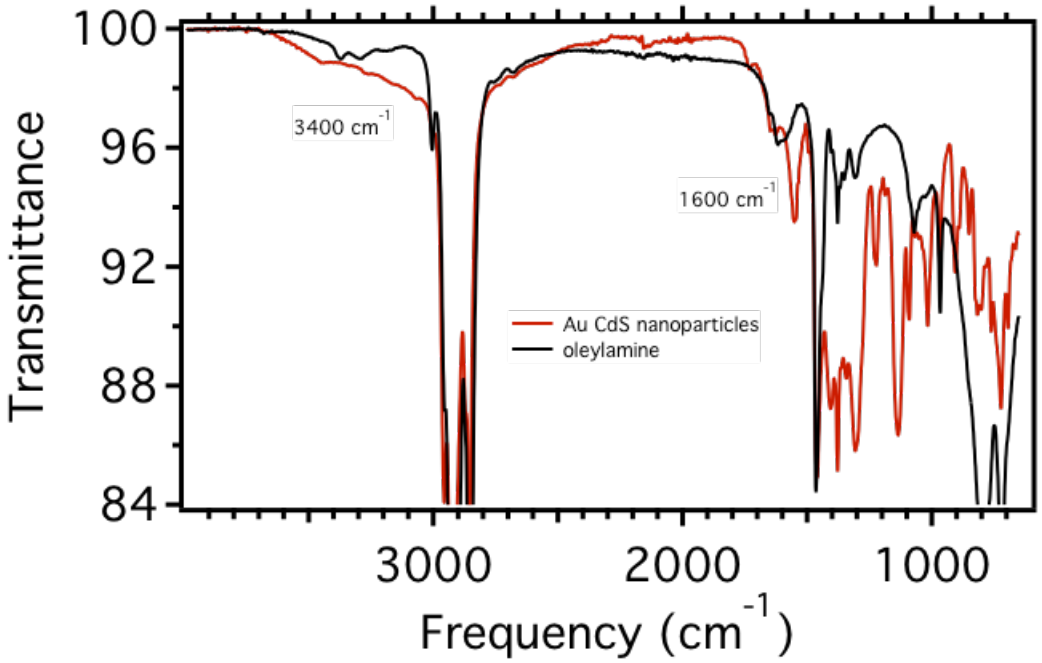

Figure 8.40 FTIR spectra of washed Hybrid CdS shelled gold nanoparticles capped with oleylamine and free oleylamine.

The FTIR spectrum in Figure 8.40 shows the chemical signal of the oleylamine capped nanoparticles and neat oleylamine. The key signals were the amine stretch at 3400

cm^{-1}, which was observed as a doublet for the neat oleylamine and the broad N-H wag at 1600 cm^{-1}. Once bound to the nanoparticles, the bound amine showed a broadening of the amine stretch at 3400 cm^{-1} and narrowing of the N-H wag. These changes point to an interaction with the nanoparticle surface, as the stretching mode was broadened and the wag was sharpened to a narrow frequency. The spectra of the free porphyrin was then compared to that of the porphyrin bound to nanoparticles to both identify binding was present and elucidate the chemical nature of the binding.

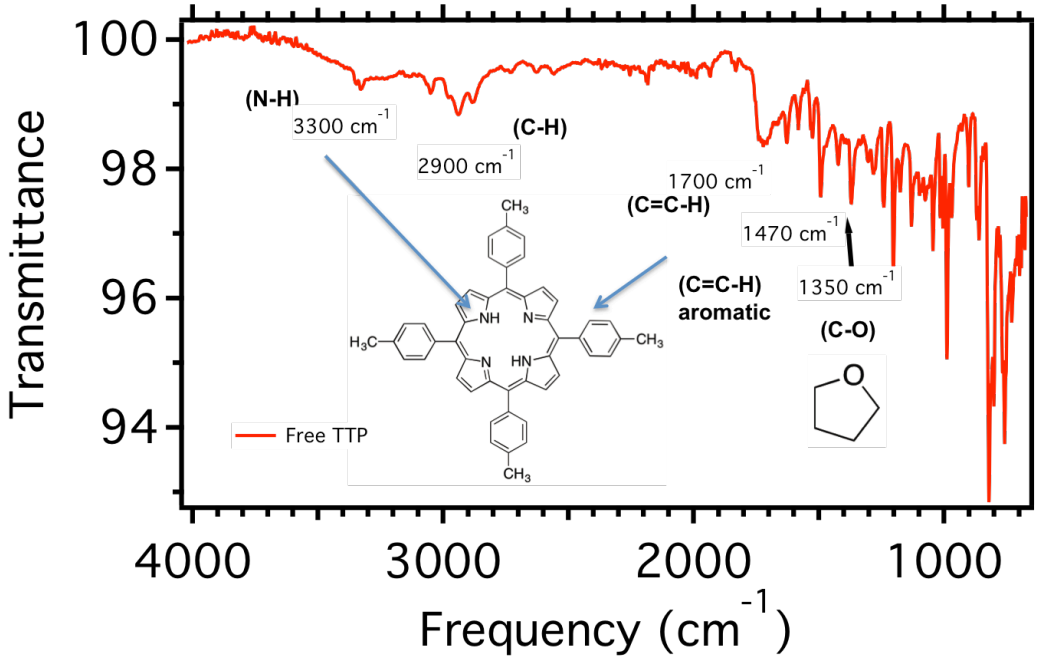

Figure 8.41 FTIR spectra of un metallated TTP porphyrin.

The FTIR spectrum in Figure 8.41 shows unmetallated TTP dried from tetrahydrofuran (THF). The peak at 1350 cm^{-1} corresponds to THF ,which may have coordinated to the porphyrin. The peaks at 3030 and 1700 correspond to alkene

hydrogens while the peak at 1470 was indicative of the aromatic alkene group of the phenyl ring. The small doublet at 3300 represents the center pyrrole hydrogen stretching modes. The rest of the spectrum was dominated by alkane stretching modes. This spectrum will be compared to the same porphyrin in the presence of hybrid nanoparticles to investigate the nature of their interaction.

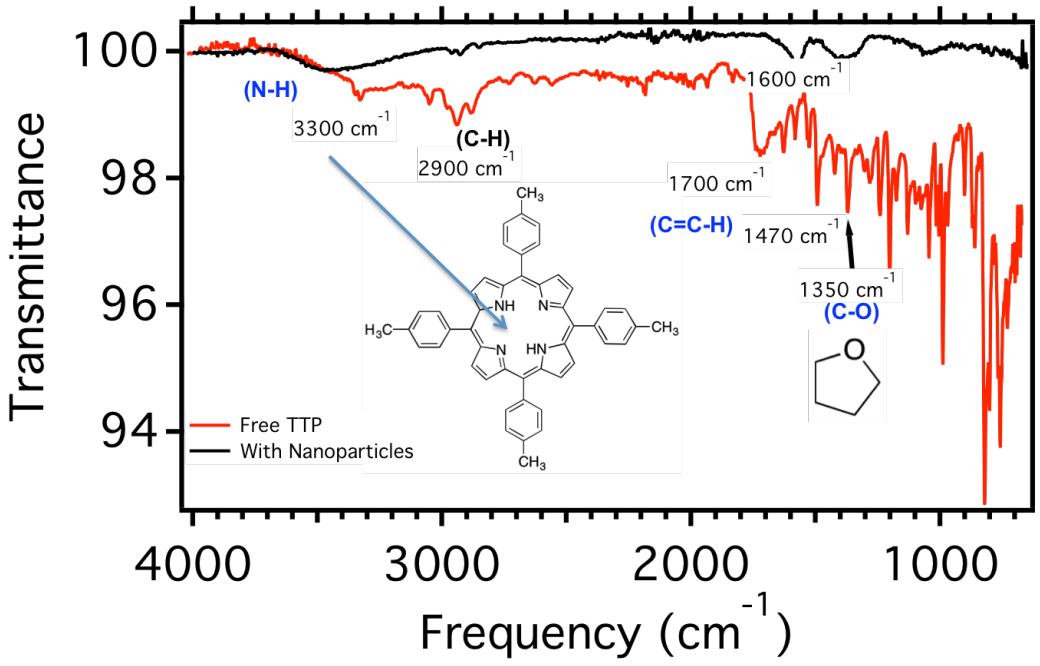

Figure 8.42 FTIR spectra of un metallated TTP and TTP mixed with hybrid gold nanoaprticles with a CdS shell.

In Figure 8.42, the spectrum of both free TTP and TTP mixed with hybrid gold nanoparticles is shown. The most significant change was the broadening of the pyrrole amine stretch and increase in frequency, indicative of interaction with the nanoparticle surface. The only other significant change in the spectrum upon mixing with the

nanoparticles was a broadening and shift of the alkene signals at 1700 and 1450 cm^{-1}. This gives insight into the nature of the interaction with the nanoparticle surface. The center ring seemed to have the strongest interaction, as observed by the large shift and broadening in the pyrrole hydrogen vibration modes, suggesting that coordination of the pyrrole units with the surface cadmium sites was occurring. The shifts in the alkene signals also suggested that the porphyrin backbone and tolyl groups on the methine positions must also be interacting with the nanoparticles. These data indicate that the porphyrin was lying flat on the nanoparticle surface.

In order to compare the effects of binding orientation and changes in the optical spectra, the FTIR of the carboxylic acid-functionalized porphyrins must also be investigated. To ensure any binding proceeds strictly through the acid group located on the outside of the porphyrin, the center ring was metallated with zinc. The spectroscopic signal was then observed in the presence of nanoparticles and without nanoparticles.

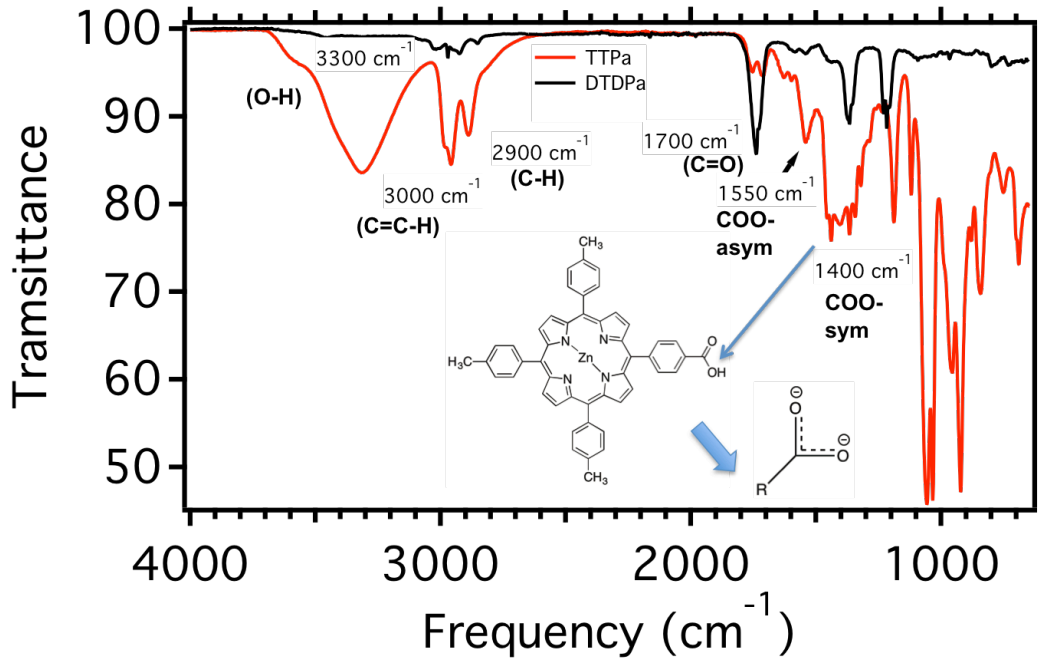

Figure 8.43 FTIR spectra of metallated TTPa and DTDPa

In Figure 8.43, the FTIR spectrum of the acid-functionalized porphyrins are shown. The stretches, although varying in intensity, lie at the same frequency for both TTPa and the DTDPa. The O-H stretch of the acid group was strongest in the TTPa but also present in DTDPa. The next significant peak was the carbonyl stretch located at 1740 cm^{-1}. The stretch is much stronger in the DTDPa porphyrin, while the TTPa porphyrin carbonyl stretch was split into a doublet.

Carboxylate stretching modes were also present in both porphyrins, with the asymmetric vibration at 1550 cm^{-1} and the symmetric at 1400 cm^{-1} for TTPa. The carboxylate modes in DTDPa lie at the same frequency with the asymmetric mode being shifted to slightly higher frequency and split into a doublet. These spectra were then compared to nanoparticles with bound porphyrin.

In order to bind the porphyrin to the nanoparticle surface, the nanoparticles are first washed with ethanol to remove the native ligand coating. The porphyrin was then mixed with ethyldiisopropyl amine in THF to ensure the acid groups remain deprotonated and the center pyrrole units do not become protonated as well. The mixture was stirred for one hour before the nanoparticles are separated via centrifugation and decantation of the supernatant containing unbound porphyrin.

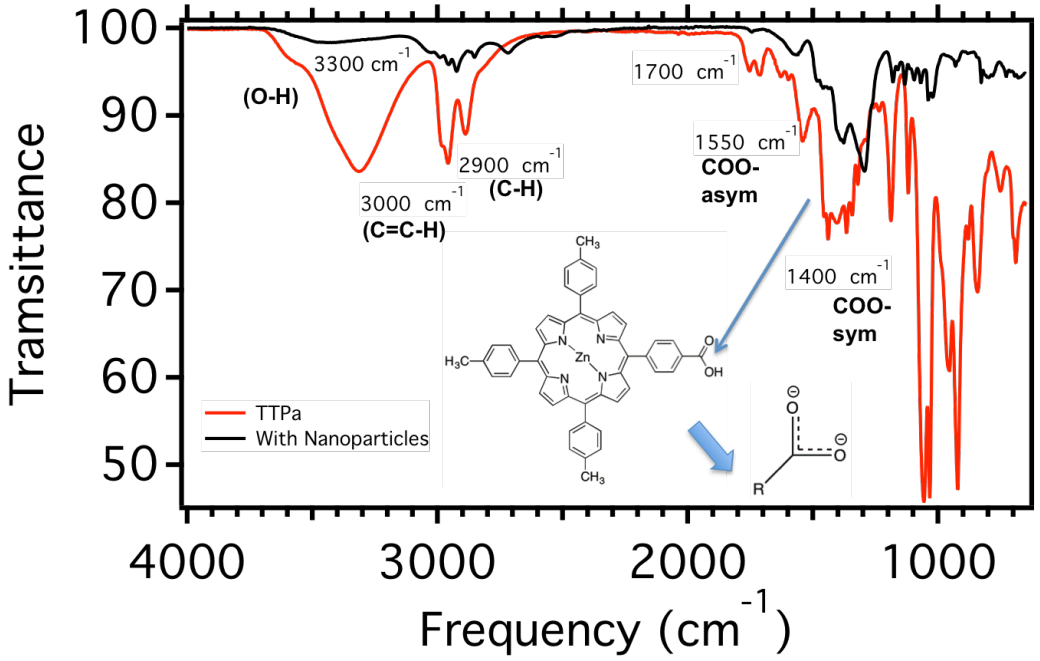

Figure 8.44 FTIR spectra of free metallated TTPa and TTPa mixed with hybrid gold nanoparticles with a CdS shell.

In Figure 8.44, the FTIR spectra of free TTPa and bound TTPA is shown. The first significant feature is the disappearance of the large O-H stretch centered at 3320 cm^{-1}, indicative of deprotonation of the carboxylic acid group in the presence of

ethyldiisopropylamine. The broadened carbonyl stretch around 1700 cm^{-1} also disappeared during the binding reaction. The disappearance of these peaks, indicates that the acid groups of the porphyrin were fully converted to the carboxylate configuration.

Finally, the carboxylate stretching modes in the free porphryin, are fused into a single broad peak, but after binding, two distinct asymmetric and symmetric stretching modes were observed at 1500 and 1350 cm^{-1} respectively. These data show that not only was the acid group deprotonated to from the carboxylate anion, but the carboxyalte anion was interacting with the nanoparticle surface.

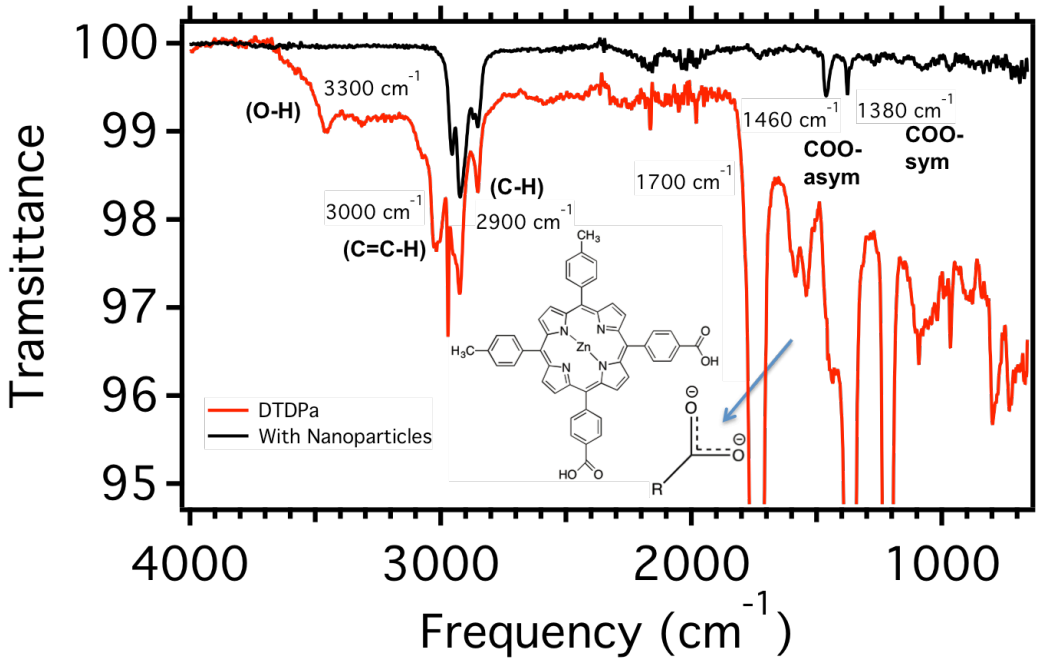

Figure 8.45 FTIR spectra of free metallated DTDPa and DTDPa mixed with hybrid gold nanoparticles with a CdS shell.

A similar trend in the FTIR spectrum, seen in Figure 8.46, was observed for the binding of DTDPa as was seen for TTPa. The oxygen-hydrogen stretch at 3300 cm^{-1} and

the carbonyl stretch at 1700 cm^{-1} both disappear upon addition of nanoparticles. The spectrum of bound DTDPA was mainly featureless for the rest of the spectrum except for two carboxylate peaks located at 1460 and 1380 cm^{-1} for the asymmetric and symmetric stretches respectively.

The FTIR spectra of the acid-substituted porphyrins varies greatly from that of TTP ,which only shows interaction between the inner pyrroles and the conjugated backbone of the porphyrin. The acid substituted TTPa and DTDPa, both showed a disappearance of the oxygen-hydrogen stretching modes and the carbonyl stretching mode upon mixing with the hybrid nanoparticles. This dissapearacne was assigned to the formation of a carboxylate anion due to the presence of N-ethyldiisopropyl amine and interaction with they nanoparticle surface.

Although, the carboxylate signal was observed in the free porphyrin, the disappearance of the carbonyl and oxygen-hydrogen stretch and the shift of the carboxylate signal upon mixing with nanoparticles, indicates a binding event. These data were used to identify the face-on binding mode for TTP and the axial binding mod for TTPa and DTDPa. The spectral effects of these different binding modes will be characterized via UV-vis absorption to elucidate the optimal configuration for absorption enhancement.

8.5: UV-vis Absorption Characterization of Porphyrin Binding

Changes in the UV-vis spectra were analyzed next. The porphyrin and nanoparticles were mixed with ethyldiisopropyl amine at room temperature, as mentioned in the previous section. The spectra of all species before and after the binding reaction were taken and compared to a calculated theoretical spectrum. The aliquots were taken

such that the concentration of porphyrin remains the same in each sample and the nanoparticle spectrum is representative of the nanoparticle concentration in the reaction vessel. This means, with careful analysis, the solution absorbance can be compared as is, without correction for concentration changes.

The goal of this project was to enhance the extinction coefficient of the porphyrin by binding to the hybrid nanoparticle surface. In order to study this enhancement, a theortetical maximum absorbance must be calculated. The theoretical spectrum was calculated by simply adding the porphyrin and nanoparticle spectrum before the binding reaction. The theoretical spectrum represents the maximum absorption if no coupling occurs between the porphyrin and nanoparticles and represents a simple mixing of the nanoparticles in solution.

A series of porphyrins were utilized to analyze the effects of binding groups in the presence of the hybrid gold nanoparticles. The unmetallated TTP was used to monitor the effect of having the center ring interacting with the nanoparticles while the metallated TTP was used to monitor coupling effects when there are no possible binding groups present. TTP represented the face-on binding of the porphyrin, where the porphyrin should lie flat on the nanoparticle surface. TTPa and the DTDPa , were utilized to monitor the affects of external binding groups, representing the axial binding porphyrin.

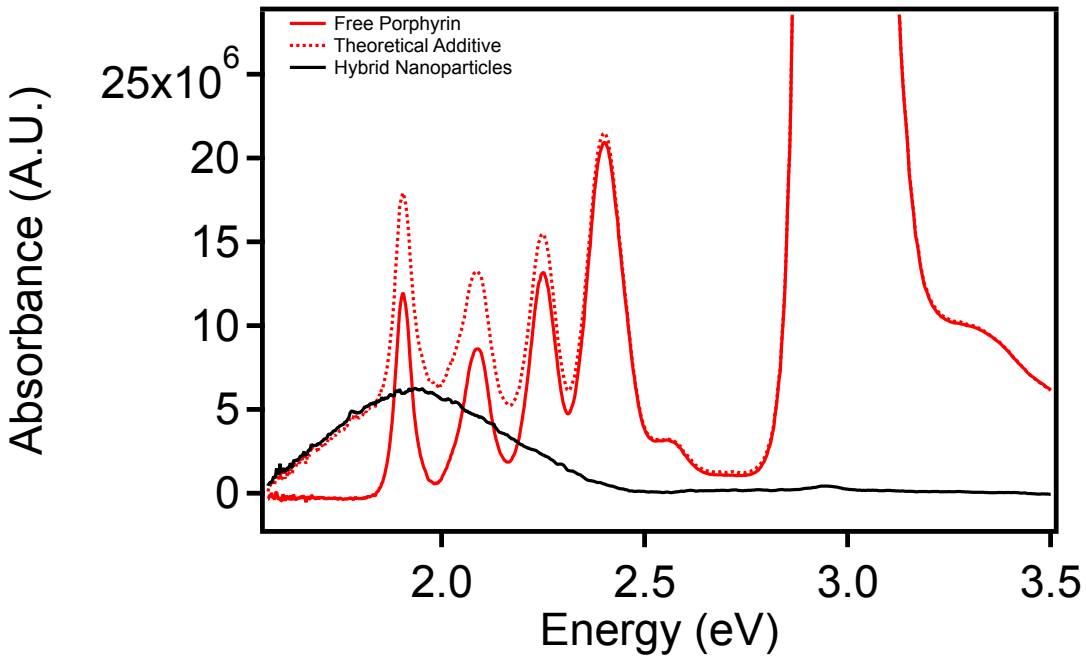

Figure 8.50 Absorbance spectra of free unmetallated TTP, hybrid gold nanoparticles with a CdS shell and the theoretical additive spectra.

The absorbance spectra in Figure 8.50, show the original nanoparticle and porphyrin spectra, as well as the theoretical additive of the two. The 4-q-band modes from 1.8 to 2.4 eV, were representative of an umetallated porphyrin and was the area where plasmonic coupling should be maximized. The large Soret absorption at 2.9 eV should show the least interaction with the plasmon mode due to the low spectral overlap, and was not shown, in order to further highlight the coupling region of the spectrum. The theoretical spectrum, follows the plasmon resonance until around 1.5 eV where the spectrum increases beyond that of both the porphyrin and the nanoparticles.

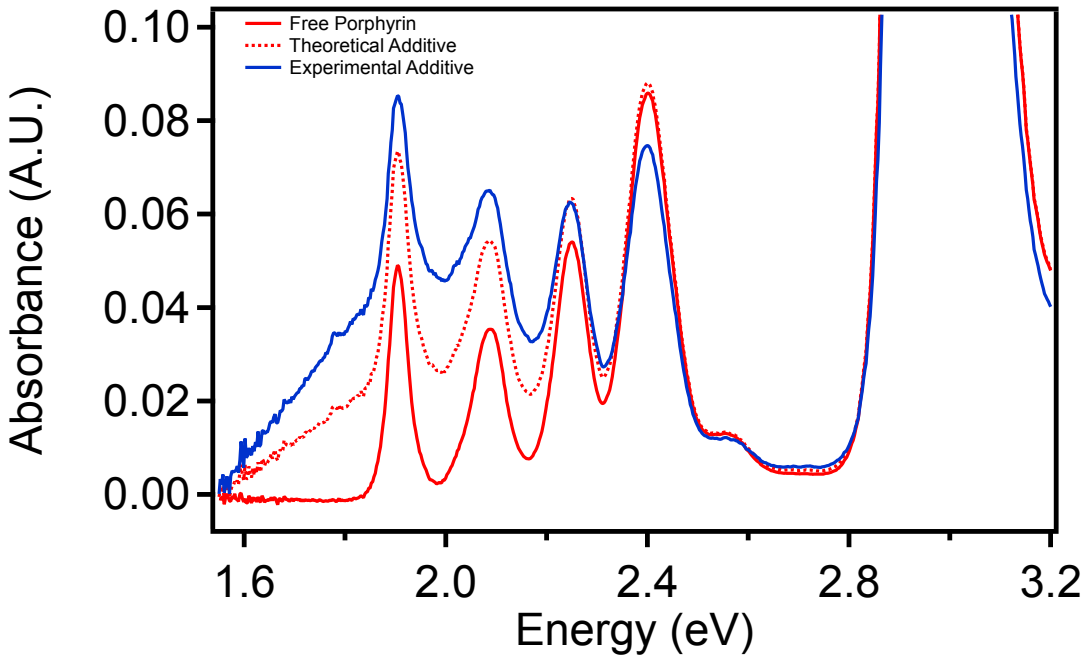

Figure 8.51 Absorbance spectra of free unmetallated TTP, hybrid gold nanoparticles with a CdS shell ,the theoretical additive and experimental spectra.

The spectra in Figure 8.51 show that of the original porphyrin solution, experimental additive, and the theoretical additive spectra. The experimental additive differs from the theoretical drastically between 1.8 and 2.1 eV, where a much larger increases was observed. The higher energy q-bands were only slightly higher than that of the original and theoretical spectra. The shape and magnitude of the experimental spectrum increased homogenously and the targeted coupling area increased by 18% more than the theoretical.

Binding through the center pyrroles or stacking of the phenyl rings would be the only interaction possible with the nanoparticle surface, according to the FTIR spectra. The absorption data shows that, when the center is unoccupied, a strong coupling is possible which resulted in an increase in absorption of the porphyrin. The metallated TTP

was used to monitor the effect when the pyrroles occupied. These data should help elucidate whether face-on binding through the center ring or peripheral phenyl rings is more effective.

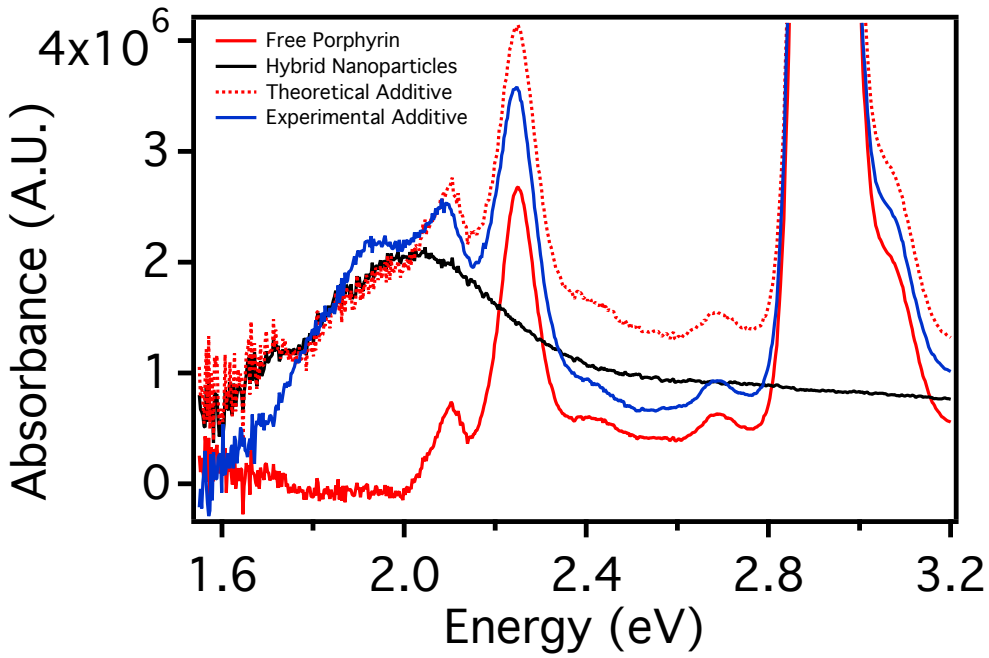

Figure 8.52 Absorbance spectra of free Zinc-metallated TTP, TTP mixed with hybrid gold nanoparticles with a CdS shell, the theoretical additive and experimental additive spectra.

In Figure 8.52, the same porphyrin binding experiment was conducted with the zinc metallated TTP. The first significant difference was a loss of the two lower energy q-bands, stemming from the increase in symmetry upon binding of a zinc ion into the center porphyrin ring. In reference to the Gouterman four orbital model, the HOMO level of the porphyrin consists of two degenerate bands. When unmetallated, the center pyrrole units are anisotropic and the HOMO bands shift slightly. This creates two extra transitions,

which are directionally-dependant. Binding of the metal eliminates this HOMO energy splitting and two q-band absorption modes remain.[124]

The experimental additive spectrum was, for the most part slightly lower than that of the theoretical spectrum. The experimental was only higher in a small region, 1.8 to 2.0 eV, which also corresponds to the maximum of the plasmon resonance. This increase was small and could stem from simply a small error in the sample aliquot. Overall, the area of the experimental additive was 52% lower than that of the theoretical additive. This decrease could be due to nanoparticle or even porphyrin aggregation in solution. The metallated TTP should have very little chance to interact with the nanoparticles, since the center ring was occupied by zinc ions. The phenyl rings could wrap around the nanoparticle but would both limit the amount of porphyrin able to interact and increase the distance of interaction.

TTPa and DTDPa were analyzed in the same manner after the binding experiments were conducted. The phenyl acid-functionalized porphryins were all previously metallated with zinc, to ensure any binding was due to the phenyl acid groups. These data will investigate the effects of the axial binding porphyrins and will then be compared to the face-only binding TTP.

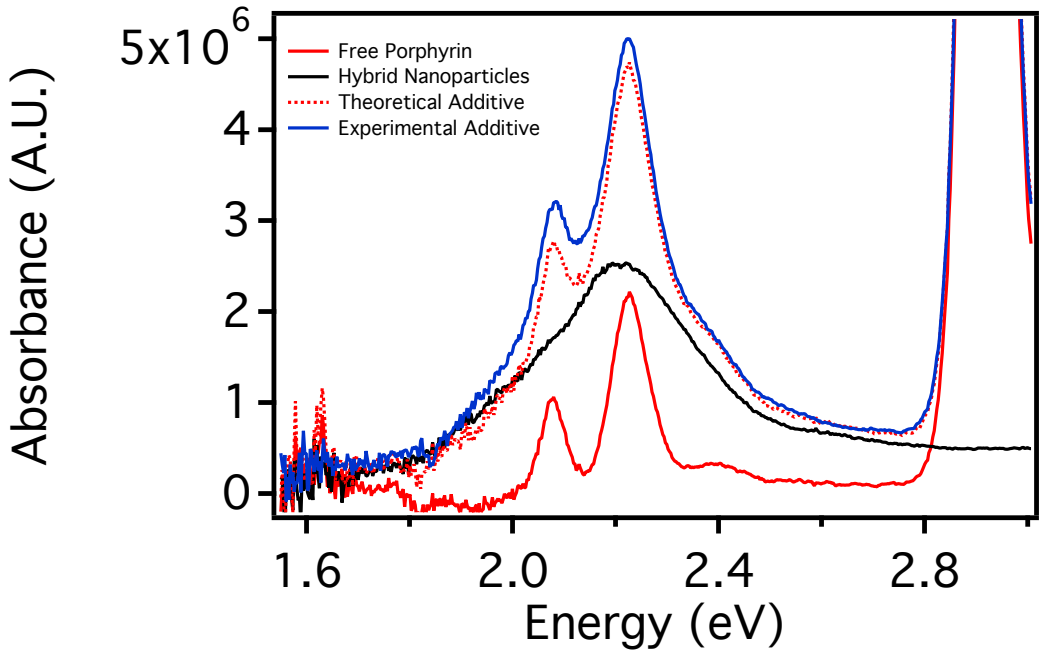

Figure 8.53 Absorbance spectra of free Zinc-metallated TTPa, TTPa mixed with hybrid gold nanoparticles with a CdS shell, the theoretical additive and experimental additive spectra.

In Figure 8.53, the spectra of the TTPa binding is shown, with the original spectra as well as the theoretical and experimental additive spectra. The experiment was run similar to the TTP experiments with the experimental additive spectra being slightly higher than the theoretical, not just at the plasmon maxima but throughout the whole curve. The shape of the porphyrin remained the same for the spectra as well but with a 13% increase compared to the theoretical additive.

This trend was markedly different from the TTP spectra which seems to change shape slightly in the presence of the nanoparticles. This could point to the difference in binding mode of the acid-functionalized porphyrin, which according to the FTIR experiments, binds axially via the acid group. The spectra seemed to match the original

and theoretical porphyrin spectra around the Soret band region, showing that the increase was solely due to interaction with the plasmon oscillation and not due to scattering, which would be the only contribution from the nanoparticles at that frequency.

The spectra was next be compared to the DTDPa porphyrin. This porphyrin should bind in a similar to TTPa, but should have a higher binding affinity due to the extra carboxylic acid group. The two phenyl acid groups, should provide a more stable anchor to the nanoparticle surface, and also help to increase the equilibrium of bound and unbound porphyrin. The extra phenyl acid group could alter the binding configuration slightly to lie somewhere in between face-on and axial, which could in turn affect the plasmonic coupling.

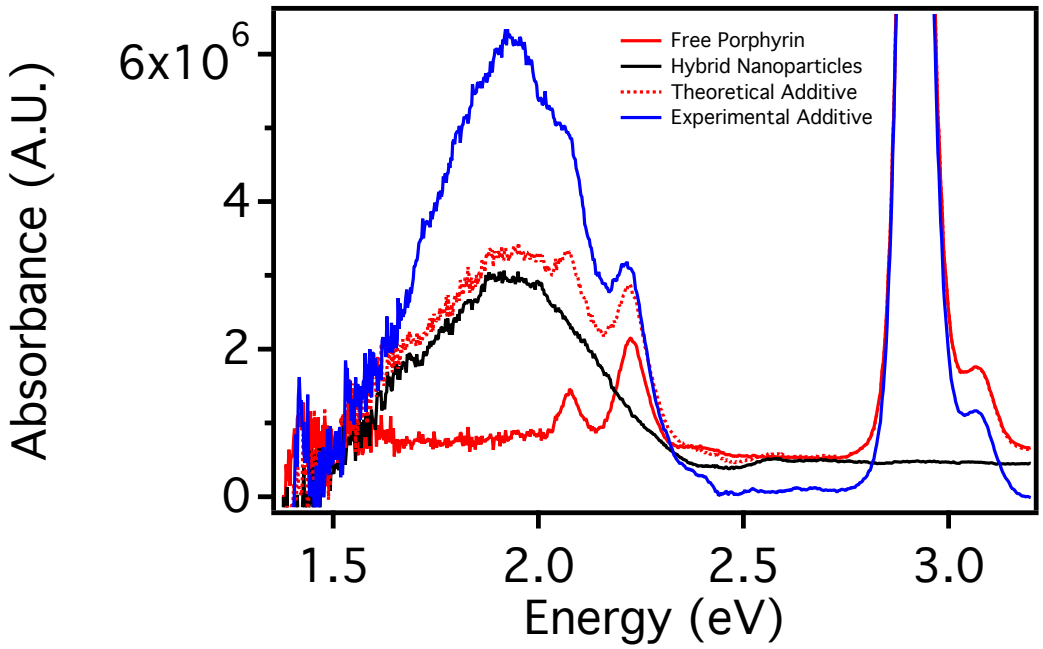

Figure 8.54 Absorbance spectra of free Zinc-metallated DTDPa porphyrin, DTDPa porphyrin mixed with hybrid gold nanoparticles with a CdS shell, the theoretical additive and experimental additive spectra.

Figure 8.54, shows the spectra of the binding conducted with the DTDPa porphyrin. A strong increase, relative to the theoretical additive spectra was observed, with the maxima centered around 2.0 eV. The experimental additive spectrum also looked very similar to that of the nanoparticle absorption with the q-band modes overlaid. This result, seemed to prove that the acid-functionalized porphyrins were optimal for increasing the solution-state absorption and that the axial binding mode was also preferred for plasmonic coupling.

The increases with DTDPa were more substantial as well, pointing to either stronger electronic interaction or an increased in the number of bound porphyrin, both due to stronger binding of the two acid groups. The shape of the porphyrin spectrum was similar to that of the nanoparticle absorbance as well, indicating either a stronger coupling of the porphyrin absorption spectrum with the nanoparticle absorbance or the presence of free nanoparticles in solution. In either case, the amount of absorbance was still enhanced from that of the separate counterparts, pointing to a strong electronic interaction between the two.

In order to quantify the increase in absorbance, the deviation from the theoretical was averaged for a series of samples utilizing TTP, TTPa and DTDPa and were plotted vs. the number of binding groups for each porphyrin type. These data help to show the effect of face-on vs. axial binding on the enhancement of the porphyrin absorption.

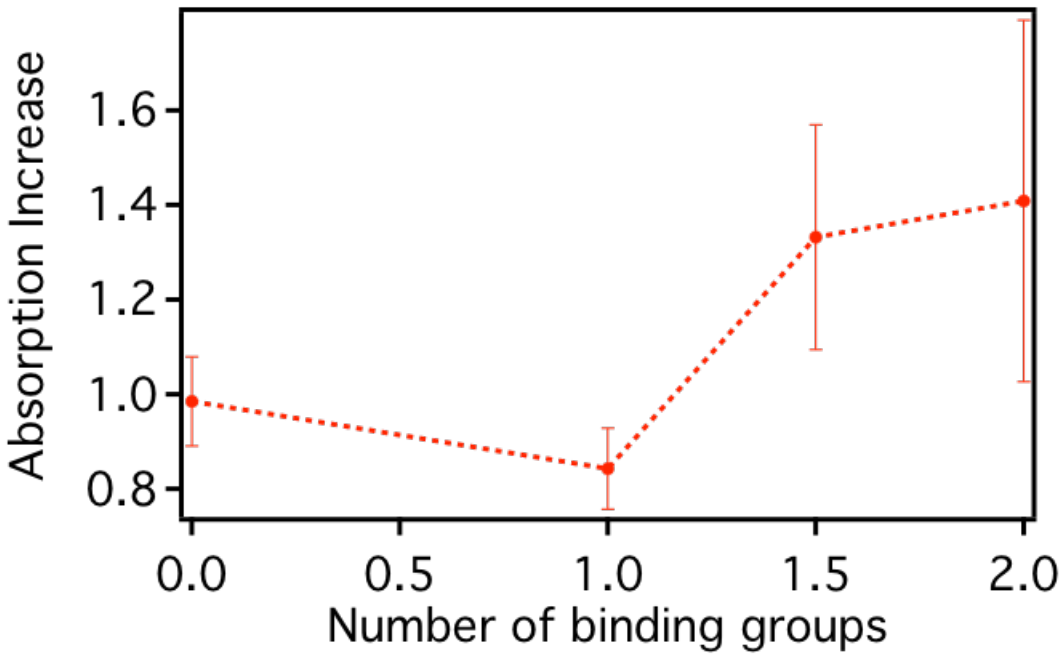

Figure 8.55 Plot of the average deviation of the absorption from the theoretical maximum vs. number of binding groups on the porphrin. Metallated TTP is counted as 0 binding groups and unmetallated TTP is counted as 1.5 binding groups with the two deptronated pyrroles.

The deviation in Figure 8.55 was calculated by taking the area of the theoretical and experimental additive spectra from 1.8 to 2.4 eV. This region represents the maximum spectral overlap of the plasmon with the q-band spectra The area of the experimental spectrum was then divided by that of the theoretical to calculate the deviation. The change was minimal ,but there is a direct correlation to the number of binding groups and the enhancement of absorption from the theoretical maximum, with the DTDPa showing the highest increase.

This increase was explained by a stronger binding due to the presence of two acid groups and the preferential, axial binding induced by having the cis confirmation of the

porpyrin. Unmetallated tetraphenyl porphyrin showed a value similar to that of the DTPA, within error, which points an equal strong binding event with the pyrrole units. The slight decreases in absorbance can be explained by the binding configuration fo TTP compared to that of DTDPa. The face-on binding is physically more cumbersome and takes up more space on the nanoparticle surface. Similar to the quantum dot binding, if some population of unbound porphyrin was present in solution, then a smaller concentration of bound porphyrin would produce a lower enhancement. The metallated tetraphenyl porphyrin was lowest which could be due to hindered and weaker face-on binding with a center zinc ion.

TTPa showed a similar value to that of metallated TTP, which was estimated to have the lowest binding affinity. This can again be explained through the equilibrium of bound to unbound porphyrin. TTPa should bind in the desired configuration, but one binding group may only provide weak coupling which can dissociate over time. This dissociation may produce a signal which is more representative of the unbound case, showing minimal enhancement. To further confirm this trend, tetra(4-carbcooctoxyphenyl) porphryin(TCO_4PP) was utilized for binding. The unmetallated TCO_4PP was expected to bind similarly to TTP. The 4 methine units contains long alkyl chains which can interact like the phenyl rings of TTP.

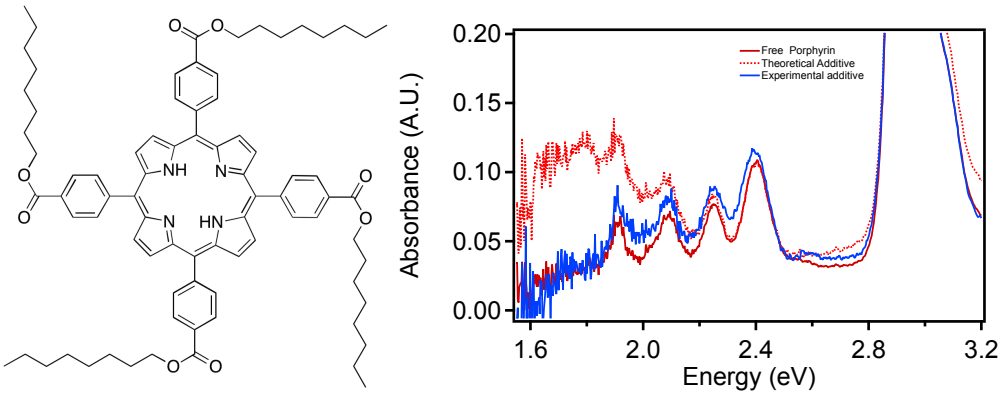

Figure 8.56 Illustration of TCO_4PP porphyrin (left) and the absorption spectra of the free porphyrin, theoretical and experimental average with CdS shelled nanoparticles.

Figure 8.56 shows both the illustration of TCO_4PP and the absorption before and after binding. The results show a 20% drop from the theoretical absorption. This value was slightly higher than the metallated TTP and slightly lower than the unmetallated TTP. This indicates a binding configuration intermediate to the two porphyrins. The carbonyl groups may show some affinity for the nanoparticle surface whiel the inner pyrrole groups are also available for binding. This means that a more stable interaction, than experienced with the metallated TTP could be seen, while the alkoxy groups could provide some spacing from the nanoparticle surface. This sets the basis for the use of TCO_4PP in fluorescence experiments. The porphyrin should interact intermediate to that of both metallated and unmetallated TTP.

8.6: Fluorescence Characterization of Porphyrin Binding

Using the assumption that the interaction between TCO_4PP and TTP are similar, fluorescence of TCO_4PP was utilized to monitor the effects of the hybrid nanoparticles on the porphyrin fluorescence, to monitor the case with no binding groups. DTDPA and TTPa were used, once again, to monitor the effect of a binding group on the porphyrin

fluorescence. Fluorescence can be useful tool to probe the extent of electronic interaction between the porphyrin and the nanoparticles.

In order to effectively model the nature of fluorescence coupling in porphyrins. The interaction between porphyrin and gold nanoparticles, without a semiconductor shell was studied. This study was conducted with TCO_4PP, which should have a strong interaction via the inner pyrrole groups. This system represents the strongest coupling regime, with the porphyrin laying flat on the nanoparticle surface. Strong electronic coupling with the gold plasmon will produce quenched fluorescence. Close proximity to the metal surface should increase the efficiency of energy transfer into the gold.[74] [43] A stronger interaction with the nanoparticle surface would also increase the amount of porphyrin loading, which should increase the quenching signal as well.

To study how the porphyrin binding configuration effects the electronic interaction, gold nanoparticles were added to a solution of TCO_4PP. The UV-vis and fluorescence signal was utilized to calculate the quantum yield of the porphyrin after addition of nanoparticles. The bare gold nanoparticles were utilized for TCO_4PP only, as this should represent the closest proximity to the gold nanoparticle surface with a face-on binding.

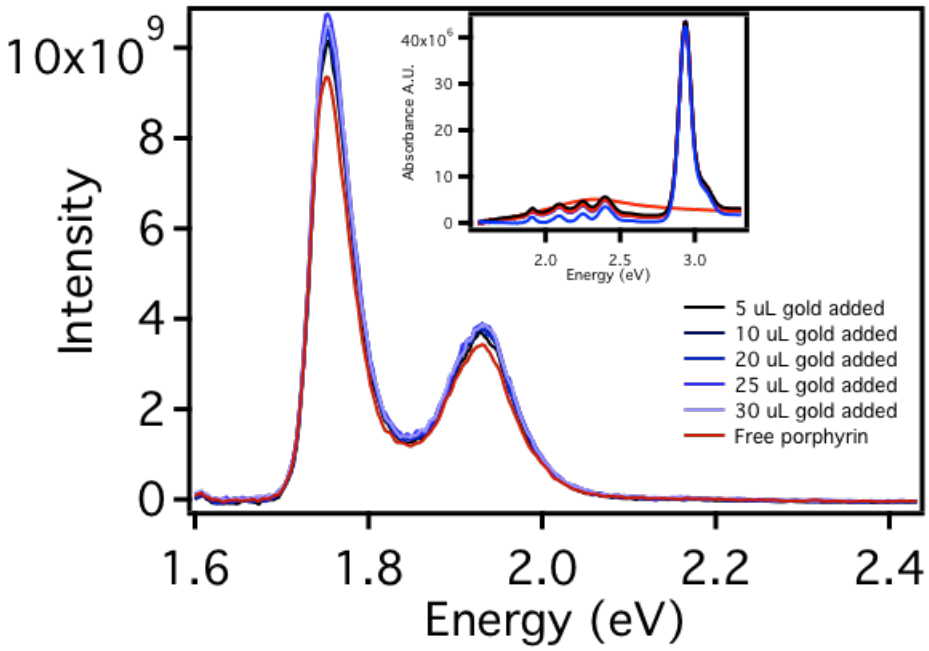

Figure 8.60. Fluorescence spectra of TCO_4PP in THF (red) and with sequential addition of gold nanoparticles (blue). As the traces get lighter blue, the gold nanoparticle concentration increases. The inset shows the corresponding absorbance spectra.

In Figure 8.60, the fluorescence and absorbance spectra for the TCO_4PP quenching experiments is shown. The red spectrum corresponds to the porphyrin without any gold added. The fluorescence spectra showed two distinct peaks at around 1.7 eV and 1.9 eV, with the former showing the highest intensity. The spectra show no shape change but do show intensity increases which correspond to the increasing gold concentration in both the absorbance and fluorescence.

In order to quantify intensity changes, the quantum yield was calculated, using the above equation, where PL is the fluorescence area of the sample, PL_{dye} is the fluorescence area of rhodamine in methanol, abs is the absorbance calculated at 400 nm, abs_{dye} is the absorbance calculated at 400 nm for rhodamine in methanol and RI is the

refractive index of the solvent used for either the dye or sample. The absorbance of the sample was taken at the excitation wavelength of 410 nm.

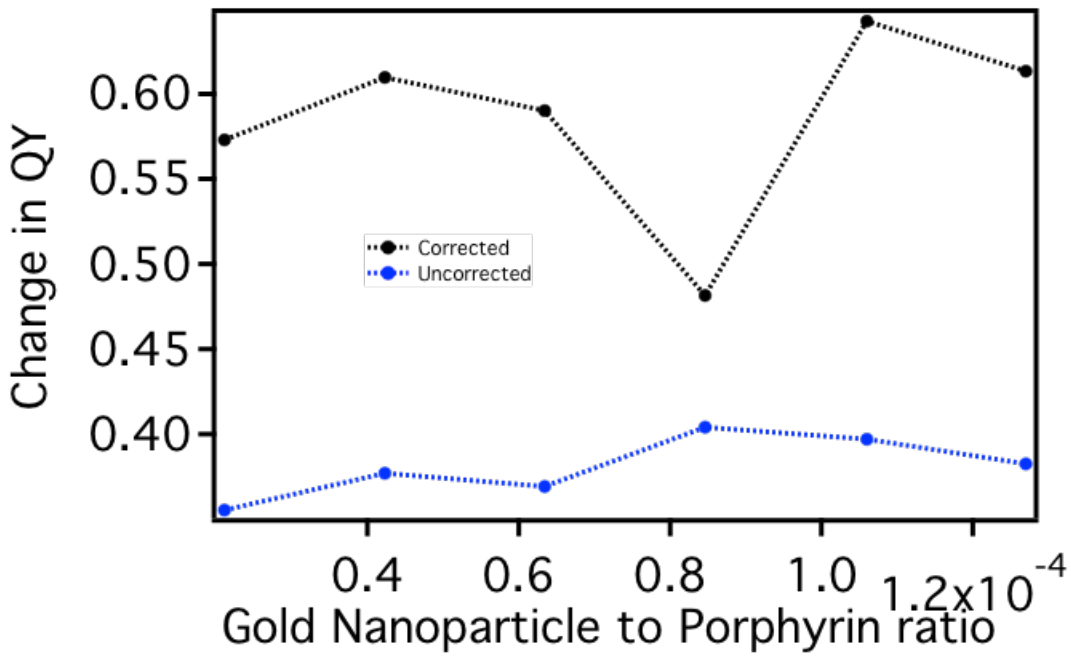

Figure 8.61 Change in Quantum yield of TCO_4PP and gold nanoparticles vs. porphyrin to gold nanoparticles ratio. The corrected spectra (blue) refers to the samples corrected for absorption of gold nanoparticles.

In Figure 8.61 the relative quantum yield vs. porphyrin to nanoparticle ratio is shown. As the plot proceeds to the right, the number of gold nanoparticles in solution increases. The general trend shows an initially sharp decrease in the quantum yield followed by a saturation at about 30% of the original quantum yield. The nanoparticles were expected to quench the porphyrin fluorescence via energy transfer of the excited porphyrin to the gold nanoparticle. The closer the porphyrin lies to the metal surface, the more efficient the energy transfer process will be. This phenomenon was evident in the

TCO_4PP sample, as the fluorescence was strongly quenched after the first addition of nanoparticles.

When the spectra was corrected for the absorption of the gold nanoparticles, the trend stays constant but the extent of quenching decreases. This pointed to absorption of the incident excitation by the nanoparticles, or inner filter effects, having around a 20% contribution to the quenching. This phenomenon seemed to change the overall magnitude of the quenching but not the overall shape ,therefore ,these effects were not accounted for in subsequent experiments.

The effect of binding to hybrid nanoparticles on the porphyrin fluorescence were next investigated. The samples were made using TCO_4PP as well as TTPa and DTDPa porphyrins. CdS shelled gold nanoparticles ,with a 5 nm radius shell were utilized to compare the quenching effects to the absorption studies in the previous chapter. The quantum yield was calculated in the same manner as the experiments in Figure 8.61

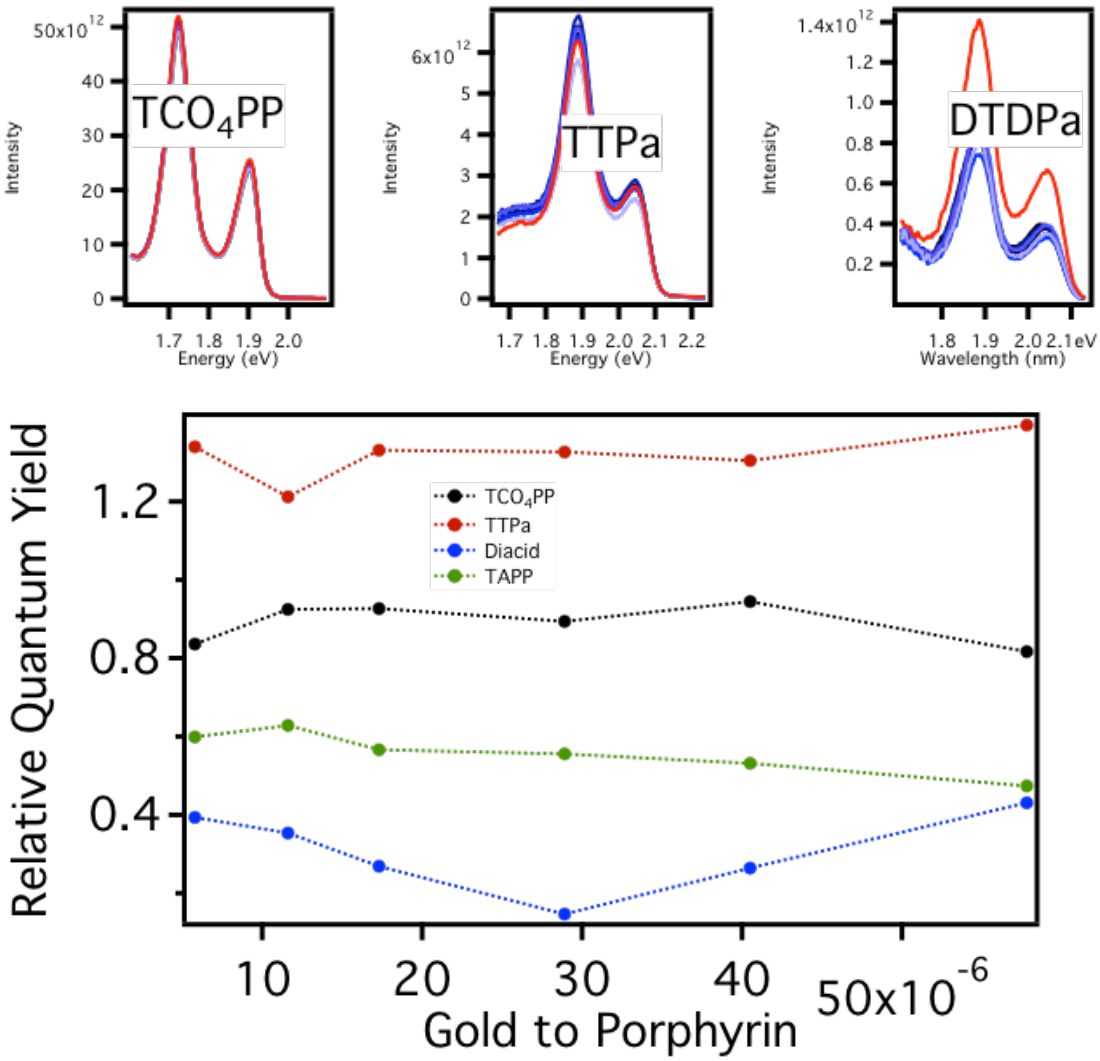

Figure 8.62. Fluorescence scans (Top) of TCO_4PP, TTPa and DTDPA (left to right). Change in Quantum yield of porphyrin as a function of gold to porphyrin ratio (bottom). The raw spectra for TAPP is not shown

The plot in Figure 8.62, shows the quantum yield as the gold concentration increases to the right. The TCO_4PP and DTDPa samples showed quenching upon nanoparticle addition, with the DTDPa showing a large initial quench that saturated around 40% of the original fluorescence. TTPa showed an enhanced quantum yield at all

concentrations. Assuming a strong electronic interaction was necessary to quench the porphyrin fluorescence, then TCO_4PP and the DTDPa show the strongest interaction.

The DTDPa proceeded through the binding of two acid groups to the surface of the nanoparticle. FTIR confirm the presence of carboxylate groups upon mixing with the hybrid nanoparticles. This binding must allow for electronic coupling resulting in quenching of the porphyrin fluorescence. In the case of TCO_4PP, the carboxy groups on the porphyrin arms may have a weak interaction with the particle surface but the unmetallated center pyrrole units would provide a stronger interaction. This face-on contact should produce significant electronic interaction in order to quench the fluorescence. The less significant quenching in the TCO_4PP was interpreted through the binding method. The face-on binding would occupy a much larger area on the nanoparticle surface, decreasing the total number of coupled porphryins. A larger percentage of the DTDPa porphyrins can be loaded on the nanoparticles surface if they bind axially, causing more drastic quenching.

The enhancement in the TTPa was interpreted as a weak plasmonic coupling with the porphyrin. The quenching was minimized since the binding interaction was weaker but the single binding group puts the nanoparticle in close enough proximity to still allow coupling of its external plasmon dipole with the porphyrin. The nanoparticles could also help to break up any porphyrin aggregates, which would effectively increase the quantum yield, although no signal of significant aggregation is observed. In order to further confirm this binding assumption, 5,10,15,20 Tetrakis (4-aminophenyl) porphyrin (TAPP) will be bound to the nanoparticle surface in the same manner

8.7: TAPP Binding

8.7.1: FTIR Characterization of TAPP Binding

TAPP is a symmetrical porphyrin with four amine groups located on the phenyl rings. The amines group have a stronger binding affinity for the nanoparticle surface, which should promote higher porphyrin binding. The amine groups should produce more of a face-on binding configuration when all four are attached to the nanoparticle surface. The porphyrin was metallated in order to compare the face-on binding, without interaction via the pyrrole units in the center ring. This binding configuration should mimic that of both TCO_4PP and DTDPA. In order to confirm this trend, FTIR, UV-vis and fluorescence spectra were utilized to compare the data.

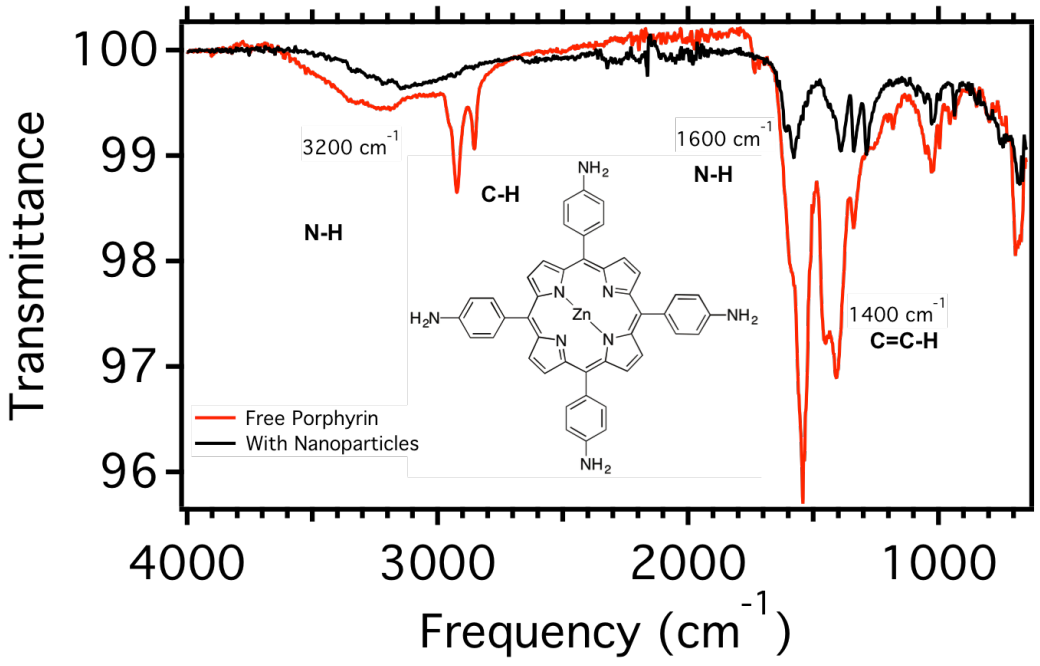

Figure 8.710 FTIR spectra of free metallated TAPP and TAPP mixed with hybrid gold nanoparticles with a CdS shell.

The FTIR in Figure 8.710 shows shifts similar to that of the binding seen by TTP . A shift in both the alkene signal at 1400 cm-1 indicated that binding through the saturated porphryin backbone was both occurring. The shifts in the amine signals at 3200 and 1600 cm-1 ,seen when the particles were mixed with the porphyrins, confirms interaction with the external amine groups. These data show that, while the porphyrin was attached via the amine groups, the conjugated porphyrin backbone is also interacting with the nanoparticle surface. This confirms that binding through all four amine groups produces a more face-on binding configuration.

8.7.2: UV-vis Absorption Characterization of TAPP Binding

The strong electronic coupling with the TAPP, through the amine groups should be similar to that of DTPA. The binding face-on binding configuration mimic that TTP and TCO_4PP. Investigation into spectral changes could further elucidate which interaction dominates. The UV-vis absorption spectra was first investigate to monitor changes in the intensity of absorption. The theoretical spectra were calculated as before in section 8.5.

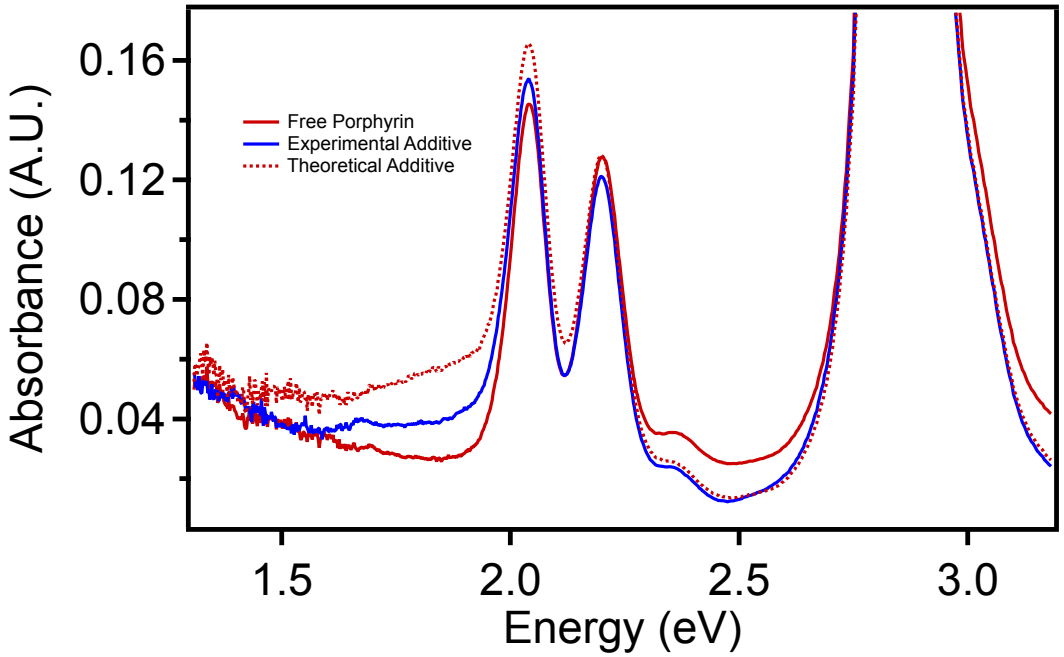

Figure 8.720 Absorbance spectra of free Zinc-metallated TAPP, TAPP mixed with hybrid gold nanoparticles with a CdS shell, the theoretical additive and experimental additive spectra.

The spectra in Figure 8.720 showed similar changes to that of the porphyrins with no binding groups. The theoretical additive spectra was 11% higher than the experimental additive. This value shows indicates little affect on the absorption, a trend that was most similar to the metallated TTP. The deviation from the theoretical absorption was also within 10% error of the metalalted TTP value, indicating a similar face-on binding, where the four phenylamine groups are also bound to unpassivated cadmium sites on the nanoparticles surface.

8.7.3: Fluorescence Characterization of TAPP Binding

Fluorescence quenching experiments were also conducted using TAPP in a similar manner as in section 8.6. TAPP was mixed with gold nanoparticles, coated in

CTAC. The experiment was conducted in water to preserve both the gold nanoparticle and TAPP solubility. The quantum yields were then calculated and plotted vs. the gold nanoparticle to porphyrin ratio. Although, the gold nanoparticles do not have a cadmium sulfide shell, the stock concentration remains the same as the hybrid nanoparticles.

In Figure 8.62 the quenching as a function of gold to porphyrin ratio is shown, with the TAPP porphyrin experiment added (green). It should be noted that the gold nanoparticles in the TAPP experiment did not have a shell. This was due to the fact that TAPP has a higher solubility in water and the gold nanoparticles are originally water soluble. The trend looked very similar to the DTDPa porphyrin showing an initial sharp decrease in the quantum yield to about 60% that of the original porphyrin, which remains constant after subsequent additions.

The unmetallated TCO_4PP showed a weak quenching which was explained by low porphyrin loading on the nanoparticle due to steric hindrance of the porphyrin. TAPP shows a much more significant quenching, due to the strong electronic interaction through the bound amine groups. The porphyrin must then either be much more strongly quenched to balance the low loading through a face-on interaction or be bound in a manner more similar to the DTDPa porphyrin. The deviation from the theoretical additive spectra of TAPP matched most closely to that of the metallated TTP, which was assumed bind face-only. These data allowed us to have a more insightful view of the binding modes and the effects on electronic interaction.

The porphyrin binding configuration, face-on or axial, seemed to have the biggest effect on the composite absorption. Face-on binding seems to result in a 20-40% lowering of the absorption, possibly through porphyrin and nanoparticle aggregation of the

samples. The use of the inner pyrrole to anchor the unmetallated TTP to the nanoparticle resulted in a small enhancement of the absorption, either allowing for higher plasmonic coupling or a decrease in aggregation. The acid functionalized porphyrin showed increases from the theoretical composite absorption, showing enhancement of the absorption through coupling with the hybrid gold nanoparticle.

DTDPa showed the largest enhancement, as consequence of the stronger binding of two acid groups, while still allowing axial binding. The quenching of the porphyrin seemed to mainly depend on the nature of the surface interaction TCO_4PP, which binds face-only with interactions via the octoxy arms, shows a weak quenching of about 20% which stays relatively constant. This binding should mimic that of TTP porphyrin, which all bind face-only.

TTPa ,however, showed a slight enhancement of the quantum yield. This enhancement could result from either decreased aggregation or a coupling with the porphyrin fluorescence transition, similar to the quantum dot coupling in chapter 7. An alternate theory to this enhancement could be due to the binding mode of the porphyrin, the acid group could provide the optimal configuration for plasmonic coupling with porphyrin excitation. This increased excitation could result in an increase in sample quantum yield as well. The increased excitation could be interpreted as the excited plasmon, donating energy to the porphyrin excitation

The DTDPa and TAPP show a strong quenching which can be attributed to the much stronger surface interaction via the two acid groups and four amine groups on the porphyrin. Fluorescence excitation was used to study the nature of electronic interaction with TTPa. TTP was also compared to that of TTPa to determine if the porphyrin was

indeed electronically coupled in both binding configuration. Excitation scans, where the emission maxima was monitored and the excitation was scanned to investigate which frequencies produced the maximum fluorescence ,were conducted. The spectra should mirror the absorption an show if the gold nanoparticles are altering the porphyrin electronic transitions.

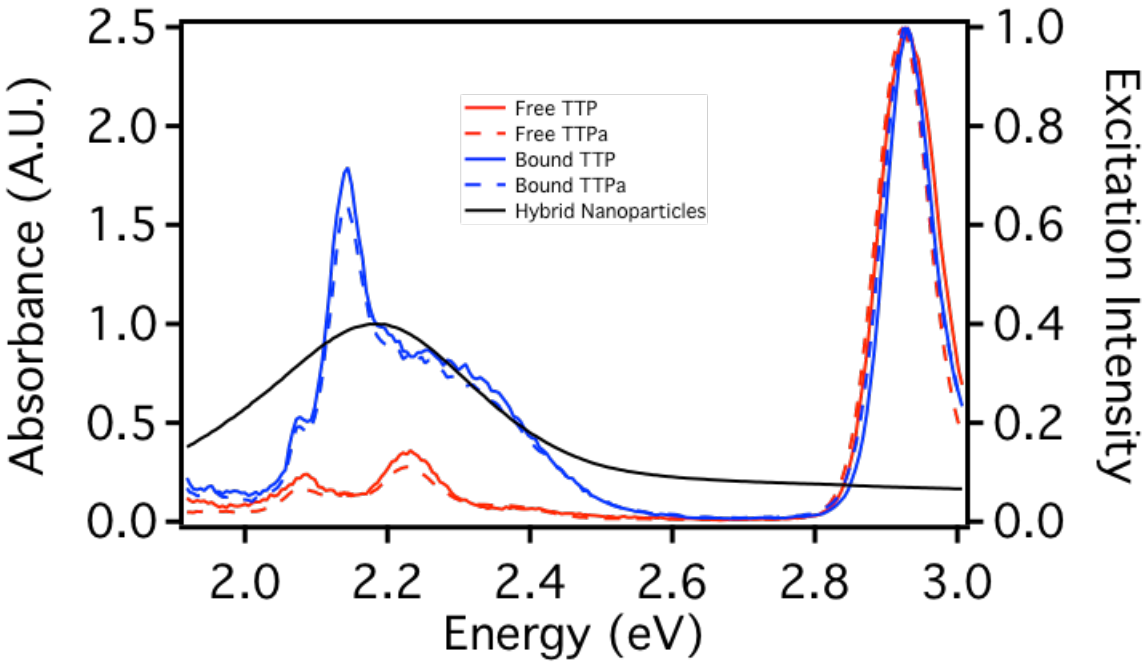

Figure 8.730 Fluoresce excitation spectra of bound TTPa (dashed blue) ,bound TTP (solid blue), free TTPa (dashed red) and free TTP (solid red). The fluorescence was monitored at the 656 nm fluorescence peak and scanned from 300 nm to 900 nm. The porphyrin spectra were normalized to the Soret peak. The plasmon resonance of the hybrid nanoparticles is also shown (solid black).

In Figure 8.730 a significant change in the excitation spectra was observed upon binding to the gold nanoparticles, for both TTP and TTPa. A broadening and increase in

intensity of the q-band contribution was observed, which mirrors the plasmon resonance of the hybrid gold nanoparticles. The spectrum was not only broadened, but the height of the q-band, relative to the Soret, was also drastically enhanced. The nanoparticles do not, show any fluorescence, therefore, any contribution to the excitation from the plasmon resonance confirms direct electronic coupling. The slight increase of the TTP excitation spectrum, in comparison to TTPa, could be due to the closer, face-on binding mode of TTP, allowing for stronger coupling with the fluorescence These observations prove that the increases in sample quantum yield were not strictly due to decreased aggregation or other solution effects but a property of increased plasmonic coupling with the radiative transition of the porphyrin.

The fluorescence experiments help to elucidate the electronic nature of the two different binding configurations and the effect of binding groups on the porphyrin. The face-on binding mode seen in TCO_4PP produces a small quenching effect, when coupled to the nanoparticle surface through the center pyrrole units. TAPP, which binds face-on but was anchored to the surface via the external amine groups, displays a much stronger quenching, which was attributed to the higher binding affinity of the four amine groups. DTPA showed a similar strong quenching, although an axial binding was observed from the FTIR. This quenching was mainly attributed to an increase in porphyrin loading and a high affinity for the nanoparticle surface. Finally, the TTPa showed an enhancement in fluorescence which was attributed to a weaker coupling which allowed for a plasmonic enhancement of both the excitation and the spontaneous fluorescence rate.

8.8: Analysis of Q-Band Degeneracy Lifting

The relative height of the q-band absorbance was used to understand changes in the electronic structure of the porphyrin upon binding. The Goutermann four-orbital model assumes that the excited state of the porphyrin consists of two HOMO levels with slightly offset energies and two degenerate LUMO levels.

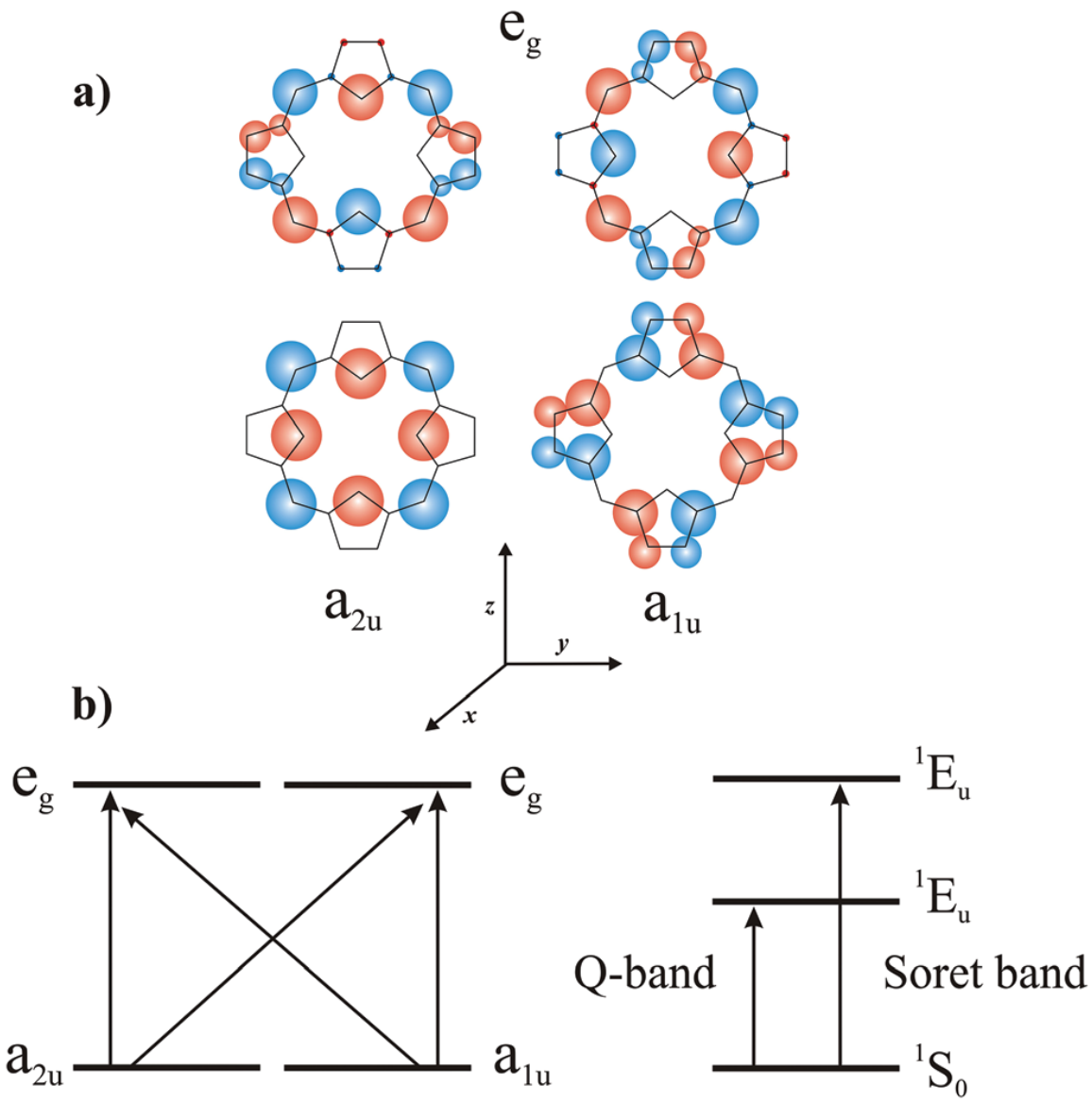

Figure 8.80 Illustration of the Four-orbitals used to describe the porphyrin excitation. The degenerate HOMO orbital diagrams are described as the a_{1u} and a_{2u} , while the LUMO orbital diagram is represented as e_g.[158]

A diagram of the porphyrin frontier orbitals, shown in Figure 8.80, gives insight into the nature of q-band height changes. Goutermann showed that the ratio of the low energy q-band absorption can be utilized to monitor the energy offset of the a_{1u} and a_{2u} HOMO levels. The electron density of the a_{2u} orbital lies on the methine carbons and the

pyrrole nitrogens, while the electron density of the a_{1u} lies on the beta positions of the center pyrrole units. Vibronic coupling between the HOMO to LUMO transitions produce a strong Soret absorption around 400 nm and the weaker q-band transitions at longer wavelengths between 500 nm and 600 nm. The cancellation of these transitions results in the lowest energy absorption band or the q_0 band, while the Soret absorption band arises from the additive result of the vibronic mixing. The higher energy q_1 transition arises from a mixing of these two transitions and therefore remains relatively constant in comparison to the q_0 band. The ratio of the q_0 band to the q_1 band can be used to estimate the relative difference in energy between the a_{2u} and a_{1u} orbital energies.[159]

TTP, TTPa and DTDPa were all metallated in order to ensure changes to the orbital energy were strictly due to porphyrin binding through the phenyl acid groups of the porphyrin, with TTP being the only exception. A comparison of the q-band absorbance ratios before and after binding was conducted in order to relate the ratios to electronic changes in the porphyrin. TAPP was compared to TTP first to analyze the q-band ratio with four equal substituents.

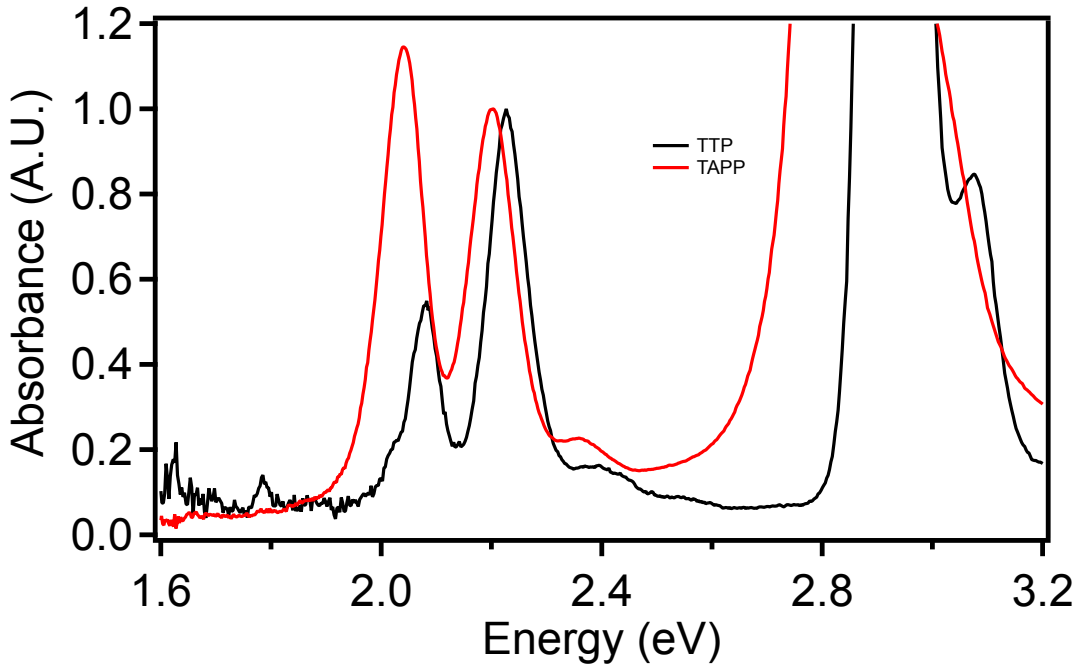

Figure 8.81 Normalized absorbance spectra of TAPP and TTP porphyrins. The spectra are normalized to q_1, which is the higher energy q-band absorbance.

In Figure 8.81 the case for externally symmetric porphyrins TAAP and TTP is shown. Not only are the q-band peaks shifted from TTP to TAPP but their relative intensities were drastically different. The assumption made was that the a_{1u} is held constant, since no modification to the beta pyrrole positions of the porphyrin were made, therefore the q-band ratio difference can be described in terms of relative a_{2u} energy. In the case of TTP, the q_0 to q_1 was much lower than for TAPP. This was directly correlated to the difference in the more electron donating phenylamine groups when compared to the phenyl rings of TPP. The electron donation increases the a_{2u} energy in comparison to TTP causing this ratio to increase higher than 1:1.

The initial q band ratios and the ratios after binding, were monitored for the phenyl acid functionalized porphyrins in order to gain insight into the nature of the

binding process and how that affects the HOMO degeneracy. The ratios were averaged for each samples and plotted vs. the number of binding groups. The binding group quantification utilized was to assume TTP possessed no binding groups, TTPa possessed one and DTDPa possessed two binding groups.

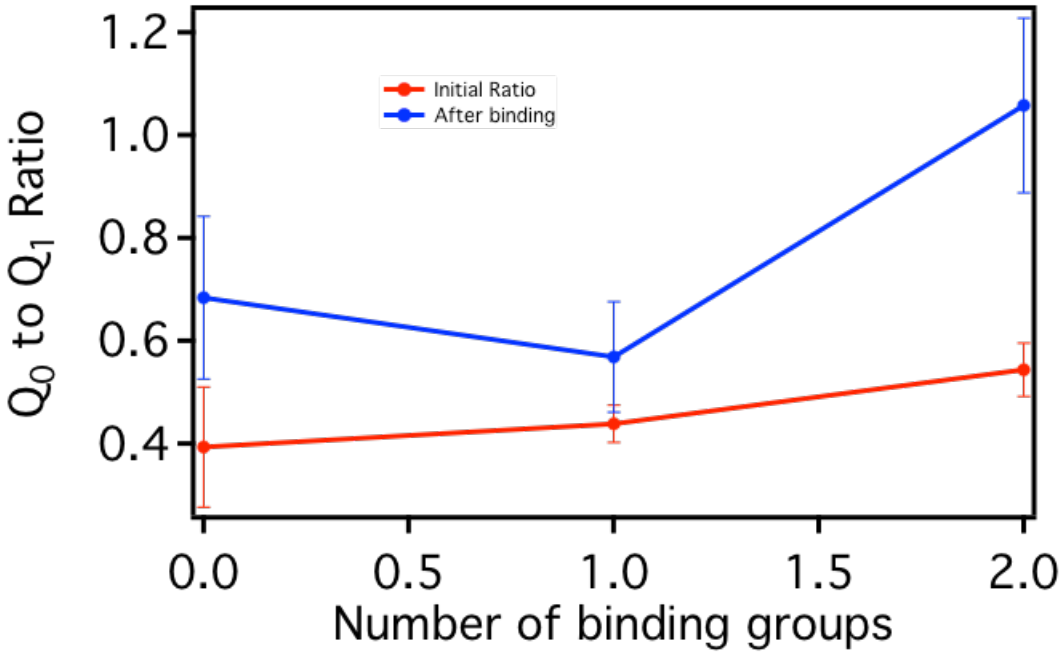

Figure 8.82: Plot of the relative q-band ratios vs. the number of binding groups. Error bars were calculated from the standard deviation of 3-4 experiments. The red plot shows the initial binding ratio while blue shows the ratio after binding.

The q-band ratios are shown both before and after binding with hybrid gold nanoparticles in Figure 8.82. Analysis of the initial q-band ratios of TTP, TTPa, and DTDPa showed a slight increase as the number of phenyl acid substiuents increases. The phenyl acid groups should act to withdraw electron density from the porphyrin, compared to the phenyl rings of TTP. The increased electron withdrawing effect should act to lower

the a_{2u} orbital energy, resulting in an increase in the energy difference between the a_{2u} and a_{1u}. This trend was confirmed experimentally with a slight increase observed in the q-band ratio with TTP showing the lowest ratio and DTDPa showing the highest.

The ratios were then calculated after a binding reaction was conducted and analyzed in the same manner, as shown in the blue plot of Figure 8.81. In general, all the porphyrins showed a higher energy offset compared to the free porphyrin, which was observed by the increased q-band ratio. This trend was indicative of an increase in the electron withdrawing nature when the nanoparticles were introduced. The q-band ratio for TTP, once bound, increased in comparison to that of TTPa. TTP and TTPa both show an increased amount of electron density, donated to the hybrid nanoparticles, but this effect was enhanced for TTP, pointing to a stronger interaction with the nanoparticle surface. The ratio for DTDPa was much larger in comparison to TTP and TTPa, explained through the stronger interaction with two phenyl acid groups present.

Increases in the q-band ratio showed electron donation into the nanoparticle surface. This electron donation should proceed through binding of the porphryin to unpassivated cadmium sites on the nanoparticle surface. Carboxylate groups, produced through deprotonation of the phenyl acid substituents should bind to these cationic surface sites. This could also indicate significant interaction with the electron-rich phenyl rings as TTP showed a larger change in the q-band ratio than did TTPa. The phenyl groups are not nucleophillic but they may still interact with the cationic surface sites on the nanoparticle. These data gave insight into the electronic nature of the porphyrin to nanoparticle interaction and can be used to monitor these effects for a variety of different surface chemistries and porphyrin species.

8.9: Calculation of Porphyrin Extinction Coefficient Enhancement

In order to quantify the extent of any enhancement seen upon binding the porphyrin to the nanoparticle surface, the porphyrin concentration was calculated for the original solution, the unbound porphyrin and the bound porphyrin. Calibration curves were constructed by drying and weighing porphyrin, followed by dissolution to 3 mM stock concentration. The cuvette final volume was held at 3 mL and porphyrin was added in a series of increasing volumes from 10 uL to 75 uL. The calculated concentration after dilution was plotted on the x-axis vs. the absorbance of the solution. TAPP was not utilized for binding runs due to difficulty in producing any product upon purification and reproducibility issues.

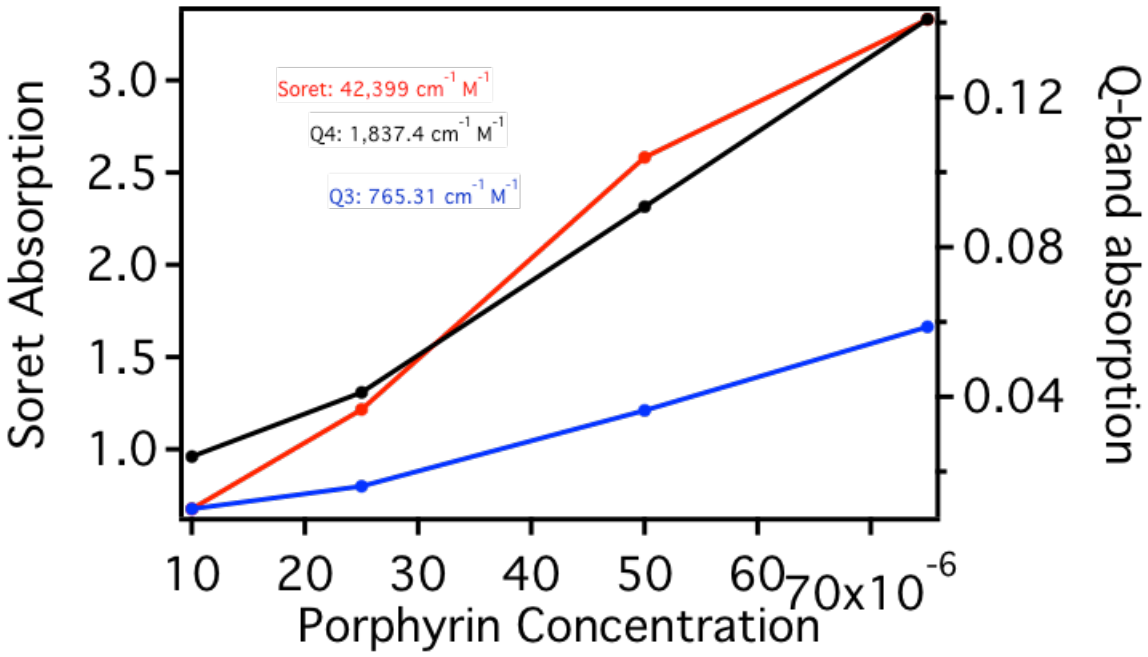

Figure 8.90: Calibration curve of metallated TTPa. The plot shows absorbance vs. concentration of the porphyrin. The calculated extinction coefficients are shown in the annotations.

In Figure 8.90 the calibration curve constructed for TTPa is shown, with the Soret band absorption shown on the left axis and the q-band absorbance shown on the right axis for clarity. The extinction coefficient calculations matched very closely to that of literature values, with the calculated Soret coefficient being 43,399, The higher energy Q4 being 1,837 and the lower energy Q3 being 765.31. These extinction coefficients were utilized for the metallated TTP, TTPa and DTDPa binding experiments as well.

To monitor the resultant bound porphyrin: nanoparticle composites, the absorbance spectra of the free porphyrin was taken before being mixed with ethyldiisopropyl amine and hybrid nanoparticles for one hour at room temp. The solution was then centrifuged at 6,500 RPM for 10 minutes in order to separate the bound porphyrin from the unbound porphyrin. Finally, the spectra of the supernatant, or unbound porphyrin was taken as well as the bound porphyrin:nanoparticle composites, dispersed into the same volume of the original porphyrin. The aliquot volumes were carefully calculated to ensure the porphyrin concentration was the same in each sample.

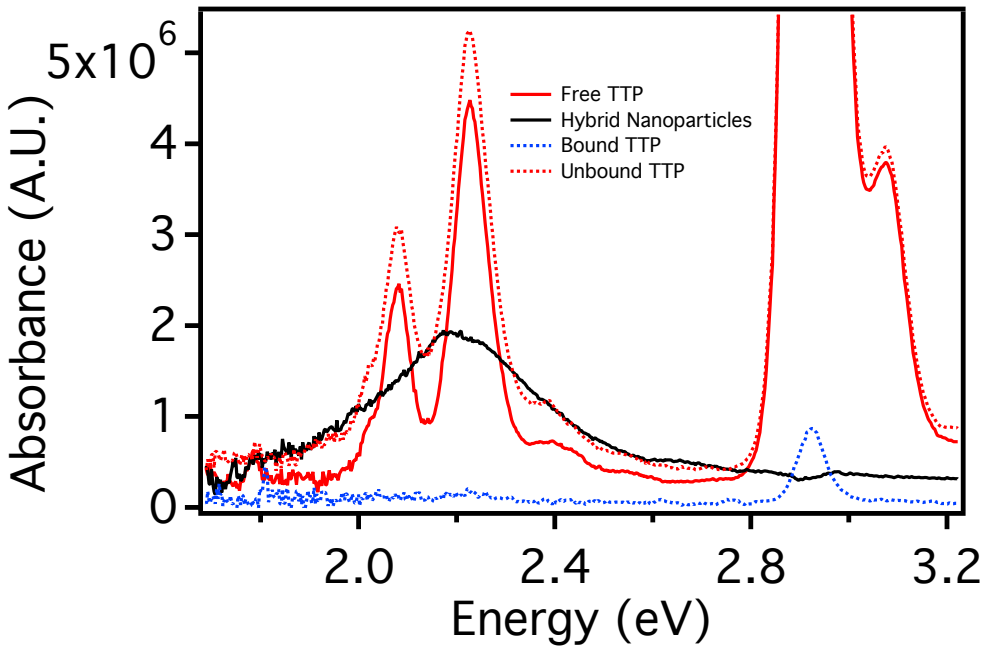

Figure 8.91: Absorbance spectra of free TTP, bound TTP, and the unbound TTP after the binding reaction.

In Figure 8.91 the absorbance spectra of the TTP before and after the binding reaction was conducted is shown. The spectra in blue corresponds to the separated nanoparticles after the binding reaction and the dotted red line refers to the supernatant collected. The intensity difference from the unbound porphyrin and the initial free TTP could be due to the presence of nanoparticles in the resulting solution. Figure 8.52 showed an increase in absorbance with minimal shape change when nanoparticles are present in solution, which was also observed here. This observation indicated minimal porphyrin binding ,resulting in a very small amount of porphyrin in the centrifuged sample. A very small nanoparticle concentration was observed in the composite which also supports the claim that nanoparticles were left soluble in solution after centrifugation.

The results of the TTP binding, supported the claims of very little binding and minimal electronic interaction from sections 8.5 and 8.6. In order to confirm this trend, binding was conducted with TTPa. TTPa showed minimal increases in the absorption spectrum and an increase in the fluorescence. These observations were correlated to a weak, axial binding via the phenyl acid groups on the porphyrin. The same binding experiment conducted for the TTP was used for TTPa.

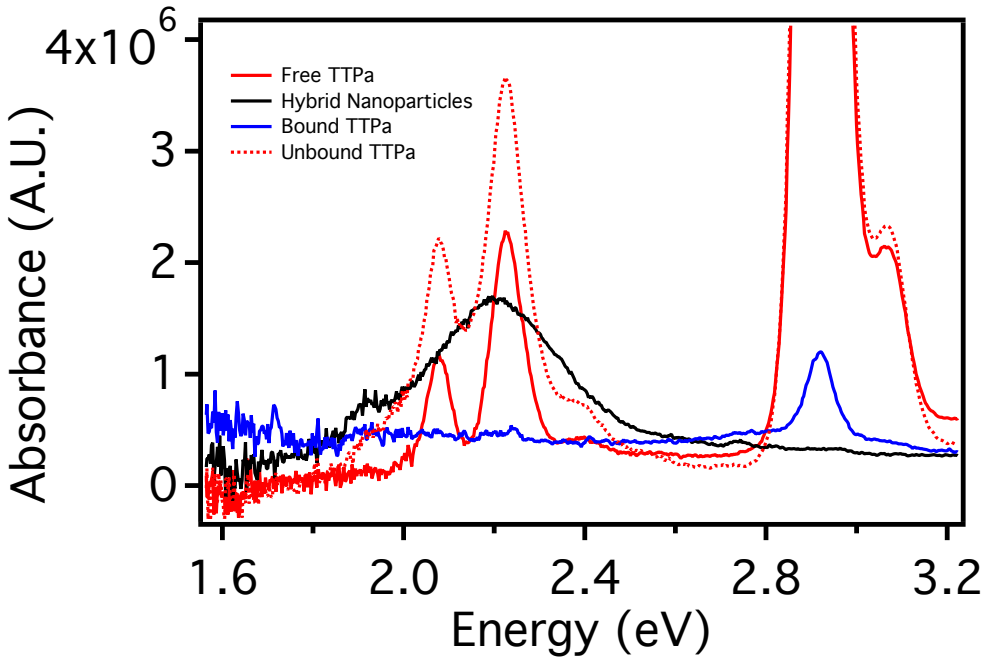

Figure 8.92: Absorbance spectra of free TTPa, bound TTPa, and the unbound TTPa after the binding reaction.

A very similar result was observed for the binding of TTPa ,shown in Figure 8.92, as was observed for the TTP. The unbound porphyrin spectra was once again higher than the initial porphyrin spectra, pointing to nanoparticles left in solution. A higher concentration of porphyrin and nanoparticles remained, however, after centrifugation, in

comparison to TTP. This indicates a slightly higher degree of interaction with one acid group but overall, the amount bound is negligible and the results were almost identical to that of TTP. These results agree with our previous assumption that the TTPa and TTP interaction are almost the same and that one binding group provides very minimal interaction with the particle surface.

DTDPA was studied next to monitor the effects of a stronger binding porphyrin. All the previous experiments indicate DTDPA has a strong, axial binding configuration. The fluorescence experiments showed a strong electronic coupling which produced quenched fluorescence, while the solution absorption indicated a significant enhancement in the q-band region. The two phenyl acid groups were shown to be bound in the carboxylate mode on the nanoparticle surface from the FTIR. DTDPA was bound to the nanoparticle surface and separated via centrifugation.

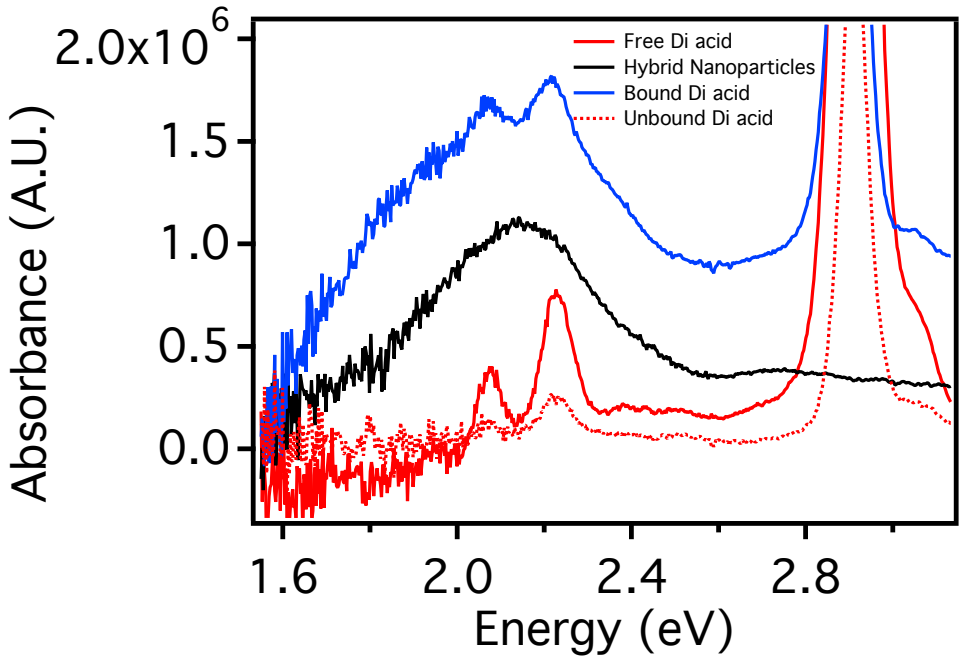

Figure 8.93: Absorbance spectra of free DTDPa, boud DTDPa, and the unbound DTDPa after the binding reaction.

The DTDPa binding is shown in Figure 8.93. A significantly higher concentration of porphyrin remains after centrifugation with a shape that matched a mixture of nanoparticle and porphyrin contribution. These data agree well with the solution experiments for the DTPA absorption change. The concentration of porphyrin in the supernatant was also significantly lower pointing to both an increase in binding. The composite was separated more efficiently from the reaction mixture, via centrifugation, due to the much larger size of the nanoparticles with bound porphyrin. Calculation of the amount of unbound porphyrin showed that only 27% of the original concentration remains in solution. An average of three different binding experiments showed 31% of porphyrin was left in the supernatant with a standard deviation of 11%, proving that the binding was both reproducible and robust.

The amount of enhancement was now calculated based on the porphyrin extinction coefficients calculated previously. The enhancement (Ef) was defined as the ratio of the enhanced extinction coefficient of each q-band to the q-bands defined from the calibration curves in Figure 8.90 and shown in equation (27) below.

$$E_f = \frac{\varepsilon_{new}}{\varepsilon_0} \tag{27}$$

The new extinction coefficient (ε_{new}) was first calculated by taking the experimental absorbance ($A_{particles}$) of the bound composite, at each q-band maxima, and dividing by the concentration of porphyrin ($[P]_{binding}$) left available for binding after centrifugation from equation (28).

$$\varepsilon_{new} = \frac{A_{particles}}{[P]_{binding}} \tag{28}$$

$$[P]_{binding} = [P]_0 - [P]_{wash} \tag{29}$$

Finally, the available porphyrin for binding was calculated by subtracting the starting porphyrin concentration ($[P]_0$) from the porphyrin concentration calculated from the supernatant after centrifugation, shown in equation (29). These calculations were conducted for the TTP, TTPa and DTDPa experiments, averaged and plotted vs. the number of binding groups, to investigate the effect of the porphyrin functionalization on the enhancement after binding.

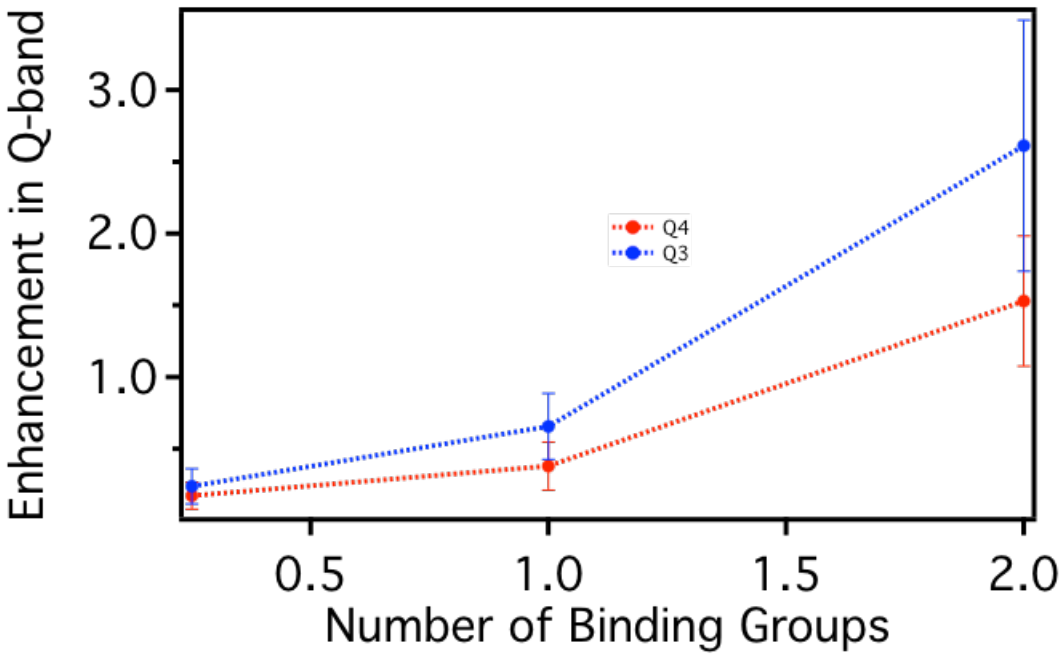

Figure 8.94: Plot of the averaged q-band enhancement factor (Ef) vs. the number of binding groups on the porphyrin. TTP, TTPa and DTDPa were utilized which represent, 0, 1 and two binding groups respectively. The TTP samples are an average of metallated and unmetallated TTP. The curve in red represents the higher energy q_4 while the blue curve represents the lower energy q_3.

The results of binding of the three different porphryins to the same CdS-shelled hybrid gold nanoparticles are shown in Figure 8.94. Binding with both metallated and unmetallated TTP showed a decrease in the extinction coefficient upon binding. Careful observation of the absorption spectra showed that particles still remained in the unbound porphyrin spectra. Almost no porphryin or hybrid nanoparticles remained in the bound porphyrin solution after the binding reaction. The particles and porphyrin were very soluble in THF, therefore after the binding reaction there were no bigger aggregates to pellet out of the solution with centrifugation. The result was free porphyrin and nanoparticles.

A very similar trend was observed for the TTPa reaction with a slightly higher concentration of porphyrin and nanoparticles remaining in the solution post reaction, although the calculated change in extinction coefficient is still below that of the starting porphyrin. This indicated minimal binding, even with one phenyl acid group on the porphryin. While small, there is still a noticeable increase in the bound porphyrin spectra for the TTPa, which indicated more binding occurred in comparison to the TTP experiment. The rational for this difference was that one phenyl acid group binds weakly and can dissociate after centrifugation or agitation of the solution. Previously, increases in the solution state are seen for both the unmetallated TTP and TTPa but after separation from the solution very little of the porphyrin: nanoparticle composite remained, suggesting the equilibrium favors the unbound case. This weak interaction can also be confirmed through observation of Figure 8.81, where the amount electron density donated to the nanoparticle, resulted in a lifting of degeneracy and shifting of the q-band ratios. These changes were almost the same for TTP and TTPa, confirming the low affinity for the nanoparticle surface.

Finally, the DTDPa binding showed a strong enhancement of the q-band absorption, more than 3 times the original extinction coefficient for the lower energy Q3 absorption band. This phenomenon was consequence of a strong electronic interaction between the DTDPa and the nanoparticles as shown through the q-band analysis, FTIR spectroscopy and the quenching studies. There was also a large percentage of bound porphyrin remaining on the nanoparticles of around 70% the original concentration, indicating the binding is both efficient and effective at changing the extinction coefficient.

8.9.1: Time-resolved Fluorescence of Bound Porphyrin

In order to be utilized for any sort of photovoltaic device, it will be imperative that any extra excitation is not simply utilized to increase the fluorescence. Porphyrin fluorescence is normally fairly weak therefore any increases in the fluorescence could drastically alter the charge transport properties of porphyrin devices. Investigation into Figure 8.730 indicated that TTPa would be least useful for devices, as the fluorescence quantum yield increases and the fluorescence excitation shows that the nanoparticles are directly contributing to this increase in quantum yield. Porphyrin without any binding groups such as TTP or TCO_4PP show decreases in fluorescence quantum yield, but show little if any increases in the extinction coefficient of the porphyrin ,once bound to the nanoparticle.

DTDPa porphyrin showed the most substantial fluorescence quenching and the highest absorption increase, correlating to the most useful for photovoltaic devices. Study of the changes in the time-resolved fluorescence will also be useful in determining if losses from fluorescence would be minimized. Extinction coefficient increases accompanied with a fluorescence lifetime and quantum yield decrease would indicate that the probability for fluorescence has been quelled and any absorption increases could be efficiently separated and utilized for current production.

Time-resolved fluorescence was utilized to monitor the decay rates of the bound and unbound porphyrin. The samples were run in conjunction with UV-vis absorption before and after the binding reaction. The samples were excited using a pulsed LED source, set at 389 nm, which should efficiently excite the Soret band. The decays were fit to a sum of exponentials, using two exponentials for the fit. The fits were plotted on a log

normal axis. The average number of counts accumulated for each samples was 10,000, with some variation. The decays were taken, monitering the higher energy fluorescence peak at 656 nm.

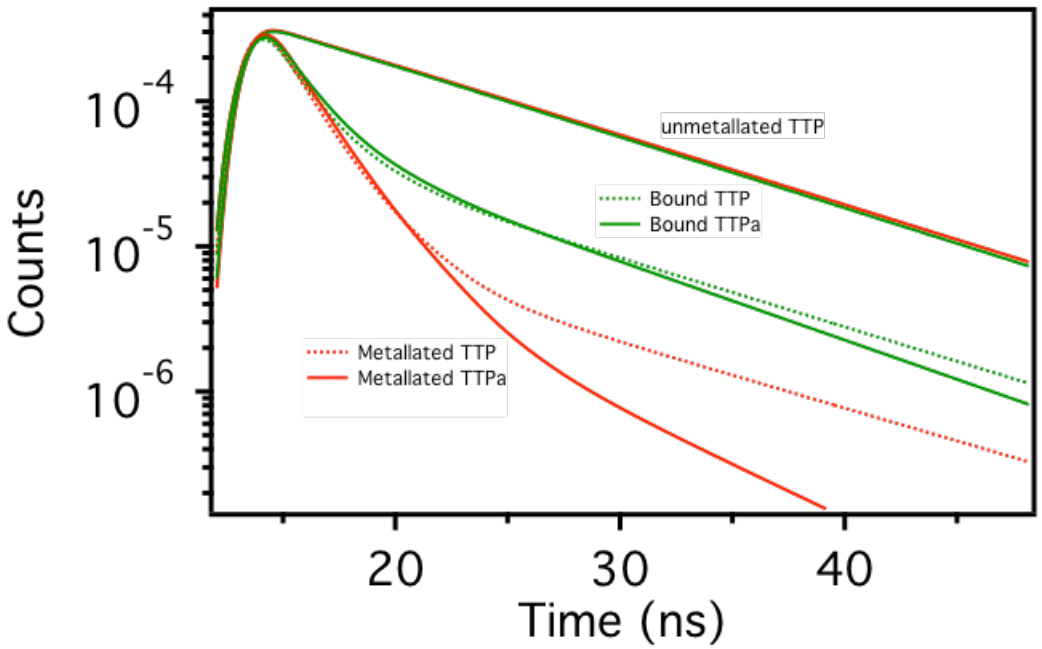

Figure 8.910: Fits to fluorescence decay measurements of metallated (top of graph) and unmetallated TTP (dotted line) and TTPa (solid line). The free porpyrin fit is shown in red and the porphyrin bound to hybrid nanoparticles is green. The spectra is taken monitoring 656 nm emission with 389 nm excitation.

In Figure 8.910, the fits to fluorescent decays for unmetallated and metallated TTP and metallated TTPa are shown. The decays were fit to a sum of exponential function using two exponentials. The lifetimes decreased for the porphyrins upon mettalation and even further when acid groups were added to the porphyrin. For the unmetallated TTP, the lifetime essentially the same as the free porphyrin with a very

slight increase with the nanoparticles added, from 9.40 ns to 9.42 ns. The fluorescence quenching for the porphyrin with no binding groups was very minimal, therefore any decrease in the average lifetime could still lead to an increase in the probability for radiative relaxation as the time between emission increases but the intensity only decrease slightly.

The metallated TTP average lifetime of 1.76 ns was slightly lower than that of TTPa of 1.99 ns. Upon binding, the average lifetime of each porphyrin increases to almost the same value, with bound TTP increasing to 4.55 and the TTPa increasing to 4.18 ns. This trend would be preferable for photovoltaic applications as the average time in between emissive relaxation events was increased upon binding. The TTPa ,however, showed a slight increase in the fluorescence quantum yield which could be due to fluorescence enhancement. Although, this increase in lifetime was preferential, the increase in fluorescence quantum yield with TTPa and minimal change in absorbance upon binding with either TTP or TTPa, negates their utility upon binding for photovoltaic applications.

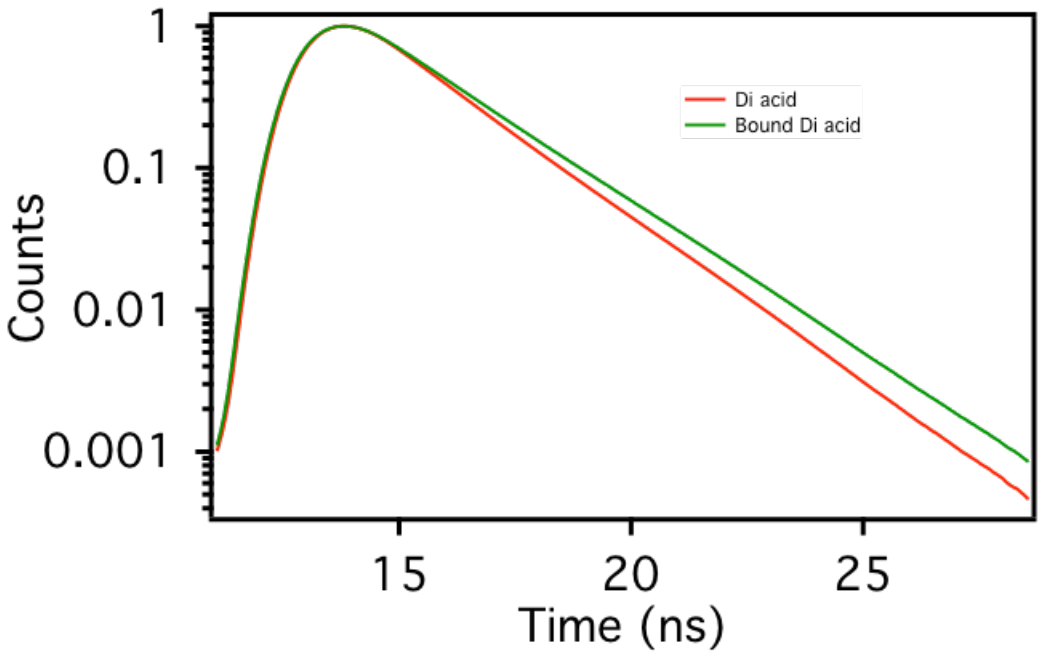

Figure 8.911: Fits to fluorescence decay measurements of metallated (top of graph) and unmetallated TTP (dotted line) and TTPa (solid line). The free porpyrin fit is shown in red and the porphyrin bound to hybrid nanoparticles is green. The spectra is taken monitoring 656 nm emission with 389 nm excitation.

In Figure 8.911, the decays of free and bound metallated DTDPa are shown in red and green respectively. The decays were also taken at 656 nm and fit using a sum of exponentials with two exponentials utilized for the fits. A similar trend to TTP and TTPa was observed where the lifetime were slightly increased upon binding to the hybrid gold nanoparticles from 1.75 ns for unbound DTDPa to 1.93 ns for bound DTDPa. Coupled with the sharp decrease in fluorescence quantum yield and increase in extinction coefficient upon binding the DTDPa to the nanoparticle surface, makes the DTDPa the most attractive for utility in a photovoltaic device.

These data help indentify DTPA as the most useful porphyrin for enhancement and incorporation into a device once optimized. Once bound, the fluorescence was

significantly quenched and the lifetime was increased from that of the original porphyrin. The hybrid nanoparticle: porphyrin composite could, theoretically, be utilized to improve the photocurrent production in a photovoltaic device by increasing the extinction coefficient of the lower energy q-band absorption modes. These results do not indicate the other porphyrin species could not be utilized but rather require further binding optimization.

8.10: Porphyrin Thin Films

Solution-state experiments were the first step in making photovoltaic devices with the porphyrin:hybrid nanoparticle composites, but studies needed to be conducted on thin films coated on glass or indium tin oxide coated glass slides. To study the utility of these composites on thin films devices, films of nanoparticles coated onto glass slides were created. First, glass slides were cleaned with a solution of 3:1 sulfuric acid to 30% hydrogen peroxide for 1 hour before being rinsed with methanol and soaked in a clean methanol solution. The films were then soaked in a 2% solution of (3-Aminopropyl)trimethoxysilane in methanol overnight.

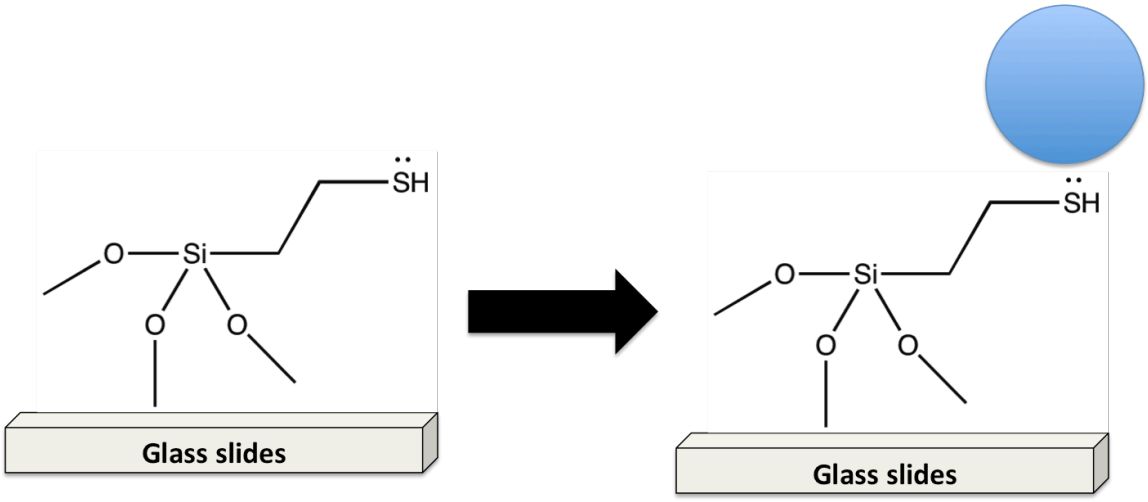

Figure 8.10.1 Illustration of (3-Aminopropyl)trimethoxysilane binding to glass slides for anchoring of nanoparticles.

In Figure 8.10.1, an illustration is shown of the silane binding to glass slides. The silane binds via the methoxy groups to the glass substrate, leaving a free amine group in solution. The slides were then washed with methanol to remove any unbound silane from the glass. Nanoparticle solutions were first washed with ethanol and centrifuged to pellet out the nanoparticles and remove the native ligand coating from the surface. The silane coated slides were finally soaked in a solution of the nanoparticles either in THF for hybrid nanoparticles or ethanol for gold nanoparticles. The slides were soaked overnight to produce glass slides with silane-anchored nanoparticles as illustrated in the right side of Figure 8.10.1.

To create the nanoparticle: porphyrin composites, the nanoparticle films were placed into a THF solution of porphyrin. The porphyrin was shaken lightly and allowed to sit overnight in order to coat the nanoparticles. The films were monitored over the course of two to three days in order to investigate the optimal time period for binding.

Gold nanoparticles and hybrid gold nanoparticles were both compared to silane coated slides soaked in porphyrin, without nanoparticles.

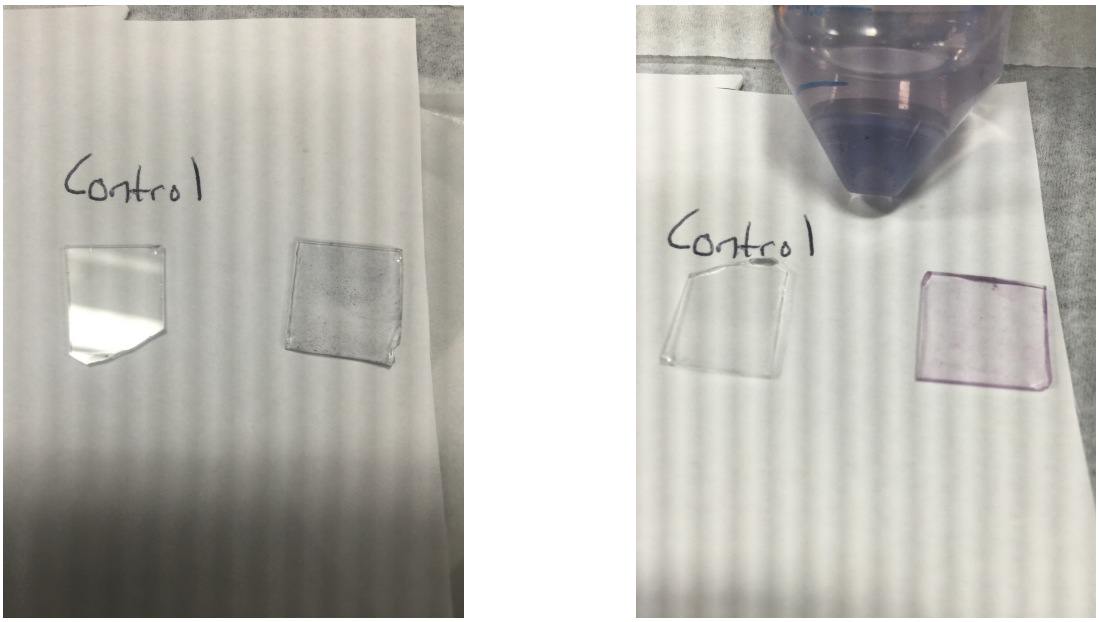

Figure 8.10.2: Pictures of glass slides coated with gold nanoparticles (left) and hybrid ZnS-shelled nanoparticles (right)

The image in Figure 8.10.2 show the glass slides after being soaked in the nanoparticle solution and washed. The gold slides turn blue upon binding to the glass surface due to slight aggregation of the gold nanoparticles on the film. The picture on the right shows the hybrid gold nanoparticle films which retain the color of the original solution. Once the nanoparticles were anchored to the glass slides, the slides were soaked in a solution of TTPa with ethyldiisopropylamine added. Three different nanoparticle solutions were utilized, gold nanoparticles, hybrid gold nanoparticles with a 5 nm shell and hybrid gold nanoparticles with a 15 nm shell. Silane coated glass slides were also

soaked in porphyrin under the same conditions to act as a control. Once the slides were soaked in porphyrin, they were then sonicated for a minute to monitor the stability of the bound porphyrin.

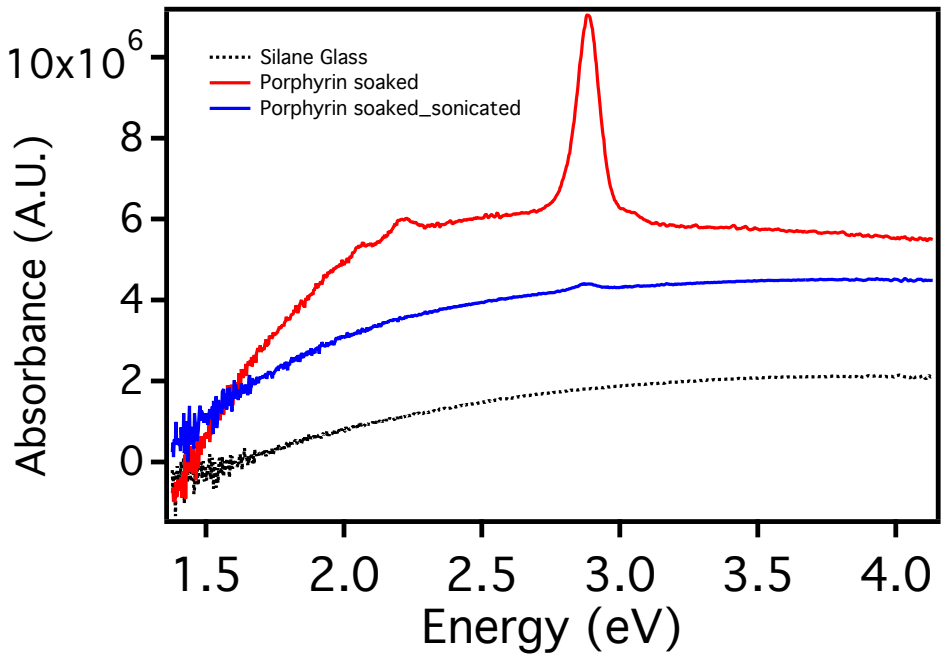

Figure 8.10.3: Absorbance spectra of the silane glass slide control. The spectrum in black is the original silane slide, the blue spectrum is the slide after being soaked in porphyrin and the red is the porphyrin soaked slide after sonication.

Figure 8.10.3 above, shows the silane glass control, both bare and soaked in porphyrin. The results showed that the silane glass by itself absorbs minimally. Once soaked in porphyrin a significant amount was bound to the film but after sonication, almost no porphyrin remains on the film. This trend was determined to be the TTPa, weakly associating with the silane on the glass film. TTPa may bind to unpassivated glass,but upon sonication the vast majority dissociates and is dissolved in the THF. This

shows that any porphyrin bound to the glass slide should not remain after sonication, and that the glass contributes minimally to the absorbance of the film.

The nanoparticle solutions soaked in porphyrin were analyzed next. The silane control shows that any porphyrin remaining after sonication, must be strongly bound to the nanoparticle surface. This experiment provides insight into which surface the porphyrin has a higher affinity for binding. Gold nanoparticles and zinc sulfide-shelled nanoparticles were compared to investigate which surface facilitated porphyrin binding most efficiently.

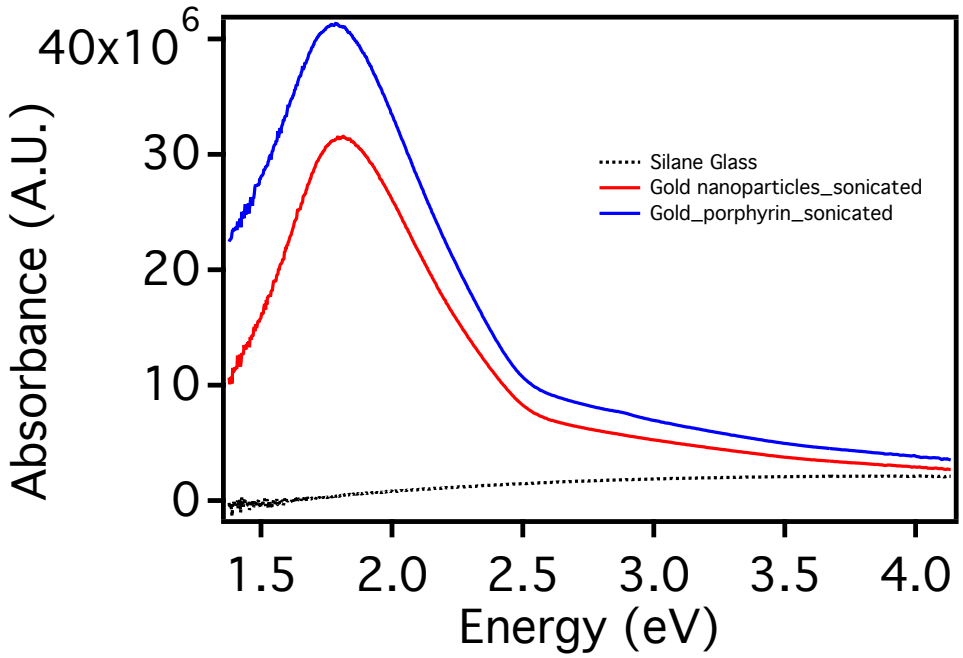

Figure 8.10.4: Absorbance spectra of the silane glass slide control and gold nanoparticles anchored onto glass slides. The spectrum in black is the original silane slide, the blue spectrum is the slide after being soaked in gold nanoparticles and the red is the slide after sonication.

The absorbance of the gold nanoparticles anchored onto the silane glass is shown in Figure 8.10.4 A very large plasmon resonance was observed around 2.0 eV, indicative of bound nanoparticles. The peak was very sharp which indicates minimal aggregation of the bound nanoparticles. After sonication, the peak retains not only the same shape but its intensity as well. This proves that the nanoparticles were very strongly bound to the surface.

The gold nanoparticle films were then soaked in the porphyrin solution. Once soaked for two days, the films were monitored with UV-vis absorption. The films were sonicated in a clean THF solution for 1 minute and monitored with UV-vis absorption again. The sonication was conducted to determine if the porphyrin was tightly bound to the surface of the nanoparticles.

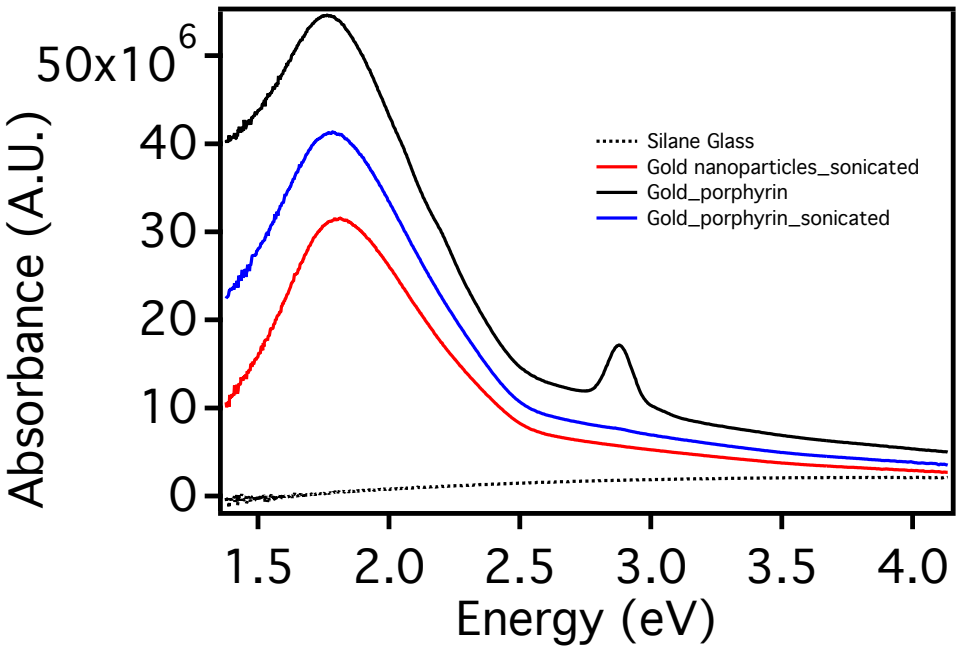

Figure 8.10.5 Absorbance spectra of the silane glass slide control and gold nanoparticles anchored onto glass slides (red,bottom). The spectrum in black is the original silane slide, the red higher red spectrum is the gold nanoparticles after being soaked in porphyrin and the blue is the porphyrin soaked nanoaparticles after sonication.

The spectra in Figure 8.10.5 shows the absorbance of gold nanoparticles before and after being soaked in a porphyrin solution. A Soret absorption band was present at 3.0 eV in the porphyrin-soaked slide, indicating that a significant concentration of porphyrin was bound to the gold nanoparticles. After sonication, however, a very small concentration of porphyrin remained bound to the gold nanoparticle slides. There were two explanations for this minimal porphyrin retention. The first explanation was the weak binding of the acid group of TTPa to the gold surface. The absorption characterization, presented in the solution experiments indicated that TTPa doesn't bind as strongly as DTDPa, therefore sonication could potentially dislodge any bound porphyrin. The

smaller gold nanoparticles, which are only 15 nm in diameter, cannot fit as many porphyrin molecules as the hybrid gold nanoparticles. This result shows that gold nanoparticles may not be optimal for use in photovoltaic films.

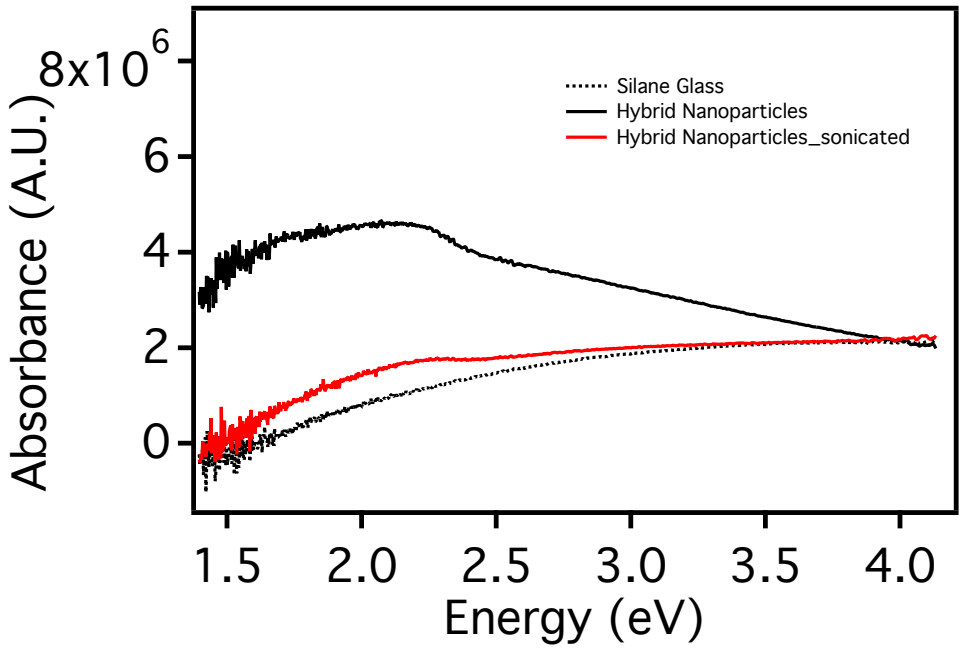

Figure 8.10.6 Absorbance spectra of the silane glass slide control and 5 nm ZnS hybrid gold nanoparticles anchored onto glass slides. The spectrum in black is the slide coated in hybrid gold nanoparticles and the red spectrum is post-sonication.

The spectrum of the hybrid gold nanoparticles in Figure 8.10.6 is drastically different from that of the gold nanoparticles anchored onto the glass slides. The first difference was the lack of a sharp plasmon resonance, observed in Figure 8.10.5. The spectrum shows a much a broader and red-shifted absorbance maxima centered at 1.8 eV. The spectrum after sonication, showed a sharp decrease in the nanoparticle absorbance

without a change in the spectral shape. This trend differs from the gold nanoparticle spectrum which did not drop in intensity significantly after sonication. This indicates the bound hybrid nanoparticles are not as strongly attached to the amine group of the silane as are the gold nanoparticles. This is not optimal for device preparation but can be alleviated through utilization of a stronger binding group on the silane.

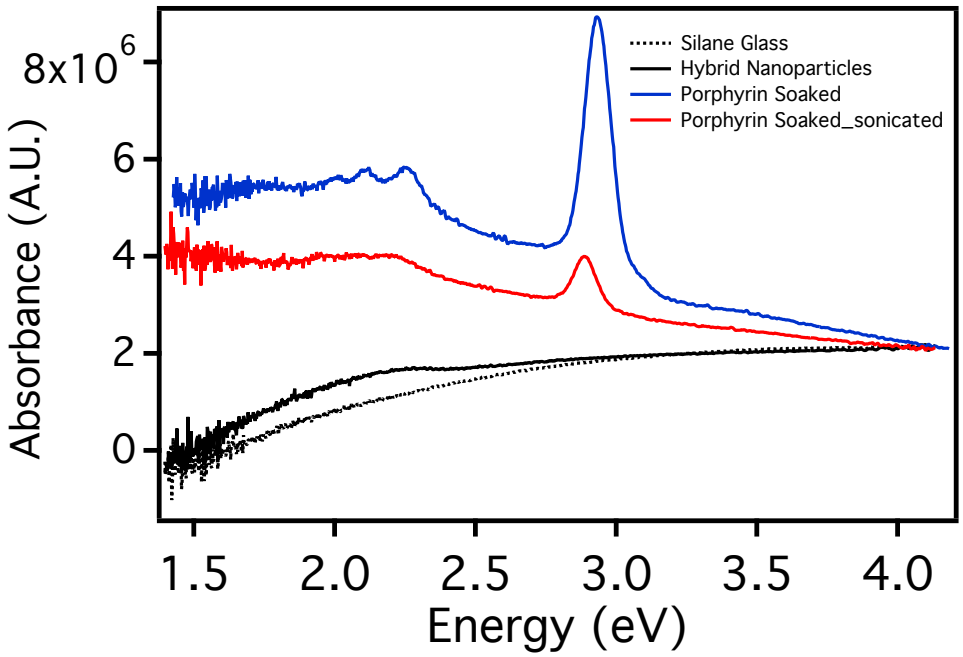

Figure 8.10.7 Absorbance spectra of the silane glass slide control and 5 nm ZnS hybrid gold nanoparticles anchored onto glass slides and soaked in the porphyrin solution. The spectrum in black is the slide coated in hybrid gold nanoparticles , the blue spectrum is after being soaked in the porphyrin solution and the red spectrum is post-sonication of the porphyrin soaked slide.

The spectra in Figure 8.10.7 shows the absorbance spectra of the 5 nm hybrid gold nanoparticles after being soaked in the porphyrin solution. The spectrum shows two

significant differences to the gold nanoparticles soaked in porphyrin. The first difference was the distinguishable q-band absorption modes which arise upon soaking in the porphyrin. These absorption bands were much lower in intensity than the Soret, suggesting either a much higher concentration of porphyrin was bound to the films or that the q-bands were significantly enhanced upon binding to the hybrid gold nanoparticles.

The second significant feature observed was the much larger concentration remaining post-sonication. This larger retention of porphyrin could be due to either a stronger bond formed between the acid group and the semiconductor surface in comparison to the gold surface, or that the sheer size difference leads to a much larger porphyrin loading onto the surface. This shows that not only was the semiconductor surface was not only preferential to the porphyrin binding but the larger particles may be able to sustain more porphyrin, which would in turn produce higher enhancements and subsequently higher output photocurrent.

In order to compare different porphyrin loading amounts, a thicker zinc sulfide shell was utilized. A shell double that of the 5 nm shell was bound to a silane film and then soaked in porphyrin in the same method as the 5 nm shelled nanoparticles. The spectrum of the bound nanoparticles was broad and featureless, similar to the thinner zinc sulfide shelled nanoparticle films. The results are shown in comparison to film after soaking in TTPa and post-sonication in clean THF.

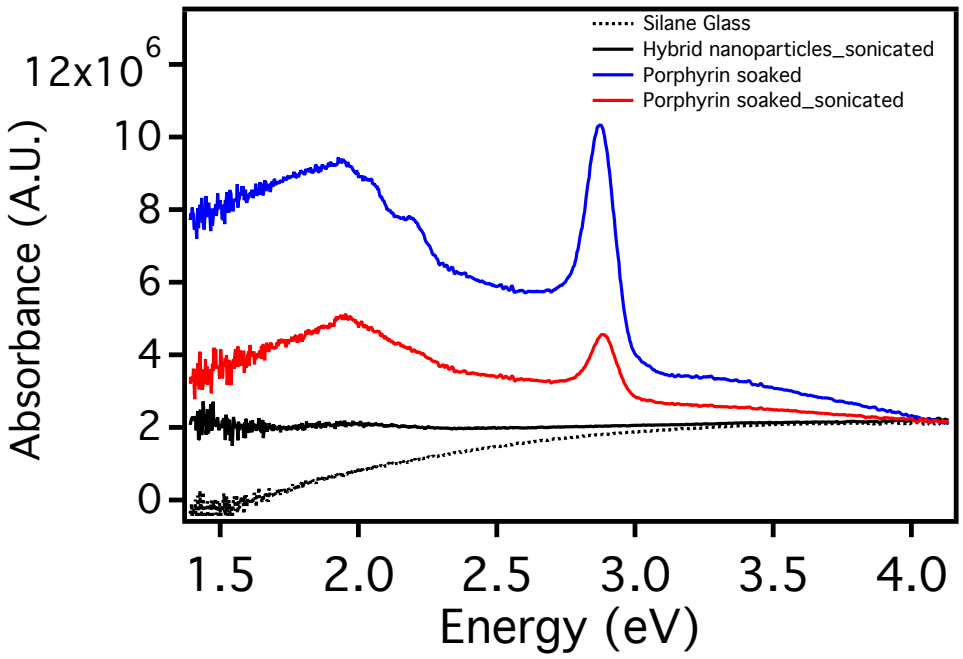

Figure 8.10.8 Absorbance spectra of the silane glass slide control and 15 nm ZnS hybrid gold nanoparticles anchored onto glass slides and soaked in the porphyrin solution. The spectrum in black is the slide coated in hybrid gold nanoparticles , the blue spectrum is after being soaked in the porphyrin solution and the red spectrum is post-sonication of the porphyrin soaked slide.

The thinner hybrid gold nanoparticles were compared to a thicker 15 nm ZnS shell. In Figure 8.10.8, the spectrum of the larger particles, post sonication and then after being soaked in the porphyrin solution are shown. The trend stays the same as for the thinner hybrid gold nanoparticles, but with a larger intensity overall once soaked in the porphyrin solution. Even after sonication, a much larger concentration of the porphyrin seems to remain on the nanoparticle film. This is direct evidence that the larger shell size produces a higher porphyrin loading and therefore a higher retention of porphyrin upon sonication. These spectra also give evidence into the origin of the large q-band absorption as the q-bands are even larger for these samples. The large q-band absorption stems from

a higher porphyrin loading, since the larger particles increase the q-band absorption more than the thinner zinc sulfide shells. Whether, this absorption increase is due to plasmonic coupling or simply an increase in concentration needs to be further investigated.

These experiments are crucial to the formation of photocurrent producing devices, as it is important to prove that the absorption was not only enhanced in solution but when anchored on glass. These experiments show that even with TTPa, one of the poorer performing porphryins in solution, a significant absorption increase was observed when bound to hybrid gold nanoparticles in comparison to bare gold nanoparticles. This result shows that not only was the porphyrin identity important but also that utilization of the hybrid gold nanoparticles was crucial. Their utilization lies in their larger size which can physically bind more porphyrin, leading to higher photocurrent output. Having a semiconductor surface also facilitates a stronger bond between the acid group of the porphyrin as well.

The production of highly absorbing films lies in the optimization of the silane binding group in order to facilitate higher hybrid nanoparticle binding. The hybrid nanoparticles didn't bind as efficiently as the gold nanoparticles to the amine group on the silane. The silanes were quite ubiquitous and can be functionalized with other nucleophillic groups such as a carboxylic acid or a thiol, which may aid in the retention of nanoparticles on the film. The use of a higher binding porphyrin such as DTDPa will help to increase the porphyrin loading onto the nanoparticle surface. TTPa was shown to not bind as well to the nanoparticle surface as DTPA. Optimization of the nanoparticle film formation and porphyrin loading will be crucial to the study of plasmonic coupling with porphryins and device production.

8.11: Concluding Remarks on Porphyrin Binding

The data in this section showed a novel technique for enhancement of porphyrin absorption for utility in photovoltaic devices. The use of hybrid gold nanoparticles for plasmonic coupling represented the first step in production of highly efficient and highly absorptive materials. The binding method utilized was straightforward and was conducted in less than 24 hours. FTIR spectroscopy can quickly and reliably confirm binding via the acid groups or amine groups present on the porphyrin. Once bound, changes in the solution absorption can then be associated with the bound or unbound porphyrin. The features of the absorption spectrum were also carefully analyzed to monitor changes in the electronic spectra of the porphyrin as well.

The q-bands are very sensitive to changes in the porphyrin structure. Changes in their degeneracy gave insight into the very nature of the porphyrin binding, which seems to be electron donation from the porphyrin to the gold nanoparticle. These changes were further confirmed utilizing fluorescence quenching. Strong electronic interaction was necessary to produce quenched fluorescence. DTDPa showed the most interaction due to the highest degree of quenching observed along with the most enhancement in the solution absorption spectrum, which was much higher than the theoretical maximum. This enhancement was then quantified by isolating the bound porphyrin and calculating an enhancement in the q-band extinction coefficient of almost 4 times that of the unbound porphyrin.

To ensure this increase in absorption does not simply lead to more fluorescence, time-resolved fluorescence was monitored to ensure average lifetimes are increased and not decreased which would result in shorter times between fluorescence events. Average

lifetimes for all porphyrins were increased, except for the unmetallated TTP which showed a slight shortening of the fluorescence lifetime. Finally, preliminary studies on nanoparticles anchored onto glass slides and then soaked in TTPa solutions were conducted to show preferential binding to hybrid gold nanoparticles.

These studies show that the larger nanoparticles and semiconductor shell seem to produce a more stable composite with higher porphyrin loading. This would produce a device with much larger photocurrent output than with gold particles or glass alone. These experiments show the great promise for porphyrin:hybrid nanoparticle composites being utilized in applications where high photocurrent output and high stability are necessary. Careful work still needs to be conducted to optimize loading and increase binding affinity including, changing functional groups on the porphyrin, studies into the optimal shell size, and the production and measurement of photocurrent devices.

CHAPTER 9: CONCLUSION

The work presented in this dissertation demonstrated novel techniques for plasmonic coupling of chromophores to semiconductor-coated gold nanoparticles. This method represents a new method for producing solution-state ,plasmonically coupled chromophore composites that are stable for long periods of time. These materials can be optimized to fit specific requirements for photo-absorption or emission applications. The optimal binding conditions for two different types of chromophores were examined and optimized for enhanced emission of quantum dots and absorption of porphyrins. The samples were characterized in terms of their chemical binding signal and by the changes in their optical properties. The binding of these chromophores was found to be reproducible and successful for producing stable bonding to the chemical surface. Once bound, the gold localized surface plasmon was found to enhance the radiative rate of quantum dots and the extinction coefficient of bound porphyrins.

We first examined the nature of the localized surface plasmon resonance and its effects on nearby chromophores. The utility of coupling with metal nanoparticles lies in their localized surface plasmon resonance, which produces a local electric field upon absorption of visible light. This local electric field can then couple with chromophores ,altering the original optical properties substantially. Energy transfer is one consequence of this coupling which can negate any positive enhancements through shorting in photovolataic devices and quenching of fluorescence. In order to take advantage of this

enhancement via coupling, methods which can effectively reduce this energy transfer needed to be employed.

It was found that energy transfer is a distance-dependent process, which can be negated through careful spacing of the chromophore from the metal surface. The origin of the enhancements can be utilized to understand the need for this spacing. Energy transfer dominates at close distances to the metal surface. Absorption enhancement, can be understood as a bending of the incident field toward the higher extinction coefficient metal. As long as the chromophore is within the plasmon field of the metal, absorption enhancements can be felt. In the case of fluorescent enhancements, the enhancement is produced through a coupling of the fluorescent transition with the plasmon resonance. The fluorophore, introduces a change in the charge distribution on the metal surface. This change results in the type of near-field wave produced by the plasmon field. At certain distances, the plasmon can behave as a propagating wave in the near-field, or a radiating plasmon is produced. This radiating plasmon has properties intermediate to that of the fluorophore and plasmon. The fluorescence is observed at the normal wavelength seen with the original fluorophore, while the decay rate of the radiating plasmon increases. This allows for the fluorescence to outcompete nonradiative relaxation and energy transfer to the metal surface, resulting in observed enhancements in florescence rates. These phenomenon lead us to the need for spatial control of the bound plasmon to the metal nanoparticle.

The literature examples of spacing chromophores from a metal surface, proceed via deposition of a dielectric spacer such as a conductive polymer or silica. Silica shells have been deposited onto gold nanoparticles, in literature, to provide controllable spacing

from the surface of gold nanoparticles. Our method was similar to this approach, in which we utilized colloidal solutions of gold nanoparticles coated with a semiconductor shell as our coupling platform. The first step to this approach was the synthesis of the semiconductor-coated nanoparticles through a 3-step cation exchange method.

Highly uniform gold nanoparticles were first synthesized with CTAC as a surfactant. These nanoparticles were highly uniform with a diameter of 15 nm on average and a standard deviation of less than half a nanometer.. The samples were then coated with silver via addition of aqueous silver nitrate in the presence of ascorbic acid. This silver deposition is tunable with nanometer precision and provided the template for the subsequent production of a semiconductor shell. The silver shell was treated with sulfur and oleylamine, in toluene to transform the silver shells to silver sulfide shells. These nanoparticles were soluble in toluene and were the last stage before the cation exchange to produce the semiconductor shell. The silver was exchanged with either cadmium or zinc in the prescence of tributylphosphine. The tributylphosphine acted as an ion shuttle to transport silver and cadmium or zinc ions away and to the shell respectively. The colloidal solutions of the hybrid gold nanoparticles were then monitored via TEM and UV-vis spectroscopy.

The TEM images showed that the shells were tunable between 1 to 15 nm in radius and single crystalline. The shells were uniform with the standard deviations dependent on the size and composition of the shell. The cadmium sulfide shells were the most uniform with standard deviations ranging from around half a nanometer for the thinnest shells up to two nanometers for the thickest shells. The zinc sulfide shells trended in a similar manner with the thickest zinc sulfide shells showing high standard

deviations around three nanometers. The deposited shells, red-shifted the plasmon resonance of the gold nanoparticles up to 1.0 eV or higher. The cadmium sulfide shells produced higher red-shifts than the zinc sulfide shells did. The shells were stable in organic solutions and were utilized for ligand exchange and binding procedures.

The goal of quantum dot binding was to enhance the radiative rate of bound quantum dots. The binding was conducted utilizing the EDC coupling mechanism. Several ligand exchange procedures were needed to prepare each nanoparticle surface for coupling. First, quantum dots were coated with hexamethylene diamine and dispersed into dichloromethane. The hybrid nanoparticles were then coated with MUA and dissolved into dichloromethane. The MUA-coated nanoparticles were then treated with EDC and NHS, in dichloromethane and DMSO, in order to form an NHS-ester from the carboxylic acid group on the nanoparticle surface. Finally, the quantum dots were mixed with the NHS-esterified nanoparticle solution in order to link the two with an amide bond. The shell thickness was varied in order to study the optimal dielectric spacing needed to maximize the radiative rate of the quantum dots upon binding.

The radiative rate of the bound unbound quantum dots was calculated from the quantum yield and average lifetime of the colloidal solutions. The unbound quantum dots were utilized as the baseline and the bound quantum dot values were compared to the baseline result. The quantum yield was found to be maximum around 6-7 nm of shell thickness. The thinner shells should values more similar to the unbound quantum dots with a slight decrease in quantum yield and thickest shells showed mainly a decrease in the quantum yield. The lifetimes were all much shorter than the original quantum dots ,with the samples showing the highest quantum yield resulting in the largest decrease in

average lifetime. The larger shells showed a recovery of the average lifetime to almost 90% that of the unbound quantum dots. These results showed a maximum in radiative rate of the bound quantum at the same value of the quantum yield maximum at 6-7 nm shell thicknesses.

TEM images confirmed that the quantum dots were indeed intimately bound to the nanoparticle surface. The TEM images showed that the unbound quantum dots remained in the solutions after the binding run. This lead us to estimate the amount of enhancement actually seen by the nanoparticles was much higher due to the presence of unperturbed quantum dots. These experiments confirmed successful enhancement of a fluorophore in a solution-state ensemble. Although binding yield still needs optimization, the successful, distance-dependent enhancement shows the promise for this method of plasmonic enhancement.

Porphyrin binding to the hybrid nanoparticles was done in order to maximize binding for enhancement of their extinction coefficients. The q-band absorption modes were the target of this enhancement as they possess a much lower extinction coefficient than the Soret absorption. The thinnest core shell samples, 3-4 nm in radius, were utilized for these binding experiments in order to take maximum advantage of the higher extinction coefficient gold nanoparticles while still spacing the porphyrin away from the metal surface. A variety of different porphyrins were used for the coupling in order to study the effect of different binding configurations. TTP and TCO_4PP porphyrins were confirmed to bind in a face-on configuration, either through the inner pyrrole groups or the exterior alkoxy or phenyl arms. The configurations were confirmed via FTIR comparison between the free porphyrins and the porphyrins in the presence of

nanoparticles. TTPa and DTDa were monitored in the same manner and confirmed to bind via the phenyl acid groups on the exterior arms of the porphyrins.

The UV-vis spectra of the bound porphyrin showed a distinct dependence on the type of binding. Metallated and unmetallated TTP were both studied in order to monitor the effect of the center pyrroles with no other binding groups. When the pyrrole groups were occupied, the porphyrin absorption was found to remain unchanged upon mixing with the nanoparticles, while a slight enhancement in the absorption of the q-bands was observed in the unmetallated porphyrins. For the axial binding, TTPa and DTDPa were used, which contain one and two phenyl acid groups respectively. TTPa showed very little if any enhancement in the q-band absorption upon binding, while DTDPa showed the largest enhancement of any porphyrin species used in the binding experiments. The nature of the binding was also investigated from the ratio of the q-bands and their increase upon binding. It was found that, even without the anchoring of acid groups such as this case for TTP, the q-bands ratios increased. This trend was indicative of electron donation onto the surface of the hybrid nanoparticles. This trend was intuitive for the nucleophillic acid groups which should bind to unpassivated, cationic cadmium sites, but adds insight into the nature of a similar interaction between the porphyrins through the inner pyrroles or through stacking of the phenyl rings of TTP.

To confirm the electronic interaction of the porphyrin with the plasmon, fluorescence quenching experiments were conducted. The larger quenching would indicate a stronger coupling with the gold nanoparticle. DTDPa was shown to have the strongest quenching effect and therefore the strongest electronic interaction with the plasmon of the gold nanoparticles due to a higher binding strength via two phenyl acid

groups. Unmetallated TCO_4PP showed a slight quenching meaning the inner pyrrole groups provided a weaker electronic interaction with the nanoparticle plasmon. TTPa showed a slight enhancement in the porphyrin fluorescence. This enhancement was defined as a weaker coupling with the nanoparticle that produced minimal electronic interaction but rather a plasmonic coupling that was more similar to the quantum dot radiative rate enhancement. The average fluorescence lifetimes of the porphyrins were shown to be relatively stable upon binding, with most cases resulting in a slight increase in the decay rate.

Finally, the amount of enhancement experienced by DTPA was investigated. The enhanced extinction coefficients were calculated and compared to the original extinction coefficients. The binding was shown to produce enhancements up to three times the original extinction coefficient when bound to the hybrid nanoparticles. The binding was also found to be efficient with 70% of the porphyrin binding to the nanoparticle surface. This enhancement was found for the lower energy q-band. The higher energy q-band mirrored the results with only 1.5 times increase in the extinction coefficient.

In order to compare to thin films, gold nanoparticles and hybrid nanoparticles were bound to glass slides via a silane linker. The films were then soaked in a porphyrin solution over the course of two days. The film absorption was monitored with UV-vis absorption and then sonicated to investigate the affinity of the porphyrin for the different nanoparticles. We found that the hybrid nanoparticles showed a much higher affinity for porphyrin binding than the gold nanoparticles. This was observed by a much lower decrease in porphyrin absorption post-sonication with the hybrid nanoparticle films than was observed with the gold nanoparticle films. The thicker-shelled nanoparticles also

showed a much larger retention of porphyrin, due to a larger loading possible by the bigger surface of the nanoparticle available.

These studies show a viable method for production of highly absorptive solutions and films of porphyrins bound to hybrid nanoparticles. The porphyrin absorption can be increased through binding to the nanoparticles. Optimization of the film binding needs to be conducted in order to compare the solution-state absorption increase to films. The advantage of film samples, is the easy production of photovoltaic devices through application of electrodes and the use of conductive ITO. This will allow for direct measurements of produced photocurrent with the enhanced porphyrin composites.

This study shows a unique approach to the study of chromophore interaction with plasmonic materials. The careful optimization of the hybrid nanoparticle synthesis allowed for the production of highly uniform platforms to couple materials with a localized surface plasmon resonance ,without intimate contact to the metal surface. The semiconductor shell shows sharp contrast to the more common silica spacing that is used as a dielectric spacer in most solution-state coupling experiments. This straightforward system allows for coupling with a variety of different chromophores, without the need to change the plasmonic platform. This system also allows for the development of a myriad of complimentary experiments that stem from plasmonic coupling to these hybrid nanoparticles. The utility of these hybrid nanoparticles is their robust nature and tunablity in size and composition. Only zinc sulfide and cadmium sulfide shells were researched in this dissertation but these shells could be expanded to include any chalcogenide such as sulfur, selenium and tellurium and metals such as cadmium, zinc or lead. This provides a

rich library of shell materials which will produce changes in the dielectric environment, the electronic coupling and surface chemistry.

A method for linking quantum dots via EDC coupling was shown but click chemistry or other cross coupling techniques could be utilized to link quantum dots or other nanoparticles to the surface. Plasmonic coupling with magnetic nanoparticles could also be realized through this method to produce plasmonically enhanced magnetic responses. The porphyrin coupling shows a robust method to link other molecular dyes to the nanoparticle surface to boost their extinction coefficients. Other molecules could be bound for sensing or even surface enhanced Raman applications with very thin-shelled nanoparticles. The utility of this approach to coupling nanomaterials lies in its versatility and ability to be expanded to many other fields of research.

Future experiments to be conducted include the study of varying the quantum dot, diamine chain length, while keeping the shell thickness constant. Since the optimal shell thickness has already been investigated, the diamine linker may effect both binding yield and the degree of coupling to the surface. Single particle spectroscopy will also be conducted in order to study fluorescent blinking changes and possible multiple exciton generation produced upon coupling to the nanoparticle surface. Pump-probe spectroscopy would also prove useful into probing and modeling the electron and hole dynamics of the quantum dots and porphyrins upon coupling to the nanoparticle surface. Thin film samples of both bound quantum dots and bound porphyrins also need to be synthesized in order to compare to the solution-state experiments and investigate the optimal configuration for coupling. Finally, extending the core shell synthesis to gold nanorods represents the next step for optimizing loading onto the nanoparticle surface. The

nanorods also add the advantage of having a visible and near-IR plasmon resonance when engineered accordingly. This could allow for coupling of two different chromophores to maximize photoabsorption or drastically increasing both excitonic and multi-excitonic generation in bound species.

This project allowed for the combination of vast amounts of synthetic research coupled with spectroscopy. The research was a combination of inorganic nanoparticle synthesis coupled with nanoparticle surface chemistry and electron microscopy characterization. The coupling relied on the use of biochemical coupling and organic coupling mechanisms. This approach allowed for the optimization of both the coupling platform and the species being coupled. This two-phase approach represents the future of nanotechnology, where we have the ability to fine tune every aspect of the experiment. The ability to use more conventional chemical techniques with nanomaterial surface and synthetic techniques allows for the production of new materials and the improvement of older ones. This allows for easier troubleshooting and more freedom in creating new experiments. This ability is crucial for the development of new-age materials, aimed at solving new energy and technology issues.

REFERENCES

1. Bergh, A. A., Bulk degradation of GaP red LEDs. *IEEE Transactions on Electron Devices* **1971,** *18* (3), 166-170.

2. Nakamura, S.; Chichibu, S. F., *Introduction to nitride semiconductor blue lasers and light emitting diodes*. CRC Press: 2000.

3. Ki, W.; Li, J., A semiconductor bulk material that emits direct white light. *Journal of the American Chemical Society* **2008,** *130* (26), 8114-8115.

4. Basu, P. K., *Theory of optical processes in semiconductors: bulk and microstructures*. Clarendon press: 1997; Vol. 4.

5. Kressel, H., *Semiconductor Lasers and Herterojunction LEDs*. Elsevier: 2012.

6. Haug, H.; Koch, S. W., *Quantum theory of the optical and electronic properties of semiconductors*. World Scientific: 2004; Vol. 5.

7. Chuang, S. L.; Chuang, S. L., Physics of optoelectronic devices. **1995**.

8. Yablonovitch, E.; Kane, E., Band structure engineering of semiconductor lasers for optical communications. *Journal of lightwave technology* **1988,** *6* (8), 1292-1299.

9. Bard, A. J., Photoelectrochemistry and heterogeneous photo-catalysis at semiconductors. *Journal of Photochemistry* **1979,** *10* (1), 59-75.

10. Weisz, P., Effects of electronic charge transfer between adsorbate and solid on chemisorption and catalysis. *The Journal of Chemical Physics* **1953,** *21* (9), 1531-1538.

11. Linsebigler, A. L.; Lu, G.; Yates Jr, J. T., Photocatalysis on TiO2 surfaces: principles, mechanisms, and selected results. *Chemical reviews* **1995,** *95* (3), 735-758.

12. Shirasaki, Y.; Supran, G. J.; Bawendi, M. G.; Bulović, V., Emergence of colloidal quantum-dot light-emitting technologies. *Nature Photonics* **2013,** *7* (1), 13-23.

13. Anikeeva, P. O.; Halpert, J. E.; Bawendi, M. G.; Bulovic, V., Quantum dot light-emitting devices with electroluminescence tunable over the entire visible spectrum. *Nano letters* **2009,** *9* (7), 2532-2536.

14. Ustinov, V. M., *Quantum dot lasers*. Oxford University Press on Demand: 2003; Vol. 11.

15. Hakimi, F.; Bawendi, M. G.; Tumminelli, R.; Haavisto, J. R., Quantum dot Laser. Google Patents: 1993.

16. Claus, P.; Brückner, A.; Mohr, C.; Hofmeister, H., Supported gold nanoparticles from quantum dot to mesoscopic size scale: effect of electronic and structural properties on catalytic hydrogenation of conjugated functional groups. *Journal of the American Chemical Society* **2000,** *122* (46), 11430-11439.

17. Daniel, M.-C.; Astruc, D., Gold nanoparticles: assembly, supramolecular chemistry, quantum-size-related properties, and applications toward biology, catalysis, and nanotechnology. *Chemical reviews* **2004,** *104* (1), 293-346.

18. Duncan, K. A.; Johnson, C.; McElhinny, K.; Ng, S.; Cadwell, K. D.; Zenner Petersen, G. M.; Johnson, A.; Horoszewski, D.; Gentry, K.; Lisensky, G., Art as an avenue to science literacy: Teaching nanotechnology through stained glass. *Journal of chemical education* **2010,** *87* (10), 1031-1038.

19. Jennings, T.; Strouse, G., Past, present, and future of gold nanoparticles. In *Bio-Applications of Nanoparticles*, Springer: 2007; pp 34-47.

20. Lazarides, A.; Kelly, K. L.; Jensen, T.; Schatz, G. C., Optical properties of metal nanoparticles and nanoparticle aggregates important in biosensors. *Journal of Molecular Structure: THEOCHEM* **2000,** *529* (1), 59-63.

21. Singh, M.; Singh, S.; Prasad, S.; Gambhir, I., Nanotechnology in medicine and antibacterial effect of silver nanoparticles. *Digest Journal of Nanomaterials and Biostructures* **2008,** *3* (3), 115-122.

22. Alexander, J. W., History of the medical use of silver. *Surgical infections* **2009,** *10* (3), 289-292.

23. Chen, X.; Schluesener, H., Nanosilver: a nanoproduct in medical application. *Toxicology letters* **2008,** *176* (1), 1-12.

24. Guo, S.; Wang, E., Synthesis and electrochemical applications of gold nanoparticles. *Analytica Chimica Acta* **2007,** *598* (2), 181-192.

25. El-Sayed, I. H.; Huang, X.; El-Sayed, M. A., Surface plasmon resonance scattering and absorption of anti-EGFR antibody conjugated gold nanoparticles in cancer diagnostics: applications in oral cancer. *Nano letters* **2005,** *5* (5), 829-834.

26. Nath, N.; Chilkoti, A., A colorimetric gold nanoparticle sensor to interrogate biomolecular interactions in real time on a surface. *Analytical chemistry* **2002,** *74* (3), 504-509.

27. Kim, Y.; Johnson, R. C.; Hupp, J. T., Gold nanoparticle-based sensing of "spectroscopically silent" heavy metal ions. *Nano Letters* **2001,** *1* (4), 165-167.

28. Raj, C. R.; Okajima, T.; Ohsaka, T., Gold nanoparticle arrays for the voltammetric sensing of dopamine. *Journal of Electroanalytical Chemistry* **2003,** *543* (2), 127-133.

29. Eustis, S.; El-Sayed, M. A., Why gold nanoparticles are more precious than pretty gold: noble metal surface plasmon resonance and its enhancement of the radiative and nonradiative properties of nanocrystals of different shapes. *Chemical society reviews* **2006,** *35* (3), 209-217.

30. Kühn, S.; Håkanson, U.; Rogobete, L.; Sandoghdar, V., Enhancement of single-molecule fluorescence using a gold nanoparticle as an optical nanoantenna. *Physical review letters* **2006,** *97* (1), 017402.

31. Ciracì, C.; Hill, R.; Mock, J.; Urzhumov, Y.; Fernández-Domínguez, A.; Maier, S.; Pendry, J.; Chilkoti, A.; Smith, D., Probing the ultimate limits of plasmonic enhancement. *Science* **2012,** *337* (6098), 1072-1074.

32. Jana, N. R.; Gearheart, L.; Murphy, C. J., Seeding Growth for Size Control of 5−40 nm Diameter Gold Nanoparticles. *Langmuir* **2001,** *17* (22), 6782-6786.

33. Liu, X.; Atwater, M.; Wang, J.; Huo, Q., Extinction coefficient of gold nanoparticles with different sizes and different capping ligands. *Colloids and Surfaces B: Biointerfaces* **2007,** *58* (1), 3-7.

34. Sun, Y.; Xia, Y., Shape-controlled synthesis of gold and silver nanoparticles. *Science* **2002,** *298* (5601), 2176-2179.

35. Ye, X.; Jin, L.; Caglayan, H.; Chen, J.; Xing, G.; Zheng, C.; Doan-Nguyen, V.; Kang, Y.; Engheta, N.; Kagan, C. R., Improved size-tunable synthesis of monodisperse gold nanorods through the use of aromatic additives. *ACS nano* **2012,** *6* (3), 2804-2817.

36. Link, S.; El-Sayed, M. A., Optical properties and ultrafast dynamics of metallic nanocrystals. *Annual review of physical chemistry* **2003,** *54* (1), 331-366.

37. Cao, Y. C.; Jin, R.; Mirkin, C. A., Nanoparticles with Raman Spectroscopic Fingerprints for DNA and RNA Detection. *Science* **2002,** *297* (5586), 1536-1540.

38. Murphy, C. J.; Gole, A. M.; Hunyadi, S. E.; Stone, J. W.; Sisco, P. N.; Alkilany, A.; Kinard, B. E.; Hankins, P., Chemical sensing and imaging with metallic nanorods. *Chemical Communications* **2008,** (5), 544-557.

39. Chen, J.; Saeki, F.; Wiley, B. J.; Cang, H.; Cobb, M. J.; Li, Z.-Y.; Au, L.; Zhang, H.; Kimmey, M. B.; Li; Xia, Y., Gold Nanocages: Bioconjugation and Their Potential Use as Optical Imaging Contrast Agents. *Nano Letters* **2005,** *5* (3), 473-477.

40. Lakowicz, J. R.; Ray, K.; Chowdhury, M.; Szmacinski, H.; Fu, Y.; Zhang, J.; Nowaczyk, K., Plasmon-controlled fluorescence: a new paradigm in fluorescence spectroscopy. *Analyst* **2008,** *133* (10), 1308-1346.

41. Lakowicz, J. R., Radiative decay engineering 5: metal-enhanced fluorescence and plasmon emission. *Analytical biochemistry* **2005,** *337* (2), 171-194.

42. Oh, E.; Hong, M.-Y.; Lee, D.; Nam, S.-H.; Yoon, H. C.; Kim, H.-S., Inhibition Assay of Biomolecules based on Fluorescence Resonance Energy Transfer (FRET) between Quantum Dots and Gold Nanoparticles. *Journal of the American Chemical Society* **2005,** *127* (10), 3270-3271.

43. Wang, L.; Yan, R.; Huo, Z.; Wang, L.; Zeng, J.; Bao, J.; Wang, X.; Peng, Q.; Li, Y., Fluorescence Resonant Energy Transfer Biosensor Based on Upconversion-Luminescent Nanoparticles. *Angewandte Chemie International Edition* **2005,** *44* (37), 6054-6057.

44. Saha, K.; Agasti, S. S.; Kim, C.; Li, X.; Rotello, V. M., Gold nanoparticles in chemical and biological sensing. *Chemical reviews* **2012,** *112* (5), 2739-2779.

45. Dulkeith, E.; Morteani, A.; Niedereichholz, T.; Klar, T.; Feldmann, J.; Levi, S.; Van Veggel, F.; Reinhoudt, D.; Möller, M.; Gittins, D., Fluorescence quenching of dye molecules near gold nanoparticles: radiative and nonradiative effects. *Physical review letters* **2002,** *89* (20), 203002.

46. Elghanian, R.; Storhoff, J. J.; Mucic, R. C.; Letsinger, R. L.; Mirkin, C. A., Selective Colorimetric Detection of Polynucleotides Based on the Distance-Dependent Optical Properties of Gold Nanoparticles. *Science* **1997,** *277* (5329), 1078-1081.

47. Sönnichsen, C.; Reinhard, B. M.; Liphardt, J.; Alivisatos, A. P., A molecular ruler based on plasmon coupling of single gold and silver nanoparticles. *Nature biotechnology* **2005,** *23* (6), 741-745.

48. Jain, P. K.; Huang, W.; El-Sayed, M. A., On the universal scaling behavior of the distance decay of plasmon coupling in metal nanoparticle pairs: a plasmon ruler equation. *Nano Letters* **2007,** *7* (7), 2080-2088.

49. Pons, T.; Medintz, I. L.; Sapsford, K. E.; Higashiya, S.; Grimes, A. F.; English, D. S.; Mattoussi, H., On the Quenching of Semiconductor Quantum Dot Photoluminescence by Proximal Gold Nanoparticles. *Nano Letters* **2007,** *7* (10), 3157-3164.

50. Li, M.; Cushing, S. K.; Wang, Q.; Shi, X.; Hornak, L. A.; Hong, Z.; Wu, N., Size-Dependent Energy Transfer between CdSe/ZnS Quantum Dots and Gold Nanoparticles. *The Journal of Physical Chemistry Letters* **2011,** *2* (17), 2125-2129.

51. Grätzel, M., Dye-sensitized solar cells. *Journal of Photochemistry and Photobiology C: Photochemistry Reviews* **2003,** *4* (2), 145-153.

52. Chamberlain, G., Organic solar cells: a review. *Solar cells* **1983,** *8* (1), 47-83.

53. Shah, A.; Torres, P.; Tscharner, R.; Wyrsch, N.; Keppner, H., Photovoltaic Technology: The Case for Thin-Film Solar Cells. *Science* **1999,** *285* (5428), 692-698.

54. Fu, Y.; Zhang, J.; Lakowicz, J. R., Plasmonic Enhancement of Single-Molecule Fluorescence Near a Silver Nanoparticle. *J Fluoresc* **2007,** *17* (6), 811-816.

55. Schaadt, D. M.; Feng, B.; Yu, E. T., Enhanced semiconductor optical absorption via surface plasmon excitation in metal nanoparticles. *Applied Physics Letters* **2005,** *86* (6), 063106.

56. Lim, S.; Mar, W.; Matheu, P.; Derkacs, D.; Yu, E., Photocurrent spectroscopy of optical absorption enhancement in silicon photodiodes via scattering from surface plasmon polaritons in gold nanoparticles. *Journal of Applied Physics* **2007,** *101* (10), 104309.

57. Hasobe, T.; Imahori, H.; Kamat, P. V.; Ahn, T. K.; Kim, S. K.; Kim, D.; Fujimoto, A.; Hirakawa, T.; Fukuzumi, S., Photovoltaic cells using composite nanoclusters of porphyrins and fullerenes with gold nanoparticles. *Journal of the American Chemical Society* **2005,** *127* (4), 1216-1228.

58. Tian, Y.; Tatsuma, T., Mechanisms and applications of plasmon-induced charge separation at TiO2 films loaded with gold nanoparticles. *Journal of the American Chemical Society* **2005,** *127* (20), 7632-7637.

59. Maaroof, A. I.; Lee, H.; Heo, K.; Park, J.; Cho, D.; Lee, B. Y.; Seong, M.-J.; Hong, S., Plasmon–Exciton Interactions in Hybrid Structures of Au Nanohemispheres and CdS Nanowires for Improved Photoconductive Devices. *The Journal of Physical Chemistry C* **2013,** *117* (46), 24543-24548.

60. Chen, Y.; Munechika, K.; Jen-La Plante, I.; Munro, A. M.; Skrabalak, S. E.; Xia, Y.; Ginger, D. S., Excitation enhancement of CdSe quantum dots by single metal nanoparticles. *Applied Physics Letters* **2008,** *93* (5), 53106-53106.

61. Xia, Y.; Halas, N. J., Shape-controlled synthesis and surface plasmonic properties of metallic nanostructures. *MRS bulletin* **2005,** *30* (05), 338-348.

62. Ozbay, E., Plasmonics: merging photonics and electronics at nanoscale dimensions. *science* **2006,** *311* (5758), 189-193.

63. Conde, J.; Doria, G.; Baptista, P., Noble metal nanoparticles applications in cancer. *Journal of drug delivery* **2011,** *2012*.

64. Linic, S.; Christopher, P.; Ingram, D. B., Plasmonic-metal nanostructures for efficient conversion of solar to chemical energy. *Nature materials* **2011,** *10* (12), 911-921.

65. Schuller, J. A.; Barnard, E. S.; Cai, W.; Jun, Y. C.; White, J. S.; Brongersma, M. L., Plasmonics for extreme light concentration and manipulation. *Nature materials* **2010,** *9* (3), 193-204.

66. Huang, X.; Tang, S.; Mu, X.; Dai, Y.; Chen, G.; Zhou, Z.; Ruan, F.; Yang, Z.; Zheng, N., Freestanding palladium nanosheets with plasmonic and catalytic properties. *Nature nanotechnology* **2011,** *6* (1), 28-32.

67. Haes, A. J.; Haynes, C. L.; McFarland, A. D.; Schatz, G. C.; Van Duyne, R. P.; Zou, S., Plasmonic materials for surface-enhanced sensing and spectroscopy. *Mrs Bulletin* **2005,** *30* (05), 368-375.

68. Wiederrecht, G. P.; Wurtz, G. A.; Hranisavljevic, J., Coherent coupling of molecular excitons to electronic polarizations of noble metal nanoparticles. *Nano Letters* **2004,** *4* (11), 2121-2125.

69. Ray, P. C.; Fortner, A.; Darbha, G. K., Gold nanoparticle based FRET asssay for the detection of DNA cleavage. *The Journal of Physical Chemistry B* **2006,** *110* (42), 20745-20748.

70. Reinhard, B. M.; Siu, M.; Agarwal, H.; Alivisatos, A. P.; Liphardt, J., Calibration of dynamic molecular rulers based on plasmon coupling between gold nanoparticles. *Nano letters* **2005,** *5* (11), 2246-2252.

71. Acuna, G. P.; Bucher, M.; Stein, I. H.; Steinhauer, C.; Kuzyk, A.; Holzmeister, P.; Schreiber, R.; Moroz, A.; Stefani, F. D.; Liedl, T., Distance dependence of single-fluorophore quenching by gold nanoparticles studied on DNA origami. *ACS nano* **2012,** *6* (4), 3189-3195.

72. Chhabra, R.; Sharma, J.; Wang, H.; Zou, S.; Lin, S.; Yan, H.; Lindsay, S.; Liu, Y., Distance-dependent interactions between gold nanoparticles and fluorescent molecules with DNA as tunable spacers. *Nanotechnology* **2009,** *20* (48), 485201.

73. Liu, G. L.; Long, Y.-T.; Choi, Y.; Kang, T.; Lee, L. P., Quantized plasmon quenching dips nanospectroscopy via plasmon resonance energy transfer. *Nature Methods* **2007,** *4* (12).

74. Choi, Y.; Kang, T.; Lee, L. P., Plasmon resonance energy transfer (PRET)-based molecular imaging of cytochrome c in living cells. *Nano letters* **2008,** *9* (1), 85-90.

75. Choi, Y.; Park, Y.; Kang, T.; Lee, L. P., Selective and sensitive detection of metal ions by plasmonic resonance energy transfer-based nanospectroscopy. *Nature nanotechnology* **2009,** *4* (11), 742-746.

76. Kinkhabwala, A.; Yu, Z.; Fan, S.; Avlasevich, Y.; Müllen, K.; Moerner, W., Large single-molecule fluorescence enhancements produced by a bowtie nanoantenna. *Nature Photonics* **2009,** *3* (11), 654-657.

77. Okamoto, K.; Niki, I.; Shvartser, A.; Narukawa, Y.; Mukai, T.; Scherer, A., Surface-plasmon-enhanced light emitters based on InGaN quantum wells. *Nature materials* **2004,** *3* (9), 601-605.

78. Vahala, K. J., Optical microcavities. *Nature* **2003,** *424* (6950), 839-846.

79. Gérard, J.; Sermage, B.; Gayral, B.; Legrand, B.; Costard, E.; Thierry-Mieg, V., Enhanced spontaneous emission by quantum boxes in a monolithic optical microcavity. *Physical review letters* **1998,** *81* (5), 1110.

80. Mikkelsen, M. H. In *Strongly Enhanced Light-Matter Interactions using Colloidally Synthesized Plasmonic Nanocavities*, Laser Science, Optical Society of America: 2015; p LTh1I. 2.

81. Mathew, S.; Yella, A.; Gao, P.; Humphry-Baker, R.; Curchod, B. F.; Ashari-Astani, N.; Tavernelli, I.; Rothlisberger, U.; Nazeeruddin, M. K.; Grätzel, M., Dye-sensitized solar cells with 13% efficiency achieved through the molecular engineering of porphyrin sensitizers. *Nature chemistry* **2014,** *6* (3), 242-247.

82. D'Andrade, B. W.; Forrest, S. R., White organic light‐emitting devices for solid‐state lighting. *Advanced Materials* **2004,** *16* (18), 1585-1595.

83. Jang, E.; Jun, S.; Jang, H.; Lim, J.; Kim, B.; Kim, Y., White‐Light‐Emitting Diodes with Quantum Dot Color Converters for Display Backlights. *Advanced Materials* **2010,** *22* (28), 3076-3080.

84. López-Lorente, A.; Simonet, B.; Valcárcel, M., Analytical potential of hybrid nanoparticles. *Analytical and bioanalytical chemistry* **2011,** *399* (1), 43-54.

85. Zhang, M.; Bai, L.; Shang, W.; Xie, W.; Ma, H.; Fu, Y.; Fang, D.; Sun, H.; Fan, L.; Han, M., Facile synthesis of water-soluble, highly fluorescent graphene quantum dots as a robust biological label for stem cells. *Journal of materials chemistry* **2012,** *22* (15), 7461-7467.

86. Chandra, S.; Doran, J.; McCormack, S. J.; Kennedy, M.; Chatten, A. J., Enhanced quantum dot emission for luminescent solar concentrators using plasmonic interaction. *Solar Energy Materials and Solar Cells* **2012,** *98*, 385-390.

87. Meinardi, F.; Colombo, A.; Velizhanin, K. A.; Simonutti, R.; Lorenzon, M.; Beverina, L.; Viswanatha, R.; Klimov, V. I.; Brovelli, S., Large-area luminescent solar concentrators based on/Stokes-shift-engineered/'nanocrystals in a mass-polymerized PMMA matrix. *Nature Photonics* **2014,** *8* (5), 392-399.

88. Amirav, L.; Alivisatos, A. P., Photocatalytic hydrogen production with tunable nanorod heterostructures. *The Journal of Physical Chemistry Letters* **2010,** *1* (7), 1051-1054.

89. Zhu, H.; Song, N.; Lv, H.; Hill, C. L.; Lian, T., Near unity quantum yield of light-driven redox mediator reduction and efficient H2 generation using colloidal nanorod heterostructures. *Journal of the American Chemical Society* **2012,** *134* (28), 11701-11708.

90. Brown, K. A.; Dayal, S.; Ai, X.; Rumbles, G.; King, P. W., Controlled assembly of hydrogenase-CdTe nanocrystal hybrids for solar hydrogen production. *Journal of the American Chemical Society* **2010,** *132* (28), 9672-9680.

91. Huang, J.; Mulfort, K. L.; Du, P.; Chen, L. X., Photodriven charge separation dynamics in CdSe/ZnS core/shell quantum dot/cobaloxime hybrid for efficient hydrogen production. *Journal of the American Chemical Society* **2012,** *134* (40), 16472-16475.

92. Aslan, K.; Gryczynski, I.; Malicka, J.; Matveeva, E.; Lakowicz, J. R.; Geddes, C. D., Metal-enhanced fluorescence: an emerging tool in biotechnology. *Current Opinion in Biotechnology* **2005,** *16* (1), 55-62.

93. Hwang, E.; Smolyaninov, I. I.; Davis, C. C., Surface plasmon polariton enhanced fluorescence from quantum dots on nanostructured metal surfaces. *Nano letters* **2010,** *10* (3), 813-820.

94. Viste, P.; Plain, J.; Jaffiol, R.; Vial, A.; Adam, P. M.; Royer, P., Enhancement and Quenching Regimes in Metal− Semiconductor Hybrid Optical Nanosources. *ACS nano* **2010,** *4* (2), 759-764.

95. Naiki, H.; Masuo, S.; Machida, S.; Itaya, A., Single-photon emission behavior of isolated CdSe/ZnS quantum dots interacting with the localized surface plasmon resonance of silver nanoparticles. *The Journal of Physical Chemistry C* **2011,** *115* (47), 23299-23304.

96. Song, M.; Wu, B.; Chen, G.; Liu, Y.; Ci, X.; Wu, E.; Zeng, H., Photoluminescence plasmonic enhancement of single quantum dots coupled to gold microplates. *The Journal of Physical Chemistry C* **2014,** *118* (16), 8514-8520.

97. Gryczynski, I.; Malicka, J.; Jiang, W.; Fischer, H.; Chan, W. C.; Gryczynski, Z.; Grudzinski, W.; Lakowicz, J. R., Surface-plasmon-coupled emission of quantum dots. *The Journal of Physical Chemistry B* **2005,** *109* (3), 1088-1093.

98. Jin, Y.; Gao, X., Plasmonic fluorescent quantum dots. *Nature nanotechnology* **2009,** *4* (9), 571-576.

99. Kulakovich, O.; Strekal, N.; Yaroshevich, A.; Maskevich, S.; Gaponenko, S.; Nabiev, I.; Woggon, U.; Artemyev, M., Enhanced luminescence of CdSe quantum dots on gold colloids. *Nano Letters* **2002,** *2* (12), 1449-1452.

100. Bian, R. X.; Dunn, R. C.; Xie, X. S.; Leung, P., Single molecule emission characteristics in near-field microscopy. *Physical review letters* **1995,** *75* (26), 4772.

101. Anger, P.; Bharadwaj, P.; Novotny, L., Enhancement and quenching of single-molecule fluorescence. *Physical review letters* **2006,** *96* (11), 113002.

102. Song, J.-H.; Atay, T.; Shi, S.; Urabe, H.; Nurmikko, A. V., Large enhancement of fluorescence efficiency from CdSe/ZnS quantum dots induced by resonant coupling to spatially controlled surface plasmons. *Nano letters* **2005,** *5* (8), 1557-1561.

103. (a) Imahori, H.; Norieda, H.; Nishimura, Y.; Yamazaki, I.; Higuchi, K.; Kato, N.; Motohiro, T.; Yamada, H.; Tamaki, K.; Arimura, M., Chain length effect on the structure and photoelectrochemical properties of self-assembled monolayers of porphyrins on gold electrodes. *The Journal of Physical Chemistry B* **2000,** *104* (6), 1253-1260; (b) Yamada, H.; Imahori, H.; Nishimura, Y.; Yamazaki, I.; Ahn, T. K.; Kim, S. K.; Kim, D.; Fukuzumi, S., Photovoltaic properties of self-assembled monolayers of porphyrins and porphyrin-fullerene dyads on ITO and gold surfaces. *Journal of the American Chemical Society* **2003,** *125* (30), 9129-9139.

104. Ni, W.; Yang, Z.; Chen, H.; Li, L.; Wang, J., Coupling between molecular and plasmonic resonances in freestanding dye− gold nanorod hybrid nanostructures. *Journal of the American Chemical Society* **2008,** *130* (21), 6692-6693.

105. Imahori, H.; Norieda, H.; Yamada, H.; Nishimura, Y.; Yamazaki, I.; Sakata, Y.; Fukuzumi, S., Light-harvesting and photocurrent generation by gold electrodes modified with mixed self-assembled monolayers of boron-dipyrrin and ferrocene-porphyrin-fullerene triad. *Journal of the American Chemical Society* **2001,** *123* (1), 100-110.

106. Liu, N.; Prall, B. S.; Klimov, V. I., Hybrid gold/silica/nanocrystal-quantum-dot superstructures: synthesis and analysis of semiconductor-metal interactions. *Journal of the American Chemical Society* **2006,** *128* (48), 15362-15363.

107. Lee, Y.-L.; Lo, Y.-S., Highly Efficient Quantum-Dot-Sensitized Solar Cell Based on Co-Sensitization of CdS/CdSe. *Advanced Functional Materials* **2009,** *19* (4), 604-609.

108. Santra, P. K.; Kamat, P. V., Mn-Doped Quantum Dot Sensitized Solar Cells: A Strategy to Boost Efficiency over 5%. *Journal of the American Chemical Society* **2012,** *134* (5), 2508-2511.

109. Campbell, W. M.; Burrell, A. K.; Officer, D. L.; Jolley, K. W., Porphyrins as light harvesters in the dye-sensitised TiO 2 solar cell. *Coordination Chemistry Reviews* **2004,** *248* (13), 1363-1379.

110. Zhang, J., *Optical Properties and Spectroscopy of Nanomaterials*. World Scientific Publishing Co. Pte. Ltd.: 2009; p 383.

111. Burda, C.; Chen, X.; Narayanan, R.; El-Sayed, M. A., Chemistry and Properties of Nanocrystals of Different Shapes. *Chemical Reviews* **2005,** *105* (4), 1025-1102.

112. Kumar, S.; Nann, T., Shape control of II–VI semiconductor nanomaterials. *Small* **2006,** *2* (3), 316-329.

113. Clapp, A. R.; Goldman, E. R.; Mattoussi, H., Capping of CdSe-ZnS quantum dots with DHLA and subsequent conjugation with proteins. *Nat. Protocols* **2006,** *1* (3), 1258-1266.

114. García-Santamaría, F.; Chen, Y.; Vela, J.; Schaller, R. D.; Hollingsworth, J. A.; Klimov, V. I., Suppressed auger recombination in "giant" nanocrystals boosts optical gain performance. *Nano letters* **2009,** *9* (10), 3482-3488.

115. Li, J. J.; Wang, Y. A.; Guo, W.; Keay, J. C.; Mishima, T. D.; Johnson, M. B.; Peng, X., Large-scale synthesis of nearly monodisperse CdSe/CdS core/shell nanocrystals using air-stable reagents via successive ion layer adsorption and reaction. *Journal of the American Chemical Society* **2003,** *125* (41), 12567-12575.

116. Campbell, W. M.; Jolley, K. W.; Wagner, P.; Wagner, K.; Walsh, P. J.; Gordon, K. C.; Schmidt-Mende, L.; Nazeeruddin, M. K.; Wang, Q.; Grätzel, M., Highly efficient porphyrin sensitizers for dye-sensitized solar cells. *The Journal of Physical Chemistry C* **2007,** *111* (32), 11760-11762.

117. Walter, M. G.; Wamser, C. C.; Ruwitch, J.; Zhao, Y.; Braden, D.; Stevens, M.; Denman, A.; Pi, R.; Rudine, A.; Pessiki, P. J., Syntheses and optoelectronic properties of amino/carboxyphenylporphyrins for potential use in dye-sensitized TiO 2 solar cells. *Journal of Porphyrins and Phthalocyanines* **2007,** *11* (08), 601-612.

118. Lindsey, J. S.; Schreiman, I. C.; Hsu, H. C.; Kearney, P. C.; Marguerettaz, A. M., Rothemund and Adler-Longo reactions revisited: synthesis of tetraphenylporphyrins under equilibrium conditions. *The Journal of Organic Chemistry* **1987,** *52* (5), 827-836.

119. Bonnett, R., Photosensitizers of the porphyrin and phthalocyanine series for photodynamic therapy. *Chemical Society Reviews* **1995,** *24* (1), 19-33.

120. Gomer, C. J.; Rucker, N.; Murphree, A. L., Differential cell photosensitivity following porphyrin photodynamic therapy. *Cancer research* **1988,** *48* (16), 4539-4542.

121. Henderson, B. W.; Dougherty, T. J., How does photodynamic therapy work? *Photochemistry and photobiology* **1992,** *55* (1), 145-157.

122. Yella, A.; Lee, H.-W.; Tsao, H. N.; Yi, C.; Chandiran, A. K.; Nazeeruddin, M. K.; Diau, E. W.-G.; Yeh, C.-Y.; Zakeeruddin, S. M.; Grätzel, M., Porphyrin-sensitized solar cells with cobalt (II/III)–based redox electrolyte exceed 12 percent efficiency. *science* **2011,** *334* (6056), 629-634.

123. Milgrom, L. R., *The colours of life: an introduction to the chemistry of porphyrins and related compounds*. Oxford University Press Oxford: 1997; Vol. 232.

124. Marsh, D.; Mink, L., Microscale Synthesis and Electronic Absorption Spectroscopy of Tetraphenylporphyrin H2(TPP) and Metalloporphyrins ZnII(TPP) and NiII(TPP). *Journal of Chemical Education* **1996,** *73* (12), 1188.

125. Standridge, S. D.; Schatz, G. C.; Hupp, J. T., Distance dependence of plasmon-enhanced photocurrent in dye-sensitized solar cells. *Journal of the American Chemical Society* **2009,** *131* (24), 8407-8409.

126. Arakawa, T.; Munaoka, T.; Akiyama, T.; Yamada, S., Effects of Silver Nanoparticles on Photoelectrochemical Responses of Organic Dyes†. *The Journal of Physical Chemistry C* **2009,** *113* (27), 11830-11835.

127. Sugawa, K.; Akiyama, T.; Kawazumi, H.; Yamada, S., Plasmon-enhanced photocurrent generation from self-assembled monolayers of phthalocyanine by using gold nanoparticle films. *Langmuir* **2009,** *25* (6), 3887-3893.

128. Akiyama, T.; Nakada, M.; Terasaki, N.; Yamada, S., Photocurrent enhancement in a porphyrin-gold nanoparticle nanostructure assisted by localized plasmon excitation. *Chem. Commun.* **2006,** (4), 395-397.

129. Costi, R.; Saunders, A. E.; Banin, U., Colloidal Hybrid Nanostructures: A New Type of Functional Materials. *Angewandte Chemie International Edition* **2010,** *49* (29), 4878-4897.

130. Murphy, C. J.; Gole, A. M.; Stone, J. W.; Sisco, P. N.; Alkilany, A. M.; Goldsmith, E. C.; Baxter, S. C., Gold Nanoparticles in Biology: Beyond Toxicity to Cellular Imaging. *Accounts of Chemical Research* **2008,** *41* (12), 1721-1730.

131. Crespo, P.; Litrán, R.; Rojas, T.; Multigner, M.; De la Fuente, J.; Sánchez-López, J.; García, M.; Hernando, A.; Penadés, S.; Fernández, A., Permanent magnetism, magnetic anisotropy, and hysteresis of thiol-capped gold nanoparticles. *Physical review letters* **2004,** *93* (8), 087204.

132. Demers, L. M.; Mirkin, C. A.; Mucic, R. C.; Reynolds, R. A.; Letsinger, R. L.; Elghanian, R.; Viswanadham, G., A fluorescence-based method for determining the surface coverage and hybridization efficiency of thiol-capped oligonucleotides bound to gold thin films and nanoparticles. *Analytical chemistry* **2000,** *72* (22), 5535-5541.

133. Leff, D. V.; Brandt, L.; Heath, J. R., Synthesis and characterization of hydrophobic, organically-soluble gold nanocrystals functionalized with primary amines. *Langmuir* **1996,** *12* (20), 4723-4730.

134. Weare, W. W.; Reed, S. M.; Warner, M. G.; Hutchison, J. E., Improved synthesis of small (d core≈ 1.5 nm) phosphine-stabilized gold nanoparticles. *Journal of the American Chemical Society* **2000,** *122* (51), 12890-12891.

135. Warner, M. G.; Reed, S. M.; Hutchison, J. E., Small, water-soluble, ligand-stabilized gold nanoparticles synthesized by interfacial ligand exchange reactions. *Chemistry of materials* **2000,** *12* (11), 3316-3320.

136. Kimling, J.; Maier, M.; Okenve, B.; Kotaidis, V.; Ballot, H.; Plech, A., Turkevich method for gold nanoparticle synthesis revisited. *The Journal of Physical Chemistry B* **2006,** *110* (32), 15700-15707.

137. Link, S.; El-Sayed, M. A., Size and temperature dependence of the plasmon absorption of colloidal gold nanoparticles. *The Journal of Physical Chemistry B* **1999,** *103* (21), 4212-4217.

138. Turkevich, J.; Garton, G.; Stevenson, P., The color of colloidal gold. *Journal of colloid Science* **1954,** *9*, 26-35.

139. Jana, N. R.; Gearheart, L.; Murphy, C. J., Seed-mediated growth approach for shape-controlled synthesis of spheroidal and rod-like gold nanoparticles using a surfactant template. *Advanced Materials* **2001,** *13* (18), 1389.

140. Millstone, J. E.; Wei, W.; Jones, M. R.; Yoo, H.; Mirkin, C. A., Iodide ions control seed-mediated growth of anisotropic gold nanoparticles. *Nano letters* **2008,** *8* (8), 2526-2529.

141. Zhang, J.; Tang, Y.; Lee, K.; Ouyang, M., Nonepitaxial Growth of Hybrid Core-Shell Nanostructures with Large Lattice Mismatches. *Science* **2010,** *327* (5973), 1634-1638.

142. Lambright, S.; Butaeva, E.; Razgoniaeva, N.; Hopkins, T.; Smith, B.; Perera, D.; Corbin, J.; Khon, E.; Thomas, R.; Moroz, P.; Mereshchenko, A.; Tarnovsky, A.; Zamkov, M., Enhanced Lifetime of Excitons in Nonepitaxial Au/CdS Core/Shell Nanocrystals. *ACS Nano* **2014,** *8* (1), 352-361.

143. Ma, Y.; Li, W.; Cho, E. C.; Li, Z.; Yu, T.; Zeng, J.; Xie, Z.; Xia, Y., Au@ Ag core− shell nanocubes with finely tuned and well-controlled sizes, shell thicknesses, and optical properties. *ACS nano* **2010,** *4* (11), 6725-6734.

144. Schaaff, T. G.; Rodinone, A. J., Preparation and characterization of silver sulfide nanocrystals generated from silver (i)-thiolate polymers. *The Journal of Physical Chemistry B* **2003,** *107* (38), 10416-10422.

145. Han, L.; Lv, Y.; Asiri, A. M.; Al-Youbi, A. O.; Tu, B.; Zhao, D., Novel preparation and near-infrared photoluminescence of uniform core-shell silver sulfide nanoparticle@ mesoporous silica nanospheres. *Journal of Materials Chemistry* **2012,** *22* (15), 7274-7279.

146. Reiss, P.; Protiere, M.; Li, L., Core/shell semiconductor nanocrystals. *small* **2009,** *5* (2), 154-168.

147. EDC coupling <https://**www.lifetechnologies.com/us/en/home/life-science/protein-biology/protein-biology-learning-center/protein-biology-resource-library/pierce-protein-methods/carbodiimide-crosslinker-chemistry.html>**.

148. Mock, J. J.; Hill, R. T.; Degiron, A.; Zauscher, S.; Chilkoti, A.; Smith, D. R., Distance-dependent plasmon resonant coupling between a gold nanoparticle and gold film. *Nano letters* **2008,** *8* (8), 2245-2252.

149. Chen, Y.; Munechika, K.; Ginger, D. S., Dependence of fluorescence intensity on the spectral overlap between fluorophores and plasmon resonant single silver nanoparticles. *Nano letters* **2007,** *7* (3), 690-696.

150. Jain, P. K.; El-Sayed, M. A., Plasmonic coupling in noble metal nanostructures. *Chemical Physics Letters* **2010,** *487* (4), 153-164.

151. Link, S.; El-Sayed, M. A., Spectral properties and relaxation dynamics of surface plasmon electronic oscillations in gold and silver nanodots and nanorods. *The Journal of Physical Chemistry B* **1999,** *103* (40), 8410-8426.

152. Ahmadi, T. S.; Logunov, S. L.; El-Sayed, M. A., Picosecond dynamics of colloidal gold nanoparticles. *The Journal of Physical Chemistry* **1996,** *100* (20), 8053-8056.

153. Logunov, S.; Ahmadi, T.; El-Sayed, M.; Khoury, J.; Whetten, R., Electron dynamics of passivated gold nanocrystals probed by subpicosecond transient absorption spectroscopy. *The Journal of Physical Chemistry B* **1997,** *101* (19), 3713-3719.

154. Zhang, M.; Cao, X.; Li, H.; Guan, F.; Guo, J.; Shen, F.; Luo, Y.; Sun, C.; Zhang, L., Sensitive fluorescent detection of melamine in raw milk based on the inner filter effect of Au nanoparticles on the fluorescence of CdTe quantum dots. *Food chemistry* **2012,** *135* (3), 1894-1900.

155. Li, X.; Qian, J.; Jiang, L.; He, S., Fluorescence quenching of quantum dots by gold nanorods and its application to DNA detection. *Applied Physics Letters* **2009,** *94* (6), 063111.

156. Dick, H. A.; Bolton, J. R.; Picard, G.; Munger, G.; Leblanc, R. M., Fluorescence lifetime of 5-(4-carboxyphenyl)-10,15,20-tritolylporphyrin in a mixed Langmuir-Blodgett film with dioleoylphosphatidylcholine. A proposed standard. *Langmuir* **1988,** *4* (1), 133-136.

157. Little, R. G.; Anton, J. A.; Loach, P. A.; Ibers, J. A., The synthesis of some substituted tetraarylporphyrins. *Journal of Heterocyclic Chemistry* **1975,** *12* (2), 343-349.

158. Namuangruk, S.; Sirithip, K.; Rattanatwan, R.; Keawin, T.; Kungwan, N.; Sudyodsuk, T.; Promarak, V.; Surakhot, Y.; Jungsuttiwong, S., Theoretical investigation

of the charge-transfer properties in different meso-linked zinc porphyrins for highly efficient dye-sensitized solar cells. *Dalton Transactions* **2014,** *43* (24), 9166-9176.

159. Spellane, P.; Gouterman, M.; Antipas, A.; Kim, S.; Liu, Y., Porphyrins. 40. Electronic spectra and four-orbital energies of free-base, zinc, copper, and palladium tetrakis (perfluorophenyl) porphyrins. *Inorganic Chemistry* **1980,** *19* (2), 386-391.

APPENDIX A: GAUSSIAN FITTING FOR ABSORBANCE SPECTRA

The figure below shows an example fit for an absorbance spectra of a gold nanoparticle solution. The peak is fit to a guassian and normalized to 1. The full-wdith at half the maximum was then used for the plot in Figure 5.42.

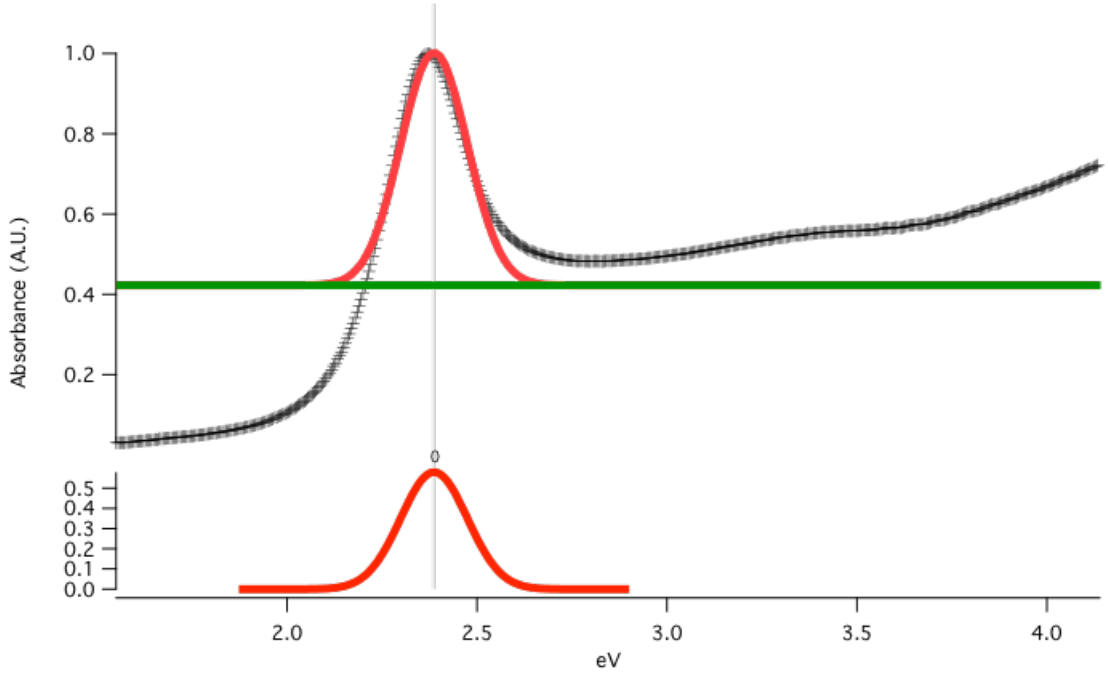

Figure A1: Absorbance spectra of a gold nanoparticle solution (black markers) and the associated Guassian fit to the plasmon resonance peak.

APPENDIX B: ESI-MASS SPECTROMETTRY OF PORPHYRIN

The porphyrins show very little error from the theoretical values, with TCO_4PP showing the highest experimental error of 6.6%. The experimental mass difference between the theoretical and experimental for TCO_4PP, could stem from a fragmentation product of one of the alkyl chains and was not further investigated. The porphyrin solutions could be separated cleanly from one another, with little to no residual traces of other porphyrin species in each batch. These porphyrins were then analyzed via FTIR spectroscopy to determine the nature of the functional groups free and in the presence of hybrid nanoparticles.

Porphyrin name	Theoretical m/z	Experimental m/z	% error
TTP	670.31	670.86	0.08%
TCO_4PP	1238.71	1156.69	6.6%
TTPa	700.28	701.45	0.17%
DTDPa	730.26	730.85	0.08%

Table B2: Comparison of experimental and theoretical m/z ratios for the porphyrins used for binding.

TCO_4PP

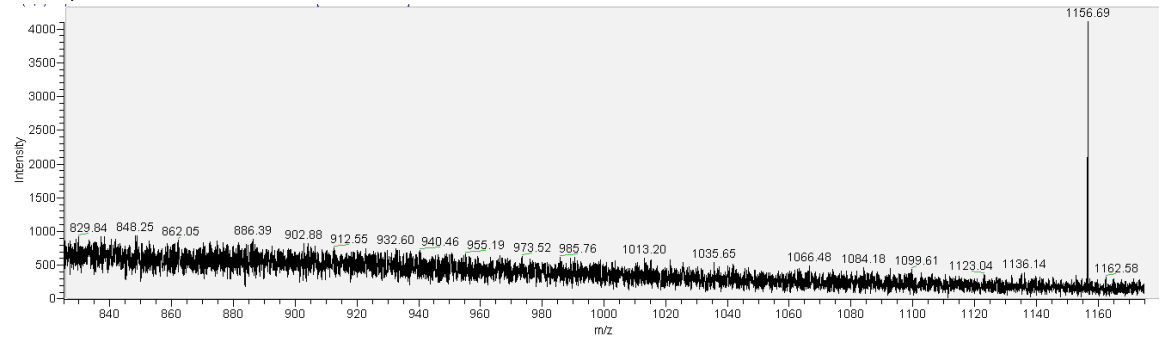

TTP

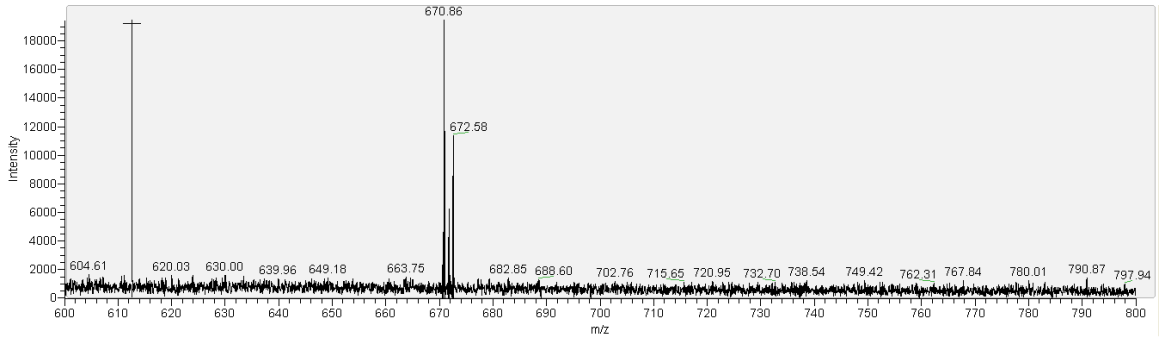

TTPa

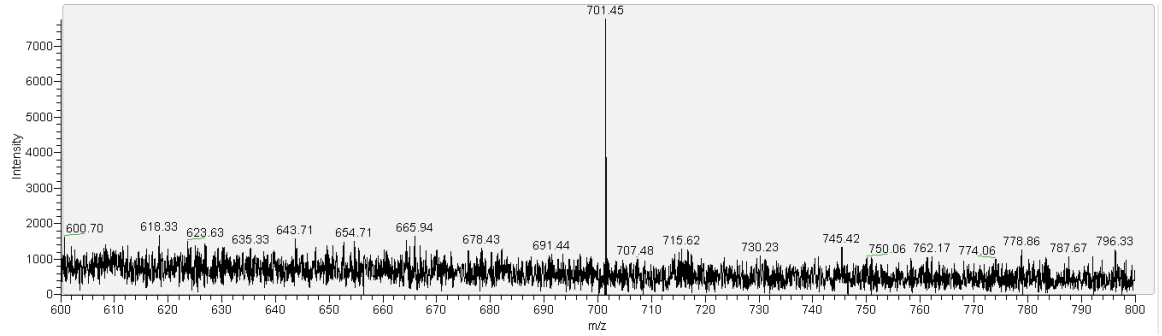

DTDPa

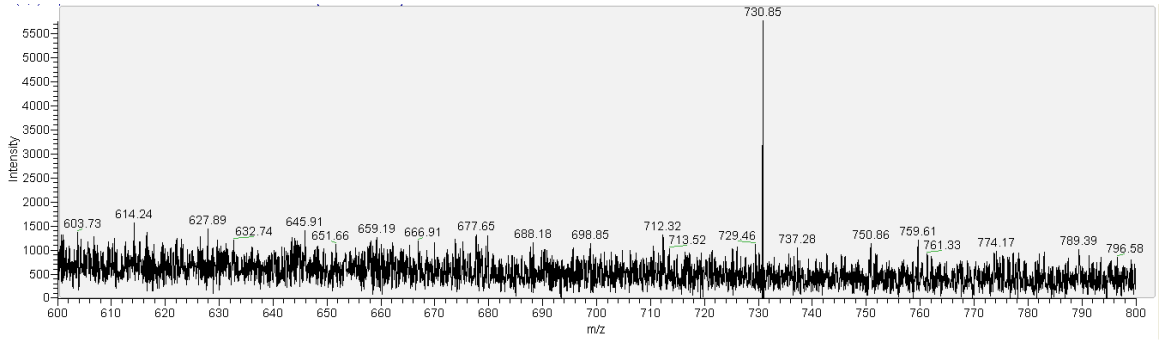

APPENDIX C: TEM IMAGES OF QUANTUM DOT COUPLING EXPERIMENTS

2.2 nm spacing

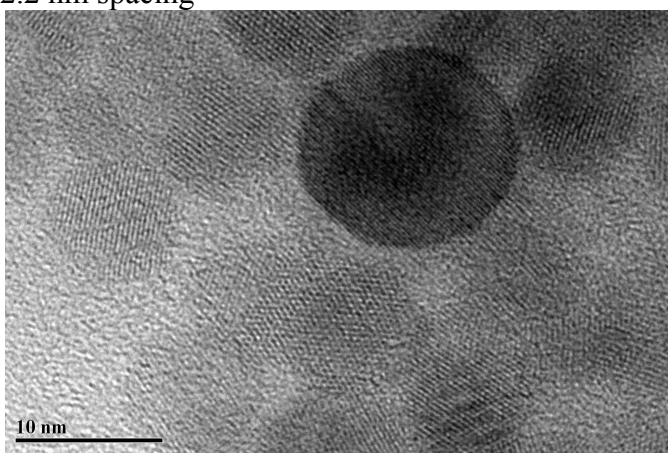

2.7 nm spacing

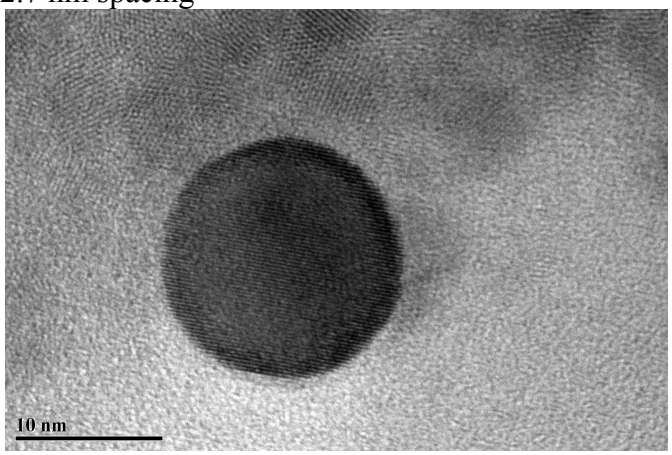

3.0 nm spacing

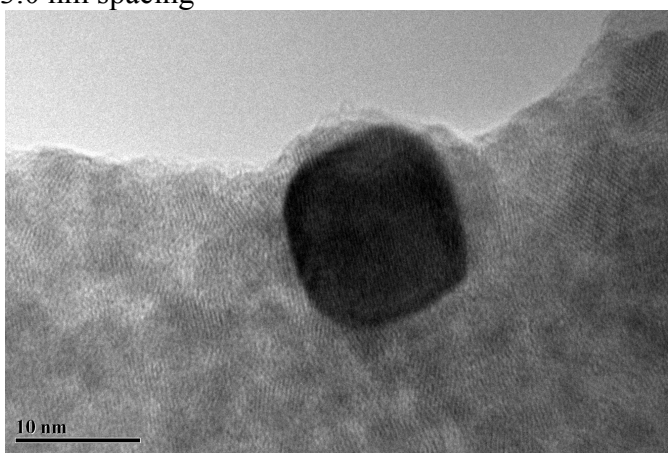

3.7 nm spacing

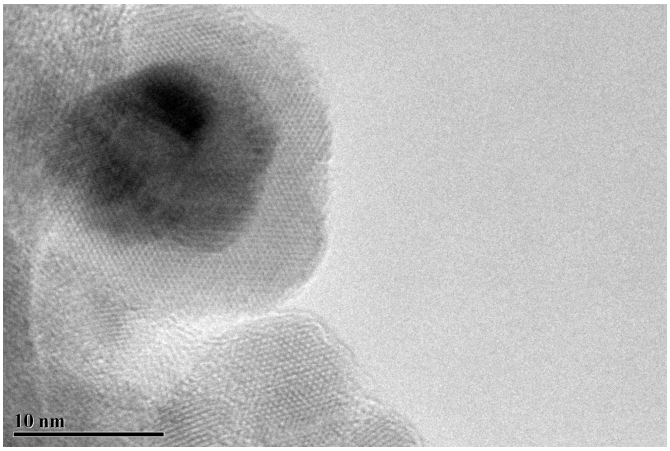

7.5 nm spacing

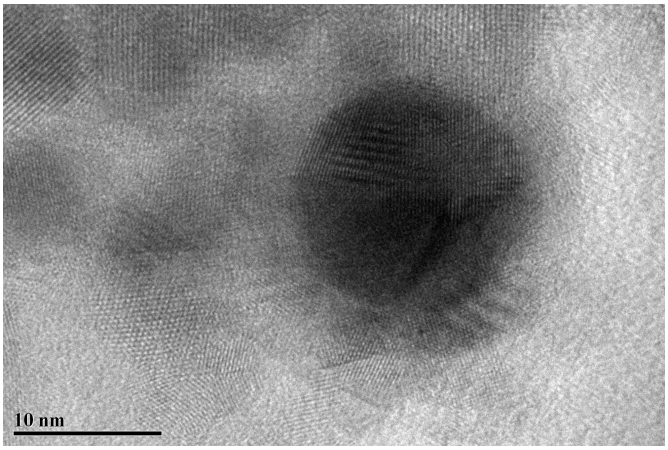

5.2 nm spacing

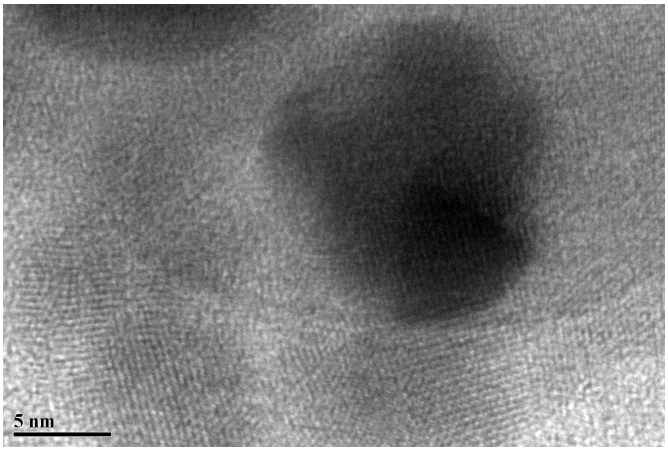

4.9 nm spacing

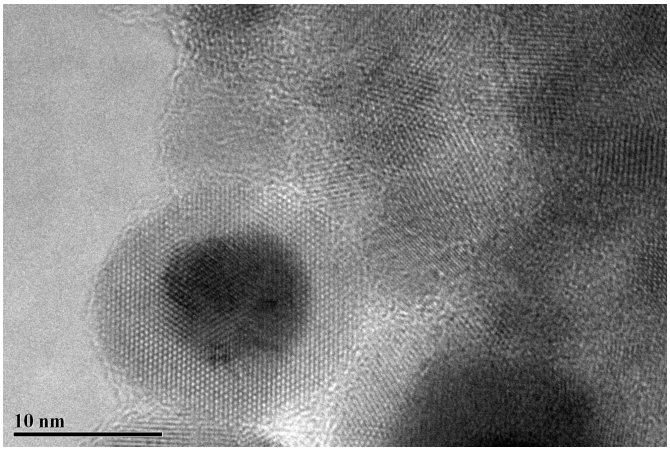

13.1nm spacing

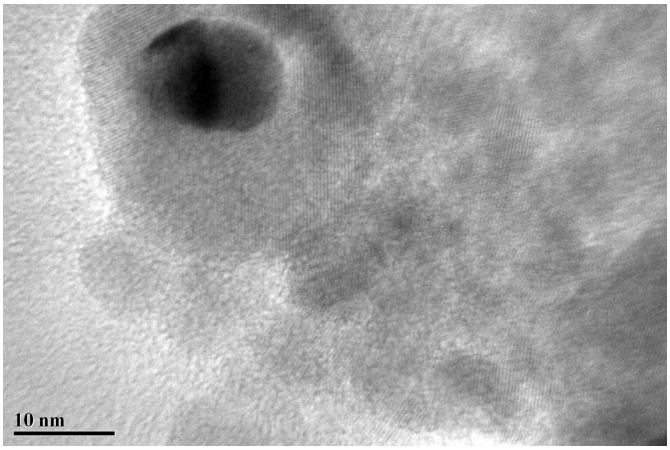

16.0 nm spacing

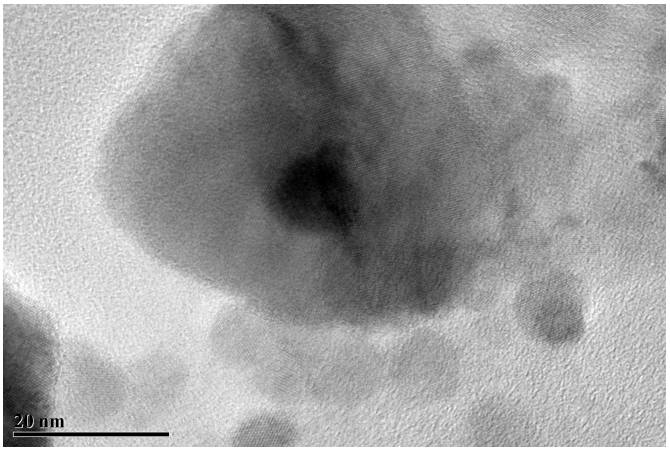

9.9 nm spacing

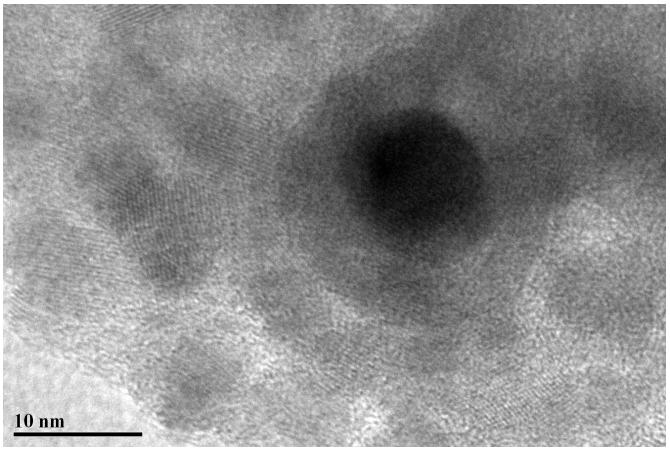
10 nm